Signal Processing Techniques for Optical Wireless Communication Systems

Ali Waqar Azim

To cite this version:

Ali Waqar Azim. Signal Processing Techniques for Optical Wireless Communication Systems. Optics / Photonic. Université Grenoble Alpes, 2018. English. NNT : 2018GREAT059 . tel-01973203

HAL Id: tel-01973203
https://theses.hal.science/tel-01973203

Submitted on 8 Jan 2019

Communauté
UNIVERSITÉ Grenoble Alpes

THÈSE

Pour obtenir le grade de

DOCTEUR DE LA COMMUNAUTE UNIVERSITE GRENOBLE ALPES

Spécialité : **OPTIQUE ET RADIOFREQUENCES**

Arrêté ministériel : 25 mai 2016

Présentée par

Ali Waqar AZIM

Thèse dirigée par **Yannis LE GUENNEC, MCF, Grenoble-INP**, et codirigée par **Ghislaine MAURY, MCF, Grenoble-INP**

préparée au sein du **Laboratoire Institut de Microélectronique, Electromagnétisme et Photonique – Laboratoire d'hyperfréquences et de caractérisation (IMEP-LAHC)**
dans **l'École Doctorale Electronique, Electrotechnique, Automatique, Traitement du Signal (EEATS)**

Signal Processing Techniques for Optical Wireless Communications

(Technique de traitement du signal pour les systemes de communication optique sans fil)

Thèse soutenue publiquement le **18 septembre 2018**
devant le jury composé de :

Monsieur Laurent CLAVIER
Professeur, Télécom Lille (Président)
Madame Anne JULIEN-VERGONJANNE
Professeur, Université de Limoges (Rapporteur)
Monsieur Mohammad-Ali KHALIGHI
Maître de conférences, Ecole Centrale Marseille (Rapporteur)
Madame Christelle AUPETIT-BERTHELEMOT
Professeur, Université de Limoges (Examinateur)
Monsieur Yannis LE GUENNEC
Maître de Conférences, Grenoble-INP (Directeur de these)
Madame Ghislaine MAURY
Maître de Conférences, Grenoble INP (Co-directeur de these)
Monsieur Laurent ROS
Maître de Conférences, Grenoble-INP (Invitè)

UNIVERSITÉ GRENOBLE ALPES

Abstract

Signal Processing Techniques for Optical Wireless Communications

by Ali Waqar AZIM

The radio-frequency (RF) spectrum is dwindling due to an increase in the demand of wireless applications. Hence, there is substantial demand of alternative spectrum regions for communications to recline the conventional RF spectrum. In this context, optical wireless communications (OWC) is explored as a likely candidate to supplement the RF communications. The current work focuses on impairment mitigation techniques and energy-efficient modulation approaches for OWC. Firstly, the peak-to-average power ratio (PAPR) for optical-orthogonal frequency division multiplexing (O-OFDM) is studied and two decision-directed PAPR reduction techniques are presented. The complexity of these methods is comparatively lower than other PAPR reduction methods, whilst, their performance is likewise analogous with other alternatives. Secondly, an optical-single-carrier frequency division multiple access (O-SCFDMA) approach, referred to as Hermitian symmetry free O-SCFDMA (HSFO-SCFDMA) is proposed, that averts Hermitian symmetry which is normally expected for other O-OFDM and O-SCFDMA approaches. The simulation results affirm that HSFO-SCFDMA is more efficient than any other O-SCFDMA approach for OWC and manifests the lowest PAPR among the other alternatives. Thirdly, the performance of precoding is analyzed for layered asymmetrically clipped O-OFDM (LACO-OFDM). Two types of precoding are employed, i.e., Fourier transform precoding and Hartley transform precoding. It is established that Hartley transform precoded LACO-OFDM exhibits the lowest PAPR and is less vulnerable to non-linear distortion introduced by the light emitting diodes (LEDs), howbeit, the signal-to-noise ratio (SNR) increase (both electrical and optical) owing to the layered structure is higher than conventional LACO-OFDM.

Acknowledgements

First, I would like to praise Allah Almighty for being the foundation of my life and for His infinite blessings upon me. Without His guidance I would never have been able to make this far.

I wish to convey my profoundest and sincerest gratitude to my supervisors *Yannis Le Guennec* and *Ghislaine Maury* for their valuable and insightful guidance, tenacious support and confidence in my abilities throughout my research work. I accomplished a lot from their vast professional vision and scientific wisdom and I couldn't ask more in my supervisors. This dissertation would not have been possible without them. It has been a real honor and priviledge to have been your student.

I owe a debt of gratitude to many people who helped me in innumerable ways over the duration of my masters and my research. It is not possible to acknowledge everyone who has helped me in some way, but I would like to mention the following. I would like to express my special thanks to Laurént Ros for his valuable feedback. I owe a special thanks to Dhalila, Isabelle, Annaick, Valerie, Brigette and Fabien for taking care of all the administrative matters.

I am grateful to Grenoble-INP for providing me the means necessary to undergo my PhD. I am thankful to French government for having conviction in me and granting me with the scholarship which aided me accomplish my PhD in an undisturbed manner. I feel indebted to the both Grenoble-INP and the French government to allocate alot in my higher eduction and providing me scholarships for both Masters and PhD.

I would like to acknowledge my friends for supporting me throughout my PhD and making my experience cheerful. I thank Boubacar and Hamza for helping me to settle in Grenoble when I arrived. I would like to thank Mohamad and Nisrine for by being my official French translators and helping me a lot in different official stuff. I thank Ekta, Victoria, Ali, Habib and Matthieu for being nice company.

I would like to express my truest gratitude and humility to my parents, for their unequivocal love, affection and support and all their sacrifices they made. I don't have ample room to express my appreciation for them; however, they deserve every bit of credit for my success. I am perpetually indebted to them forever. I thank my sisters and my brother, for their support and encouragement.

Last but not the least, special thanks to my wife, *Mahrukh*, for her devotion, support, encouragement and understanding throughout my PhD and above all, for always being by my side through this journey of my life. I don't have words to express my love for my son, *Abdullah*. He has been a transcendent source of delight through out this period.

On a concluding note, the quote below is dedicated to all the people who have helped, inspired and encouraged me along the way. Thank you all!

There is no such thing as a "self-made" man. We are made up of thousands of others. Everyone who has ever done a kind deed for us, or spoken one word of encouragement to us, has entered into the make-up of our character and of our thoughts.

Contents

List of Figures

List of Tables

List of Abbreviations

ACO-OFDM	Asymmetrically Clipped Optical-Orthogonal Frequency-Division Multiplexing
ACO-SCFDE	Asymmetically Clipped Optical-Single-Carrier Frequency Domain Equalization
ACO-SCFDMA	Asymmetically Clipped Optical-Single-Carrier Frequency-Division Multiple-Access
ADC	Analog-to-Digital Converter
AP	Access Point
ASE-DMT	Augmented Spectral Efficiency Discrete Multi-Tone
AWG	Arbitrary Waveform Generator
AWGN	Additive White Gaussian Noise
BER	Bit Error Rate
C2C	Chip-to-Chip
CCDF	Complementary Cumulative Distribution Function
CIR	Channel-Impulse Response
CLT	Central Limit Theorem
CN	Core Network
$\mathbf{C0_2}$	Carbon Dioxide
CP	Cyclic Prefix
D2D	Device-to-Device
DAC	Digital-to-Analog Converter
DC	Direct-Current
DCO-OFDM	Direct-Current biased Optical-Orthogonal Frequency-Division Multiplexing
DFT	Discrete Fourier Transfrom
DFB	Distributed Feedback
DHT	Discrete Hartley Transfrom
DMT	Discrete Multi-Tone
DSO	Digital Sampling Oscilloscope
ECG	Electrocardiography
EM	Electromagnetic
EMG	Electromyography
ENOB	Effective Number of Bits
eU-OFDM	Enhanced Unipolar-Orthogonal Frequency-Division Multiplexing
EVM	Error Vector Magnitude
FD	Frequency-Domain
FDCDR	Frequency-Domain Clipping Distortion Removal
FEC	Forward Error Correcting
FFT	Fast Fourier Transform
FSO	Free Space Optics
FTN	Faster Than Nyquist

FTP-ACO-OFDM	Fourier Transform Precoded Asymmetrically Clipped Optical-Orthogonal Frequency-Division Multiplexing
FTP-DCO-OFDM	Fourier Transform Precoded Direct-Current biased Optical-Orthogonal Frequency-Division Multiplexing
FTP-LACO-OFDM	Fourier Transform Precoded Layered Asymmetrically Clipped Optical-Orthogonal Frequency-Division Multiplexing
FoV	Field-of-View
GaS	Gallium Arsenide
GaN	Gallium Nitride
HD	High Definition
HS	Hermitian Symmetry
HSFO-SCFDMA	Hermitian Symmetry Free Optical-Single-Carrier Frequency-Division Multiple-Access
HTP-ACO-OFDM	Hartley Transform Precoded Asymmetrically Clipped Optical-Orthogonal Frequency-Division Multiplexing
HTP-LACO-OFDM	Hartley Transform Precoded Layered Asymmetrically Clipped Optical-Orthogonal Frequency-Division Multiplexing
IDFT	Inverse Discrete Fourier Transform
IDHT	Inverse Discrete Hartley Transform
IEEE	Institute of Electrical and Electronics Engineers
IFFT	Inverse Fast Fourier Transform
IM-DD	Intensity-Modulation and Direct-Detection
IoT	Internet-of-Things
IR	Infrared
IrDA	Infrared Data Association
IS	Image Sensor
I-SCFDMA	Interleaved-Single-Carrier Frequency-Division Multiple-Access
ISI	Inter-Symbol Interference
LAN	Local Area Network
LACO-OFDM	Layered Asymmetrically Clipped Optical-Orthogonal Frequency-Division Multiplexing
LD	Laser-Diode
LED	Light-Emitting Diode
LiFi	Light-Fidelity
LoS	Line-of-Sight
M2M	Machine-to-Machine
MA	Multiple-Access
MAN	Metropolitan Area Network
MC	Multi-Carrier
MIMO	Multiple-Input Multiple-Output
MMSE	Minimum Mean Square Error
mmWave	Millimeter Wave
NOMA	Non-orthogonal Multiple Access
NLOS	Non-Line-of-Sight
OFDM	Orthogonal Frequency-Division Multiplexing
OFDMA	Orthogonal Frequency-Division Multiple-Access
OCC	Optical Camera Communication

OMEGA	hOME Gigabit Access
O-OFDM	Optical-Orthogonal Frequency-Division Multiplexing
OOK	On-Off Keying
O-SCFDMA	Optical-Single-Carrier Frequency-Division Multiple-Access
OWC	Optical Wireless Communication
P2P	Point-to-Point
PA	Pilot-Assisted
PAM	Pulse-Amplitude Modulation
PAM-DMT	Pulse-Amplitude Modulation Discrete Multi-Tone
PAPR	Peak-to-Average Power Ratio
PD	Photo-Diode
PDF	Probability Density Function
PPM	Pulse-Position Modulation
PSD	Power Spectral Density
P/S	Parallel-to-Serial
PTS	Partial Transmit Sequence
QAM	Quadrature-Amplitude Modulation
RF	Radio-Frequency
RGB	Red-Green-Blue
RCLED	Resonant Cavity Light-Emitting Diode
SC	Single-Carrier
SCO-FDM	Single-Carrier Frequency Division Multiplexing
SE	Spectral Efficiency
SLM	Selected-Mapping
SNR	Signal-to-Noise Ratio
S/P	Serial-to-Parallel
TD	Time-Domain
TDCSR	Time-Domain Clipped Sample Reconstruction
TIA	Trans-Impedance Amplifier
TR	Tone Reservation
TV	Television
UE	User Equipment
UL	Upper-Level
U-OFDM	Unipolar-Orthogonal Frequency-Division Multiplexing
UV	Ultraviolet
V2V	Vehicle-to-Vehicle
V2X	Vehicle-to-Infrastructure
VL	Visible Light
VLC	Visible Light Communication
VLCC	Visible Light Communication Consortium
WBAN	Wireless Boday Area Network
WDM	Wavelength Division Multiplexing
WiFi	Wireless-Fidelity
WLAN	Wireless Local Area Network
WPAN	Wireless Personal Area Network

ZF	Zero-Forcing
μ**LED**	Micro Light-Emitting Diode

List of Notations (In order of occurance)

$P_{(\text{opt})}$	Transmitted optical power in Watt
$R(\phi)$	Radiation profile of light source
m	Lambertian emission order
$\phi_{1/2}$	Half power semi angle
$G_{\text{OF}}(\psi)$	Gain of optical filter
ψ	Incident angle at the receiver
G_{OF}	Gain of optical concentrator
n_{ref}	Effective refractive index
ψ_{FoV}	Field-of-view at the receiver
A_{PD}	Area of the photodiode
A_{eff}	Effective area of the photodiode
ϖ	Responsitivity of photodetector in Ampere/Watt
$x(t)$	Intensity waveform
$u(t)$	Optical intensity signal
ω	Electrical-to-optical conversion factor
$h(t)$	Channel impulse response
$g(t)$	Photodetected signal
$w(t)$	Additive white Gaussian noise
$y(t)$	Received analog signal
N_0	Noise power spectral density
$h_{\text{chan}}(t)$	Optical wireless channel impulse response
$h_{\text{led}}(t)$	Channel impulse response of LED/LED driver combination
$H(f)$	Frequency response of the channel
$H_{\text{chan}}(f)$	Frequency response of the optical wireless channel
$H_{\text{led}}(f)$	Frequency response of the LED/LED driver combination
$\mathcal{S}$	Lighting source
$\overrightarrow{a}_{\text{s}}$	Location vector of lighting source
$\overrightarrow{o}_{\text{s}}$	Orientation vector of lighting source
$\mathcal{R}$	Receiving element
$\overrightarrow{a}_{\text{r}}$	Location vector of receiving element
$\overrightarrow{o}_{\text{r}}$	Orientation vector of receiving element
D	Euclidean distance between lighting source and receiving element
ϕ	Radiant angle
H_{DC}	DC gain of optical wireless channel
$\mathcal{S}_{\text{tx}}$	Transmitting source
$\mathcal{R}_{\text{rx}}$	Receiving source
$\delta(\cdot)$	Delta function

c	Speed of light
$h^{[0]}\left(t, \mathcal{S}_{\mathrm{tx}}, \mathcal{R}_{\mathrm{rx}}\right)$	Line-of-sight channel impulse response
i_{bounce}	Number of reflection/bounces
N_{LED}	Number of light-emitting-diodes
N_{b}	Number of blocks in reflecting element
$\overrightarrow{a}_{\mathrm{b}}$	Location vector of block
$\overrightarrow{o}_{\mathrm{b}}$	Orientation vector of block
$\mathcal{S}_{\mathrm{b}}$	Souce block
$\mathcal{R}_{\mathrm{b}}$	Receiving block
ρ	Reflectivity coefficient
ρ_b	Reflectivity coefficient of the block
ΔA	Physical area of the receiving block
ψ_{b}	Incident angle at block receiver
ϕ_{b}	Radiant angle at block source
D_{b}	Euclidean distance between the souce and receiving block
N_0^{shot}	Power spectral density of shot noise
N_0^{thermal}	Power spectral density of thermal noise
q	Charge on electron in Coulombs
P_{rx}	Received optical power
R_{L}	Equivalent resistance of the receiver circuit
T_{k}	Temperature of the receiver circuit
k_{b}	Boltzmann constant
$\hat{I}_{\mathrm{min}}$	Minimum current to turn on the light emitting diode
$\hat{P}^{\mathrm{min}}_{(\mathrm{opt})}$	Minimum optical power to turn on the light emitting diode
$\hat{I}_{\mathrm{max}}$	Saturation current of light emitting diode
$\hat{P}^{\mathrm{max}}_{(\mathrm{opt})}$	Saturation optical power of light emitting diode
G	Conversion coefficient from input current to optical output power
I_{in}	Input current to the light emitting diode
I^{max}	Maximum current to the light emitting diode
$P^{\mathrm{max}}_{(\mathrm{opt})}$	Maximum optical power at light emitting diode
$r(n)$	Arbitrary time-domain signal
$R(k)$	Arbitrary frequency-domain signal
$\mathbb{C}$	Complex numbers
$\mathbb{R}$	Real numbers
$\mathrm{IDFT}[\cdot]$	Inverse discrete Fourier transform
$\mathrm{DFT}[\cdot]$	Discrete Fourier transform
$\mathrm{IDHT}[\cdot]$	Inverse discrete Hartley transform
$\mathrm{DHT}[\cdot]$	Discrete Hartley transform
n	Index identifier time-domain samples
k	Index identifier of frequency-domain symbols
$\exp(\cdot)$	Exponent function
$\cos(\cdot)$	Cosine function
$\sin(\cdot)$	Sine function
N	Number of subcarriers/subchannels

j	The imaginary number, i.e., $\sqrt{-1}$
$\boldsymbol{\mathcal{Q}}$	Quadrature-amplitude modulation (QAM) constellation set
M	QAM modulation order
$X^{(\mathrm{D})}(\cdot)$	Frequency-domain symbols modulation for DCO-OFDM with Hermitian symmetry
$k^{(\mathrm{D})}$	Index identifier for DCO-OFDM frequency-domain symbols
$X(\cdot)$	Frequency-domain symbols for all techniques
$x(n)$	Discrete time-domain signal
$\tilde{x}(t)$	Analog time-domain signal for DCO-OFDM/FTP-DCO-OFDM prior to bias-index addition
$\hat{x}(t)$	Analog time-domain signal for DCO-OFDM/FTP-DCO-OFDM after bias-index addition
$(\cdot)^*$	Congujate operation
$\Re[\cdot]$	Real part of complex number
$\Im[\cdot]$	Imaginary part of complex number
$\beta_{\mathrm{DC}}^{(\mathrm{D})}$	Bias-index for DCO-OFDM
$\varsigma_{(\mathrm{D})}$	Constant of proportionality to evaluate bias-index of DCO-OFDM
$n_{\mathrm{c}}(\beta_{\mathrm{DC}}^{(\mathrm{D})})$	Bias-index dependent clipping noise
$Y(\cdot)$	Frequency-domain symbols at the receiver for all modulation techniques
$\hat{Y}(\cdot)$	Equalized frequency-domain symbols at the receiver for all modulation techniques
$\hat{X}(\cdot)$	Estimated transmitted symbols at the receiver after equalization
$Z(\cdot)$	AWGN coloured by frequency-domain channel coefficients
$\hat{X}^{(\mathrm{D})}(\cdot)$	Estimated frequency-domain symbols for DCO-OFDM
X_{Q}	All elements in $\boldsymbol{\mathcal{Q}}$
B	Bandwidth of the signal
T_{sym}	O-OFDM symbol period
T_{OFDM}	O-OFDM symbol duration after addition of CP
R_{b}	Date-rate
η_{DCO}	Spectral efficiency of DCO-OFDM
λ	Peak-to-average power ratio
$\vert \cdot \vert$	Absolute operator
$(\cdot)^2$	Square operation
$E(\cdot)$	Statistical expectation
σ_x^2	Variance of the signal
$p(\cdot)$	Probability density function
$Q(\cdot)$	Q-function
$\mathbb{R}^+$	Set of real non-negative values
$P_{(\mathrm{opt,DCO})}$	Optical power for DCO-OFDM
$P_{(\mathrm{elec,DCO})}$	Electrical power for DCO-OFDM
$\alpha_{\mathrm{DCO}}^{\mathrm{OE}}$	Optical-to-electrical conversion efficiency of DCO-OFDM
$E_{\mathrm{b}_{(\mathrm{elec})}}$	Electrical energy per bit
$E_{\mathrm{b}_{(\mathrm{opt})}}$	Optical energy per bit
$E_{\mathrm{b}_{(\mathrm{opt})}}/N_0$	Electrical signal-to-noise ratio (SNR) per bit
$E_{\mathrm{b}_{(\mathrm{opt})}}/N_0$	Optical signal-to-noise ratio (SNR) per bit
$X^{(\mathrm{A})}(\cdot)$	Frequency-domain symbols modulation for ACO-OFDM with Hermitian symmetry
$k^{(\mathrm{A})}$	Index identifier for ACO-OFDM frequency-domain symbols
$\tilde{x}(n)$	Discrete time-domain signal for ACO-OFDM prior to clipping

$\tilde{n}^{(A)}$	Index identifier used to illustrate the anti-symmetric property of ACO-OFDM
$N_{\mathrm{c}}(k)$	Frequency-domain clipping noise due to zero-level clipping of ACO-OFDM
$X_{\mathrm{c}}(k)$	Frequency-domain signal for ACO-OFDM after zero-level clipping
$\hat{X}^{(\mathrm{A})}(\cdot)$	Estimated frequency-domain symbols for ACO-OFDM
η_{ACO}	Spectral efficiency of ACO-OFDM
$P_{(\mathrm{opt,ACO})}$	Optical power for ACO-OFDM
$P_{(\mathrm{elec,ACO})}$	Electrical power for ACO-OFDM
$\alpha_{\mathrm{ACO}}^{\mathrm{OE}}$	Optical-to-electrical conversion efficiency of ACO-OFDM
$x^{(\mathrm{PD})}(\cdot)$	Time-domain symbols for FTP-DCO-OFDM prior to precoding
$n^{(\mathrm{PD})}$	Index identifier for time-domain FTP-DCO-OFDM symbols
$X^{(\mathrm{PD})}(\cdot)$	Frequency-domain precoded symbols for FTP-DCO-OFDM
$k^{(\mathrm{PD})}$	Index identifier for frequency-domain FTP-DCO-OFDM symbols
$\beta_{\mathrm{DC}}^{(\mathrm{PD})}$	Bias-index for FTP-DCO-OFDM
$\varsigma_{(\mathrm{PD})}$	Constant of proportionality to evaluate bias-index of FTP-DCO-OFDM
$\hat{y}(\cdot)$	Time-domain symbols for FTP-DCO-OFDM/FTP-ACO-OFDM/HTP-ACO-OFDM/SCO-FDM prior to demodulation
$\hat{x}^{(\mathrm{PD})}(\cdot)$	Estimated symbols for FTP-DCO-OFDM
η_{PD}	Spectral efficiency of FTP-DCO-OFDM
$P_{(\mathrm{opt,PD})}$	Optical power for FTP-DCO-OFDM
$P_{(\mathrm{elec,PD})}$	Electrical power for FTP-DCO-OFDM
$\alpha_{\mathrm{PD}}^{\mathrm{OE}}$	Optical-to-electrical conversion efficiency of FTP-DCO-OFDM
$x^{(\mathrm{PA})}(\cdot)$	Time-domain symbols for FTP-ACO-OFDM prior to precoding
$n^{(\mathrm{PA})}$	Index identifier for time-domain FTP-ACO-OFDM symbols
$X^{(\mathrm{PA})}(\cdot)$	Frequency-domain precoded symbols for FTP-ACO-OFDM
$k^{(\mathrm{PA})}$	Index identifier for frequency-domain FTP-ACO-OFDM symbols
$\tilde{n}^{(PA)}$	Index identifier used to illustrate the anti-symmetric property of FTP-ACO-OFDM
$\hat{x}^{(PA)}(\cdot)$	Estimated symbols for FTP-ACO-OFDM
η_{PA}	Spectral efficiency of FTP-ACO-OFDM
$P_{(\mathrm{opt,PA})}$	Optical power for FTP-ACO-OFDM
$P_{(\mathrm{elec,PA})}$	Electrical power for FTP-ACO-OFDM
$\alpha_{\mathrm{PA}}^{\mathrm{OE}}$	Optical-to-electrical conversion efficiency of FTP-ACO-OFDM
$\beta_{\mathrm{PA}}^{\mathrm{pen}}$	Penalty in optical-to-electrical conversion efficiency for FTP-ACO-OFDM w.r.t ACO-OFDM
$\boldsymbol{\mathcal{P}}$	Pulse-amplitude modulation (PAM) constellation set
$x^{(\mathrm{HPA})}(\cdot)$	Time-domain symbols for HTP-ACO-OFDM prior to precoding
$n^{(\mathrm{HPA})}$	Index identifier for time-domain HTP-ACO-OFDM symbols
$X^{(\mathrm{HPA})}(\cdot)$	Frequency-domain precoded symbols for HTP-ACO-OFDM
$k^{(\mathrm{HPA})}$	Index identifier for frequency-domain HTP-ACO-OFDM symbols
$H_{\mathrm{e}}(k)$	Even component of channel frequency response
$H_{\mathrm{o}}(k)$	Odd component of channel frequency response
$\hat{x}^{(HPA)}(\cdot)$	Estimated symbols for HTP-ACO-OFDM
η_{HPA}	Spectral efficiency of HTP-ACO-OFDM
$P_{(\mathrm{opt,HPA})}$	Optical power for HTP-ACO-OFDM
$P_{(\mathrm{elec,HPA})}$	Electrical power for HTP-ACO-OFDM
$\alpha_{\mathrm{HPA}}^{\mathrm{OE}}$	Optical-to-electrical conversion efficiency of HTP-ACO-OFDM
$\beta_{\mathrm{HPA}}^{\mathrm{pen}}$	Penalty in optical-to-electrical conversion efficiency for HTP-ACO-OFDM w.r.t ACO-OFDM

$x^{(\mathrm{SCO})}(\cdot)$	Time-domain symbols for SCO-FDM prior to precoding
$n^{(\mathrm{SCO})}$	Index identifier for time-domain SCO-FDM symbols
$X^{(\mathrm{SCO})}(\cdot)$	Frequency-domain precoded symbols for SCO-FDM
$k^{(\mathrm{SCO})}$	Index identifier for frequency-domain SCO-FDM symbols
$\tilde{x}_1\left(n^{(\mathrm{SCO})}\right)$	First frame of symmetric time-domain signal for SCO-FDM
$\tilde{x}_2\left(n^{(\mathrm{SCO})}\right)$	Second frame of symmetric time-domain signal for SCO-FDM
$\tilde{x}_2\left(n^{(\mathrm{SCO})}\right)$	Third frame of symmetric time-domain signal for SCO-FDM
$\tilde{x}_3\left(n^{(\mathrm{SCO})}\right)$	Fourth frame of symmetric time-domain signal for SCO-FDM
$r^{+}\left(n^{(\mathrm{SCO})}\right)$	Positive values of real-component from first frame of SCO-FDM time-domain signal
$r^{-}\left(n^{(\mathrm{SCO})}\right)$	Negative values of real-component from second frame of SCO-FDM time-domain signal
$i^{+}\left(n^{(\mathrm{SCO})}\right)$	Positive values of imaginary-component from third frame of SCO-FDM time-domain signal
$i^{-}\left(n^{(\mathrm{SCO})}\right)$	Negative values of imaginary-component from fourth frame of SCO-FDM time-domain signal
$y_r^{+}\left(n^{(\mathrm{SCO})}\right)$	Received signal corresponding to positive values of real-component for SCO-FDM
$y_r^{-}\left(n^{(\mathrm{SCO})}\right)$	Received signal corresponding to negative values of real-component for SCO-FDM
$y_i^{+}\left(n^{(\mathrm{SCO})}\right)$	Received signal corresponding to positive values of imaginary-component for SCO-FDM
$y_i^{-}\left(n^{(\mathrm{SCO})}\right)$	Received signal corresponding to negative values of imaginary-component for SCO-FDM
$Y_r^{+}\left(k^{(\mathrm{SCO})}\right)$	Frequency-domain counterpart of $y_r^{+}\left(n^{(\mathrm{SCO})}\right)$
$Y_r^{-}\left(k^{(\mathrm{SCO})}\right)$	Frequency-domain counterpart of $y_r^{-}\left(n^{(\mathrm{SCO})}\right)$
$Y_i^{+}\left(k^{(\mathrm{SCO})}\right)$	Frequency-domain counterpart of $y_i^{+}\left(n^{(\mathrm{SCO})}\right)$
$Y_i^{-}\left(k^{(\mathrm{SCO})}\right)$	Frequency-domain counterpart of $y_i^{-}\left(n^{(\mathrm{SCO})}\right)$
$\hat{Y}_r\left(k^{(\mathrm{SCO})}\right)$	Equalized frequency-domain signal of the real-componets of SCO-FDM
$\hat{Y}_i\left(k^{(\mathrm{SCO})}\right)$	Equalized frequency-domain signal of the imaginary-componets of SCO-FDM
$\hat{Y}\left(k^{(\mathrm{SCO})}\right)$	Received frequency-domain signal for SCO-FDM
$\hat{x}^{(\mathrm{SCO})}(\cdot)$	Estimated symbols forSCO-FDM
η_{SCO}	Spectral efficiency of SCO-FDM
$P_{(\mathrm{opt,SCO})}$	Optical power for SCO-FDM
$P_{(\mathrm{elec,SCO})}$	Electrical power for SCO-FDM
$\alpha_{\mathrm{SCO}}^{\mathrm{OE}}$	Optical-to-electrical conversion efficiency of SCO-FDM
$\beta_{\mathrm{SCO}}^{\mathrm{pen}}$	Penalty in optical-to-electrical conversion efficiency for SCO-FDM w.r.t ACO-OFDM
U	Cardinality of phase sequences used for selected-mapping (SLM)
$P^{(u)}(k)$	uth phase sequence vector
$R^{(u)}(k)$	Signal obtained after multiplication of uth phase sequence vector with frequency-signal
$r^{(u)}(n)$	Time-domain counterpart of $R^{(u)}(k)$
$\lambda^{(u)}$	PAPR obtained for the uth phase sequence
$\log_2\lfloor r\rfloor$	Greatest integer lower than r
$\mathbb{Z}$	Set of integers
ξ_{upper}	Upper level clipped amplitude
ξ_{upper}	Lower level clipped amplitude
γ	Clipping threshold
$x^{\mathrm{c}}(n)$	Clipped discrete time-domain signal
α	Linear attenuation factor

$d(n)$	Clipping distortion components
$x^{\mathrm{c}}(t)$	Clipped analog time-domain signal
$\mathrm{erfc}(\cdot)$	Complementary error function
$\mathrm{erf}(\cdot)$	Error function
$\sigma^2_{x^{\mathrm{c}}}$	Variance of clipped signal
σ^2_{d}	Power of clipping distortion
Γ_{elec}	Electrical SNR
ζ_{B}	Bandwidth utlization factor of double sided bandwidth B
ζ_{DC}	Attenuation to electrical signal due to bias-index
i	Number of iterations for TDCSR and FDCDR
$\hat{r}(n)$	Reference signal for TDCSR
$\theta^{(i)}(k)$	Input Frequency-domain symbols to TDCSR and FDCDR for ith iteration
$\hat{\theta}^{(i)}(k)$	Decisions on $\theta^{(i)}(k)$ for ith iteration for both TDCSR and FDCDR
$\hat{s}^{(i)}(n)$	Time-domain counterpart of $\hat{\theta}^{(i)}(k)$ for ith iteration for both TDCSR and FDCDR
$\tilde{r}^{(i)}(n)$	Reconstructed signal of TDCSR for the ith iteration
$\theta_r^{(i)}(k)$	Frequency-domain counterpart of $\tilde{r}^{(i)}(n)$
$D^{(i)}(k) = 0$	Frequency-domain clipping distortion for the ith iteration of FDCDR
$\hat{c}^{(i)}(n)$	Clipped time-domain signal at the ith iteration in FDCDR
$\hat{\theta}_c^{(i)}(k)$	Frequency-domain counterpart of $\hat{c}^{(i)}(n)$ at the ith iteration in FDCDR
Q_b	Effective number of bits (ENOB) for the digital-to-analog converter DAC
$\mathcal{L}$	Quantization levels for the DAC
$\triangle\xi$	Signal amplitude dynamic
σ^2_{DAC}	Variance of the quantization noise imposed by DAC
μ	Difference between two adjacent quantization levels
$\langle E_{\mathrm{b}_{(\mathrm{elec})}}/N_0\rangle$	The expected $E_{\mathrm{b}_{(\mathrm{elec})}}/N_0$ for a BER of 10^{-3}
$x^{(\mathrm{H})}(\cdot)$	Time-domain symbols for HSFO-SCFDMA prior to precoding
$n^{(\mathrm{H})}$	Index identifier for time-domain HSFO-SCFDMA symbols
$X^{(\mathrm{H})}(\cdot)$	Frequency-domain precoded symbols for HSFO-SCFDMA
$k^{(\mathrm{H})}$	Index identifier for frequency-domain HSFO-SCFDMA symbols
$x_{\Re}^{(\mathrm{H})}(\cdot)$	Real components for obtained from the first frame of $x(n)$ for HSFO-SCFDMA
$x_{\Im}^{(\mathrm{H})}(\cdot)$	Imaginary components for obtained from the first frame of $x(n)$ for HSFO-SCFDMA
$\tilde{x}(\tilde{n})$	Real valued bipolar signal for HSFO-SCFDMA after addition of CP
$\beta_{\mathrm{DC}}^{(\mathrm{H})}$	Bias-index for HSFO-SCFDMA
$\varsigma_{(\mathrm{H})}$	Constant of proportionality to evaluate bias-index of HSFO-SCFDMA
$\boldsymbol{y}_{\Re}$	Received vector corresponding to real valued HSFO-SCFDMA time-domain signal
$\boldsymbol{y}_{\Im}$	Received vector corresponding to imaginary valued HSFO-SCFDMA time-domain signal
$\boldsymbol{w}_{\Re}$	AWGN vector for real transmitted signal vector
$\boldsymbol{w}_{\Im}$	AWGN vector for imaginary transmitted signal vector
$\boldsymbol{H}_{\Re}$	Channel frequency response for real transmitted signal vector
$\boldsymbol{H}_{\Im}$	Channel frequency response for imaginary transmitted signal vector
$Y_{\Re}(\cdot)$	Frequency-domain components corresponding to $\boldsymbol{y}_{\Re}$
$Y_{\Im}(\cdot)$	Frequency-domain components corresponding to $\boldsymbol{y}_{\Im}$
$\hat{\boldsymbol{Y}}_{\Re}$	Equalized frequency-domain sub-block corresponding to real components
$\hat{\boldsymbol{Y}}_{\Im}$	Equalized frequency-domain sub-block corresponding to imaginary components

$\hat{y}_{\Re}(\cdot)$	Time-domain components corresponding to $\hat{\mathbf{Y}}_{\Re}$ vector
$\hat{y}_{\Im}(\cdot)$	Time-domain components corresponding to $\hat{\mathbf{Y}}_{\Im}$ vector
$P_{(\text{opt,HSFO})}$	Optical power for HSFO-SCFDMA
$P_{(\text{elec,HSFO})}$	Electrical power for HSFO-SCFDMA
$\alpha^{\text{OE}}_{\text{HSFO}}$	Optical-to-electrical conversion efficiency of HSFO-SCFDMA
$M^{'}$	Modulation order for PAM alphabets
η	General parameter used to represent spectral efficiency
$\xi_{\text{peak,HSFO}}$	Peak value of HSFO-SCFDMA time-domain signal
σ^2_{HSFO}	Variance of HSFO-SCFDMA time-domain signal
λ_{HSFO}	PAPR of HSFO-SCFDMA
$\xi_{\text{peak,SCO}}$	Peak value of SCO-FDM time-domain signal
σ^2_{SCO}	Variance of SCO-FDM time-domain signal
λ_{SCO}	PAPR of SCO-FDM
$\xi_{\text{peak,HTP-ACO}}$	Peak value of HTP-ACO-OFDM time-domain signal
$\sigma^2_{\text{HTP-ACO}}$	Variance of HTP-ACO-OFDM time-domain signal
$f_{3\text{dB}}$	3-dB cut-off frequency for LED/LED driver combination
$E^{\text{OOK}}_{\text{b}_{(\text{opt})}}/N_0$	Required optical power by the average optical SNR per bit required for OOK in an AWGN channel with no bandwidth limitation
P_{b}	Target bit-error rate
$\lceil\cdot\rceil$	Ceiling operation to nearest integer
$\gamma_{(\text{H})}$	Number of distinct levels of time-domain signal for HSFO-SCFDMA
$\gamma_{(\text{S})}$	Number of distinct levels of time-domain signal for SCO-FDM
K	Number of users for multiple-access in HSFO-SCFDMA
$x^{(\text{H})}_{l}(\cdot)$	Time-domain signal for the lth user in HSFO-SCFDMA
$n^{(l)}$	Index identifier for the samples of time-domain signal of lth user
$X^{(\text{H})}_{l}(\cdot)$	Frequency-domain signal for the lth user in HSFO-SCFDMA
$k^{(l)}$	Index identifier for the samples of frequency-domain signal of lth user
$X_l(\cdot)$	Frequency-domain signal after subchannel allocation to different users in HSFO-SCFDMA
$x_l(\cdot)$	Time-domain counterpart of $X_l(\cdot)$
$x_{\Re,l}(\cdot)$	Real sub-block for lth user in HSFO-SCFDMA
$x_{\Im,l}(\cdot)$	Imaginary sub-block for lth user in HSFO-SCFDMA
L	Number of layers used in LACO-OFDM and precoded LACO-OFDM approaches
$S^{(l)}(\cdot)$	Frequency-domain symbols at lth layer for LACO-OFDM and precoded LACO-OFDM approaches
$k^{(l)}$	Index identifer at for frequency-domain symbols at lth layer
$s^{(l)}(\cdot)$	Time-domain samples at lth layer for precoded LACO-OFDM approaches prior to precoding
$n^{(l)}$	Index identifer at for time-domain symbols at lth layer
$x^{(l)}(\cdot)$	Antisymmetric time-domain signal at lth layer for LACO-OFDM and precoded LACO-OFDM approaches
$\lfloor x^{(l)}(\cdot)\rfloor$	Clipped time-domain signal at lth layer for LACO-OFDM and precoded LACO-OFDM approaches
$\tilde{S}^{(l)}(\cdot)$	Frequency-domain symbols at lth layer for LACO-OFDM and precoded LACO-OFDM after subcarrier/subchannel demapping
$\hat{S}^{(l)}(\cdot)$	Detected frequency-domain symbols at lth layer for LACO-OFDM

$\tilde{s}^{(l)}(\cdot)$	Time-domain symbols at lth layer for precoded LACO-OFDM after decoding
$\hat{s}^{(l)}(\cdot)$	Detected time-domain symbols at lth layer for precoded LACO-OFDM approaches
$\lfloor \hat{x}^{(l)}(\cdot) \rfloor$	Estimated clipped time-domain signal at lth layer for LACO-OFDM and precoded LACO-OFDM approaches
$\hat{X}^{(l)}(\cdot)$	Estimated frequency-domain signal at lth layer for LACO-OFDM and precoded LACO-OFDM approaches
$\hat{X}_{\mathrm{c}}^{(l)}(\cdot)$	Estimated frequency-domain clipping distortion at lth layer for LACO-OFDM and precoded LACO-OFDM approaches
$x_{\mathrm{D}}^{(l)}(\cdot)$	Time-domain data carrying signal at lth layer in LACO-OFDM and preoceded LACO-OFDM approaches
$x_{\mathrm{C}}^{(l)}(\cdot)$	Time-domain clipping distortion at lth layer in LACO-OFDM and preoceded LACO-OFDM approaches
$k_{\mathrm{D}}^{(l)}$	Index identifer for data-carrying subcarriers/subchannels
$k_{\mathrm{C}}^{(l)}$	Index identifer for clipping distorted subcarriers/subchannels
$X_{\mathrm{D}}^{(l)}(\cdot)$	Frequency-domain counterpart of $x_{\mathrm{D}}^{(l)}(\cdot)$
$X_{\mathrm{C}}^{(l)}(\cdot)$	Frequency-domain counterpart of $x_{\mathrm{C}}^{(l)}(\cdot)$
$P_{(\mathrm{elec},\cdot)}^{(l)}$	Parameter used to represent electrical power of the lth layer LACO-OFDM or precoded LACO-OFDM
$P_{(\mathrm{elec,LACO})}^{(l)}$	Electrical power of the lth layer LACO-OFDM
$P_{(\mathrm{elec,FTP})}^{(l)}$	Electrical power of the lth layer FTP-LACO-OFDM
$P_{(\mathrm{elec,HTP})}^{(l)}$	Electrical power of the lth layer HTP-LACO-OFDM
$P_{(\mathrm{elec},\cdot)}$	Parameter used to represent combined electrical power of all the lth layer LACO-OFDM or precoded LACO-OFDM
Θ	Average number of bits encoded in layered variants with L layers
$\alpha_{(\cdot)}(L,\cdot)$	The increase in $E_{\mathrm{b}_{(\mathrm{elec})}}/N_0$ for L layers in LACO-OFDM and precoded LACO-OFDM approaches
$\alpha_{\mathrm{LACO}}(L)$	The increase in $E_{\mathrm{b}_{(\mathrm{elec})}}/N_0$ for L layers in LACO-OFDM
$\alpha_{\mathrm{FTP}}(L, M)$	The increase in $E_{\mathrm{b}_{(\mathrm{elec})}}/N_0$ for L layers in FTP-LACO-OFDM
$\alpha_{\mathrm{HTP}}(L, \sqrt{M})$	The increase in $E_{\mathrm{b}_{(\mathrm{elec})}}/N_0$ for L layers in HTP-LACO-OFDM
$P_{(\mathrm{opt},\cdot)}$	Parameter used to represent combined optical power of all the lth layer LACO-OFDM or precoded LACO-OFDM
$\alpha_{(\cdot)}^{\mathrm{OE}}$	Parameter used to represent the optical-to-electrical conversion efficiency of LACO-OFDM and precoded LACO-OFDM approaches
$\alpha_{\mathrm{LACO}}^{\mathrm{OE}}(L)$	Optical-to-electrical conversion efficiency of LACO-OFDM
$\alpha_{\mathrm{FTP}}^{\mathrm{OE}}(L, M)$	Optical-to-electrical conversion efficiency of FTP-LACO-OFDM
$\alpha_{\mathrm{HTP}}^{\mathrm{OE}}(L, \sqrt{M})$	Optical-to-electrical conversion efficiency of HTP-LACO-OFDM
β_{FTP}	The reduction in required $E_{\mathrm{b}_{(\mathrm{elec})}}/N_0$ for giver BER for FTP-LACO-OFDM in a multipath channel
β_{HTP}	The reduction in required $E_{\mathrm{b}_{(\mathrm{elec})}}/N_0$ for giver BER for HTP-LACO-OFDM in a multipath channel
η_{LACO}	Spectral efficiency of LACO-OFDM
η_{FTP}	Spectral efficiency of FTP-LACO-OFDM
η_{HTP}	Spectral efficiency of HTP-LACO-OFDM
$\lambda_{(\cdot)}^{\mathrm{max}}$	Quantifies the maximum value of PAPR at CCDF $= 0.1$ for LACO-OFDM/precoded LACO-OFDM
$\lambda_{\mathrm{LACO}}^{\mathrm{max}}(L)$	Maximum value of PAPR at CCDF $= 0.1$ for LACO-OFDM
$\lambda_{\mathrm{FTP}}^{\mathrm{max}}(L, M)$	Maximum value of PAPR at CCDF $= 0.1$ for FTP-LACO-OFDM

$\lambda_{\mathrm{HTP}}^{\max}(L, \sqrt{M})$	Maximum value of PAPR at CCDF $= 0.1$ for HTP-LACO-OFDM
τ	Clipping ratio in dB
$\mathcal{C}_{\mathrm{LACO}}$	Computational complexity of LACO-OFDM
$\mathcal{C}_{\mathrm{FTP}}$	Computational complexity of FTP-LACO-OFDM
$\mathcal{C}_{\mathrm{HTP}}$	Computational complexity of HTP-LACO-OFDM
$\mathcal{G}(N, L)$	Relative gain parameter in complexity reduction for HTP-LACO-OFDM over LACO-OFDM
I_k	Ideal inphase constellation points for the kth symbol
Q_k	Ideal quadrature constellation points for the kth symbol
$\tilde{I}_k$	Received inphase constellation points for the kth symbol
$\tilde{Q}_k$	Received quadrature constellation points for the kth symbol
e_k	Error in ideal and received constellation points
$\hat{H}(\cdot)$	Estimated channel frequency response

*To my parents, **Azim** and **Nasreen**,*
I always feel their prayers with me
*and to my wife, **Mahrukh**,*
for her love, support and cooperation,
*and to my son **Abdullah**,*
he is all the world to me!

Résumé

Les systèmes de communications radiofréquences (RF) ont connu un développement exponentiel durant ces dernières années, ce qui a conduit à une véritable congestion spectrale. Le spectre RF a été sujet à une réutilisation spatiale intensive, ce qui a conduit à de nombreuses problématiques d'interférences entre canaux, impactant la qualité de service. A l'origine de cette montée en puissance des systèmes de communications sans fil, on trouve la croissance soutenue du trafic de données, qui tend à s'accélérer avec l'émergence de l'internet des objets (IoT), qui permettra de connecter plus de 30 milliards d'objets à l'horizon 2025. Dans ce contexte, des techniques de communications alternatives, permettant de surmonter le goulot d'étranglement spectral, sont envisagées. Récemment, les communications optiques sans-fil dans le visible (VLC) ont été reconnues comme une solution technologique à fort potentiel pour décongestionner le spectre. Par ailleurs, avec l'utilisation massive pour l'éclairage de diodes électroluminescentes (LED), les communications VLC laissent entrevoir la possibilité d'une connectivité massive à partir de ce type d'émetteur bas coût et faible consommation. Les systèmes VLC permettraient alors de disposer d'une ressource spectrale optique très importante et sans licence, d'une sécurité de transmission due au confinement de la lumière (à une pièce d'un bâtiment par exemple), d'aucune interférence avec les ondes radio.

Pour les systèmes VLC, la modulation à multiplexage de fréquences orthogonales (OFDM) est souvent considérée comme prometteuse car elle permet des hauts débits, une haute efficacité spectrale, une égalisation simple (dans le domaine fréquentiel) au niveau du récepteur, ainsi qu'une résistance naturelle aux interférences entre symboles provoquées par le caractères dispersif en temps du canal de propagation optique. Les systèmes VLC utilisent préférentiellement la modulation d'intensité combinée à la détection directe (IM-DD) pour transmettre les données, ce qui signifie que l'intensité lumineuse émise par la LED est modulée par le signal d'information à transmettre et cette modulation d'intensité est directement convertie, en réception, en modulation d'amplitude du courant photodétecté. Pour implémenter l'IM-DD, le signal temporel doit être nécessairement réel et positif. Pour obtenir un signal temporel réel avec la modulation OFDM, la symétrie hermitienne est requise pour les symboles fréquentiels envoyés à l'entrée du modulateur à base de transformée de Fourier inverse. Pour satisfaire la contrainte de non-négativité, plusieurs solutions existent pour l'OFDM ; une manière directe consiste à ajouter une composante continue (DC) au signal de modulation bipolaire. D'autres approches définissent des formes d'ondes unipolaires spécifiques. Ainsi de nombreuses techniques de modulations, dérivées de l'OFDM, ont été démontrées dans la littérature pour répondre aux contraintes des systèmes IM-DD comme le DCO-OFDM, l'écrêtage asymétrique (AC)O-OFDM, le Flip 0FDM, l'unipolaire (U)-OFDM et l' OFDM sans symétrie Hermitienne (HSF)-OFDM, etc. Ces shémas diffèrent principalement dans l'arrangement des porteuses qui portent l'information, et/ou dans la manière dont la forme d'onde qui module l'intensité est obtenue. L'ACO-OFDM, le Flip-OFDM, l'U-OFDM, et le HSF-OFDM présentent une efficacité spectrale moitié plus faible que celle du DCO-OFDM. Cependant, le DCO-OFDM est moins efficace en termes de consommation optique pour de faibles ordres de constellation à cause de la composante DC requise pour rendre le signal unipolaire. Pour augmenter l'efficacité spectrale et maintenir l'avantage de l'ACO-OFDM sur le DCO-OFDM pour des ordres de constellation élevés, une méthode d'empilements en couches a été proposée dans la littérature (LACO-OFDM). Néanmoins, dans cette version, la moitié des porteuses sont sacrifiées pour incorporer la symétrie hermitienne.

des déclinaisons à empilement) est l'inévitable fort facteur de crête (PAPR) qui le rend très sensible aux non-linéarités des circuits utilisés. Par exemple, le facteur de crête de l'O-OFDM est en effet un paramètre critique compte tenu de la linéarité limitée des LEDs en modulation d'amplitude. Par conséquent, pour un signal présentant un fort facteur de crête, des distorsions sont susceptibles de dégrader fortement la qualité du signal d'information numérique transmis. Aussi, la limitation en résolution (nombre de bits) des convertisseurs numérique/analogiques (DAC) et analogique/numérique (ADC) est un autre facteur impactant les performances globales des systèmes VLC, à cause de l'influence du bruit de quantification. Pour réduire ces effets néfastes, de nombreuses techniques de réduction de facteur de crêtes, dédiées aux signaux O-OFDM, ont été proposées dans la littérature, comme les algorithmes SLM (selected mapping), PA (pilot assisted), etc. Néanmoins, ces techniques entraînent un accroissement important de la complexité des émetteur/récepteur, au regard d'une amélioration somme toute assez faible des performances du système.

Par ailleurs, pour implémenter un réseau VLC complet, il est nécessaire de définir une technique d'accès (MA) efficace. De manière assez simple, dans le domaine fréquentiel, il est possible de dériver une technique d'accès O-OFDMA de la technique de modulation OFDM. Dans l'O-OFDMA, les porteuses sont allouées dynamiquement à différents utilisateurs au moyen d'une matrice d'allocation de ressources.

Pour surmonter l'effet des distorsions introduites par le facteur de crête du signal O-OFDM et aussi pouvoir utiliser une technique d'accès simple dans le domaine fréquentiel, une technique optique mono-porteuse à accès multiple par répartition en fréquence (O-SCFDMA) peut être utilisée. Les approches O-SCFDMA offrent l'avantage de réduire considérablement le facteur de crête. Elles peuvent être considérées comme des variantes pré-codées, par transformée de Fourier (FTP), de l'O-OFDMA. Dans la littérature, des techniques O-SCFDMA, inspirées de l'O-OFDMA, ont été proposées : le (FTP)-ACO-OFDM et le FTP-DCO-OFDM. Néanmoins, contrairement à leurs homologues dans le domaine de la radiofréquence, pour lesquels le pré-codage FTP s'applique sur la totalité des symboles dans le domaine fréquentiel pour générer un signal strictement mono-porteuse, les techniques de pré-codage pour les systèmes VLC voient seulement la moitié des symboles temporels bénéficier du traitement FTP à cause de la contrainte de symétrie hermitienne. Par conséquent, les techniques qui suppriment l'usage de la symétrie hermitienne après la réalisation du pré-codage FTP, présentent de meilleurs résultats en termes de réduction du facteur de crêtes que les techniques qui imposent la symétrie hermitienne. Ainsi, récemment, la modulation mono-porteuse optique (SCO)-FDM a été proposée. Elle présente un facteur de crête réduit comparé au FTP-ACO-OFDM et à l'ACO-OFDM tout en ayant les mêmes performances en termes de taux d'erreurs binaires (BER) en canal à bruit additif blanc gaussien. Par ailleurs, une technique à faible complexité, basée sur un pré-codage par transformée de Hartley (HTP)-ACO-OFDM, a été proposée par Zhou and Qiao pour les systèmes IM-DD. Le HTP-ACO-OFDM présente un facteur de crête moindre que le FTP-ACO-OFDM pour un ordre de modulation d'amplitude par impulsion (PAM) faible. Cependant, pour un ordre de modulation élevé, le facteur de crête se trouve largement dégradé.

Les techniques mono-porteuses classiques comme la modulation tout ou rien (OOK), la modulation en positions d'impulsion (M-PPM) et M-PAM sont des manières très directes d'implémenter un système VLC IM-DD. Pourtant, pour le M-PPM, le facteur de crête croît avec la racine carrée du nombre d'états M et nécessite une synchronisation symbole précise. Le M-PPM est très sensible à l'impact du canal dispersif en temps, et le M-PAM nécessite lui aussi une égalisation complexe en réception en cas d'effet néfaste des interférences entre symboles, lorsque la profondeur du canal optique devient significative par rapport à la durée du symbole. Pour ces dernières modulations, l'implémentation d'une technique d'accès dans le domaine fréquentiel alourdit considérablement la complexité des transmetteur/récepteur, alors que, dans le domaine temporel, des problèmes importants de synchronisation sont prévisibles.

Une autre solution prometteuse pour les communications optiques sans fil (OWC) est d'utiliser la transmission mono-porteuse (SC) avec égalisation dans le domaine fréquentiel (SCFDE). La technique SCFDE combine avantageusement les propriétés de l'O-OFDM et de la transmission SC. Comme pour l'O-OFDM, le processus d'égalisation est effectué dans le domaine de Fourier et la partie transmission est traitée bloc par bloc. Le PAPR des signaux SCFDE est particulièrement faible, ce qui est un avantage. Différentes techniques SCFDE, comme PAM-SCFDE, OOK-SCFDE, SCFDE optique basée sur la répétition et l'écrêtage (RCO)-SCFDE et SCFDE optique avec décomposition quadratique (DQO)-SCFDE ont été proposées. Malheureusement, ces techniques ne sont pas compatibles avec les techniques d'accès multiple par division de fréquence (FDMA), intéressantes pour les scénarios comportant plusieurs utilisateurs.

Dans ce travail, l'objectif est de discuter de techniques de modulations O-OFDM/O-SCFDMA qui sont efficaces en terme d'énergie et de bande fréquentielle occupée tout en étant par nature moins sensibles aux distorsions non linéaires, c'est-à-dire ayant un faible PAPR. Ainsi, nous avons proposé deux méthodes qui permettent de diminuer le PAPR par rapport aux approches O-OFDM de l'état de l'art.

Nous avons étudié les techniques de réduction de PAPR proposées dans la littérature pour contrecarrer le PAPR élevé des techniques classiques O-OFDM, c'est-à-dire DCO-OFDM et ACO-OFDM. Il a été montré que l'approche la plus adaptée pour à la fois diminuer un PAPR élevé et adapter le signal à la dynamique réduite en amplitude de modulation de la LED, est de l'écrêter à une amplitude prédéfinie. Néanmoins, l'écrêtage génère une distorsion significative qui peut sévèrement diminuer les performances du système. Dans ce contexte, nous introduisons dans ce travail deux méthodes itératives dirigées par décision. L'objectif est d'écrêter le signal à un seuil donné avant la transmission et d'essayer de restaurer l'information perdue au niveau du récepteur, à l'aide d'une des méthodes proposées. Ces méthodes remplissent les conditions de IM-DD et sont compatibles avec les deux techniques DCO-OFDM et ACO-OFDM. Une analyse statistique de l'écrêtage est aussi présentée. Une des méthodes proposées atténue la distorsion due à l'écrêtage dans le domaine temporel et l'autre la réduit dans le domaine de Fourier. Selon le domaine d'opération, les méthodes sont appelées TDCSR comme reconstruction des échantillons écrêtés dans le domaine temporel et FDCSR comme reconstruction des échantillons écrêtés dans le domaine fréquentiel. Les résultats de ces méthodes sont comparés à ceux de SLM (sélection de mapping) et il a été déterminé que les méthodes proposées sont de loin les moins complexes pour contrecarrer le PAPR élevé.

Ce travail sur les techniques de réduction de PAPR a montré que ces techniques causaient un surcroît de complexité considérable, qui n'est pas souhaitable. En conséquence, il a été établi qu'un précodage O-SCFDMA pourrait être un choix plus adapté pour réduire le PAPR sans augmenter la complexité de calcul. Pour rester compatible avec les contraintes IM-DD, les approches O-SCFDMA, comme FTP-DCO-OFDM et FTP-ACO-OFDM appliquent la contrainte de symétrie hermitienne HS qui a pour conséquence que le PAPR ne peut pas être réduit de manière substantielle. Ainsi, les approches qui excluent l'utilisation de HS, comme HTP-ACO-OFDM et SCO-FDM, peuvent présenter un PAPR plus faible que les autres approches O-SCFDMA qui utilisent HS. Néanmoins, comme mentionné précédemment, pour HTP-ACO-OFDM, la réduction de PAPR devient moins impérieuse lorsque l'alphabet de modulation est augmenté, et pour SCO-FDM, le processus de génération d'un signal non négatif ne permet pas de réduire significativement le PAPR. Contre cet inconvénient, la technique O-SCFDMA sans HS (HSF-O-SCFDMA) est proposée. Cette technique est compatible avec l'accès multiple et évite aussi l'utilisation de la HS. Les résultats de simulation montrent que l'on peut obtenir le même PAPR qu'avec la technique RF de SCFDMA entrelacé (I-SCFDMA). C'est la première fois qu'une technique O-SCFDM pour les systèmes OWC qui permet d'atteindre un PAPR aussi petit est proposée. Les résultats de simulation montrent que la technique HSFO-SCFDMA est l'approche O-SCFDMA la plus efficace en terme de puissance tout en présentant le plus faible PAPR.

Pour les approches O-OFDM/O-SCFDMA de l'état de l'art, toutes les sous-porteuses/tous les sous-canaux, ne peuvent pas être modulés à cause de l'exigence de HS. La moitié des sous-porteuses/sous-canaux doivent être abandonnés pour permettre la HS. De plus, pour ACO-OFDM er FTP-ACO-OFDM, seulement les sous-porteuses impaires peuvent être modulées pour générer un signal non négatif, ce qui réduit encore plus l'efficacité spectrale. Cela entraîne que les approches ACO-OFDM et FTP-ACO-OFDM sont moins efficaces en occupation spectrale que DCO-OFDM et FTP-DCO-OFDM. Comme expliqué plus haut, l'efficacité spectrale de ACO-OFDM peut être améliorée en utilisant LACO-OFDM. Malgré tout, aussi avec LACO-OFDM, la moitié des sous-porteuses sont sacrifiées pour incorporer la HS, et LACO-OFDM présente encore un PAPR important. Les méthodes de réduction de PAPR pour ce type d'approches exigent des ressources de calcul importantes. C'est pourquoi, les performances du pré-codage par transformée de Fourier et transformée de Hartley sont étudiées pour LACO-OFDM. Nous montrons qu'en utilisant la transformée de Hartley (pour le précodage et décodage, le multiplexage et démultiplexage) avec des alphabets PAM, une nouvelle approche, appelée HTP-LACO-OFDM, peut être développée, dans laquelle tous les sous-canaux peuvent être modulés tout en générant une onde modulée en intensité, sans l'utilisation de la HS. Les techniques FTP-LACO-OFDM et HTP-LACO-OFDM sont les variantes avec superposition des techniques respectivement FTP-ACO-OFDM et HTP-ACO-OFDM.

Enfin, nous présentons des démonstrations expérimentales pour TDCSR/FDCDR et HSFO-SCFDMA en utilisant un système à fibre optique IM-DD. Un système IM-DD à fibre optique est utilisé car nous n'avons pas de prototype de système OWC. Les résultats expérimentaux sont en accord avec les résultats de simulation. Il est démontré à partir des résultats expérimentaux que les deux approches permettent de retrouver l'information perdue à cause de l'écrêtage. Les résultats expérimentaux montrent que les performances de HSFO-SCFDMA sont significativement meilleures que celles de DCO-OFDM.

Grâce à l'étude effectuée dans ce travail, les avantages suivants peuvent être obtenus par rapport aux approches de l'état de l'art:

- Les méthodes de réduction de PAPR, TDCSR et FDCDR peuvent réduire avec succès la distorsion d'écrêtage, pour DCO-OFDM et ACO-OFDM. Ces méthodes atteignent des améliorations substantielles en terme de performance optique par rapport aux techniques DCO-OFDM, grâce à la réduction de la polarisation puisque l'écrêtage est effectué au niveau de l'émetteur. Pour ACO-OFDM, une perte de performance marginale est obtenue par rapport aux techniques conventionnelles ACO-OFDM et FTP-ACO-OFDM. De plus, la complexité de ces méthodes est considérablement plus faible que celle des méthodes classiques de réduction de PAPR.
- HSFO-SCFDMA possède la même efficacité spectrale que FTP-DCO-OFDM, cela implique que les efficacités spectrales de FTP-ACO-OFDM, HTP-ACO-FDM et SCO-FDM valent la moitié de celle de HSFO-SCFDMA. De plus, la caractéristique la plus marquante de HSFO-SCFDMA est qu'elle manifeste un PAPR significativement plus faible que celui des autres approches de l'état

de l’art, conduisant à une bonne efficacité en puissance, que ce soit en consommation de puissance électrique ou optique, et à une sensibilité plus faible vis-à-vis des défauts non linéaires de la LED. Les contraintes de résolution des DAC et ADC peuvent alors aussi être relâchées, et cela conduit à une réduction du coût total. HSFO-SCFDMA est moins complexe en calcul numérique que la plupart des techniques proposées dans la littérature.

- L’analyse de performance des techniques précodées par transformée de Fourier et de Hartley LACO-OFDM, respectivement (FTP)-LACO-OFDM et (HTP)-LACO-OFDM montrent qu’elles ont de meilleures performances que les techniques sans précodage avec un canal dispersif, grâce à l’effet de moyennage du décodeur au niveau du récepteur. Mais avec un canal AWGN, les performances de taux d’erreurs binaires sont meilleures avec LACO-OFDM qu’avec les deux techniques LACO-OFDM avec pré-codage. Une autre conclusion est aussi que grâce à la structure par superposition, les techniques LACO-OFDM non pré-codées aboutissent à la pénalité en terme de SNR la plus faible. De plus, les deux approches ACO-OFDM pré-codées présentent un PAPR plus faible que les techniques conventionnelles LACO-OFDM. Parmi les approches pré-codées, HTP-LACO-OFDM présente le PAPR le plus faible, grâce au pré-codage tout en évitant aussi la HS. La complexité de FTP-LACO-OFDM est plus grande que celle de LACO-OFDM, atténuant toutes les autres améliorations de cette technique, tandis que la complexité de HTP-LACO-OFDM est plus faible que celle de LACO-OFDM. Ainsi, en conclusion, HTP-LACO-OFDM peut être un formidable substitut à LACO-OFDM pour les systèmes VLC.

Chapter 1

General Context of Optical Wireless Communication Systems and Technologies

Since the discovery of electromagnetic (EM) waves, wireless communication has turned into a revolution. It has witnessed many paradigm shifts, from the development of invention of radio to the wireless telephone. Nowadays, there has been a pervasive presence of wireless applications and devices because of a substantial increase in deployment of wireless systems. Soon, applications, such as music, web browsing, video telephony, television, virtual reality, high-definition (HD) video streaming would demand high capacity and high data-rates to endure with the requirements. Substaintial interest in Internet-of-Things (IoT) will also connect more than 30 billions of connected devices by 2020. At the same time, the demand for ubiquitous connectivity mobility and communication is exponentially growing as determined by global network traffic statistics predicted by Cisco [1], which are illustrated in Fig. 1.1. It can be observed that the global network traffic is continuously increasing at an expeditious pace and this forecasted global network traffic inflation is predicted to prevail in the successive years. Some important predictions by Cisco are:

- there shall be 3.5 network devices and connections per person by 2021;
- the average internet traffic per person per month will be 61 GB by 2021;
- there shall be 4.6 billion internet users with 27.1 billion network devices and connections around the globe by 2021.

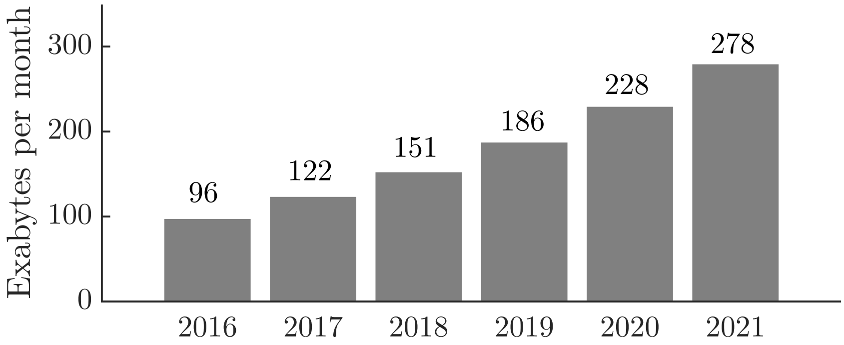

FIGURE 1.1: Global visual network Index predictions [1].

The term ’wireless’ is generally labeled for radio-frequency (RF) technologies, as most of the technologies in use are based on RF devices and systems. The RF spectrum from 3 kHz to 300 GHz is a natural resource which is exclusively overseen and controlled by the state which appropriates privileges and optimize the use of spectrum. Several applications, e.g., analog and digital radio broadcasting, television (TV) broadcasting, radars, satellite communications, mobile communications, wireless local area networks (WLANs), different government, industrial and public applications and so on need RF spectrum. In the last couple of decades, with the inflated demand for data hungry wireless applications, a tremendous amount of RF spectrum is being consumed. Most of the RF spectrum has been allocated and the current trend would cause spectral congestion. This threat can wreak havoc and leave behind a considerable gap between the deliverable potentials of prevailing systems and the demands for exponentially increasing network traffic. Between $2011 - 2016$, the global network traffic increased approximately 18 times, which affirms that spectrum scarcity is becoming a reality. Therefore, spectral management to evade spectral exhaustion is imperative. Various solutions have been suggested to address this issue, some leading solutions are:

- The first solution is to be spectrally more efficient with the prevailing systems. This has been accomplished for the last decade by introducing techniques, such as multiple-input and multiple-output (MIMO), which increase the system capacity. These approaches try to improve the spectral efficiency bits/s/Hz, however, this solution is coming close to saturation.
- Another method is to be more vigorous temporally and spatially by reusing the spectrum. This approach is exploited by the use of cognitive radio, where the spectrum is dynamically allocated to avoid interference between different users and to avoid congestion. Further, there is a concept of off-loading in which a high density of small cells are employed by scaling down the cell coverage area. The concept of femtocells and attocells are investigated in this regard, however, one demerit of this approach is increased interference between the access nodes. The aim of these methods is to enhance bits/s/Hz/m^2.
- The third approach is to use the parts of spectrum which are traditionally not used for communication purposes. In this context, the concept of millimetre wave (mmWave) communications has earned significant interest. In mmWave communications, the unconventional parts of the spectrum from 28 GHz to 250 GHz are used for communication purposes [2]. mmWave systems are realized using massive MIMO technology which enables multiple small antennas within an area because of smaller wavelengths. Wave propagation for shorter wavelength, however, is restricted to just line-of-sight (LoS) scenarios and therefore, surrender pervasive coverage advantage over RF [2]. Another possible limitation for mmWave systems is the the lack of high bandwidth/low power consumption mmWave transceivers for high frequencies. To use such systems a sizable part of the existing infrastructure needs to be replaced. Terahertz (THz) communication systems are also explored as an alternative which can offer large available spectrum between 1000 GHz to 3000 GHz, however, THz transmiter and receiver design is the major issue.

Beyond the RF spectrum of 3 kHz to 300 GHz, there is optical spectrum which comprises infrared (IR), visible light (VL) and ultraviolet (UV) spectrum, which ranges between 300 GHz to 30 petahertz (PHz) as shown in Fig. 1.2. This optical spectrum can be exploited for communication primarily because of enormous un-regulated, un-licensed bandwidth which can deliver high data-rates and can be a potential solution for the last mile problem. Optical wireless communication (OWC) uses the optical spectrum which is thousands of times broader than the RF spectrum. Nevertheless, the OWC systems come with its own challenges, such as diminished sensitivity owing to obstacles and limited transmitted optical power, etc.

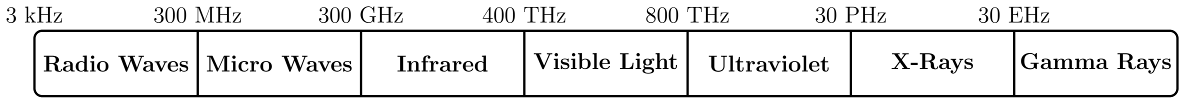

FIGURE 1.2: The electromagnetic (EM) spectrum.

In OWC, the message can be transmitted by intensity-modulation and direct detection (IM-DD) methods, wherein, the data is modulated on the envelop of the electromagnetic radiation which is photo-detected at the receiver [2, 3]. IM-DD relies on the use of electrical-to-optical transceiver, such as light emitting diodes (LEDs) and laser diodes (LDs) at the transmitter, and optical-to-electrical transceivers like photo-diodes (PDs) at the receiver. Apart from the availability of huge unregulated spectrum available for OWC, several other motivating factor on why OWC shall be used are provided in the subsequent section.

1.1 Motivations for Optical Wireless Communications

OWC technologies are seen as a potential solution for the last mile problem and can bridge the gap between the end users and the optic fiber backbone infrustructure [4]. The interest in the use of OWC is driven by the following factors:

- *Energy Efficiency:* OWC systems does not require exclusive energy resources as the energy used for lighting (for visible light communications (VLC)) can be utilized for communication as well. Furthermore, LEDs, which are used for VLC are more energy efficient compared to other lighting sources and have a significantly lower carbon dioxide (CO_2) footprint which could lead to *green communication* technology [5]. By replacing existing lightings by LEDs, the CO_2 emissions are expected to be reduced by 10 gigatons which reduces the oil consumption by 962 million barrels which could lead to cost saving of trillions of dollars and energy savings of 1.9×10^{20} joules over a decade [5, 6].

- *Data Security:* Unlike RF waves, the light intensity signal used for OWC cannot penetrate through the walls or any other obstacles which makes them a safer option for communication since snooping can be avoided. Moreover, the light intensity signal is constrained in the area surrounded by opaque boundries, so, all the communication happening inside the room stay within the room which is not possible with RF waves.

- *Safety:* The use of luminaries for OWC have no apparent health hazards and conform with the eye-and-skin safety regulations making it safe in practical communication scenarios [5].

- *Interferences:* The use of light intensity signal for OWC is intrinsically safe and offers zero interference with RF signals or RF sensitive equipment [7]. Therefore, this technology is safe to use in places where RF signals are restricted or not allowed due to interferences with RF sensitive equipments, such as hospitals and aerospace platforms, etc. [8, 5].

- *Spatial Resuse and Beam Steering:* In indoor OWC systems, the light intensity signal is confined due to reflections from walls, roof and ceiling. Hence, this highly confined and directed light beam makes it possible to create multiple non-interfereing beams in close proximity. This allows greater data density and reuse of modulation bandwidth in adjacent cells [9, 10, 11]. Additionally, unlike RF wireless technologies which need complex and costly equipments for beam steering, light can be easily directed using low-cost optical equipments [12].

- *Easy Integration to Existing Infrastructure and Hardware Reuse:* The integration of OWC systems to the existing infrastructure is very simple because it only requires addition of low-cost front end components, such as LEDs and related drivers, such as, PDs and related amplification stages [5, 13]. For indoor OWC systems, the existing lighting infrastructure intended for illumination can be leveraged to integrate communications [14] and an initial set-up cost of an entire new system can be evaded. On the other hand, RF/mmWave and THz communications need to design, assemble and deploy dedicated complex transceivers which can increase the cost of integration.
- *Low Recurring Cost:* The components used for OWC incurs very low recurring costs because: (i) generally, they are energy efficient which incurs low cost in billings; (ii) contrary to RF no specific equipments are need for wireless transmission which reduces the fuel cost for keeping the RF base stations in working order. As an example, RF links with the transmission distance and rate of 10 m and 1 Mbps in 2.4 GHz band incur a cost of nealy 5 US dollars, whereas, OWC is capable of achieving 4 Mbps over short distances and cost around 1 US dollar [5].

1.2 Applications of Optical Wireless Communications

OWC has a wide range of potential applications [15, 5, 4]. Fig. 1.3 provides a graphical illustration of potential OWC application platforms. Some potential application platforms include airports, petrochemical plants, smart homes and cities, railway stations, healthcare, data-centers, transportation, underwater communication, etc. Within these platforms, diverse communication strategies, like chip-to-chip (C2C), device-to-device (D2D) and machine-to-machine (M2M) can be implemented. Eventually, these strategies can be invaluable in developing IoT, where millions of smart devices could be connected to each other [15]. OWC can be more prosperous in such platform, where RF signals can interfere with other sensitive equipments, such as hospitals/healthcare and petrochemical plants, etc. Another example for OWC is related to reliable communications strategy for military submarines, where internal communications can be established in silent mode.

One fundamental consideration which is requisite for the deployment of OWC technologies, is the communication distance. Based on the communication distance, OWC applications can be classified into [15, 5, 4] ultra-short range, short range, medium range, long range and ultra-long range as depicted in Fig. 1.4. This implies the OWC applications range from C2C communications with a distance of a few micro-meters to inter-satellite and deep space links with the distances of thousands of kilometers as shown in Fig. 1.5. Following are some examples:

- *Ultra-Short Range OWC Applications:* Optical interconnects are gaining a substantial importance because of high bandwidth and low latency, and are forecasted to oust copper based electrical interconnects which are bulky and prove to be a bottleneck in the system design [17]. OWC in optical interconnects can be used for C2C communication which can be a flexible, less bulky solution to the traditional electrical wire counterparts.

FIGURE 1.3: Potential applications of OWC [15].

- *Short Range OWC Applications:* For short range OWC in the order of tens of centimeters, typical examples can be wireless body area network (WBAN) and wireless personal area network (WPAN) [18, 19]. In WBANs, many sensors/detectors can be placed on the body to monitor the health parameter, such as, heart rate, blood pressure etc. WBAN based on RF signal might not be a good option for hospitals, where the equipments are sensitive to the RF signals. In OWC based WBANs, sensors based on VL can be incorporated into clothings or wearable devices from which the vitals can be collected on a smartphone. In WPAN, all the devices gathered around an individual are linked to each other, which is the main concept of IoT.
- *Medium Range OWC Applications:* Common application of OWC for medium transmission distances is WLANs. Traditionally, RF wireless links are utilized, however, as aforementioned, RF

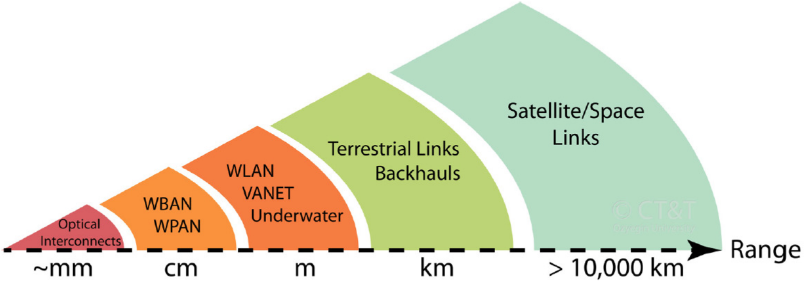

FIGURE 1.4: Categorization of OWC applications based on the transmission range [16].

spectrum is virtually depleted, accordingly, OWC can be a possible substitute. With the concept of using LEDs for both lighting and communication, the development of WLANs using OWC can become a reality for inter-building wireless connectivity. VLC can also be used for outdoor scenarios, such as traffic lights, street lamps, advertising displays, car headlights/taillights. This can lead to vehicle-to-infrustructure (V2X), vehicle-to-vehicle (V2V) communications.

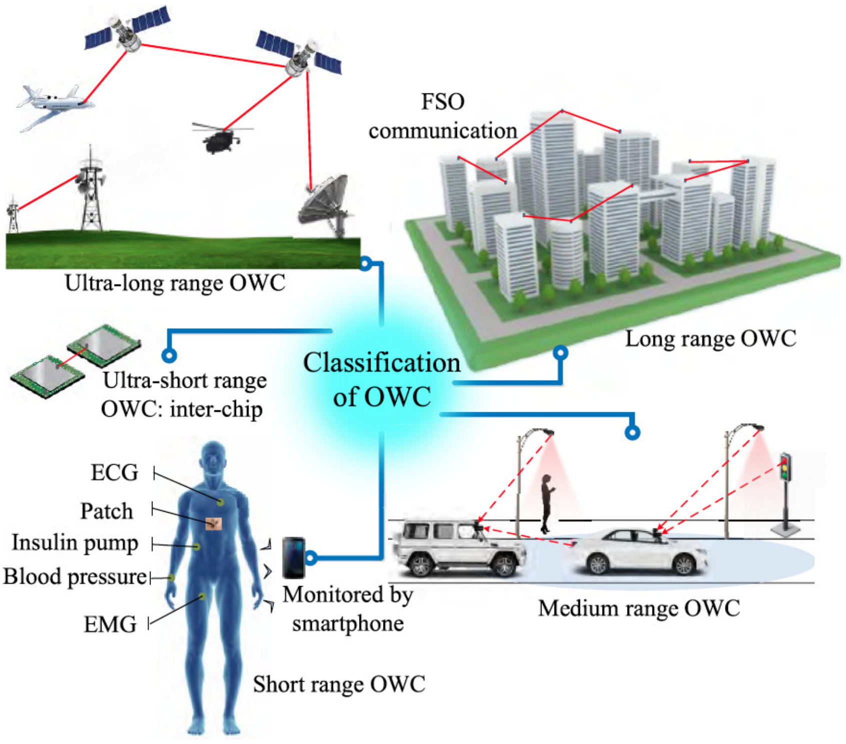

FIGURE 1.5: OWC application classification based on communication distance [15]. Here, FSO: free space optics, ECG: Electrocardiography and EMG: Electromyography

- *Long Range OWC Applications:* For long range applications, OWC can be used to connect one WLAN to another WLAN. Free space optics (FSO) networks offer high bandwidth, high data-rates by the order of Tbps and are easy to reconfigure. The long range OWC links can be used as backhaul connections to surmount the bottleneck in traditional coaxial cables. Nowadays, the free space optical links are also employed for aerospace applications [20].
- *Ultra-Long Range OWC Applications:* For distances of thousands of kilometers, such as ground-to-satellite and inter-satellite communications, free space optic links can be a powerful means for communication. Several inter-satellite free space optic links have been investigated, e.g., [21, 22] shows the potential of OWC for long range FSO applications.

1.3 Envisioned Technologies for Optical Wireless Communications

There are numerous envisioned technologies for OWC, such as visible light communication (VLC), light-fidelity (LiFi), optical camera communications (OCC) and free space optics (FSO). In this section, a succinct introduction of enabling technologies for OWC is presented. A basic architecture of user equipment (UE) to core network (CN) for medium range OWC is presented in Fig. 1.6. The backhaul connections that connect access points (APs) to the CN can be FSO links, satellite links or optical fiber connections. The transmitters in OWC can either be LEDs or LDs, while, the receiver can be PDs, camera or image sensor (IS). These technologies are primarily distincted by the type of receiver or the region of optical spectrum which they use.

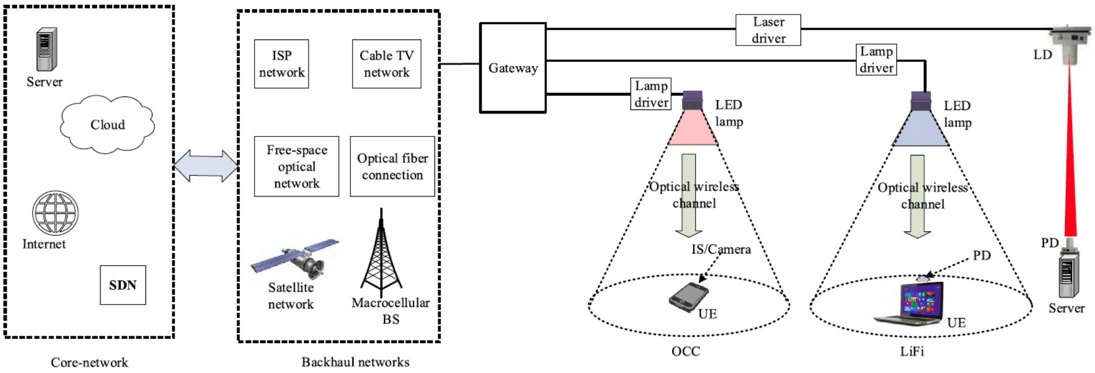

FIGURE 1.6: Basic architecture of user equipment (UE) to core network (CN) for OWC [15].

1.3.1 Visible Light Communication (VLC)

Within the subset of OWC, there is a considerable interest in VLC. VLC, as the name indicates, is an OWC technology which employs the VL spectrum. It is foreseen that VLC can be complementary technology to the prevailing RF systems and can fulfill the requirements of IoT [23]. However, VLC can operate within limited transmission ranges. It can be used for various applications in homes, vehicles, aerospace, trains etc. without the constraint of limited usable spectral bandwidth. The omnipresence of LEDs makes the deployment of VLC easy. LEDs can rapidly switch between different intensities indistinguishable to the human eye, furthermore, the light emitted by the LEDs used for lighting purpose, is, of course, harmless to the humans. As LEDs can be used for communication, the existing lighting infrastructure can be used for VLC. Data-rates of up to 10 Gbps have been validated utilizing LEDs [24]. Several applications of VLC include; smart lighting, smart cities, wireless connectivity, use in RF sensitive environments, indoor localization, augmented reality, etc [15].

1.3.2 Light-Fidelity (LiFi)

LiFi is closely related to VLC, however, LiFi offers a complete networking solution which allows multiuser communication and seamless maneuverability of the UE by configuring attocells within heterogenous wireless systems. Other fundamental differences include [15]:

- VLC can only use VL spectrum, while, LiFi uses VL spectrum on the down-link and have the possibility to manipulate IR, VL or UV spectrum in the uplink [25, 26, 27, 28];
- VLC systems are unidirectional [29] or bidirectional [30], however, LiFi should invariably be bidirectional [27];
- Seamless user mobility is essential for LiFi systems [27], whilst, it is not a prerequisite for VLC;

- LiFi systems should support multi-user communication via multiple access techniques, however, VLC systems can be point-to-point (P2P), point-to-multi-point and multi-point-to-point.

Indeed, a VLC system can be regarded as a LiFi system if they support multi-user communications and mobility of the UE. Conversely, a LiFi system is equivalent to a VLC system if only VL spectrum is used in both up-link and down-link [15].

FIGURE 1.7: Application scenarios for VLC/LiFi; (a) indoor applications and (b) outdoor applications [15].

As both the technologies are somewhat alike, their applications are practically similar. Fig. 1.7 shows various application scenarios for both VLC and LiFi. Fig. 1.7(a) displays the indoor applications for both VLC and LiFi. In the indoor environments, both lighting and communication is administered together, however, LiFi also supports mobility. Some outdoor applications of both systems are suggested in Fig. 1.7(b). The outdoor applications may consist of either communication scenarios, e.g., vehicle taillights and traffic lights; or both communication and lighting prospects, such as street lights and vehicle headlights. Smartphone to street lamp communication may be an example of both VLC and LiFi, whilst, V2X and V2V communication scenarios are examples of VLC.

1.3.3 Free Space Optics (FSO)

FSO is a form of OWC which uses light propagating in free space to wirelessly transmit data. FSO communication uses IR, VL and UV spectrum [4, 31, 32, 22]. Since, this frequency range employed by FSO is thousands of times larger than RF spectrum, accordingly, high data-rates can be attained. The exclusive purpose of FSO is communication, unlike VLC, where illumination is likewise required concurrently with communication. FSO use narrow beam LDs as transmitters which can deliver high power, monochromatic and directive radiation to establish a communication link. Because of the use of higher wavelengths in LDs, FSO is usually an eye unsafe technology. Several implementations of FSO links have been carried out, particularly, a 40 Gbps FSO link has been established for a transmission range of 20 m [31], and data-rates of 10 Gbps are obtained for long range transmission [33]. Despite advantages, FSO links suffer from the problem of link reliability for long range communications primarily because of weather conditions and physical obstacles.

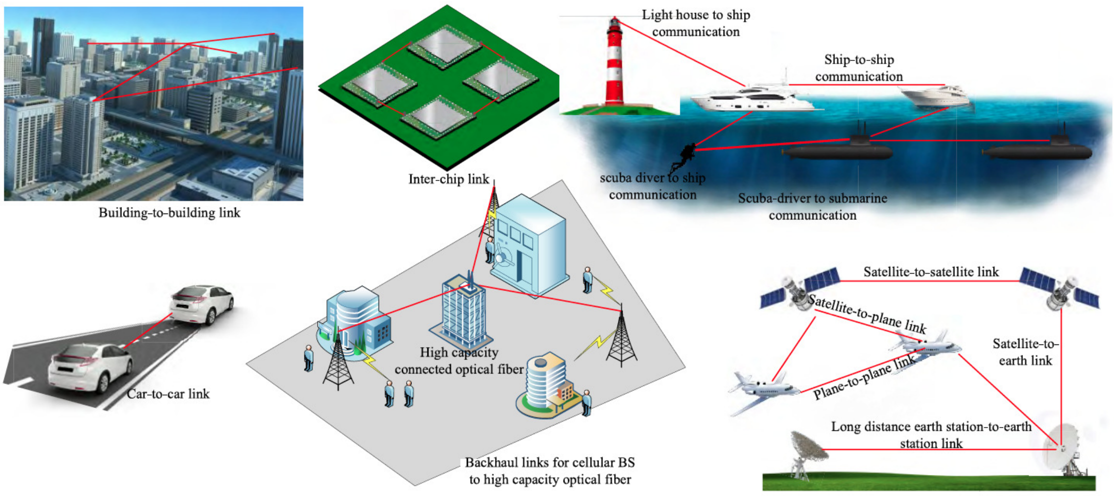

FIGURE 1.8: Application scenarios for FSO [15].

Fig. 1.8 present application scenarios for FSO. For ultra-short range communications, FSO links can be established for C2C communications; long range FSO links can serve as backhaul connections for cellular networks and for monitoring applications, etc. Further, FSO links can be used for connecting one metropolitan area network (MAN) to another and can likewise connect several local area networks (LANs). Some other examples of FSO are inter-satellite communications, underwater communication and aerospace communications.

1.3.4 Optical Camera Communication (OCC)

Due to the omnipresence of smart phones with front and/or rear cameras, an envisioned technology for OWC is OCC, which is attracting significant interest [34, 35, 36, 37, 38]. In OCC, flashlights and cameras of smartphones can be re-purposed as the transceiver with no alteration in the hardware with no additional requirement of photodiode for IM-DD. Precisely, LEDs or any other lighting sources can be used as transmitters (LDs cannot be used) and cameras (or IS) can be used as receivers. OCC uses either IR or VL spectrum. Even though the performance of OCC in indoor scenarios can be reasonable, in outdoor environments, the performance is unreliable because of short communication distances, interference due to ambient light sources and difficulty of signal detection under direct sunlight because of absence of dedicated PD. Some other practical limitations for OCC is low data-rate communication due to low frame rates of the cameras. Nevertheless, OCC can have a large number of applications in indoor scenario as depicted in Fig. 1.9, e.g., digital signage for smart and grab applications, biomedical applications in which body vitals can be monitored if wearable skin patches are used, indoor localization, vehicle-to-vehicle (V2V) and V2X communication (with a dedicated camera) etc.

FIGURE 1.9: Application scenarios for OCC [15].

1.4 Thesis Contributions

Significant research is carried out in OWC which envisages the technology to be viable and promising. Howbeit, establishing suitable energy efficient modulation schemes consistent with the constraints of IM-DD still needs analyzing. The work presented in this thesis mainly focuses on the impairment mitigation techniques and design of novel modulation schemes for OWC systems. Several single-carrier (SC) modulation approaches have been investigated in the literature for IM-DD based OWC systems, however, there are certain limitations for such approaches: (i) generally, the spectral efficiency (SE) of these approaches is less than that of multi-carrier (MC) modulation approaches [3, 39]; (ii) due to the time dispersive nature of OWC channel and due to the inter-symbol interference (ISI), complex equalization might be required [39] (frequency-domain equalization (FDE) can be used to reduce the equalization complexity [40]); and (iii) multiple-access (MA) is not straightforward to implement. All these practical limitations can be overcomed by using optical-orthogonal frequency division multiplexing (O-OFDM) approaches. The SE can be further enhanced for O-OFDM by using the so-called hybrid/layered O-OFDM approaches. Howbeit, O-OFDM approaches manifest high peak-to-average power ratio (PAPR), which exacerbate the nonlinear distortion due to the limited dynamic range of the LEDs and may increase the quantization noise because of limited bit resolution converter at the transmitter. Another possible alternative to reduce the high PAPR is to employ optical-SC frequency division multiple access (O-SCFDMA) approaches. O-SCFDMA methods are the precoded variants of O-OFDM. Furthermore, Hermitian symmetry (HS) is enforced in the frequency-domain (FD) to achieve a real-valued time-domain (TD) signal for both O-OFDM and O-SCFDMA. As a consequence, only half of the TD symbols manifests SC like properties due for O-SCFDMA. Hence, the PAPR is not significantly reduced. Against this background, following contributions have been made:

1. Two iterative decision directed clipping mitigation methods which are used to alleviate the clipping distortion have been developed for O-OFDM. These methods employ clipping at the transmitter to counteract the high PAPR. At the receiver, the derogatory impact of clipping is mitigated by using these methods.
2. An O-SCFDMA approach which averts the use of HS has been proposed. As the approach evades the HS requirement, the PAPR performance of the proposed approach is considerably better than state-of-the-art O-OFDM approaches.
3. The performance of Fourier transform and Hartley transform precoding has been analyzed for hybrid O-OFDM approaches to enhance the bandwidth efficiency of the system.

1.5 Thesis Layout

The rest of the thesis is organized as follows. *Chapter 2* introduces the theoretical concepts of OWC systems, such as, the optical wireless channel, noise sources, transmitter front-ends, receiver front-ends, etc. These concepts are imperative for understanding, designing, modelling and evaluation of OWC systems. Moreover, the chapter also provides a brief introduction on the state-of-the art O-OFDM (precoded/non-precoded) approaches which will be used in the subsequent chapters.

After analyzing the PAPR charactertics of O-OFDM approaches from chapter 2, in *chapter 3*, the decision-directed PAPR reduction methods are presented. Simulation results performed under different scenarios acknowledge that the high PAPR of O-OFDM can be reduced using clipping, with efficient clipping mitigation at the receiver, these methods can lessen the derogatory effects of clipping with a reasonable complexity compared to state-of-the-art PAPR reduction approaches for O-OFDM.

In *Chapter 4*, O-SCFDMA approach, which avoid the use of HS is introduced. Key performance parameters, such as, PAPR, bit error rate (BER), optical power penalty, system complexity, quantization, electrical power and SE are determined, which reveals the superiority of the proposed O-SCFDMA over other alternatives.

In *Chapter 5*, the performance of Fourier transform and Hartley transform precoding is analyzed for hybrid/layered O-OFDM approaches. It is demonstrated that precoded hybrid/layered approaches exhibits the lower PAPR compared to conventional hybird/layered O-OFDM counterparts. Furthermore, important performance criteria, such as, the impact of nonlinear distortion on BER, the increase in required signal-to-noise ratio (SNR) due to the layered structure, etc have also been evaluated.

In *Chapter 6*, proof-of-concept experimental results of PAPR reduction methods and O-SCFDM are presented. The experimental results also corroborate the simulation results.

Chapter 2

State-of-the-art and Objectives

2.1 Introduction

Optical communications embodies any form of propagation through the use of optical carriers, i.e., visible light (VL), infrared (IR) or ultraviolet (UV) [4]. Using this approach, the acquisition of information from the surroundings using the sense of sight can be recognized as optical wireless communication (OWC). Through the history, many examples of OWC systems can be gathered, e.g., the archaic Greeks used fire flares to forewarn about the enemy threat. Another mechanism of signalling using the smoke was developed by a Greek historian Polybius through which the messages could be conveyed using Greek alphabets. The ancient Chinese warriors used light beacons to indicate an impending threat. Nowadays, smoke signals are employed for some traditional practices, e.g., the successful election of a Pope by the cardinals is pronounced by a smoke signal from the Vatican. Moreover, for navigation, lighthouses are yet used. A realization of such systems was demonstrated by Carl Friedrich in 1810, when he developed the *heliograph*, which was a wireless solar telegraph that signalled using beams of sunlight by either interrupting the beam with the shutter or using pivoting mirror. The world's first wireless telephone system, *photophone* was developed by Alexander Graham Bell in 1880. Bell was able to modulate voice messages onto a light signal by using vibrating mirrors at the transmitter; the vibrations were reflected and projected by the sunlight. The receiver of photophone used Selenium for which the resistance is highly sensitive to light intensity in order to retrieve the voice signal from the modulated light beam [41]. Based on scientific innovation, early technological application of OWC was *semaphore lines* which were developed by a French engineer, Claude Chappe in 1972.

The modern perception of OWC relates to the optical transmission of digital signals using visible light (VL), infrared (IR) or ultra-violet (UV) as a propagation medium using either laser diodes (LDs) or light emitting diodes (LEDs) as transmitters [4, 15]. Pioneering work in this domain commenced with the invention of LD in the 1960s when an experimental OWC link using light emitting Gallium Arsenide (GaAs) diode was demonstrated at Massachusetts Institute of Technology (MIT) Lincoln Labs which could transmit television (TV) signals over a distance of 30 miles [42, 43]. Initially, it was anticipated that OWC would be the primary application field for LDs, however, after several OWC demonstrations carried out during $1960 - 1970$ [44], it was rather established that OWC systems might not be suitable due to the large beam divergence of the lasers and degrading atmospheric effects. After the advancement of optical fiber systems, the focus from OWC was shifted to the fiber based systems as they were capable of eliminating the deteriorating impacts faced by OWC systems.

OWC re-gained interest when an OWC technology for short-range indoor environments was presented by Gfeller and Bapst in 1979. They established that an IR based wireless communication system could theoretically reach transmit data-rates of up to hundreds of Mbps. Moreover, they experimentally demonstrated an IR based OWC link capable of attaining transmission speed of 100 kbps [45]. With considerable improvement in IR technology, the infrared data association (IrDA) formulated protocol standards for wireless IR communication between portable devices within short range to the transmitter [46]. In 2009, O'Brien *et al.* developed an OWC system capable of delivering transmission data-rate of 300 Mbps using IR light [47]. More recent work on short range IR technology intended for cable replacement has led to a 10 Gbps IR standard [48]. Furthermore, IR based systems and network concepts have been reported in the literature. Kahn *et al.* experimentally demonstrated a 50 Mbps diffuse IR wireless link employing on-off keying (OOK) in [49]. Angle diversity concepts [50], imaging [49] and holographic [51] receivers for IR wireless have also been documented. However, eye safety regulations requires the amount of maximum emission power by IR transmitters to be controlled. This presents significant limitation for link budget for IR networks [52], consequently, typical indoor scenarios cannot be served by a single access point (AP) and cannot achieve high data-rates. High data-rates and an efficient convergence require multiple APs and receivers which increases the complexity overhead and system cost.

With progress in solid-state lighting, there has been a trend to succeed the incandescent and fluorescent lamps with white-LED. LEDs have become the most distinguished contenders for off-the-shelf lighting sources because of their reliability and higher energy efficiency, e.g. 5 % compared to 30 % in favor of the LEDs compared to incandescent and fluorescent lamps [53]. Moreover, it is envisaged that LEDs lighting infrastructures will oust the conventional luminaries in the coming decades [52, 14, 54, 55, 56, 57]. This trend gives an opportunity to incorporate the lighting infrastructures with wireless transmission by visible light communication (VLC) based OWC systems. The idea of using LEDs for communication and fast switching was suggested by Pang *et al.* [58] in 1999. The pioneering work on using white-LEDs for communication and lighting began to take shape in early 2000s at Keio University in Japan, when Komine and Nakagawa presented the system model for VLC [56]. Following are some other achievements in this domain. First experimental demonstration of optical orthogonal-frequency-division multiplexing (O-OFDM)-based VLC system was presented by Afghani *et al.* in 2006 [59]. In 2007, VLC Consortium (VLCC) was founded to standardize the VLC technology [60]. In [61], Khalid *et al.* have achieved a data-rate of 1 Gbps by using an optimized discrete multi-tone modulation (DMT) (an alternate nomenclature used for O-OFDM) technique and adaptive bit- and power-loading algorithms. In their subsequent work [62], the authors experimentally realized a gigabit indoor VLC system using commercially available Red-Green-Blue (RGB) White LED and exploiting an optimized DMT modulation. A data-rate of 1.5 Gbps was achieved with a single channel and 3.4 Gbps was obtained by implementing wavelength-division multiplexing (WDM) transmission. In [24], the authors investigated the communication capabilities of off-the-shelf LDs which indicate that optical wireless access data-rates in the excess of 100 Gbps are possible. In 2011, the Institute of electrical and Electronics Engineers (IEEE) published VLC standard 802.15.17 [63]. In 2008, hOME Gigabit Access project (OMEGA) was launched in Europe with an aim to deliver gigabit data-rates to the home users. This project explored OWC as a potential supplementary technology to existing radio-frequency (RF) technologies [64].

The purpose of this chapter is to find the *shortcomings* of state-of-the-art techniques available in the literature to justify the study of proposed techniques in the following chapters.

2.2 Setup of Optical Wireless Communication Systems

A basic setup of the down-link of an OWC system is presented in Fig. 2.1. The transmission of data from the transmitter to the receiver, or in other words, from an AP to the user-equipment (UE) is known as down-link communication [52].

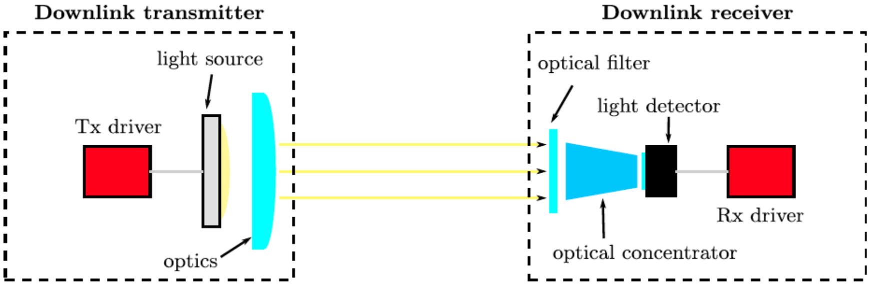

FIGURE 2.1: Key components of an OWC system [52].

2.2.1 Transmitter

In OWC systems, the conversion of electrical signals into optical signals is achieved by either the use of LEDs or LDs. Both LEDs and LDs offer unique advantages and limitations. LDs produce coherent light, hence, all the light waves travel in an analogous fashion, in a same direction and with a same phase [15]. This increases the possibility of effectively exploiting the electromagnetic spectrum by forming smaller cells and reusing the frequency etc. Because of coherent behavior, the light emitted by the LDs can travel to longer distances and suffers lesser co-channel interferences. Moreover, LD have a larger modulation bandwidth than LEDs [65, 66]. However, due to narrowband wavalength emission, efficient color mixing techniques or dedicated LD based devices are required to produce white light which results in an increased complexity to design LD-based illumination devices. Also, the radiation levels of LDs have to be adjusted in the inhabited environments to ensure eye safety and to avoid health problems due to thermal effects of laser radiation [15].

LEDs operating in the VL spectrum are the most suitable candidates for transmitter front-ends in OWC because of enhanced deployment, energy efficiency, longer life-span, lower heat generation, reduced usage of harmful materials in design, and improved color interpreting [67, 15]. Moreover, the LEDs can switch between various light intensities rapidly. This functionality makes LEDs efficient transmitters for high-speed OWC and lighting sources at the same time. It has to be ensured that LEDs are operated with a non-negative real-valued signal [52]. Commercially available white-LED have two major variants: (i) the white light is obtained by the combination of RGB LED emitters; or (ii) the blue light emitted by Gallium Nitride (GaN) emitter is coupled with the yellow emission of inorganic phosphor to generate white light [52]. The slow response of the yellow phosphor limits the 3 dB bandwidth of white LEDs to a few MHz [68, 52]. The 3 dB cut-off frequency of the LEDs can be enlarged by decreasing the size of the LEDs, this has led to the emergence of micro-LEDs (μLEDs). μLEDs have a bandwidth of several hundreds of MHz [52]. Another option to augment the bandwidth of the LEDs is to replace the un-optimized color conversion from phosphors by semiconductor [69] or perovskite materials [70]. However, the impact of using these materials on other parameters, such as conversion efficiency, speed and the overall power efficiency has yet to be examined fully [52]. There have been attempts to introduce the LD design approach in LED design to increase the modulation speed of the LEDs without altering the output efficiency, this has lead to the design of resonant-cavity LEDs (RCLEDs) [71, 72].

For a given light source, the radiant/luminous intensity varies with the location, therefore, the radiation pattern of the light emitting from such a source can be modeled by generalized Lambertian law [3, 52]. The optical intensity at a radiant angle of ϕ of the light source can be expressed as [3, 52]:

$$P_{(\mathrm{opt})}R(\phi) = P_{(\mathrm{opt})}\frac{(m+1)}{2\pi}\cos^{m}(\phi) \quad (\mathrm{W/steradian}), \tag{2.1}$$

where $P_{(\mathrm{opt})}$ is the overall transmitted optical power in Watt (W), $R(\phi)$ (1/steradian) is the radiation profile of the light source and m is the Lambertian emission order which depends on half power semi-angle, $\phi_{1/2}$, as [52]:

$$m = -\frac{1}{\log_2(\cos[\phi_{1/2}])}. \tag{2.2}$$

LED intensity profile can be well approximated as a Lambertain source with $m = 1$ which corresponds to half-angle of $\phi_{1/2} = 60°$.

2.2.2 Receiver

The typical receiver for an OWC system is depicted on the right of Fig. 2.1. At the receiver, the received light is concentrated on the photodetector via an optical concentrator.

Optical filters can be employed to confine the spectrum of light, weaken the impact of ambient light sources and for blue filtering [73] (to restrict the slow light from the yellow phosphor color conversion) [52]. The gain of the optical filter, $G_{\mathrm{OF}}(\psi)$, is a function of the incident angle at the receiver, ψ. The optical concentrator focuses the received light from the wide field-of-view (FoV) to a photo-diode (PD). The optical gain of a concentrator is expressed as [74, 52]:

$$G_{\mathrm{OC}}(\psi) = \begin{cases} \frac{n_{\mathrm{ref}}^2}{\sin^2(\psi_{\mathrm{FoV}})}, & |\psi| \leq \psi_{\mathrm{FoV}} \\ 0, & |\psi| > \psi_{\mathrm{FoV}} \end{cases}, \tag{2.3}$$

where n_{ref} is the effective refractive index of the optical material, ψ is the incident angle to the receiver and ψ_{FoV} is the FoV of the receiver which is the incidence angle exceeding which the receiver does not admit any light.

Several types of photodetectors/light detectors, such as, image sensors [75, 34, 76], solar panels [77] or even LEDs [78, 79] can be used. However, various limiting factors, such as, slow frequency response and less efficiency for high speed communication make the above mentioned components less desirable candidates for photodetectors. The photodetector (PD) converts the received optical signal to an electrical signal which is amplified via a trans-impedance amplifier (TIA) prior to analog-to-digital conversion and signal processing for data recovery [52]. The performance of the receiver is influenced by the bandwidth, sensitivity and the area of the PD. The amount of the light that can be concentrated by a PD is related to its area; A_{PD}. This implies that if A_{PD} is enlarged, the received power can be strengthened which augments the sensitivity, thus, making the system more viable for seamless mobility. Howbeit, a larger A_{PD} culminates in slow switching speed of the device which depreciates the frequency response profile. On the other hand, low area of the PD proceeds in low capacitance and high bandwidth. It may be noticed that $G_{\mathrm{OF}}(\psi)$ and $G_{\mathrm{OC}}(\psi)$ depend on the light incidence angle at the receiver, accordingly, the angle of light incidence at the receiver, alters the effective area, A_{eff}, of the photodetector. According to [74], the variation in A_{eff} corresponds to $\cos(\psi)$, and, hence, A_{eff} can be appraised as:

$$A_{\mathrm{eff}}(\psi) = \begin{cases} A_{\mathrm{PD}} G_{\mathrm{OF}}(\psi) G_{\mathrm{OC}}(\psi) \cos(\psi), & |\psi| \leq \psi_{\mathrm{FoV}} \\ 0, & |\psi| > \psi_{\mathrm{FoV}} \end{cases} . \tag{2.4}$$

Another critical parameter which impacts the performance of the system is the responsitivity of the PD, ϖ (Ampere/Watt) which quantifies the amount of current induced for a given optical power. ϖ varies with the wavelength of the light, therefore, it can be evaluated by integrating it for individual wavelengths over the entire spectrum of transmitted light reaching the PD.

2.2.3 The Optical Wireless Communication Channel

Consider the block diagram of an OWC system depicted in Fig. 2.2.

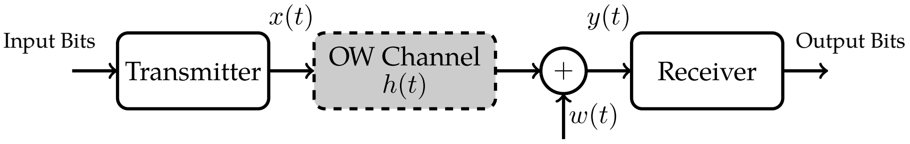

FIGURE 2.2: A block diagram of an OWC system.

An OWC system relies on intensity-modulation and direct-detection (IM-DD) [74] techniques. Therefore, both the phase and amplitude of the electromagnetic wave cannot be modulated and the transmitted information is exclusively encoded on the signal intensity [74]. Consider $x(t)$ to be the data-carrying intensity waveform which modulates the brightness of the transmitter. $x(t)$ is translated to an optical intensity signal as $u(t) = \omega x(t)$, where ω (Watt/Ampere) is the electrical-to-optical conversion factor. For simplicity, perfect synchronization [80, 81], and a linear response for the transmitter for simplification. The channel impulse response (CIR) is expressed as $h(t)$. The photo-detected signal is expressed as $g(t) = \varpi u(t)$, where ϖ is the responsitivity of the PD. Without loss of generality, it is considered that $\omega = \varpi = 1$, hence, $g(t) = u(t) = x(t)$. The received signal is filtered by the channel and is corrupted by noise, $w(t)$, in the electrical-domain, thus, the received signal at the PD can be written as:

$$y(t) = h(t) \otimes x(t) + w(t), \tag{2.5}$$

$w(t)$ is modeled as independent and identically distributed additive white Gaussian noise (AWGN) with single-sided power spectral density (PSD) of N_0 and $\otimes$ denotes the convolution operator. From here onwards, a VLC system in which LEDs are employed as transmitters shall be considered. The optical wireless channel impulse response (CIR), $h(t)$ comprises all the distortive implements from the generation of the electrical signal that modulates the data onto the LED to obtaining an electrical signal at the receiver output. The condition of an OWC link can be determined by the output signal-to-noise ratio (SNR). Some key factors which can impact the SNR are: (i) the limited bandwidth of the front-ends; (ii) the frequency selectivity of the optical wireless channel; (iii) the attenuation of the optical wireless channel: and (iv) the non-linearity of te LED device [52]. From here onward, solely the indoor environments are dealt with to evaluate the CIR of the optical wireless channel.

LEDs in an OWC system introduce low-pass filter response in the CIR. Moreover, because of the indoor environments, the receiver gathers the signal after multiple bounces, which may introduce a time dispersive (i.e., a frequency-selective) response (based on the dimensions of the room). The overall CIR is equal to the concatenation of two filters connected in series [52], where, the LED/LED driver combination CIR and optical wireless CIR can be modeled as separate filters. Hence, the overall CIR can be given as:

$$h(t) = h_{\text{chan}}(t) \otimes h_{\text{led}}(t), \tag{2.6}$$

where $h_{\text{chan}}(t)$ is the CIR due to propagation of light in indoor optical wireless channel and $h_{\text{led}}(t)$ is the CIR of the LED/LED driver combination. If the overall CIR, $h(t)$, is known, the corresponding frequency response can be evaluated by using the Fourier transform as [52]:

$$H(f) = \int_0^\infty h(t) e^{-2\pi f t} \mathrm{d}t = H_{\text{chan}}(f) \cdot H_{\text{led}}(f). \tag{2.7}$$

The combined effects of the transmitter and the receiver lead to low-pass filter characteristics primarily because of LED/LED driver combination. The LED low-pass characteristics have been studied in numerous experimental studies [61, 82, 68], which have determined that the 3 dB bandwidth of LEDs range from 10 MHz to 60 MHz. However, with an optimized driver, the 3 dB cut-off frequency, $f_{3\text{dB}}$ of between 60 MHz and 180 MHz for a common high-power phosphorescent white-light LED has been measured [83, 84]. The frequency response of the LED is modeled as a Gaussian low-pass filter [84]:

$$H_{\text{led}}(f) = e^{-\ln(2)\left(\frac{f}{f_{3\text{dB}}}\right)^2}. \tag{2.8}$$

As aforementioned, the CIR of optical wireless channel also impacts the system performance. If there is an unobstructed propagation from the LED to the PD, then there is a line-of-sight (LoS) path between them. However, due to multiple paths inside the indoor environments, a non-LoS (NLoS) contribution also exists in $h_{\text{chan}}(t)$.

For brevity, a lighting source, $\mathcal{S}$ which emits the impulse of optical intensity can be denoted by an ordered three tuple (Fig. 2.3) [85] as:

$$\mathcal{S} = \left\{\overrightarrow{a}_{\text{s}}, \overrightarrow{o}_{\text{s}}, m\right\}, \tag{2.9}$$

where $\overrightarrow{a}_{\text{s}}$ is the location vector, $\overrightarrow{o}_{\text{s}}$ is the orientation vector and m is the Lambertian emission order. Similarly, the receiving element, $\mathcal{R}$, with location vector, $\overrightarrow{a}_{\text{r}}$, direction vector, $\overrightarrow{o}_{\text{r}}$, area A_{PD} and FoV of ψ_{FoV} as illustrated in Fig. 2.3 shall be denoted by an ordered four tuple as [85]:

$$\mathcal{R} = \left\{\overrightarrow{a}_{\text{r}}, \overrightarrow{o}_{\text{r}}, A_{\text{PD}}, \psi_{\text{FoV}}\right\}, \tag{2.10}$$

If the lighting source, $\mathcal{S}$ and a receiving element, $\mathcal{R}$ are separated by a Euclidean distance of D, then, at a radiant angle of ϕ with respect to the source and at an incidence angle of ψ at the receiver, thus, at the receiving element, $\mathcal{R}$, the attenuation is calculated as [85]:

$$H_{\text{DC}} = \frac{(m+1)}{2\pi D^2} A_{\text{PD}} G_{\text{OF}}(\psi) G_{\text{OC}}(\psi) \cos^m(\phi)\cos(\psi), \tag{2.11}$$

where H_{DC} is the DC gain of the optical wireless channel. The parameters, D, $\cos(\phi)$ and $\cos(\psi)$ are evaluated as [85]:

$$D = \| \overrightarrow{a}_{\mathrm{s}} - \overrightarrow{a}_{\mathrm{r}} \|, \tag{2.12}$$

$$\cos(\phi) = \langle \overrightarrow{o}_{\mathrm{s}}, (\overrightarrow{a}_{\mathrm{r}} - \overrightarrow{a}_{\mathrm{s}}) \rangle / D, \tag{2.13}$$

and

$$\cos(\psi) = \langle \overrightarrow{o}_{\mathrm{r}}, (\overrightarrow{a}_{\mathrm{s}} - \overrightarrow{a}_{\mathrm{r}}) \rangle / D, \tag{2.14}$$

where $\langle \overrightarrow{x}, \overrightarrow{y} \rangle$ is the scalar product of $\overrightarrow{x}$ and $\overrightarrow{y}$.

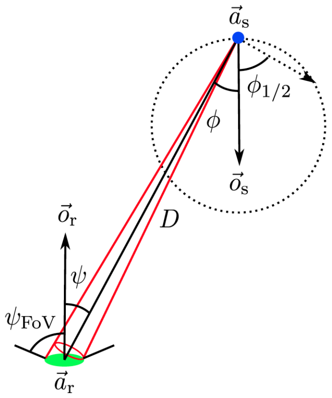

FIGURE 2.3: Optical wireless channel DC gain geometry [52].

A setup of an optical wireless channel with LoS and NLoS components is depicted in Fig. 2.4. Taking into account the DC gain given in (2.11), the LoS CIR for a given transmitter $\mathcal{S}_{\mathrm{tx}}$ and receiver $\mathcal{R}_{\mathrm{rx}}$ is evaluated as:

$$h^{[0]}(t, \mathcal{S}_{\mathrm{tx}}, \mathcal{R}_{\mathrm{rx}}) = \frac{(m+1)}{2\pi D^2} A_{\mathrm{PD}} G_{\mathrm{OF}}(\psi) G_{\mathrm{OC}}(\psi) \cos^m(\phi) \cos(\psi) \delta\left(t - \frac{D}{c}\right), \tag{2.15}$$

where $\delta(\cdot)$ is delta function and c is the speed of light.

Many studies have been carried out to calculate the NLoS CIR for optical wireless channel. To evaluate $h_{\mathrm{chan}}(t)$, usually the room dimensions are specified. The received optical signal endures time dispersion from the reflections inside the room. If the indoor fixtures of the room are assumed purely diffusive, the reflections from them are likewise diffusive and can be sufficiently modeled as Lambertian [85]. It is considered that all the objects inside the room are immobile. Moreover, it is troublesome to evaluate the CIR due to human bodies present inside the room, therefore, in the evaluation of NLoS CIR, it is considered that the rooms are unoccupied.

The overall optical wireless CIR from the transmitter, $\mathcal{S}_{\mathrm{tx}}$ to receiver, $\mathcal{R}_{\mathrm{rx}}$ undergoing i_{bounce} reflections/bounces with number of LEDs equal to N_{LED} is evaluated as [85]:

$$h_{\mathrm{chan}}(t, \mathcal{S}_{\mathrm{tx}}, \mathcal{R}_{\mathrm{rx}}) = \sum_{n=1}^{N_{\mathrm{LED}}} \sum_{i=0}^{\infty} h^{[i_{\mathrm{bounce}}]}(t, \mathcal{S}_{\mathrm{tx}}^{n}, \mathcal{R}_{\mathrm{rx}}). \tag{2.16}$$

For $i_{\mathrm{bounce}} = 0$, (2.16) coresponds to LoS CIR. To evaluate NLoS CIR, the internal surface area of the reflecting elements inside the room is subdivided into N_{b} blocks. The location vector and the direction vector of each block is expressed as $\overrightarrow{a}_{\mathrm{b}}$ and $\overrightarrow{o}_{\mathrm{b}}$, respectively. Each block acts like a transmitter and receiver. In the receiving mode, each block can be regarded as a receiver, $\mathcal{R}_\mathrm{b}$ because it absorbs the impinged light from the source. In the transmitting mode, each block is recognized as a source, $\mathcal{S}_\mathrm{b}$ as the absorbed light is re-emitted from with a generalized Lambertian pattern, the intensity of which hinges on the reflectivity coefficient, ρ_b. Maximum light incidence angle at the receiving element can be $\psi_\mathrm{FoV} = \pi/2$ [52]. The receiving block has a physical area of ΔA and the received power for each block should be scaled by ρ_b while transmitting. The optical wireless CIR undergoing i bounces is evaluated from the CIR with $i-1$ bounces as [85]:

$$\begin{aligned} h^{[i_\mathrm{bounce}]}\left(t, \mathcal{S}_\mathrm{tx}, \mathcal{R}_\mathrm{rx}\right) &= \sum_{b=1}^{N_\mathrm{b}} h^{[0]}\left(t, \mathcal{S}_\mathrm{tx}, \mathcal{R}_\mathrm{b}\right) \otimes h^{[i_\mathrm{bounce}-1]}\left(t, \mathcal{S}_\mathrm{b}, \mathcal{R}_\mathrm{rx}\right) \\ &= \frac{(m+1)}{2\pi} \sum_{b=1}^{N_\mathrm{b}} \frac{\rho_\mathrm{b} \cos^m\left(\phi_\mathrm{b}\right) \cos\left(\psi_\mathrm{b}\right)}{D_\mathrm{b}^2} h^{[i_\mathrm{bounce}-1]}\left(t - \frac{D_\mathrm{b}}{c}, \{\vec{a}_\mathrm{b}, \vec{o}_\mathrm{b}, 1\}, \mathcal{R}_\mathrm{rx}\right) \Delta A, \end{aligned} \tag{2.17}$$

for $\psi_\mathrm{b} \leq \pi/2$. Here, the quantities D_b, ϕ_b and ψ_b are the distance for the LoS link from the surface block, b to the receiver, the angle of transmission and the angle of incidence. The accuracy for evaluating CIR can be increased if N_b are increased or ΔA is decreased [52].

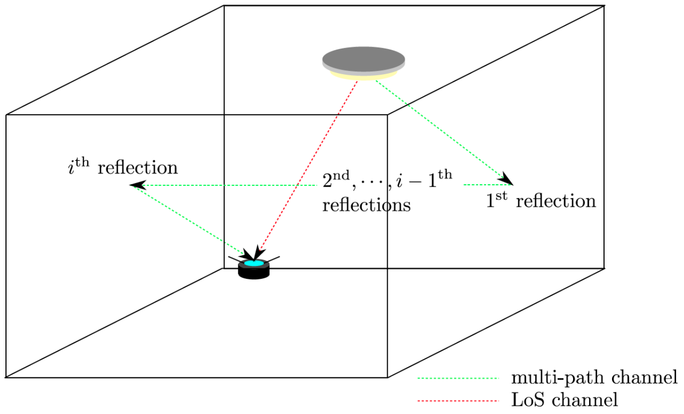

FIGURE 2.4: Illustration of LoS and NLoS multipath optical wireless propagation channel [52].

Subsequently, in this work the power delay profile or CIR for a realistic VLC scenario presented in [86] is considered, which is graphically illustrated in Fig. 2.5. An empty cubic room of dimension (5.0 m × 5.0 m × 3.0 m) with plaster walls is considered. Four luminaries with a symmetrical arrangement having coordinates (1.5 m, 1.5 m, 3.0 m), (1.5 m, 3.5 m, 3.0 m), (3.5 m, 1.5 m, 3.0 m) and (3.5 m, 3.5 m, 3.0 m) are installed on the ceiling. Each luminary consists of 100 LED chips and each chip radiates an optical power of 0.45W. A PD receiver is located at the cornor of the floor (0.5 m, 1.0 m, 0.0 m) pointing vertically towards the ceiling. The receiver FOV is set to 85°. The reflection coefficient, ρ, of the Lambertian reflectors, such as the floor, plaster wall, and the ceiling is considered to be 0.63, 0.83, and 0.40, respectively [86]. Readers are referred to [86] for a comprehensive evaluation of VLC channel model. The CIR is evaluated with a sampling time of 1 ns. It is highlighted that the first peak in the CIR the is due to LOS signal from the LED, whereas, the other peaks are due to reflections from the walls.

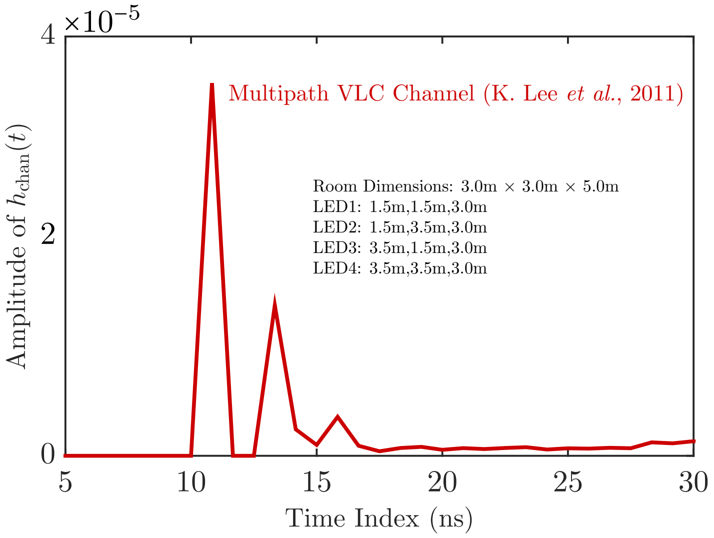

FIGURE 2.5: Power delay profile for 4 LED transmitters in a cubic room with plaster walls [86].

Following [87], we consider that the transmitter and the receiver and perfectly synchronized, such that the channel is tapped from the time of the arrival of the LOS signal (after a delay of D/c second). The VLC channel parameters are summarized in Table 2.1.

TABLE 2.1: VLC channel model parameters

Parameter	**Value**
Transmitted optical power	0.45 W per LED chip
Field-of-view (FOV)	85°
Area of PD (A_{PD})	1 cm^2
Lambertian emission order (m)	1
Sampling time (T_s)	1 ns
Room topology	(5.0 m × 5.0 m × 3.0 m)
Number of LEDs (N_{LED})	4
Viewing angle of LED ($\phi_{1/2}$)	60°
LED Coordinates	LED1: (1.5 m, 1.5 m, 3.0 m) LED2: (1.5 m, 3.5 m, 3.0 m) LED3: (3.5 m, 1.5 m, 3.0 m) LED4: (3.5 m, 3.5 m, 3.0 m)
PD coordinates	(0.5 m × 1.0 m × 0.0 m)
Reflection coefficients	Floor: 0.63 Ceiling: 0.40 Plaster walls: 0.83

2.3 Impairments in Optical Wireless Communication

2.3.1 Noise Components

In OWC system, the electronic elements and parasitic optical sources introduce noise to the information signal. In an OWC system there are three primary noise sources, i.e., [67]:

- *Ambient optical/background noise* due to solar radiations from doors and windows in the room and due to other lighting/illumination sources in the background, such as incandescent and fluorescent lamps present in proximity. The ambient noise proceeds in a white noise interference. The limiting impact of ambient noise due to artificial light sources can be cancelled out by employing electrical high pass filters at the receiver. Moreover, the ambient noise would be different at different places inside the room and depends on the time of the day and orientation of the windows and doors [67]. However, the modeling of ambient noise from solar radiations is cumbersome as it relies on the location of doors and windows which may differ from place to place [52].

- *Shot noise* emanates from the intrinsic statistical randomness in the generation of electrons by the photons at the PD [74, 88] and increases with an increase in light intensity because higher light intensities can contribute to a higher number of photon-electron interactions [89]. Shot noise can appear because of two reasons. Firstly, the ambient light due to solar radiation and other lighting sources also increase the shot noise which is inevitable and is detrimental. Secondly, the OWC information signal itself is responsible [74, 89]. The shot noise can be modeled as an arbitrary AWGN with a PSD of [89]:

$$N_0^{\text{shot}} = 2q\varpi P_{\text{rx}} \quad (\text{A}^2/\text{Hz}), \tag{2.18}$$

  where q is the charge on the electron in Coulombs (C) which is equal to 1.602×10^{-19} C, P_{rx} is the average received optical power.

- *Thermal noise* is from the random thermal motion of electrons in the receiver circuit of equivalent resistance R_{L} and temperature T_{k}. It is a white noise and is modeled as AWGN [88, 90, 91]. The PSD of thermal noise for IM-DD is [88, 90]:

$$N_0^{\text{thermal}} = \frac{4k_{\text{B}}T_{\text{k}}}{R_{\text{L}}} \quad (\text{A}^2/\text{Hz}), \tag{2.19}$$

  where $k_{\text{B}} = 1.381 \times 10^{-23}$ (Joule/Kelvin) is the Boltzmann constant and T_{k} is the device temperature in Kelvin.

Both the shot noise and the thermal noise are modeled as uncorrelated AWGNs. Thus, incorporating (2.18) and (2.19) the overall AWGN single-sided PSD at the receiver is [88, 90, 91]:

$$N_0 = N_0^{\text{shot}} + N_0^{\text{thermal}}. \tag{2.20}$$

2.3.2 Nonlinear Distortions

Apart from various noise components as described previously, there is nonlinear distortion due to the limited dynamic range of the LED [52]. To avoid any nonlinear distortion, the LED should have linear channel response and a large dynamic range [92]. The typical input/output characteristics of an LED are depicted in Fig. 2.6 which reveal that LEDs have a quasi-linear response within a limited dynamic range, thus, ideally, the transmitted signal should be between the linear range. To obtain a linear response of the LED, a minimum current, $\hat{I}_{\text{min}}$ with reciprocal optical power, $\hat{P}^{\text{min}}_{\text{(opt)}}$ is required to turn-on the LED. Similarly, there is a saturation point for the LED at current level and optical power of $\hat{I}_{\text{max}}$ and $\hat{P}^{\text{max}}_{\text{(opt)}}$. An aftermath of a limited linear dynamic range is that the amplitude of input signal that stretches beyond the linear range of the LED would be clipped, which seriously degrades the performance of the system. The optical power can be modeled as:

$$P_{\text{(opt)}} = \begin{cases} GI_{\text{in}}, & 0 \leq I_{\text{in}} \leq I^{\text{max}} \\ P^{\text{max}}_{\text{(opt)}}, & I > I^{\text{max}} \end{cases}, \tag{2.21}$$

where G is the conversion coefficient from the input current, I_{in}, to the output optical power. The linear response exist only if the condition $I_{\text{in}} < I^{\text{max}}$ is met. An almost ideal linear relationship between input current and the output optical power for the LED is obtainable if pre-distortion techniques are incorporated for current-voltage (I-V) curve [93, 94, 52] as shown in Fig. 2.6. Moreover, the optical power can also saturate at $P^{\text{max}}_{\text{(opt)}}$ for $I_{\text{in}} > I^{\text{max}}$ for eye safety regulations and/or design requirements such as signal dimming.

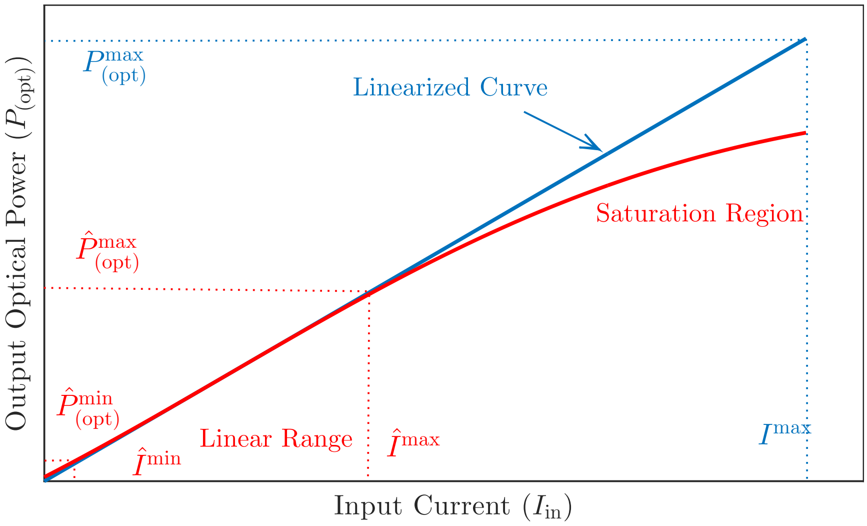

FIGURE 2.6: Relationship between driving current and output optical power of a LED. The red curve shows a typical nonlinear relationship between the driving current and the optical output power. The blue curve shows an ideal linearized conversion after pre-distortion.

2.4 Modulation Schemes for Optical Wireless Communication

There is an inherent distinction between the modulation techniques adopted in RF communication and OWC. As in OWC, either LEDs or LDs are used as transmitter front-ends, therefore, the transmit data is encoded in amplitude to modulate light intensity, but not in both amplitude and phase of the optical field, which would need coherent detection, and the LED emitter is not a coherent source [67, 5, 52]. The data/information can be transmitted and demodulated using IM-DD. To implement a modulation scheme using IM-DD certain conditions have to be satisfied:

- the transmit signal should be real-valued because complex signal cannot be used to vary the intensity of the emitted light;
- the information signal should be non-negative, since, the transmitter front-ends used in OWC only have positive dynamic range.

The constraints on the modulation signal inhibit the set of modulation techniques that can be used for OWC. In the sequel, the underlying focus is to review the performance of multi-carrier (MC) approaches, i.e., O-OFDM and precoded O-OFDM which possesses quasi single-carrier (SC) like characteristics and can also provide simple equalization technique for frequency selective optical wireless channel. However, a succinct introduction of simple SC modulation approaches, such as OOK, pulse-position modulation (PPM) and M-ary pulse-amplitude modulation (PAM) is likewise presented.

SC modulation approaches, such as OOK, PPM or unipolar M-ary PAM can be implemented for OWC systems because [89]:

1. the implementation complexity is relatively less compared to MC modulation approaches;
2. they are less sensitive to nonlinear distortions;
3. attain better bit-error rate (BER) performance in flat fading channels.

In M-PPM, one pulse reciprocal to a certain bit is transmitted in one of the M time-slots of a symbol period. M-PPM is more power efficient compared to OOK, but, is less bandwidth efficient [95, 96]. Moreover, with an increase in M, the peak-to-average power (PAPR) of M-PPM rises proportional to the square root of M. Also, M-PPM is more complex compared to OOK because it demands a strict bit and symbol synchronization at the receiver [97]. M-ary PAM is another simple modulation scheme where the data is modulated into the amplitude of the signal pulse which uses multiple intensity levels and therefore, can be implemented in a forthright manner [5]. It is highlighted that OOK is a special case of M-ary PAM, i.e., 2-PAM, where the intensity of the LED can be switched between high (bit 1) and low (bit 0) to modulate data.

Though these schemes are easy to implement, however, in case of time dispersive channel for which the delay spread is significant with respect to the symbol duration, these approaches suffer from inter-symbol interference (ISI). To eliminate ISI, complex equalization process might be appropriated. Moreover, for a complete networking solution, OWC system should be capable of multiple access (MA), implementing which in FD might be a challenge for the above mentioned approaches, whereas, time-division multiple access (TDMA) gives rise to synchronization issues. Recently, non-orthogonal multiple access (NOMA) has been proposed to incorporate MA for SC approaches [98]. On the other hand, O-OFDM is regarded as an efficient approach for OWC, as it achieves high data-rate by using multiple orthogonal subcarriers to concurrently transmit parallel data streams; can be used for multiple access (MA) eliminates the need for complex equalizers; embodies an inherent resilience to combat ISI; and straightforward extention for MA [99, 100, 101, 102]. Generally, to attain a real-valued TD O-OFDM signal (also known as DMT), Hermitian symmetry (HS) is enforced in the FD, however, the achieved TD signal is bipolar. HS is a property of DFT which states that the DFT of a real-valued signal results in a Hermitian symmetric signal, i.e., the obtained FD signal for the positive frequencies is the complex conjugate of the FD signal for the negative frequencies. The inverse of this property is exploited for IDFT to obtain a real-valued TD signal. On the other hand, many strategies exist to generate a non-negative signal. A forthright approach is to incorporate a bias to eliminate the negative excursions, however, the addition of bias translates to an optical energy inefficiency. This approach is referred to as direct-current (DC) biased O-OFDM (DCO-OFDM) [99]. Other approaches capitalize on the frame structure of O-OFDM to attain a non-negative signal, such as, asymmetrically clipped O-OFDM (ACO-OFDM) [100], PAM-DMT [103], Flip-OFDM [104], unipolar (U)-OFDM [105]. In ACO-OFDM and PAM-DMT, an anti-symmetric TD signal is achieved, for which, the negative signal amplitudes are clipped to zero without loss of information. Besides, Flip-OFDM and U-OFDM are conceptually identical, where, the positive and the reversed-negative samples of the bipolar signals are sequentially transmitted. Moving forward, the discussions are restricted to DCO-OFDM and ACO-OFDM because these are the classical state-of-the-art O-OFDM approaches discussed in the literature. It may be noticed that DCO-OFDM is spectrally more efficient than ACO-OFDM, whereas, ACO-OFDM is more power efficient compared to DCO-OFDM for low order constellations at an expense of reduced spectral efficiency (SE) [106].

It is highlighted that the non-negative signal generation process for ACO-OFDM, PAM-DMT, Flip-OFDM, and U-OFDM halves the SE compared to DCO-OFDM. This SE sacrifice is either due to halving of the modulated subcarriers or doubling the transmit time of a symbol. To augment the SE towards that of DCO-OFDM, so-called *hybrid* approaches are proposed. These schemes maintain a power advantage over DCO-OFDM without relinquishing half of the SE. The hybrid counterpart of ACO-OFDM is layered ACO-OFDM (LACO-OFDM) [107, 108], which stacks numerous layers of ACO-OFDM with each successive layer modulating the empty subcarriers left by the preceding layers. Similarly, augmented SE-DMT (ASE-DMT) [109] and enhanced U-OFDM (eU-OFM) [110] are hybrid approaches for PAM-DMT and U-OFDM/Flip-OFDM, respectively. However, the hybrid approaches still manifest a high PAPR and are generally more complex compared to the DCO-OFDM.

Despite numerous advantages, O-OFDM approaches suffer from a number of drawbacks, which are [40]:

1. Using HS to realize a real-valued signal incurs a SE loss. Half of the subcarriers are at least sacrificed to incorporate HS constraint, consequently, there is a SE loss by a factor two for both DCO-OFDM and ACO-OFDM. Moreover, to attain an anti-symmetric signal in ACO-OFDM, only odd subcarriers are modulated, which further reduces the SE by a factor of two. So, compared to base-band approaches, a SE loss of two and four is incurred by DCO-OFDM and ACO-OFDM, respectively.

2. One practical limitation of O-OFDM approaches is high PAPR. TD O-OFDM signal is generated by addition of multiple subcarriers with distinct frequencies. Due to addition of these multiple subcarriers, the TD O-OFDM signal manifests a highly fluctuating noise like envelope. If the instantaneous amplitude and phases of the subcarriers are aligned, then, due to constructive addition, the instantaneous power is relatively higher than the average power, which results in high PAPR. The constructive addition of the subcarriers is demonstrated in Fig. 2.7 and an illustration of high PAPR (which signifies large amplitude excursion that exceeds the limited linear dynamic range of the transmitter) of O-OFDM signal is presented in Fig. 2.8. As mentioned previously, the OWC transmitter front-ends have a limited linear dynamic range, so, if a signal with high PAPR is input to the transmitter, a drastic performance degradation is foreseen due to the nonlinear distortions.

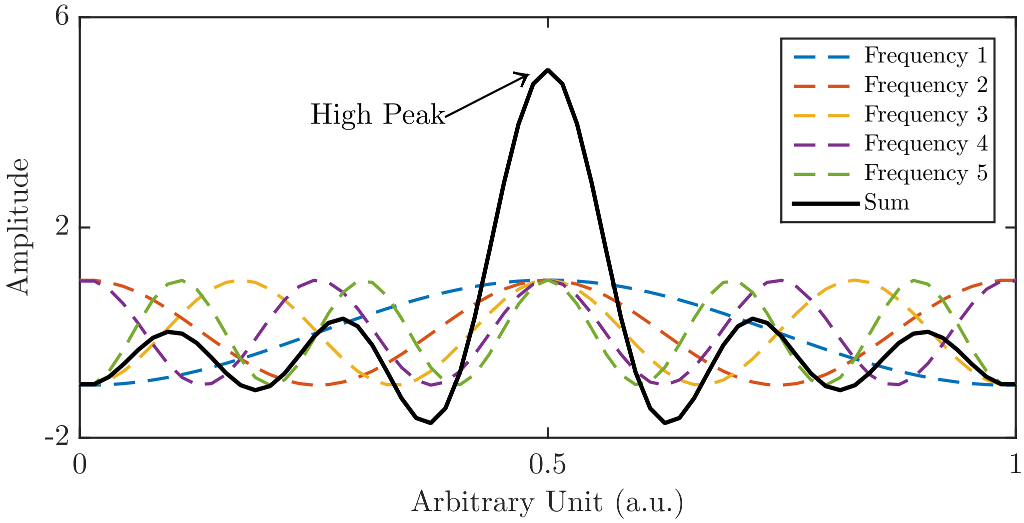

FIGURE 2.7: Constructive addition of multiple subcarriers which results in a highly fluctuating noise like envelop which results in high PAPR.

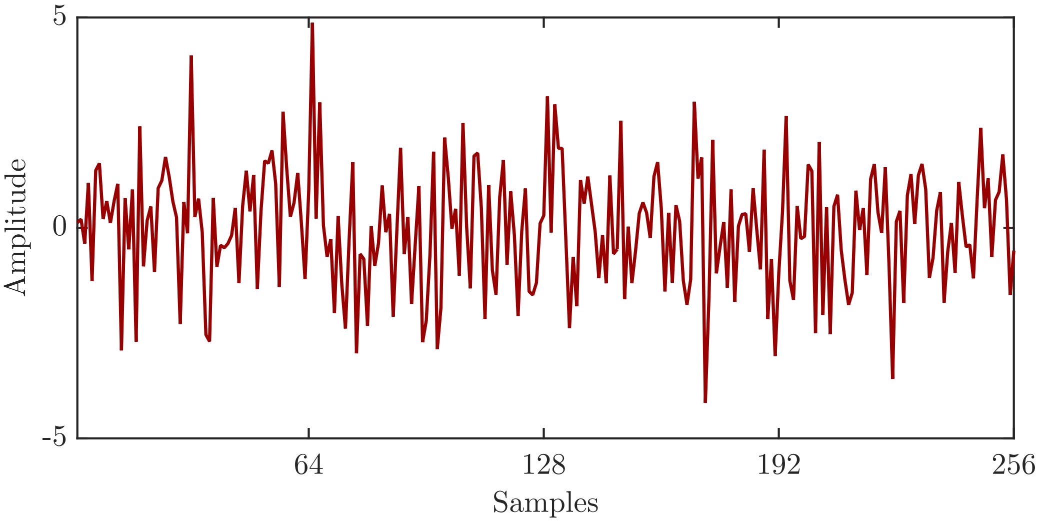

FIGURE 2.8: A graphical illustration of TD O-OFDM exhibiting high PAPR.

2.4.1 Transforms

Fourier Transform

For conciseness in notation, the orthogonal transforms that have been subsequently used are presented in this section. N-order discrete Fourier transform (DFT) for an arbitrary TD signal, $r(n) \in \mathbb{C}$ is given as:

$$R(k) = \mathrm{DFT}\left[r(n)\right] = \frac{1}{\sqrt{N}} \sum_{n=0}^{N-1} r(n) \exp\left(\frac{-j2\pi nk}{N}\right), \tag{2.22}$$

where $k = 0, 1, \cdots, N-1$ and $j^2 = -1$. Whereas, N-order Inverse DFT (IDFT) for an arbitrary FD signal $R(k) \in \mathbb{C}$ reads:

$$r(n) = \text{IDFT}\left[R(k)\right] = \frac{1}{\sqrt{N}} \sum_{k=0}^{N-1} R(k) \exp\left(\frac{j2\pi nk}{N}\right), \tag{2.23}$$

for $n = 0, 1, \cdots, N-1$.

Hartley Transform

Conventionally, most O-OFDM approaches employ IDFT/DFT for multiplexing/demultiplexing of the subcarriers. An alternative is to use discrete Hartley transform (DHT) or inverse DHT (IDHT), if the input alphabets are drawn from real constellations, e.g., M-ary PAM. N-order DHT for an arbitrary real-valued TD signal, $r(n) \in \mathbb{R}$, is

$$R(k) = \text{DHT}\left[r(n)\right] = \frac{1}{\sqrt{N}} \sum_{n=0}^{N-1} r(n)\text{cas}\left(\frac{2\pi kn}{N}\right), \tag{2.24}$$

where $k = 0, 1, \cdots, N-1$ and $\text{cas}(\cdot) = \cos(\cdot) + \sin(\cdot)$. Furthermore, N-order IDHT for an arbitrary FD signal, $R(k) \in \mathbb{R}$ is given as:

$$r(n) = \text{IDHT}\left[R(k)\right] = \frac{1}{\sqrt{N}} \sum_{k=0}^{N-1} R(k)\text{cas}\left(\frac{2\pi kn}{N}\right), \tag{2.25}$$

where $n = 0, 1, \cdots, N-1$. The kernel for both DHT and IDHT is identical, so, the same algorithm can carry out both processes [111]. Moreover, a real-valued input results in a real-valued output for DHT/IDHT. This property is advantageous for IM, for which, a real-valued TD signal can be obtained without requiring HS, whilst, to realize a real-valued output using DFT/IDFT, the input must be Hermitian symmetric.

2.4.2 Simulation Environment

All the subsequent simulation that have been carried out subsequently are performed using MATLAB in conjuntion with *Communication Toolbox* and *Signal Processing Toolbox* in MATLAB.

2.4.3 Direct-Current (DC) biased O-OFDM (DCO-OFDM)

DCO-OFDM is one of the most studied modulation approach for OWC which was proposed by Carruthers and Kahn in [99]. Consider a DCO-OFDM tranmission with N subcarriers, as portrayed in Fig. 2.9.

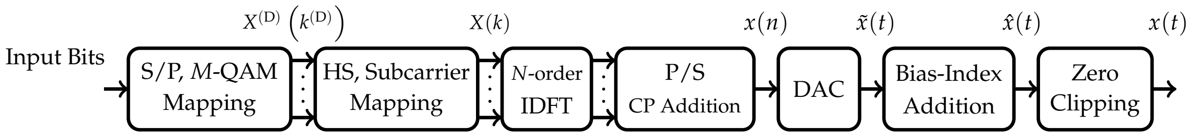

FIGURE 2.9: Block diagram of DCO-OFDM Transmitter.

The serially incoming bits are parsed into $N/2-1$ parallel streams. These bits are modulated to Gray-mapped complex M-ary quadrature-amplitude modulation (QAM) alphabets drawn from the constellation set $\boldsymbol{\mathcal{Q}} = \{\mathcal{Q}_0, \mathcal{Q}_1, \cdots, \mathcal{Q}_{M-1}\}$, resulting in FD symbols, $X^{(D)}\left(k^{(D)}\right)$, $k^{(D)} = 0, 1, \cdots, N/2-2$. The $N/2-1$ FD symbols are assigned to a N-dimensional signal, $X(k)$, $k = 0, 1, \cdots, N-1$ obeying HS as:

$$X(k) = \begin{cases} X^{(D)}\left(k^{(D)}\right), & k = k^{(D)}+1 \\ X^{*(D)}\left(k^{(D)}\right), & k = N-(k^{(D)}+1) \\ 0, & \text{elsewhere} \end{cases}, \tag{2.26}$$

where $(\cdot)^*$ represents the conjugate operation. To avoid any residual complex component in the TD signal, $X(0)$ and $X(N/2)$ are set to zero. Note that, HS is incorporated to obtain a real-valued TD signal. A graphical illustration of the real and the imaginary components of $X(k)$, i.e., $\Re\left[X(k)\right]$ and $\Im\left[X(k)\right]$ is presented in Fig. 2.10 (a) and Fig. 2.10(b), respectively to signify the impact of HS on the generation of TD signal. It can be observed from Fig. 2.10 (a) that the real components of the second half of subcarriers are the mirrored image of the first half of the subcarriers. Moreover, from Fig. 2.10 (b), it may be noticed that the imaginary components of the second half of $X(k)$ are inverted mirror image of the imaginary components of the first half.

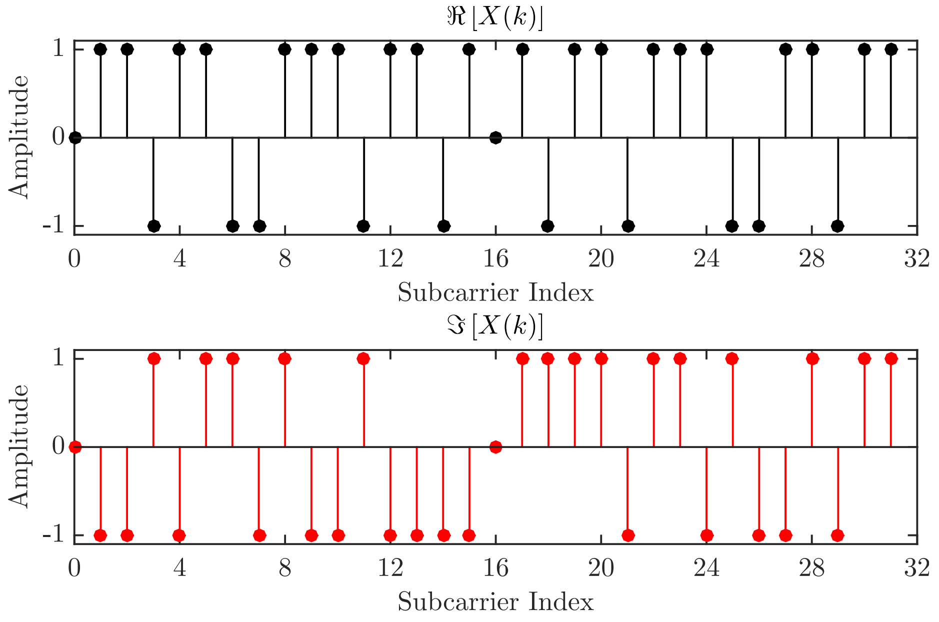

FIGURE 2.10: HS illustration for 4−QAM DCO-OFDM. (a) $\Re\left[X(k)\right]$; and (b) $\Im\left[X(k)\right]$

The Hermitian symmetric FD symbols, $X(k)$ are fed to N-order IDFT to multiplex the orthogonal subcarriers which results a TD signal given by:

$$x(n) = \text{IDFT}\left[X(k)\right], \tag{2.27}$$

for $n = 0, 1, \cdots, N-1$. It is highlighted that due to HS, $x(n)$ is real-valued but bipolar. An example of the conversion of complex FD symbol incorporating HS to real-valued TD signal is illustrated in Fig. 2.11. It is demonstrated that if HS is enforced in the FD, the output TD signal would be real-valued.

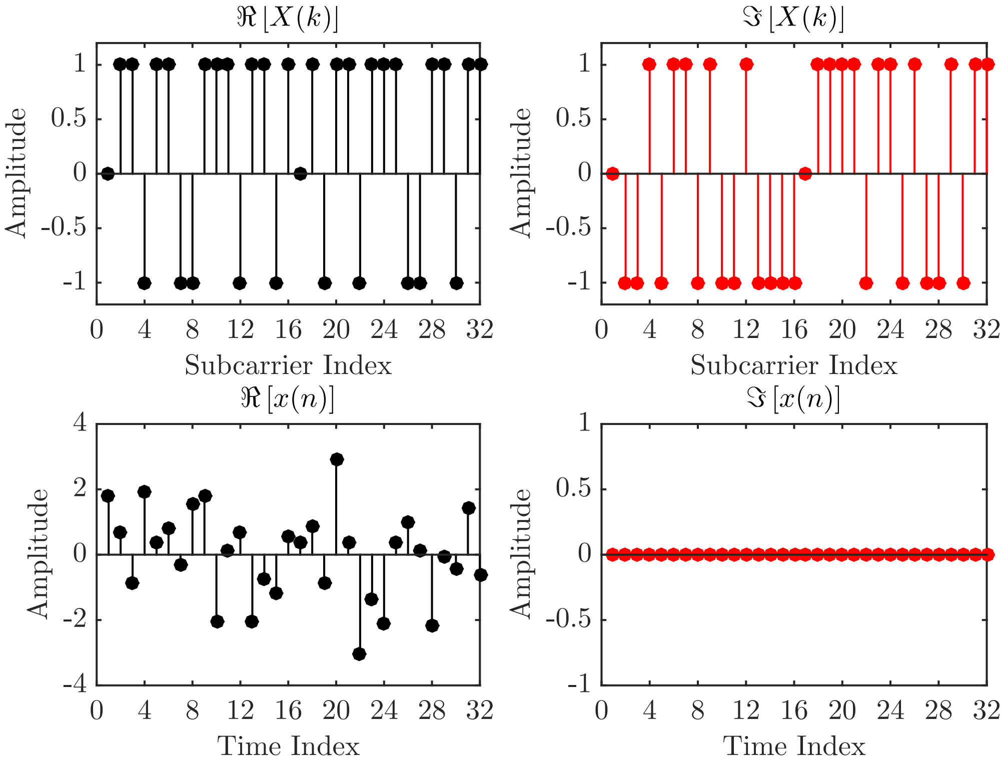

FIGURE 2.11: An example of DCO-OFDM signal conversion from FD to TD with HS.

A continuous TD signal $\tilde{x}(t)$ is obtained by feeding $x(n)$ to a digital-to-analog converter (DAC) and adding a cyclic prefix (CP) of length N_{CP} which is, at least, equal to the root-mean-square (rms) delay spread of the channel. In order to convert the bipolar signal into a unipolar signal, a forthright approach is to add suitable bias-index, $\beta_{\text{DC}}^{(\text{D})}$. $\beta_{\text{DC}}^{(\text{D})}$ is prescribed relative to the standard deviation of $\tilde{x}(t)$ as:

$$\beta_{\text{DC}}^{(\text{D})} = \varsigma_{(\text{D})}\sqrt{E\left(|\tilde{x}(t)|^2\right)}, \quad \varsigma_{(\text{D})} > O, \tag{2.28}$$

where $\varsigma_{(\text{D})}$ is the constant of proportionality. The bias-index on the decibel (dB) scale is defined as $10\log_{10}(\varsigma_{(\text{D})}^2 + 1)$ dB. The TD signal after the addition of $\beta_{\text{DC}}^{(\text{D})}$ is

$$\hat{x}(t) = \tilde{x}(t) + \beta_{\text{DC}}^{(\text{D})}. \tag{2.29}$$

Numerous levels of bias-index can be incorporated in the bipolar signal. The most convenient approach is to adopt *sufficient biasing*, in which, $\varsigma_{(\text{D})}$ is adjusted such that all the negative excursions of $\hat{x}(t)$ after the addition of $\beta_{\text{DC}}^{(\text{D})}$ are eliminated. However, in these cases, the value of $\beta_{\text{DC}}^{(\text{D})}$ is relatively large, which renders DCO-OFDM inefficient in term of optical power. Hence, a better option can be to employ a moderate value of $\beta_{\text{DC}}^{(\text{D})}$ and eliminate the remaining negative peaks by hard clipping $\hat{x}(t)$ as:

$$x(t) = \begin{cases} \hat{x}(t), & \hat{x}(t) \geq 0 \\ 0, & \hat{x}(t) < 0 \end{cases} = \hat{x}(t) + n_{\text{c}}(\beta_{\text{DC}}^{(\text{D})}). \tag{2.30}$$

where $n_\mathrm{c}(\beta_\mathrm{DC}^{(\mathrm{D})})$ is $\beta_\mathrm{DC}^{(\mathrm{D})}$ dependent clipping noise, which can severly impact the performance of the system. A graphical illustration of the biasing expressed in (2.29) and the clipping process after adding the bias-index given in (2.30) is given in Fig. 2.12.

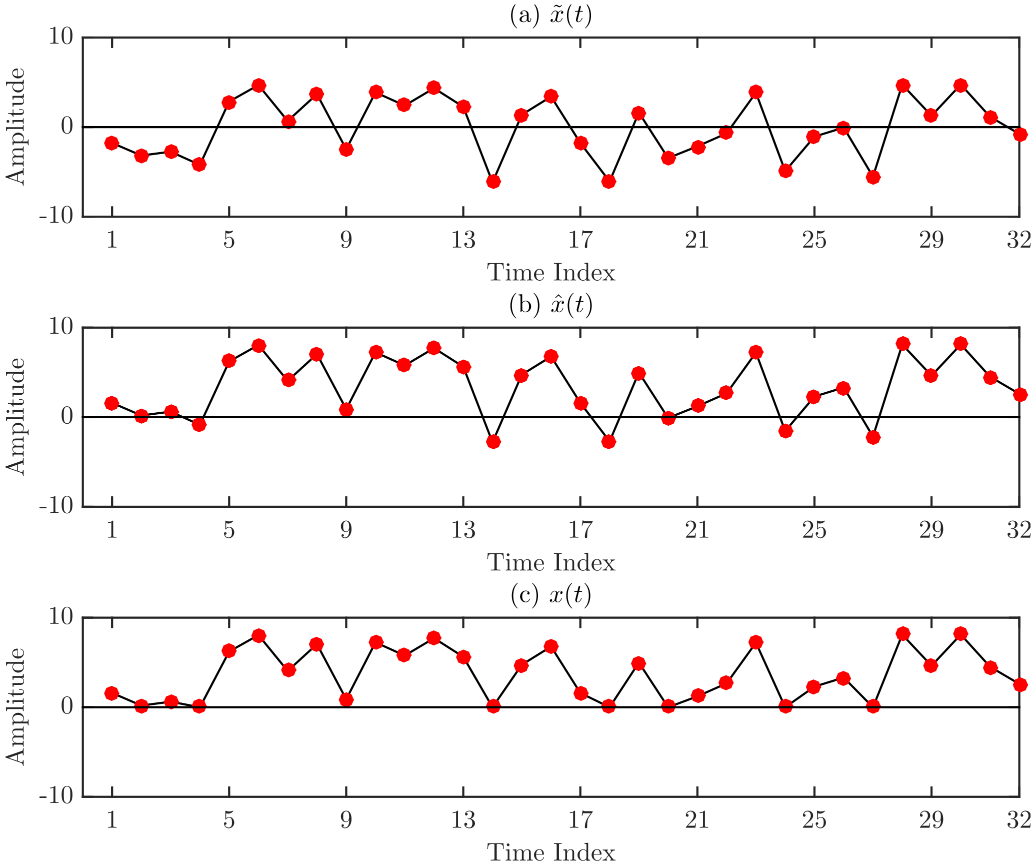

FIGURE 2.12: TD representation of DCO-OFDM (a) signal before biasing, $\tilde{x}(t)$ (b) biased signal, $\hat{x}(t)$ (c) biased signal after clipping, $x(t)$.

$n_\mathrm{c}\left(\beta_\mathrm{DC}^{(\mathrm{D})}\right)$ can be decreased by increasing $\beta_\mathrm{DC}^{(\mathrm{D})}$. For sufficient biasing, $n_\mathrm{c}\left(\beta_\mathrm{DC}^{(\mathrm{D})}\right) = 0$. Moreover, with an increase in N, the PAPR increases. Therefore, larger values $\beta_\mathrm{DC}^{(\mathrm{D})}$ are required to minimize $n_\mathrm{c}(\beta_\mathrm{DC}^{(\mathrm{D})})$. On the other hand, if smaller $\beta_\mathrm{DC}^{(\mathrm{D})}$ is utilized, more subcarriers are affected by the clipping process. The impact of adding bias-index on DCO-OFDM constellation in a noise-less scenario (only the impact of clipping noise due to remaining negative excursions) is illustrated in Fig. 2.13. It is observed that for lower bias-index, the recovered constellation (after clipping) has a larger splatter around the ideal constellation points due to exacerbated clipping noise. However, with an increase in value of bias-index, the clipping noise decreases, therefore, the recovered constellation is almost identical to the ideal constellation.

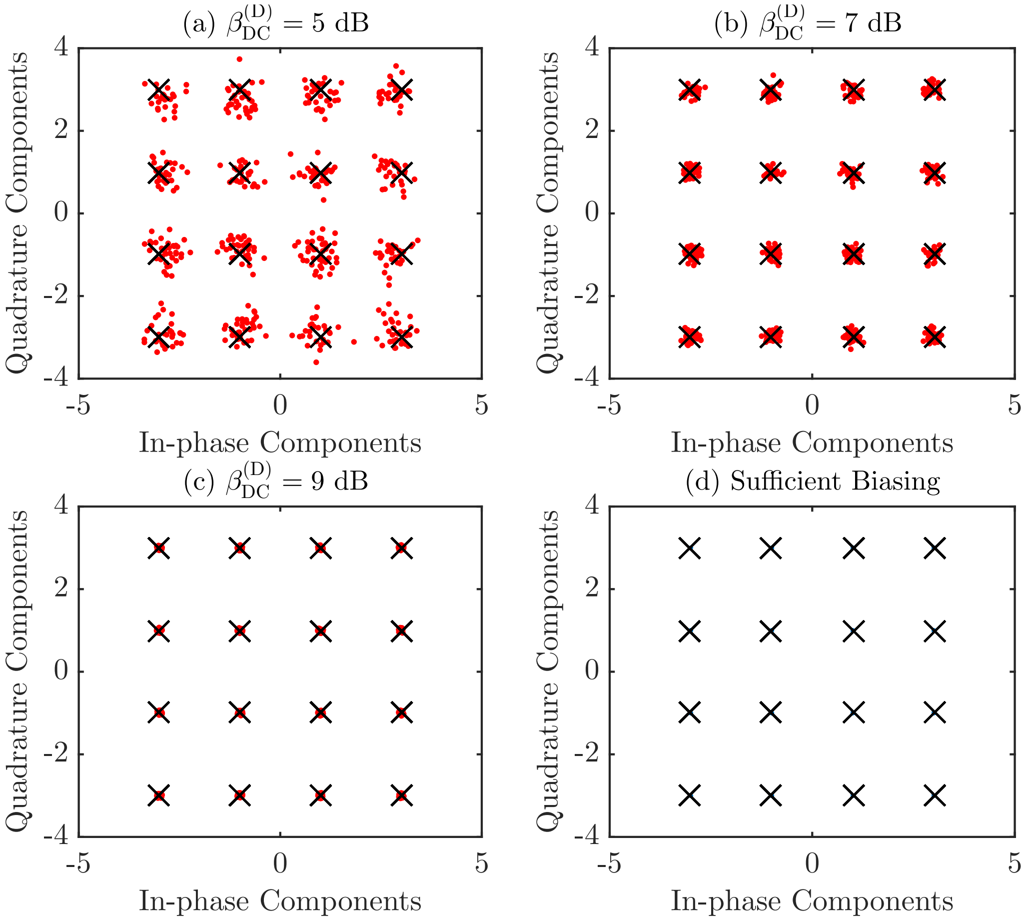

FIGURE 2.13: The impact of increasing bias, $\beta_{\mathrm{DC}}^{(\mathrm{D})}$, on the clipping noise, $n_{\mathrm{c}}\left(\beta_{\mathrm{DC}}^{(\mathrm{D})}\right)$ using $M = 16$‡.

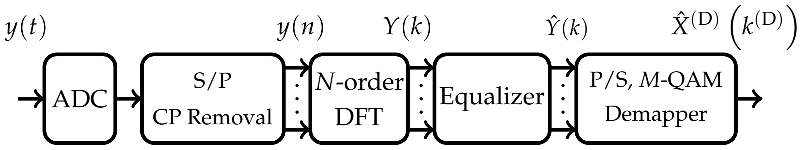

FIGURE 2.14: Block diagram of DCO-OFDM Receiver.

At the receiver (Fig. 2.14), $y(n)$ is obtained by impinging the photo-detected signal ,$y(t)$, on the analog-to-digital converter (ADC) followed by S/P conversion and CP removal. The received FD symbols, $Y(k)$ are obtained by N-order DFT as:

$$Y(k) = \mathrm{DFT}\left[y(n)\right] = H(k)X(k) + W(k). \tag{2.31}$$

where $H(k)$ is the channel frequency response for the kth subcarrier. Subsequently, a single-tap equalization is perfomed in the FD, which results in

$$\hat{Y}(k) = \hat{X}(k) + Z(k), \tag{2.32}$$

where $\hat{X}(k)$ are the estimated received FD symbols after (zero-forcing) equalization and $Z(k) = W(k)/H(k)$. The transmitted data is detected as:

$$\hat{X}^{(\mathrm{D})}\left(k^{(\mathrm{D})}\right) = \arg\min_{X_{\mathrm{Q}} \in \boldsymbol{\mathcal{Q}}} \left\| \hat{Y}\left(k^{(\mathrm{D})}+1\right) - X_{\mathrm{Q}} \right\|. \tag{2.33}$$

where X_{Q} represents all the elements in $\boldsymbol{\mathcal{Q}}$.

To evaluate the SE, consider M-ary QAM alphabets and N subcarriers which are separated by the symbol duration, T_{sym}. Hence, the total bilateral bandwidth B is N/T_{sym}. After the addition of CP, the O-OFDM symbol duration is given as $T_{\mathrm{OFDM}} = T_{\mathrm{sym}} + T_{\mathrm{CP}}$, where, T_{CP} is the CP duration. Since, in DCO-OFDM, only $N/2-1$ subcarriers are modulated, therefore, the data rate, R_{b} is $\log_2(M)(N/2-1)/T_{\mathrm{OFDM}}$. Thus, the SE of DCO-OFDM η_{DCO} is given as:

$$\eta_{\mathrm{DCO}} = \frac{R_{\mathrm{b}}}{B} = \frac{\log_2(M)(N/2-1)}{(N+N_{\mathrm{CP}})} \quad \text{(bits/s/Hz)}. \tag{2.34}$$

Another vital performance parameter which should be considered in the PAPR of the modulation teachnique. PAPR, ξ, is the measure of variation of the TD signal about its mean. Mathematically, PAPR of an arbitrary L-order signal, $r(n)$ can be expressed as:

$$\mathrm{PAPR} = \lambda \triangleq= \frac{\max_{0 \le n \le L-1}\left(|r(n)|^2\right)}{E\left(|r(n)|^2\right)}, \tag{2.35}$$

PAPR of a TD signal is graphically illustrated using complementary cumulative distribution function (CCDF) which is the probability that PAPR of signal will exceed a given threshold, PAPR_{ϵ} , i.e., CCDF $=$ $\mathrm{Prob}(\mathrm{PAPR} > \mathrm{PAPR}_{\epsilon})$.

The PAPR performance of DCO-OFDM is presented in Fig. 2.15. However, it is highlighted that the PAPR performance of DCO-OFDM is independent of the modulation order, M of the QAM alphabets.

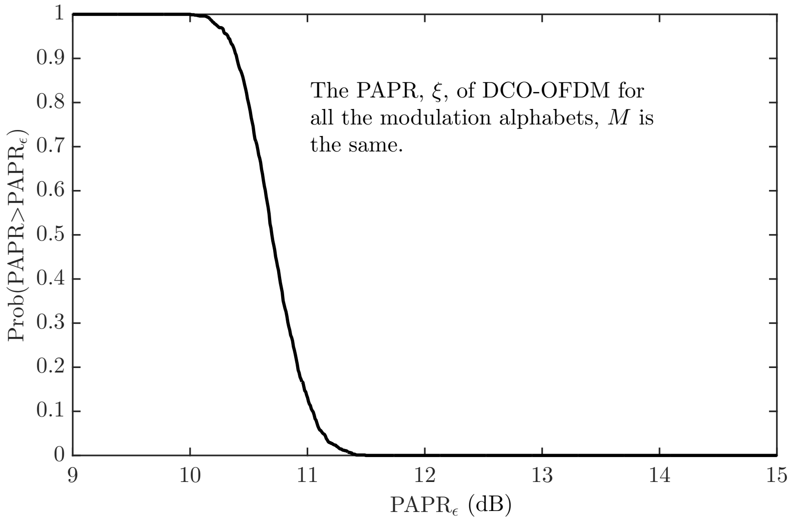

FIGURE 2.15: CCDF curves for PAPR illustration of DCO-OFDM obtained using $M = 4$ and $N = 1024$.

Statistical Characterization of DCO-OFDM

By using central limit theorem, for $N \geq 64$, $\hat{x}(t)$ exhibits a Gaussian probability density function (pdf) with mean equal to $\beta_{\mathrm{DC}}^{(\mathrm{D})}$ and variance equal to $\sigma_x^2 = E\left(|\tilde{x}(t)|^2\right) = E\left(|x(n)|^2\right)$. After hard clipping to eliminate negative excursions, a clipped Gaussian distribution is obtained for $x(t)$, which is given by [112, 113, 114]:

$$p\left(x(t)\right) = \frac{1}{\sigma_x\sqrt{2\pi}} \exp\left(\frac{-\left(\hat{x}(t) - \beta_{\mathrm{DC}}^{(\mathrm{D})}\right)^2}{2\sigma_x^2}\right) u\left(\hat{x}(t)\right) + Q\left(\frac{\beta_{\mathrm{DC}}^{(\mathrm{D})}}{\sigma_x}\right)\delta\left(\hat{x}(t)\right), \tag{2.36}$$

where $u(\cdot)$ is the unit step function and $\delta(\cdot)$ is the dirac delta function and $Q(\cdot)$ is the complementary error function given as:

$$Q(r) = \frac{1}{\sqrt{2\pi}} \int_0^r \exp\left(\frac{-t^2}{2}\right) \mathrm{d}t, \tag{2.37}$$

for any r in $\mathbb{R}^+$.

Using (2.36) and for simplicity considering that the proportionality constant between the input modulating current and the optical power is set to 1, i.e., $\omega = 1$, the optical power of the DCO-OFDM, $P_{(\mathrm{opt,DCO})}$ is evaluated as:

$$\begin{aligned} P_{(\mathrm{opt,DCO})} &= E\left(x(t)\right) = \int_0^\infty x(t) p(x(t)) \mathrm{d}x(t) \\ &= \frac{\sigma_x}{2\pi} \exp\left(\frac{\left(\beta_{\mathrm{DC}}^{(\mathrm{D})}\right)^2}{2\sigma_x^2}\right) + \beta_{\mathrm{DC}}^{(\mathrm{D})}\left[1 - Q\left(\frac{\beta_{\mathrm{DC}}^{(\mathrm{D})}}{\sigma_x}\right)\right]. \end{aligned} \tag{2.38}$$

Similarly, the electrical power for DCO-OFDM, i.e., $P_{(\mathrm{elec,DCO})}$ is [113, 114] is given by:

$$\begin{aligned} P_{(\mathrm{elec,DCO})} &= E\left(|x(t)|^2\right) = \int_0^\infty x(t)^2 p(x(t)) \mathrm{d}x(t) \\ &= \left(\sigma_x^2 + \left(\beta_{\mathrm{DC}}^{(\mathrm{D})}\right)^2\right)\left[1 - Q\left(\frac{\beta_{\mathrm{DC}}^{(\mathrm{D})}}{\sigma_x}\right)\right] + \frac{\sigma_x \beta_{\mathrm{DC}}^{(\mathrm{D})}}{\sqrt{2\pi}} \exp\left(-\frac{\left(\beta_{\mathrm{DC}}^{(\mathrm{D})}\right)^2}{2\sigma_x^2}\right) \end{aligned} \tag{2.39}$$

For sufficient biasing, equation (2.38) and (2.39) can be simplified to [115]

$$P_{(\mathrm{opt,DCO})} = \beta_{\mathrm{DC}}^{(\mathrm{D})}, \tag{2.40}$$

and

$$P_{(\mathrm{elec,DCO})} = \sigma_x^2 + \left(\beta_{\mathrm{DC}}^{(\mathrm{D})}\right)^2, \tag{2.41}$$

respectively. Under the assumption of sufficient biasing, the optical-to-electrical conversion efficiency for DCO-OFDM is given as:

$$\alpha_{\mathrm{DCO}}^{\mathrm{OE}} = \frac{P_{(\mathrm{elec,DCO})}}{P_{(\mathrm{opt,DCO})}} = \frac{\sigma_x^2 + \left(\beta_{\mathrm{DC}}^{(\mathrm{D})}\right)^2}{\beta_{\mathrm{DC}}^{(\mathrm{D})}}. \tag{2.42}$$

$P_{(\mathrm{opt,DCO})} = 1$ is used to provide a fair comparison between all the modulation techniques. This normalization essentially means that $\beta_{\mathrm{DC}}^{(\mathrm{D})} = 1$, where , $\beta_{\mathrm{DC}}^{(\mathrm{D})} = \varsigma_{(\mathrm{D})}\sigma_x$. Hence, (2.42) can be re-written as:

$$\alpha_{\mathrm{DCO}}^{\mathrm{OE}} = \sigma_x^2 + 1 = \frac{1+\varsigma_{(\mathrm{D})}^2}{\varsigma_{(\mathrm{D})}^2}. \tag{2.43}$$

The value of $\alpha_{\mathrm{DCO}}^{\mathrm{OE}}$ decreases with an increase in $\beta_{\mathrm{DC}}^{(\mathrm{D})}$ as illustrated in Fig. 2.16. This essentially means that with an increase in $\beta_{\mathrm{DC}}^{(\mathrm{D})}$, the optical power consumption for DCO-OFDM is increased while signal distortion is decreased. Note that the case for severe clipping will be extensively studied in Chapter 3.

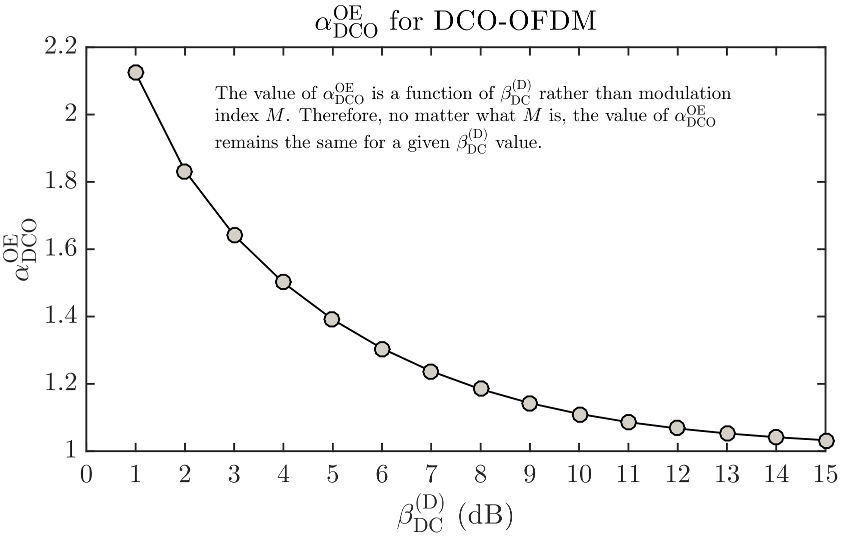

FIGURE 2.16: Evaluation of $\alpha_{\mathrm{DCO}}^{\mathrm{OE}}$ for different $\beta_{\mathrm{DC}}^{(\mathrm{D})}$ values.

By defining electrical and optical energy-per-bit, i.e., $E_{\mathrm{b}_{(\mathrm{elec})}}$ and $E_{\mathrm{b}_{(\mathrm{opt})}}$ as $E_{\mathrm{b}_{(\mathrm{elec})}} = P_{(\mathrm{elec,DCO})}/B\eta_{\mathrm{DCO}}$ and $E_{\mathrm{b}_{(\mathrm{opt})}} = P_{(\mathrm{opt,DCO})}/B\eta_{\mathrm{DCO}}$, respectively, the optical and electrical SNR per bit, i.e., $E_{\mathrm{b}_{(\mathrm{opt})}}/N_0$ and $E_{\mathrm{b}_{(\mathrm{opt})}}/N_0$ for DCO-OFDM are given by:

$$\frac{E_{\mathrm{b}_{(\mathrm{opt})}}}{N_0} = \frac{P_{(\mathrm{opt,DCO})}}{\eta_{\mathrm{DCO}} B N_0} \tag{2.44}$$

and

$$\frac{E_{\mathrm{b}_{(\mathrm{elec})}}}{N_0} = \frac{P_{(\mathrm{elec,DCO})}}{\eta_{\mathrm{DCO}} B N_0} \tag{2.45}$$

respectively, where B is the bandwidth of the signal in Hertz (Hz) and N_0 is the noise spectral density. Moreover, by exploiting, (2.43), the relationship between $E_{\mathrm{b}_{(\mathrm{elec})}}/N_0$ and $E_{\mathrm{b}_{(\mathrm{opt})}}/N_0$ is

$$\frac{E_{\mathrm{b}_{(\mathrm{opt})}}}{N_0} = \frac{1}{\alpha_{\mathrm{DCO}}^{\mathrm{OE}}} \frac{E_{\mathrm{b}_{(\mathrm{elec})}}}{N_0} = \frac{\varsigma_{(\mathrm{D})}^2}{1+\varsigma_{(\mathrm{D})}^2} \frac{E_{\mathrm{b}_{(\mathrm{elec})}}}{N_0}, \tag{2.46}$$

where $\varsigma_{(\mathrm{D})}$ is defined in (2.28). If $\beta_{\mathrm{DC}}^{(\mathrm{D})}$ is increased, $\alpha_{\mathrm{DCO}}^{\mathrm{OE}}$ tends to have smaller values, consequently, increasing the $E_{\mathrm{b}_{(\mathrm{opt})}} N_0$ requirement for DCO-OFDM. This identifies that the primary demerit of DCO-OFDM is the required $E_{\mathrm{b}_{(\mathrm{opt})}}/N_0$ to obtain a given bit error rate (BER). As the optical-to-electrical power conversion depends on the bias-index used, the required $E_{\mathrm{b}_{(\mathrm{opt})}}/N_0$ increases with an increase in bias-index or vice versa.

2.4.4 Asymmetrically Clipped O-OFDM (ACO-OFDM)

Another approach which avoids the bias-index altogether to realize a non-negative TD signal is ACO-OFDM. Since no bias-index is required, ACO-OFDM is more power efficient compared to DCO-OFDM, however, only for lower order modulation alphabets. This scheme was proposed by Armstrong and Lowery in [100]. ACO-OFDM transmission with N subcarriers shall be considered. The block diagram of ACO-OFDM is presented in Fig. 2.17.

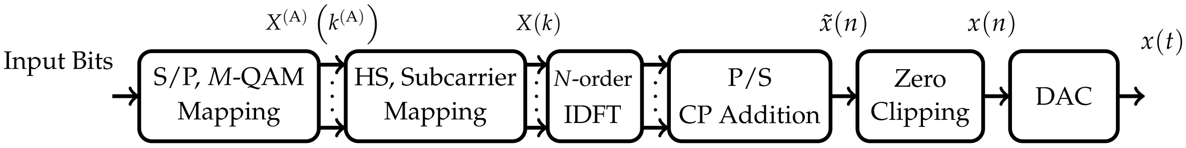

FIGURE 2.17: Block diagram of ACO-OFDM Transmitter.

The serially incoming bits streams are mapped onto $N/4$ M-ary QAM alphabets, $X^{(\mathrm{A})}\left(k^{(\mathrm{A})}\right)$, $k^{(\mathrm{A})} = 0, 1, \cdots, N/4 - 1$ drawn from constellation set $\mathcal{Q}$ after serial-to-parallel conversion (S/P). The symbols, $X^{(\mathrm{A})}\left(k^{(\mathrm{A})}\right)$ are then assigned to odd indexes/subcarriers of N-dimensional signal, $X(k), k = 0, 1, \cdots, N-1$ as:

$$X(k) = \begin{cases} X^{(\mathrm{A})}\left(k^{(\mathrm{A})}\right), & k = 2k^{(\mathrm{A})} + 1 \\ X^{*(\mathrm{A})}\left(k^{(\mathrm{A})}\right), & k = N - \left(2k^{(\mathrm{A})} + 1\right) \\ 0, & \text{elsewhere} \end{cases}, \tag{2.47}$$

and HS is also enforced. Via N-order IDFT, a TD signal, i.e.,

$$\tilde{x}(n) = \mathrm{IDFT}\left[X(k)\right], \tag{2.48}$$

is obtained, where $n = 0, 1 \cdots, N-1$. The frame structure of $X(k)$ ensures that $\tilde{x}(n)$ is anti-symmetric, i.e.,

$$\tilde{x}\left(\tilde{n}^{(\mathrm{A})}\right) = -\tilde{x}\left(\tilde{n}^{(\mathrm{A})} + \frac{N}{2}\right) \tag{2.49}$$

for $\tilde{n}^{(\mathrm{A})} = 0, 1, \cdots, N/2 - 1$. Because of this anti-symmetric property, the negative excursions of $\tilde{x}(n)$ can be clipped to zero using hard clipping process without loss of useful information to yield:

$$x(n) = \lfloor \tilde{x}(n) \rfloor = \begin{cases} \tilde{x}(n), & \tilde{x}(n) > 0 \\ 0, & \tilde{x}(n) \leq 0 \end{cases}. \tag{2.50}$$

where $\lfloor \cdot \rfloor$ represents the zero level clipping process. The zero level clipping process results in a unipolar signal which is compatible with IM-DD. A graphical illustration of $\tilde{x}(n)$ and $x(n)$ is portrayed in Fig. 2.18, where it is illustrated that after zero level clipping process all the negative amplitudes of the TD ACO-OFDM signals are eliminated.

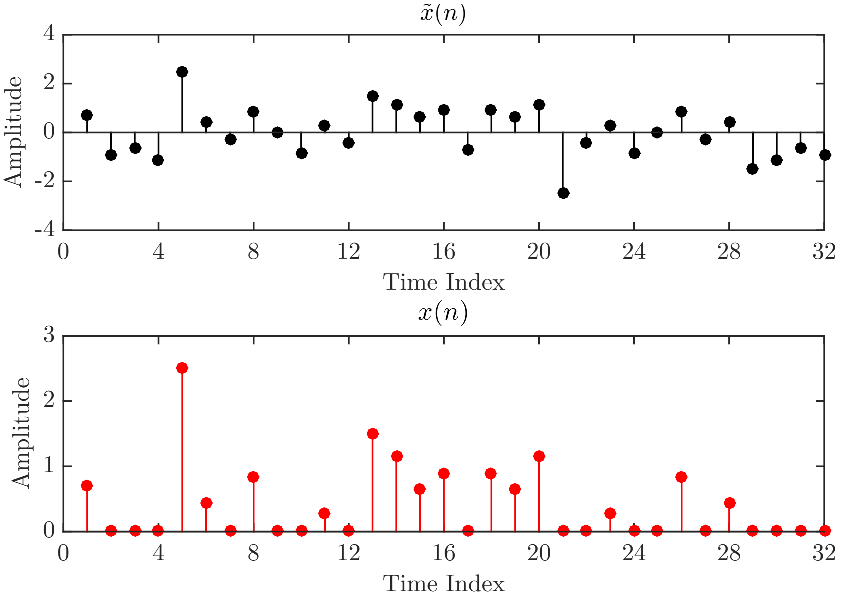

FIGURE 2.18: TD representation of ACO-OFDM signal before and after clipping.

In the FD, the clipping distortion, $N_c(k)$ resulting from the zero level clipping in (2.50) only impacts the even subcarriers, while the odd subcarriers remain unaffected. So, the symbols can be readily extracted by choosing the data-carrying odd subcarriers. However, the amplitude of the symbols is reduced to half because of clipping operation. The mathematical representation of FD counterpart of $x(n)$ is given as:

$$X_c(k) = \begin{cases} X(k)/2, & k = 2k^{(A)} + 1 \\ N_c(k) & k = N - \left(2k^{(A)} + 1\right) \end{cases}. \tag{2.51}$$

The impact of clipping is graphically illustrated in Fig. 2.19.

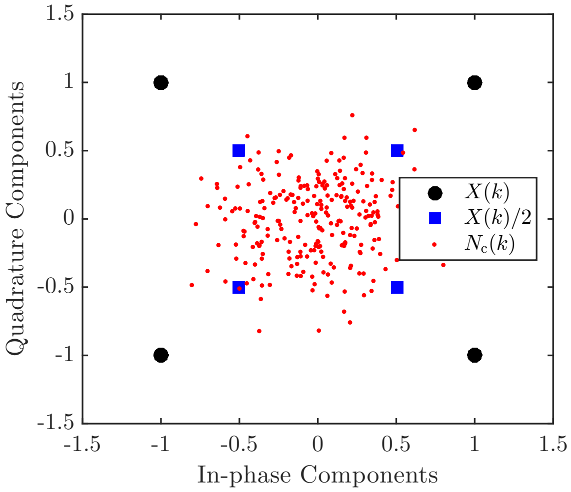

FIGURE 2.19: Constellation of ACO-OFDM before and after clipping (2.51) for 4-QAM. Black constellation points illustrate the data on odd subcarriers before clipping and blue points after clipping. Red points depict the distortion on even subcarrier after clipping.

After zero level clipping, $x(n)$ is impinged on a DAC to obtain $x(t)$ which is transmitted using LED to an optical wireless channel.

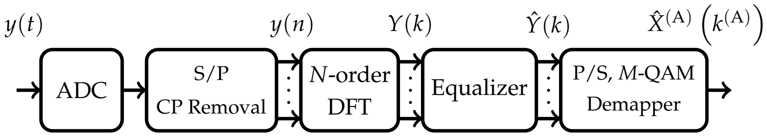

FIGURE 2.20: Block diagram of ACO-OFDM Reveiver.

The receiver of ACO-OFDM is portrayed in Fig. 2.20. $y(n)$ is obtained after analog-to-digital conversion of $y(t)$. Via N-order DFT, $y(n)$ is transformed into a FD signal on which the equalization is performed. Subsequent to the equalization process, $\hat{Y}(k)$ is obtained (same as depicted in (2.32)), from which the transmitted symbols can be detected as:

$$\hat{X}^{(A)}\left(k^{(A)}\right) = \arg \min_{X_Q \in \mathcal{Q}} \left\| 2\hat{Y}\left(2k^{(A)}+1\right) - X_Q \right\|, \tag{2.52}$$

where the factor of 2 is to counterbalance the impact of halving of the amplitude of the symbols.

In ACO-OFDM, only $N/4$ among N available subcarriers can be modulated, since half of the subcarriers are sacrifized to satisfy HS, whereas, the remaining $N/4$ subcarriers are used to realize an anti-symmetric TD signal. Therefore, following the same approach as in DCO-OFDM, the SE of ACO-OFDM is evaluated as:

$$\eta_{\text{ACO}} = \frac{\log_2(M)(N/4)}{(N+N_{\text{CP}})}(\text{bits/s/Hz}). \tag{2.53}$$

From (2.53) it is deduced that $\eta_{\text{ACO}} = 0.5\eta_{\text{DCO}}$ for same CP length. So, for the same constellation size, M, and sampling frequency, the data-rate of DCO-OFDM is twice as compared to ACO-OFDM [116].

The PAPR performance of ACO-OFDM is compared with that of DCO-OFDM in Fig. 2.21. It is observed that ACO-OFDM manisfests higher PAPR compared to DCO-OFDM because of the fact that in the TD signal, half of the samples are forced to zero because of zero clipping resulting in reduction of mean power of the signal.

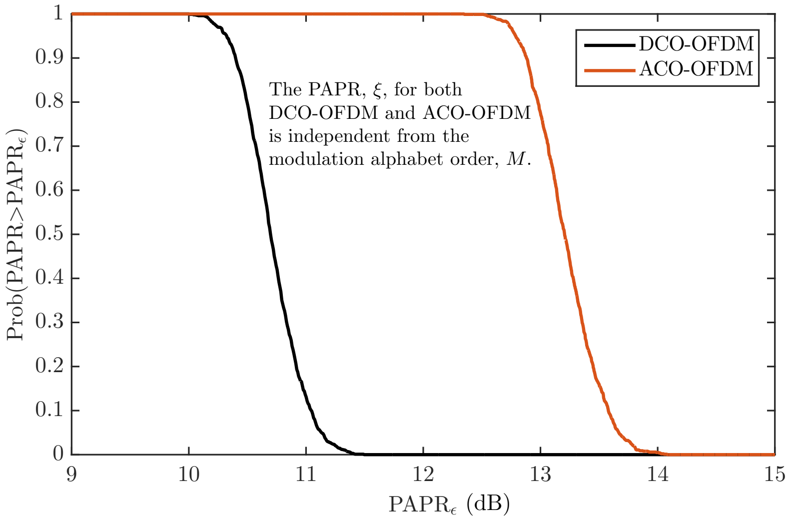

FIGURE 2.21: CCDF curves for PAPR illustration of DCO-OFDM and ACO-OFDM obtained using $M = 4$ and $N = 1024$.

Statistical Charaterization of ACO-OFDM

Using the central limit theorem, it is shown that the pdf of $x(t)$ for ACO-OFDM is [112, 117]:

$$p\left(x(t)\right) = \frac{1}{\sqrt{2\pi\sigma_A^2}} \exp\left(\frac{-x(t)^2}{2\sigma_A^2}\right) u(x(t)) + \frac{1}{2}\delta(x(t)), \tag{2.54}$$

where σ_A^2 is the variance of the un-clipped signal i.e., $\sigma_A^2 = \mathrm{E}\left(|\tilde{x}(n)|^2\right)$. It is recalled that $u(\cdot)$ is the unit step function and $\delta(\cdot)$ is the dirac delta function.

Using (2.54), the optical power of ACO-OFDM $P_{(\text{opt,ACO})}$ is calculated as:

$$P_{(\text{opt,ACO})} = E\left(x(t)\right) = \int_0^\infty x(t)p(x(t))\mathrm{d}x(t) = \frac{\sigma_A}{\sqrt{2\pi}}. \tag{2.55}$$

Similarly, the electrical power of ACO-OFDM, $\mathrm{P}_{(\text{elec,ACO})}$, is given by:

$$P_{(\text{elec,ACO})} = E\left(|x(t)|^2\right) = \int_0^\infty x(t)^2 p(x(t))\mathrm{d}x(t) = \frac{\sigma_A^2}{2}. \tag{2.56}$$

By exploiting (2.55) and (2.56), the optical-to-electrical conversion efficiency for ACO-OFDM is

$$\alpha_{\text{ACO}}^{\text{OE}} = \frac{P_{(\text{elec,DCO})}}{P_{(\text{opt,DCO})}} = \frac{\sigma_A^2/2}{\sigma_A/\sqrt{2\pi}}. \tag{2.57}$$

By normalizing $P_{(\text{opt,ACO})}$ to unity, (2.57) is given as:

$$\alpha_{\text{ACO}}^{\text{OE}} = \pi. \tag{2.58}$$

This implies that for all the spectral efficiencies or any modulation index, M, the value of $\alpha_{\text{ACO}}^{\text{OE}}$ is a constant, i.e., equal to π.

Incorporating (2.55) and (2.56), $E_{\mathrm{b}_{(\text{opt})}}/N_0$ and $E_{\mathrm{b}_{(\text{elec})}}/N_0$ for ACO-OFDM is evaluated as:

$$\frac{E_{\mathrm{b}_{(\text{opt})}}}{N_0} = \frac{P_{(\text{opt,ACO})}}{\eta_{\text{ACO}} B N_0}, \tag{2.59}$$

and

$$\frac{E_{\mathrm{b}_{(\text{elec})}}}{N_0} = \frac{P_{(\text{elec,ACO})}}{\eta_{\text{ACO}} B N_0}, \tag{2.60}$$

respectively. Moreover, by taking into account, (2.58), $E_{\mathrm{b}_{(\text{elec})}}/N_0$ and $E_{\mathrm{b}_{(\text{opt})}}/N_0$ are related as [116]:

$$\frac{E_{\mathrm{b}_{(\text{opt})}}}{N_0} = \frac{1}{\alpha_{\text{ACO}}^{\text{OE}}} \frac{E_{\mathrm{b}_{(\text{elec})}}}{N_0} = \frac{1}{\pi} \frac{E_{\mathrm{b}_{(\text{elec})}}}{N_0}. \tag{2.61}$$

From (2.61) it is discerned that the problem of increase in $E_{\mathrm{b}_{(\text{opt})}}/N_0$ due to requirement of bias-index for DCO-OFDM can be eliminated in ACO-OFDM. However, this is done at the expense of halving of the SE. Furthermore, (2.61) also signifies that the required $E_{\mathrm{b}_{(\text{opt})}}/N_0$ would always be approximately 4.8 dB lesser than $E_{\mathrm{b}_{(\text{elec})}}/N_0$ for all M.

In ACO-OFDM, the clipping noise on the even subcarriers is completely discarded, however, numerous researches [112, 118] later revealed that instead of treating the signal on even subcarriers as detrimental noises, the clipping noise actually contains instructive information about the transmitted signal which can be exploited to increase the demodulation performance. In [112], a noise cancellation receiver for ACO-OFDM has been proposed which improves the demodulation process and realizes a reduction of approximately 3 dB in required $E_{\mathrm{b}_{(\mathrm{elec})}}/N_0$ in an AWGN channel. In [118], the authors argue that the theoretical gain presented in [112] are un-realizable in practical systems since the technique is extremely sensitive to the distortion at the lower frequencies, i.e., the zeroth subcarrier. Also, the zeroth subcarrier for the scheme in [112] depends on the DC component and the low frequency noise in the system. So, in [118], a diversity combining approach is proposed, which is also capable of eliminating the DC component and also attains a gain of 3 dB in required $E_{\mathrm{b}_{(\mathrm{elec})}}/N_0$ in an AWGN channel. Moreover, there have been a large number of approaches which are variants of ACO-OFDM with all of the approaches exhibiting the same PAPR as that of ACO-OFDM. However, these approaches are not presented here as in the sequel, primary focus is on those techniques which manifest lower PAPR than DCO-OFDM and ACO-OFDM.

2.4.5 Fourier Transfom Precoded DCO-OFDM (FTP-DCO-OFDM)

As aforementioned, due to constructive addition of subcarriers, O-OFDM suffers from the classical limitation of high PAPR which can be a significant limitation for IM-DD systems because the LEDs have a limited linear range. In the literature, precoded approaches have been proposed to lessen the PAPR of O-OFDM because of their quasi SC like behavior. In the sequel, instead of using the term *subcarriers*, the term *subchannels* is used for precoded approaches. For OWC systems, Fourier transform precoded (FTP)-DCO-OFDM, inspired by the DCO-OFDM is proposed by R. Mesleh *et al.* in [94], and the block diagram of which is illustrated in Fig 2.22.

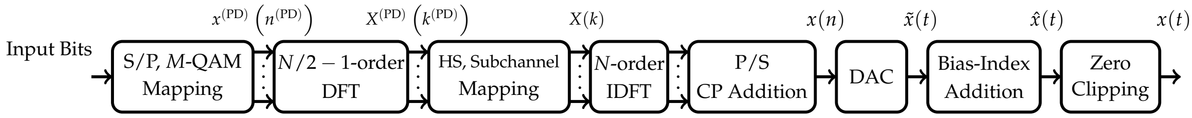

FIGURE 2.22: Block diagram of FTP-DCO-OFDM Transmitter.

In FTP-DCO-OFDM, the input bits are modulated according to $N/2-1$ M-ary QAM alphabets drawn from constellation $\mathcal{Q}$, resulting in TD symbols, $x^{(\mathrm{PD})}\left(n^{(\mathrm{PD})}\right), n^{(\mathrm{PD})}=0,1,\cdots,N/2-2$. These $N/2-1$ TD symbols are FTP using $N/2-1$-order DFT as:

$$X^{(\mathrm{PD})}\left(k^{(\mathrm{PD})}\right)=\mathrm{DFT}\left[x^{(\mathrm{PD})}\left(n^{(\mathrm{PD})}\right)\right], \tag{2.62}$$

to obtain FD symbols $X^{(\mathrm{PD})}\left(k^{(\mathrm{PD})}\right)$ for $k^{(\mathrm{PD})}=0,1,\cdots,N/2-2$. Afterwards, these FD symbols are allocated to a N-length signal, $X(k)$ by obeying HS as:

$$X(k)=\begin{cases} X^{(\mathrm{PD})}\left(k^{(\mathrm{PD})}\right), & k=k^{(\mathrm{PD})}+1 \\ X^{*(\mathrm{PD})}\left(k^{(\mathrm{PD})}\right), & k=N-(k^{(\mathrm{PD})}+1) \\ 0, & \text{elsewhere} \end{cases}. \tag{2.63}$$

Like DCO-OFDM, $X(0)$ and $X(N/2)$ are set to zero. Following N-order IDFT on $X(k)$, a TD signal, $x(n)$ is obtained which is given as:

$$x(n) = \text{IDFT}\left[X(k)\right], \tag{2.64}$$

for $n = 0, 1, \cdots, N-1$. In DCO-OFDM, the IDFT converts the FD symbols to TD symbols that have very high PAPR. whereas, in FTP-DCO-OFDM, the PAPR is reduced because the N-order IDFT impact is mostly cancelled out by the $N/2-1$-order DFT and the resulting TD symbols are much alike the TD symbols drawn from the M-ary QAM constellation, and therefore, manifest a lower PAPR.

After analog-to-digital conversion of $x(n)$, a continuous bipolar TD signal, $\tilde{x}(t)$, is obtained. To obtain a non-negative TD signal, a bias-index, $\beta_{\text{DC}}^{(\text{PD})}$ is added. $\beta_{\text{DC}}^{(\text{PD})}$ for FTP-DCO-OFDM is evaluated as:

$$\beta_{\text{DC}}^{(\text{PD})} = \varsigma_{(\text{PD})} \sqrt{E\left(|\tilde{x}(t)|^2\right)}, \tag{2.65}$$

for $\varsigma_{(\text{PD})} > 0$, which is the constant of proportionality. Similar to DCO-OFDM, the bias-index on the dB scale for FTP-DCO-OFDM is calculated as $10\log_{10}(\varsigma_{(\text{PD})}^2 + 1)$ and the biased signal for FTP-DCO-OFDM is given as:

$$\hat{x}(t) = \tilde{x}(t) + \beta_{\text{DC}}^{(\text{PD})}. \tag{2.66}$$

When sufficient biasing is not used, $\hat{x}(t)$ is clipped at zero level to realize a non-negative TD signal, $x(t)$ compatible with IM-DD implementation. The impact of introducing the bias-index is the same as in DCO-OFDM, i.e., if less bias-index is used, clipping noise would be exacerbated, whereas, if higher values of bias-index is used, the optical power consumption would be significant. In both DCO-OFDM and FTP-DCO-OFDM, the bias-index to sufficiently bias is correlated to the PAPR of the TD signal. However, because of IDFT precoding, the TD signal manifests lower PAPR, consequently, the bias-index needed to sufficiently bias the TD signal is also lowered. Fig. 2.23 portrays the sufficient biasing for DCO-OFDM and FTP-DCO-OFDM as a function of SE; which affirms that a lesser bias-index is required to sufficiently bias FTP-DCO-OFDM.

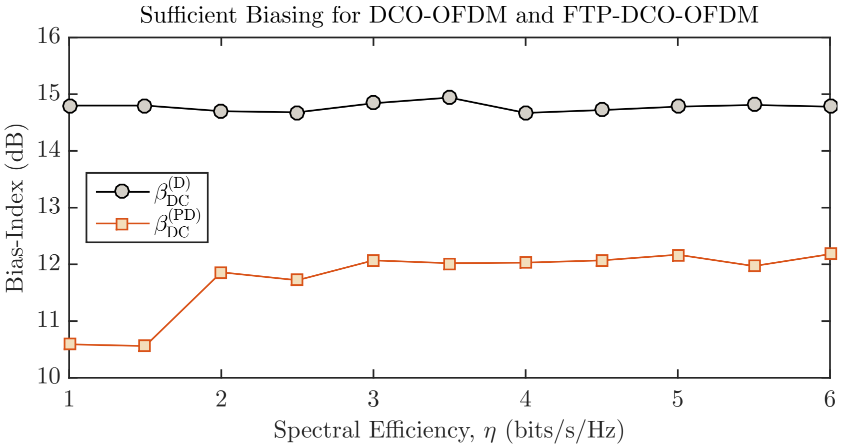

FIGURE 2.23: Analysis of sufficient biasing comparison for DCO-OFDM and FTP-DCO-OFDM for different spectral efficiencies, η. The results are obtained using $N = 1024$ and are averaged for 200000 symbols.

The block diagram of the receiver for FTP-DCO-OFDM is illustrated in Fig. 2.24.

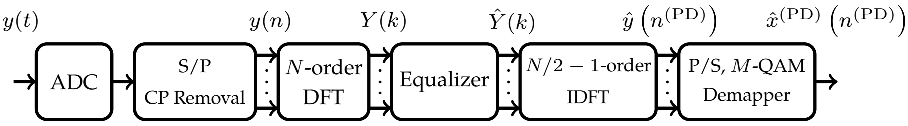

FIGURE 2.24: Block diagram of FTP-DCO-OFDM receiver.

After analog-to-digital conversion using an ADC, the received signal, $y(t)$ is given as $y(n)$. Subsequent to the N-order DFT and equalization, the FD symbols, $\hat{Y}(k)$ for $k = 0, 1, \cdots, N-1$ are attained. From $\hat{Y}(k)$, the $N/2-1$ useful symbols are extracted as $\hat{Y}\left(k^{(\mathrm{PD})}\right)$, where $k^{(\mathrm{PD})} = 0, 1, \cdots, N/2-2$, by excluding the redundent Hermitian symmetric symbols. Subsequently, $N/2-1$-order IDFT operation is peformed on $\hat{Y}\left(k^{(\mathrm{PD})}\right)$ to inverse the impact of precoding. This is mathematically respresented as:

$$\hat{y}\left(n^{(\mathrm{PD})}\right) = \mathrm{IDFT}\left[\hat{Y}\left(k^{(\mathrm{PD})}+1\right)\right] \tag{2.67}$$

for $n^{(\mathrm{PD})} = 0, 1, \cdots, N/2-2$. The estimated transmitted symbols are recognized as:

$$\hat{x}^{(\mathrm{PD})}\left(n^{(\mathrm{PD})}\right) = \arg\min_{X_{\mathrm{Q}} \in \mathcal{Q}} \left\| \hat{y}\left(n^{(\mathrm{PD})}\right) - X_{\mathrm{Q}} \right\|. \tag{2.68}$$

The SE of FTP-DCO-OFDM, η_{PD} is equal to the SE of DCO-OFDM, i.e., η_{DCO}, since only $N/2-1$ subchannels among N carry useful data are used.

The PAPR behaviour of FTP-DCO-OFDM is presented and compared with that of DCO-OFDM in Fig. 2.25. The simulation results reveal that the PAPR of FTP-DCO-OFDM is relatively reduced compared to DCO-OFDM, however, it depends on the modulation alphabet that has been used. So, it can be observed that when modulation alphabet size, M is increased the PAPR also increases and vice versa.

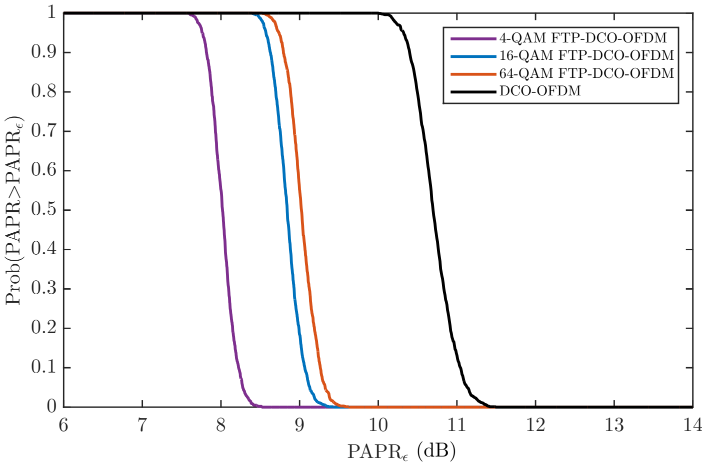

FIGURE 2.25: CCDF curves for PAPR illustration of FTP-DCO-OFDM obtained using $N = 1024$.

Statistical Characterization of FTP-DCO-OFDM

Unlike DCO-OFDM, the TD signal for FTP-DCO-OFDM is not Gaussian distributed. Moreover, the distribution of the TD signal and is associated with QAM modulation order, M as shown in Fig. 2.26.

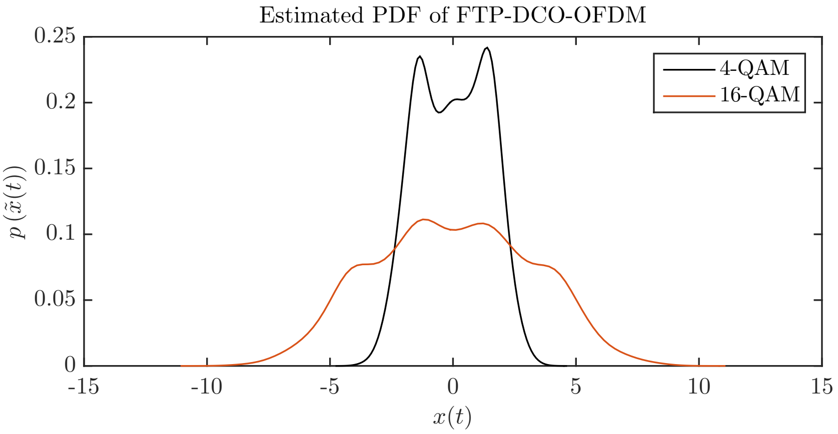

FIGURE 2.26: Estimated pdf of FTP-DCO-OFDM for $M = \{4, 16\}$.

As a result, it is tedious to formulate a closed-form expression of pdf for such signals. However, if the TD signal is sufficiently biased, the electrical and optical power can be evaluated in a straightforward manner. So, considering $\sigma_x^2 = E\left(|x(t)|^2\right)$ and sufficient biasing, the optical power for FTP-DCO-OFDM is evaluated as:

$$P_{(\text{opt,PD})} = E\left(x(t)\right) = \beta_{\text{DC}}^{(\text{PD})}, \tag{2.69}$$

and the electrical power for FTP-DCO-OFDM is evaluated as:

$$P_{(\text{elec,PD})} = E\left(|x(t)|^2\right) = \sigma_x^2 + \left(\beta_{\text{DC}}^{(\text{PD})}\right)^2. \tag{2.70}$$

From (2.69) and (2.70), the optical-to-electrical conversion efficiency for FTP-DCO-OFDM is evaluated as:

$$\alpha_{\text{PD}}^{\text{OE}} = \frac{P_{(\text{elec,PD})}}{P_{(\text{opt,PD})}} = \frac{\sigma_x^2 + \left(\beta_{\text{DC}}^{(\text{PD})}\right)^2}{\beta_{\text{DC}}^{(\text{PD})}}. \tag{2.71}$$

By scaling $P_{(\text{opt,PD})} = 1$, (2.71) can be rewritten as:

$$\alpha_{\text{PD}}^{\text{OE}} = \frac{1 + \varsigma_{(\text{PD})}^2}{\varsigma_{(\text{PD})}^2}. \tag{2.72}$$

(2.72) is exactly the same expression as obtained for DCO-OFDM in (2.42), however, $\varsigma_{(\text{D})}$ is replaced by $\varsigma_{(\text{PD})}$. Moreover, from (2.72), it is discerned that $\alpha_{\text{PD}}^{\text{OE}}$ for FTP-DCO-OFDM also decreases rapidly with an increase in bias-index, consequently, $E_{\text{b}_{(\text{opt})}}/N_0$ requirement of FTP-DCO-OFDM could increase with an increase in the bias-index as in conventional DCO-OFDM. Note that, if we have $\beta_{\text{DC}}^{(\text{D})} = \beta_{\text{DC}}^{(\text{PD})}$ then $\alpha_{\text{DCO}}^{\text{OE}} = \alpha_{\text{PD}}^{\text{OE}}$. However, generally $\varsigma_{(\text{PD})} < \varsigma_{(\text{D})}$ because of precoding, therefore, $\alpha_{\text{DCO}}^{\text{OE}} > \alpha_{\text{PD}}^{\text{OE}}$, which essentially implies that $E_{\text{b}_{(\text{opt})}}/N_0$ requirement for DCO-OFDM could be worse than that of FTP-DCO-OFDM. A graphical illustration of $\alpha_{\text{DCO}}^{\text{OE}}$ for different bias-index values is presented in Fig. 2.16 for DCO-OFDM. Note that, $\alpha_{\text{PD}}^{\text{OE}}$ would also have the same trend for a given value of the bias-index.

The optical and electrical SNR per bit for FTP-DCO-OFDM can be evaluated using (2.44) and (2.45) and replacing $P_{(\text{opt,DCO})}$ and $P_{(\text{elec,DCO})}$ with (2.69) and (2.70), and η_{DCO} with η_{PD}. Similarly, the relationship between $E_{b_{(opt)}}/N_0$ and $E_{b_{(elec)}}/N_0$ for FTP-DCO-OFDM can be evaluated by replacing α^{OE}_{DCO} with α^{OE}_{PD} in (2.46).

2.4.6 Fourier Transform Precoded ACO-OFDM (FTP-ACO-OFDM)

The precoded variant of ACO-OFDM, which is referred to as FTP-ACO-OFDM has been proposed in [119, 94] and [120]. Different authors have used different names for the same approach. In [119], the authors refer to this approach as ACO-single-carrier frequency domain equalization (ACO-SCFDE). R. Mesleh *et al.* in [94] has referred to the approach as ACO-single-carrier frequency division multiple access (ACO-SCFDMA), whereas, authors in [120] analyse ACO-OFDM with DFT precoding, the concept of which is similar to ACO-SCFDE and ACO-SCFDMA.

The underlying concept of FTP-ACO-OFDM is the same as that of ACO-OFDM, however, the modulation alphabets are precoded prior to subchannel assignment. Consider FTP-ACO-OFDM transmission with N subchannels, the block diagram of which is presented in Fig. 2.27.

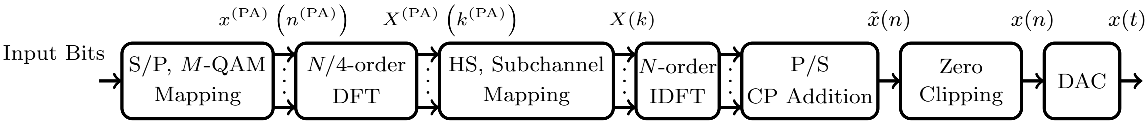

FIGURE 2.27: Block diagram of FTP-ACO-OFDM Transmitter.

The input bits are mapped to $N/4$ TD Gray-coded M-ary QAM alphabets drawn fom constellation $\mathcal{Q}$ which are represented as $x^{(PA)}\left(n^{(PA)}\right)$ for $n^{(PA)} = 0, 1, \cdots, N/4-1$. Subsequently, the $N/4$ TD symbols are fed to $N/4$-order DFT for FT precoding, which results in the following FD symbols:

$$X^{(PA)}\left(k^{(PA)}\right) = \text{DFT}\left[x^{(PA)}\left(n^{(PA)}\right)\right], \tag{2.73}$$

where $k^{(PA)} = 0, 1, \cdots, N/4-1$. These FD symbols, $X^{(PA)}\left(k^{(PA)}\right)$ are assigned to odd subchannels of N-dimensional signal, $X(k), k = 0, 1, \cdots, N-1$ as:

$$X(k) = \begin{cases} X^{(PA)}\left(k^{(PA)}\right), & k = 2k^{(PA)} + 1 \\ X^{*(PA)}\left(k^{(A)}\right), & k = N - (2k^{(PA)} + 1) \\ 0, & \text{elsewhere} \end{cases}, \tag{2.74}$$

$X(0)$ and $X(N/2)$ are set to zero and HS is enforced. Afterwards the N-length signal, $X(k)$ is fed to an N-order IDFT to obtain a real-valued TD signal, $\tilde{x}(n)$ as:

$$\tilde{x}(n) = \text{IDFT}\left[X(k)\right] \tag{2.75}$$

for $n = 0, 1, \cdots, N-1$. Like ACO-OFDM, as only the odd subchannel are used, $\tilde{x}(n)$ is anti-symmetric, i.e.,

$$\tilde{x}\left(\tilde{n}^{(PA)}\right) = -\tilde{x}\left(\tilde{n}^{(PA)} + \frac{N}{2}\right), \tag{2.76}$$

for $\tilde{n}^{(PA)} = 0, 1, \cdots, N/2-1$. Because of the anti-symmetric property (2.76), the TD signal, $\tilde{x}(n)$ is clipped at zero level to realize a non-negative TD signal, $x(n)$ for IM-DD implementation. Afterwards, a analog signal, $x(t)$ is obtained by impinging $x(n)$ on a DAC. $x(t)$ is transmitted to an optical wireless channel through the LED.

The receiver for FTP-ACO-OFDM is presented in Fig. 2.28.

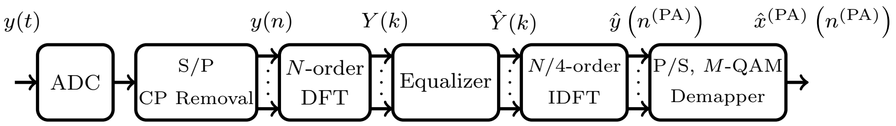

FIGURE 2.28: Block diagram of FTP-ACO-OFDM Receiver.

$y(n)$ is attained after digitizing the received signal, $y(t)$. Subsequently, N-order DFT and equalization is performed to achieve $\hat{Y}(k)$. From $\hat{Y}(k)$, the odd subcahnnels are extracted as $\hat{Y}\left(2k^{(\mathrm{PA})}+1\right)$ for $k^{(\mathrm{PA})}=0,1,\cdots,N/4-1$. Afterwards, via $N/4$-order IDFT the precoding operation is reversed as:

$$\hat{y}\left(n^{(\mathrm{PA})}\right)=\mathrm{IDFT}\left[\hat{Y}\left(2k^{(\mathrm{PA})}+1\right)\right], \tag{2.77}$$

for $n^{(\mathrm{PA})}=0,1,\cdots,N/4-1$. The decisions on the transmitted alphabets are made according to:

$$\hat{x}^{(\mathrm{PA})}\left(n^{(\mathrm{PA})}\right)=\arg\min_{X_Q\in\mathcal{Q}}\left\|2\hat{y}\left(n^{(\mathrm{PA})}\right)-\mathrm{X_Q}\right\|. \tag{2.78}$$

Since the frame structure of FTP-ACO-OFDM is similar to that of ACO-OFDM, hence, the SE of FTP-ACO-OFDM, η_{PA} is the same as that of ACO-OFDM, i.e., $\eta_{\mathrm{PA}}=\eta_{\mathrm{ACO}}$.

The PAPR of FTP-ACO-OFDM for different modulation alphabets is presented and compared with that of ACO-OFDM in Fig. **??**. It is recalled that the PAPR for all the modulation alphabets used in ACO-OFDM is the same (under Gaussain pdf assumption). Moreover, it is discerned that the PAPR of FTP-ACO-OFDM is distinctively less compared to ACO-OFDM. However, like the PAPR behaviour of FTP-DCO-OFDM, the PAPR of FTP-ACO-OFDM also depends on the modulation alphabet size as can be seen in Fig. 2.29.

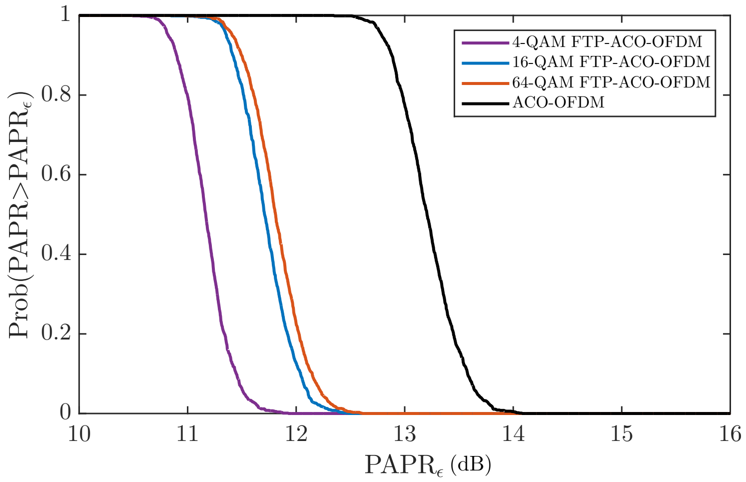

FIGURE 2.29: CCDF curves for PAPR illustration of FTP-ACO-OFDM obtained using $N=1024$.

Statistical Characterization for FTP-ACO-OFDM

Like FTP-DCO-OFDM, the evaluation of closed-form expression for the pdf of the TD signal of FTP-ACO-OFDM is a cumbersome task. For the sake of understanding, the pdf of un-clipped discrete signal, $\tilde{x}(n)$ is presented in Fig. 2.30. Considering $\sigma_{\tilde{x}}^2 = E\left(|\tilde{x}(n)|^2\right)$, the electrical power for FTP-ACO-OFDM can be given as:

$$P_{(\text{elec,PA})} = \frac{\sigma_{\tilde{x}}^2}{2}. \tag{2.79}$$

Because M-ary QAM modulation alphabet has an average energy equal to $M - 1/12$, so, in FTP-ACO-OFDM as half of the subchannels are modulated, therefore, $P_{(\text{elec,PA})}$ is equal to $M - 1/6$. However, the closed-form expression for $P_{(\text{opt,PA})}$ cannot be evaluated due to unavailabilty of closed-form pdf.

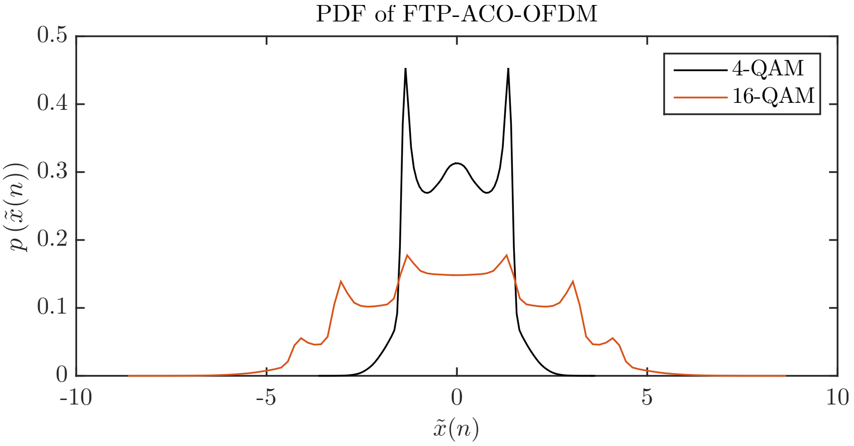

FIGURE 2.30: Estimated pdf of FTP-ACO-OFDM for $M = \{4, 16\}$.

Hereby, only the simulation results for the optical-to-electrical conversion for FTP-ACO-OFDM, $\alpha_{\text{PA}}^{\text{OE}}$, are presented. It is determined that due to precoding,

$$\alpha_{\text{PA}}^{\text{OE}} < \alpha_{\text{ACO}}^{\text{OE}}. \tag{2.80}$$

An illustration of $\alpha_{\text{PA}}^{\text{OE}}$ for different spectral efficiencies is presented in Fig. 2.31.

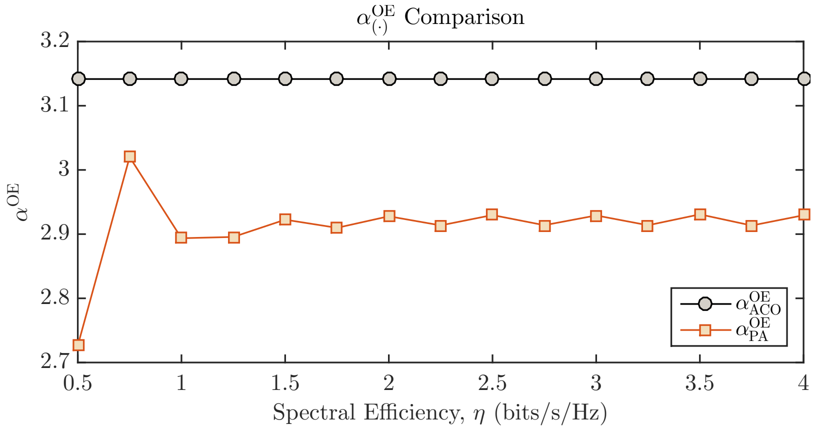

FIGURE 2.31: Comparison of α^{OE} for ACO-OFDM and FTP-ACO-OFDM for different spectral efficiencies.

The lower value of $\alpha_{\mathrm{PA}}^{\mathrm{OE}}$ compared to $\alpha_{\mathrm{ACO}}^{\mathrm{OE}}$ implies that under ideal conditions, FTP-ACO-OFDM requires a larger value of $E_{\mathrm{b}_{(\mathrm{opt})}}/N_0$ to attain a given BER compared to conventional ACO-OFDM. The penalty in terms of required $E_{\mathrm{b}_{(\mathrm{opt})}}/N_0$ for FTP-ACO-OFDM compared to ACO-OFDM to attain a similar BER on a dB scale can be quantified as:

$$\beta_{\mathrm{PA}}^{\mathrm{pen}} = 10\log_{10}\left(\frac{\alpha_{\mathrm{ACO}}^{\mathrm{OE}}}{\alpha_{\mathrm{PA}}^{\mathrm{OE}}}\right) \quad (\mathrm{dB}). \tag{2.81}$$

and is graphically illustrated in Fig. 2.32.

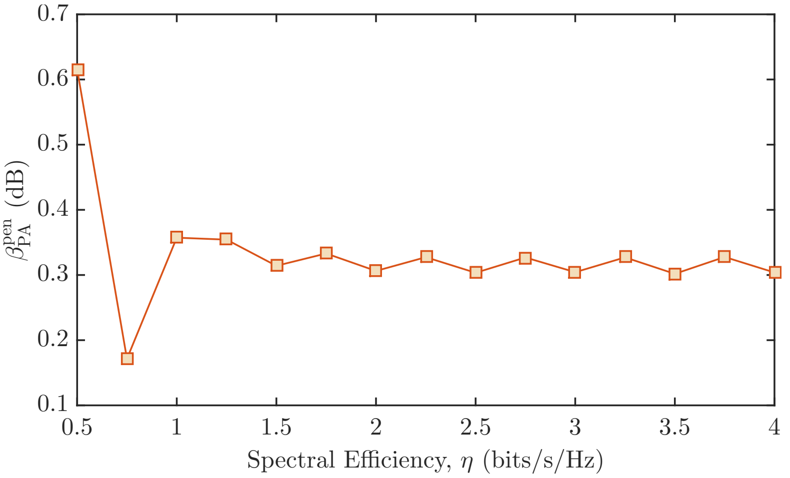

FIGURE 2.32: The penalty in terms of required $E_{\mathrm{b}_{(\mathrm{opt})}}/N_0$ for FTP-ACO-OFDM compared to ACO-OFDM.

The optical and electrical SNR per bit for FTP-ACO-OFDM can be evaluated by using (2.59) and (2.60) and replacing $P_{(\mathrm{opt,ACO})}$ and $P_{(\mathrm{elec,ACO})}$ with $P_{(\mathrm{opt,PA})}$ and $P_{(\mathrm{elec,PA})}$, and η_{ACO} with η_{PA}. Similarly, the relationship between $E_{\mathrm{b}_{(\mathrm{opt})}}/N_0$ and $E_{\mathrm{b}_{(\mathrm{elec})}}/N_0$ for FTP-ACO-OFDM is evaluated by replacing $\alpha_{\mathrm{ACO}}^{\mathrm{OE}}$ with $\alpha_{\mathrm{PA}}^{\mathrm{OE}}$ in (2.61).

2.4.7 Hartley Transform Precoded ACO-OFDM (HTP-ACO-OFDM)

The precoded approaches, such as, FTP-DCO-OFDM and FTP-ACO-OFDM reduce the PAPR of the TD signals. However, Wu *et al.* [121] identified that only half of the TD symbols exploit SC like benefits because of HS requirement, hence, FT-precoding results in a less compelling PAPR reductioncompared to classical SC-FDMA for RF. Consequently, the precoded schemes which can preclude HS may manifest a lower PAPR compared to the approaches which use HS. A low complexity PAM based DHT precoded ACO-OFDM, i.e., HTP-ACO-OFDM is proposed by Zhou and Qiao in [111] and [122] which averts HS. The usefulness of DHT is that if a real-valued signal is input to the transform, the output would also be real-valued, hence, if PAM alphabets are used no additional processing is needed to attain a real-valued signal.

Consider the block diagram of HTP-ACO-OFDM illustrated in Fig. 2.33, where N subchannels are used for the transmission.

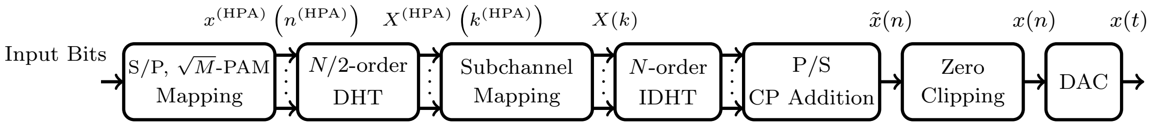

FIGURE 2.33: Block diagram of HTP-ACO-OFDM Transmitter.

The incoming bit stream is mapped onto $\sqrt{M}$-PAM $N/2$ TD symbols, $x^{(\mathrm{HPA})}\left(n^{(\mathrm{HPA})}\right)$ with $n^{(\mathrm{HPA})} = 0, 1, \cdots, N/2-1$. These TD symbols are drawn from PAM constellation set $\boldsymbol{\mathcal{P}} = \left\{\mathcal{P}_0, \mathcal{P}_1, \cdots, \mathcal{P}_{\sqrt{M}-1}\right\}$. The $N/2$ TD symbols, $x^{(\mathrm{HPA})}\left(n^{(\mathrm{HPA})}\right)$, are transformed to a FD symbols, $X^{(\mathrm{HPA})}\left(k^{(\mathrm{HPA})}\right)$ for $k^{(\mathrm{HPA})} = 0, 1, \cdots, N/2-1$ via $N/2$-order DHT as:

$$X^{(\mathrm{HPA})}\left(k^{(\mathrm{HPA})}\right) = \mathrm{DHT}\left[x^{(\mathrm{HPA})}\left(n^{(\mathrm{HPA})}\right)\right]. \tag{2.82}$$

It is highlighted that in ACO-OFDM, $N/4$-QAM alphabets are modulated on the odd subcarriers in the first half (of the total subcarriers), whereas, the second half of subcarriers/subchannels is used to satisfy the HS constraint. In HTP-ACO-OFDM, since HS is no longer needed, $N/2$ PAM alphabets are modulated on all the odd subchannels. However, in $\sqrt{M}$-PAM alphabet, the number of bits are half of M-QAM alphabet, as a result, the aversion of HS does not improve the SE of HTP-ACO-OFDM.

The $N/2$ FD symbols are allocated to the odd subchannels of the N-length signal, $X(k)$, as:

$$X(k) = \left\{ \begin{array}{cc} X^{(\mathrm{HPA})}\left(k^{(\mathrm{HPA})}\right), & k = 2k^{(\mathrm{HPA})} + 1 \\ 0, & \text{elsewhere} \end{array} \right., \tag{2.83}$$

$X(k)$ is then fed to N-order IDHT to realize an anti-symmetric TD signal, $\tilde{x}(n)$ as:

$$\tilde{x}(n) = \mathrm{IDHT}\left[X(k)\right], \tag{2.84}$$

for $n = 0, 1, \cdots, N-1$. Like ACO-OFDM and FTP-ACO-OFDM, zero level clipping can be performed on $\tilde{x}(n)$ to attain a non-negative signal, $x(n)$ without loss of useful information. $x(n)$ can be obtained from $\tilde{x}(n)$ by using (2.50) or an alternative expression can be:

$$x(n) = \frac{1}{2}\left(\tilde{x}(n) + |\tilde{x}(n)|\right). \tag{2.85}$$

$x(n)$ is then impinged on a DAC and transmitted to an optical channel throught the LED.

The block diagram of HTP-ACO-OFDM receiver is presented in Fig. 2.34.

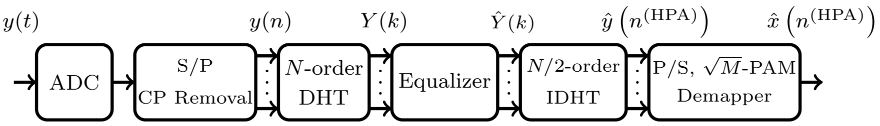

FIGURE 2.34: Block diagram of HTP-ACO-OFDM Receiver.

After analog to digital conversion using an ADC of the received waveform, $y(t)$, a digitized TD signal, $y(n)$ is obtained. Afterwards, N-order DFT is applied to attain FD symbols, $Y(k)$ as:

$$Y(k) = \text{DHT}\left[y(n)\right], \tag{2.86}$$

where $k = 0, 1, \cdots, N-1$. Then, the equalization process is performed on the FD symbols, $Y(k)$ to realize $\hat{Y}(k)$. Unlike DFT, the convolution in TD is not multiplication in FD in DHT, therefore, the conventional equalization process cannot be implemented for $Y(k)$ in case of HTP-ACO-OFDM [123]. To understand the equalization process, consider the following photodetected signal after discretization at the receiver:

$$y(n) = h(n) \otimes x(n), \tag{2.87}$$

for $n = 0, 1, \cdots, N-1$, where $h(n)$ is the CIR, $x(n)$ are the transmitted signal components and $\otimes$ denotes the convolution operator. For simplicity of analysis and without loss of generality, the noise components, $w(n)$ are not considered. After DHT on (2.87), the signal for demultiplexing can be written as:

$$Y(k) = X(k)H_{\text{e}}(k) + X(N-k)H_{\text{o}}(k), \tag{2.88}$$

where $H_{\text{e}}(k)$ and $H_{\text{o}}(k)$ are the even and odd components of the DHT of $h(n)$ which are computed as:

$$H_{\text{e}}(k) = \frac{[H(k) + H(N-k)]}{2} = \frac{1}{\sqrt{N}} \sum_{n=0}^{N-1} h(n) \cos\left(\frac{2\pi kn}{N}\right), \tag{2.89}$$

and

$$H_{\text{o}}(k) = \frac{[H(k) - H(N-k)]}{2} = \frac{1}{\sqrt{N}} \sum_{n=0}^{N-1} h(n) \sin\left(\frac{2\pi kn}{N}\right), \tag{2.90}$$

respectively for $k = 0, 1, \cdots, N-1$. Moreover, $X(k)$ and $H(k)$ are given by:

$$X(k) = \frac{1}{\sqrt{N}} \sum_{n=0}^{N-1} x(n)\text{cas}\left(\frac{2\pi kn}{N}\right), \tag{2.91}$$

and

$$H(k) = \frac{1}{\sqrt{N}} \sum_{n=0}^{N-1} h(n)\text{cas}\left(\frac{2\pi kn}{N}\right) = H_{\text{e}}(k) + H_{\text{o}}(k), \tag{2.92}$$

respectively. The equalization process that can be used to remove the distortive impact of the channel can be presented as [124]:

$$X(k) = \frac{H_{\text{e}}(k)Y(k) - H_{\text{o}}(k)Y(N-k)}{H_{\text{e}}^2(k) + H_{\text{o}}^2(k)}, \tag{2.93}$$

$$X(N-k) = \frac{H_{\text{o}}(k)Y(k) + H_{\text{e}}(k)Y(N-k)}{H_{\text{e}}^2(k) + H_{\text{o}}^2(k)}, \tag{2.94}$$

for $k = 0, 1, \cdots, N-1$. From (2.93) and (2.94) it can be discerned that the equalization process for HTP-ACO-OFDM requires two real-valued multiplications per subchannel. Therefore, if N subchannels are considered, then $2N$ real-valued multiplications are required for HTP-ACO-OFDM. In conventional O-OFDM approaches, one complex-valued multiplication per subcarrier is needed and the equalization process is implemented on half of the subcarrier. Generally, a complex-valued multiplication requires, four real-valued multiplications. So, the total multiplications required in this case as well is $2N$. Therefore, it can be concluded that the equalization process with either DHT-based or DFT-based O-OFDM has the same computational complexity.

In practical scenarios, the noise samples are taken into account, therefore, the equalized FD symbol is expressed as $\hat{Y}(k)$. From $\hat{Y}(k)$, the data on the modulated subchannels can be extracted as $\hat{Y}(k) = \hat{Y}\left(2k^{(\mathrm{HPA})}+1\right)$. To reverse the precoding operation, $N/2$-order IDHT is applied on the data at the modulated subchannels as:

$$\hat{y}\left(n^{(\mathrm{HPA})}\right) = \mathrm{IDHT}\left[\hat{Y}\left(2k^{(\mathrm{HPA})}+1\right)\right], \tag{2.95}$$

where $n^{(\mathrm{HPA})} = 0, 1, \cdots, N/2-1$. The decisions on the transmitted $\sqrt{M}$-PAM alphabets can be made as:

$$\hat{x}^{(\mathrm{HPA})}\left(n^{(\mathrm{HPA})}\right) = \arg\min_{X_P \in \boldsymbol{\mathcal{P}}} \left\| 2\hat{y}\left(n^{(\mathrm{HPA})}\right) - X_\mathrm{P} \right\|, \tag{2.96}$$

where X_P represents all the elements in $\boldsymbol{\mathcal{P}}$.

Since HS is not required for HTP-ACO-OFDM, $N/2$ among N subchannels can be modulated, therefore, the SE of HTP-ACO-OFDM is given as:

$$\eta_{\mathrm{HPA}} = \frac{\log_2\left(\sqrt{M}\right)(N/2)}{N} \tag{2.97}$$

which is equal to the SE of conventional ACO-OFDM, i.e., η_{ACO}.

The PAPR of HTP-ACO-OFDM for different PAM modulation alphabets is presented in Fig. 2.35. Like FTP-ACO-OFDM, the PAPR of HTP-ACO-OFDM also depends on the modulation alphabet size and with an increase in modulation alphabet size, the PAPR increases. However, it can be observed that the PAPR of HTP-ACO-OFDM is the least compared to DCO-OFDM, ACO-OFDM, FTP-DCO-OFDM and FTP-ACO-OFDM primarily because HS has been averted.

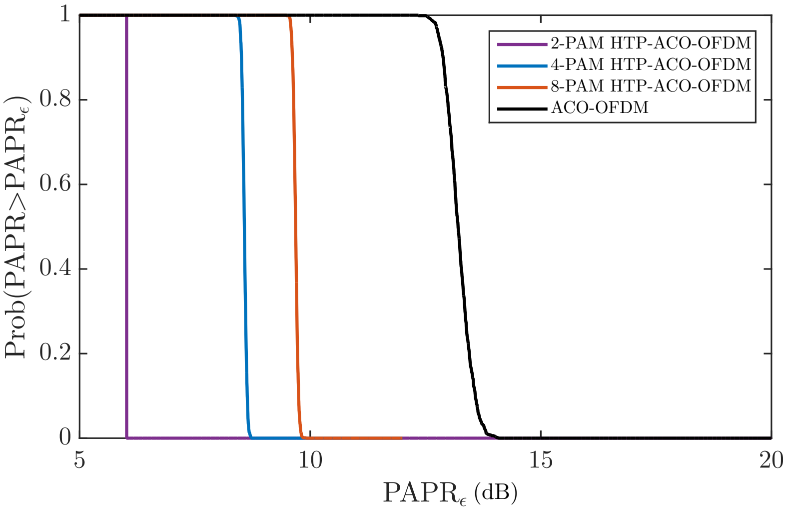

FIGURE 2.35: CCDF curves for PAPR illustration of HTP-ACO-OFDM obtained using $N = 1024$.

Statistical Characterization of HTP-ACO-OFDM

The statistical characterization of HTP-ACO-OFDM is difficult to carry out because the TD signals does not follow a known pdf as depicted in Fig. 2.36, where the pdf of unclipped HTP-ACO-OFDM TD signal, $\tilde{x}(n)$ is illustrated.

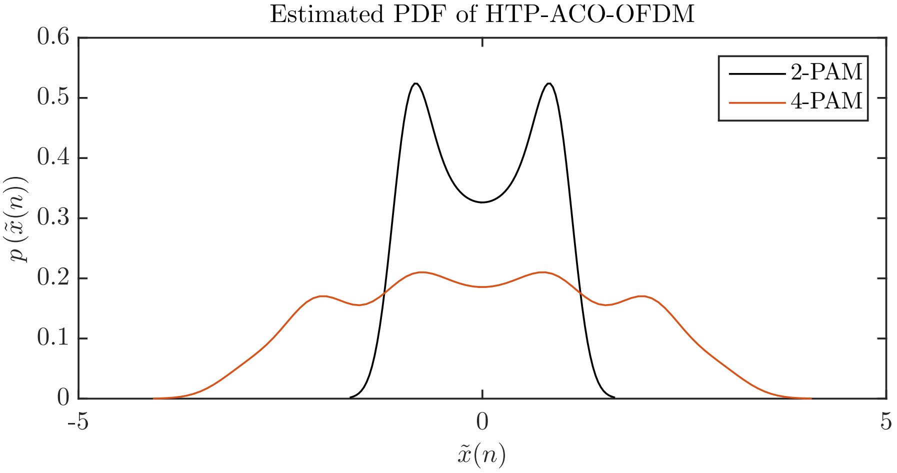

FIGURE 2.36: Estimated pdf of HTP-ACO-OFDM for $M = \{4, 16\}$.

The shape of the estimated pdf can be explained using (6) in [122], from which it can be shown that the anti-symmetric (un-clipped) TD signal, i.e., given by (2.84) after the DHT process is given as:

$$\tilde{x}(n) = \begin{cases} \frac{1}{\sqrt{2}}\left[x^{(\mathrm{HPA})}(n)\cos\left(\frac{2\pi n}{N}\right) + x^{(\mathrm{HPA})}\left(\frac{N}{2}-n\right)\sin\left(\frac{2\pi n}{N}\right)\right] & 0 \le n \le \frac{N}{2}-1 \\ \frac{1}{\sqrt{2}}\left[x^{(\mathrm{HPA})}\left(n-\frac{N}{2}\right)\cos\left(\frac{2\pi n}{N}\right) + x^{(\mathrm{HPA})}(N-n)\sin\left(\frac{2\pi n}{N}\right)\right] & \frac{N}{2} \le n \le N-1 \end{cases}, \tag{2.98}$$

which clearly implies that the amplitudes of the TD signal (un-clipped) depends on the $\cos(\cdot)$ and $\sin(\cdot)$ function.

For HTP-ACO-OFDM, considering $\sigma_x^2 = E\left(|\tilde{x}(n)|^2\right)$, the electrical power for $\sqrt{M}$-ary PAM is computed as:

$$P_{(\mathrm{elec,HPA})} = \frac{\sigma_x^2}{2} = \frac{M-1}{12}. \tag{2.99}$$

because $\sqrt{M}$-ary PAM alphabets have total energy equal to $M - 1/24$. However, it is difficult to establish a closed-form expression for $P_{(\mathrm{opt,HPA})}$. Moreover, the optical-to-electrical conversion efficiency for HTP-ACO-OFDM, $\alpha_{\mathrm{HPA}}^{\mathrm{OE}}$ is evaluated using numerical simulations which is portrayed in Fig. 2.37. $\alpha_{\mathrm{HPA}}^{\mathrm{OE}}$ is compared to the optical-to-electrical conversion efficiency of ACO-OFDM and FTP-ACO-OFDM, i.e., $\alpha_{\mathrm{ACO}}^{\mathrm{OE}}$ and $\alpha_{\mathrm{PA}}^{\mathrm{OE}}$. It is demonstrated that the $\alpha_{\mathrm{HPA}}^{\mathrm{OE}}$ is lower compared to $\alpha_{\mathrm{ACO}}^{\mathrm{OE}}$ and $\alpha_{\mathrm{PA}}^{\mathrm{OE}}$, i.e.,

$$\alpha_{\mathrm{HPA}}^{\mathrm{OE}} < \alpha_{\mathrm{PA}}^{\mathrm{OE}} < \alpha_{\mathrm{ACO}}^{\mathrm{OE}}. \tag{2.100}$$

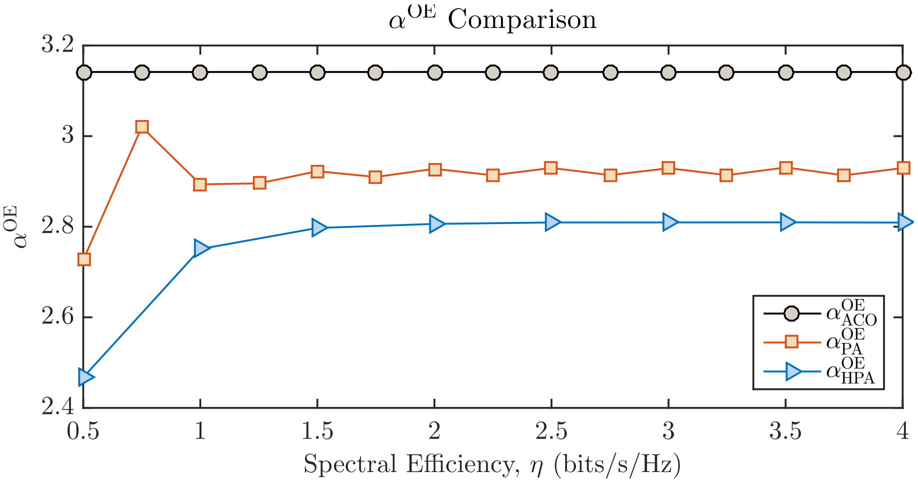

FIGURE 2.37: Comparison of α^{OE} for ACO-OFDM, FTP-ACO-OFDM and HTP-ACO-OFDM for different spectral efficiencies.

It has been previously established that the required $E_{b_{(\text{opt})}}/N_0$ for FTP-ACO-OFDM is higher than that of ACO-OFDM. Moreover, according to (2.100), for HTP-ACO-OFDM it is even higher than that of FTP-ACO-OFDM implying that the penalty incurred by HTP-ACO-OFDM is higher than both FTP-ACO-OFDM and ACO-OFDM. The penalty for HTP-ACO-OFDM in terms of required $E_{b_{(\text{opt})}}/N_0$ with respect to ACO-OFDM on the dB scale can be evaluated as:

$$\beta^{\text{pen}}_{\text{HPA}} = 10\log_{10}\left(\frac{\alpha^{\text{OE}}_{\text{ACO}}}{\alpha^{\text{OE}}_{\text{HPA}}}\right) \quad \text{(dB)}. \tag{2.101}$$

with

$$\beta^{\text{pen}}_{\text{HPA}} > \beta^{\text{pen}}_{\text{PA}}. \tag{2.102}$$

So, it can be concluded that to attain a similar BER, the required $E_{b_{(\text{opt})}}/N_0$ for HTP-ACO-OFDM is the highest as can be seen from Fig. 2.38.

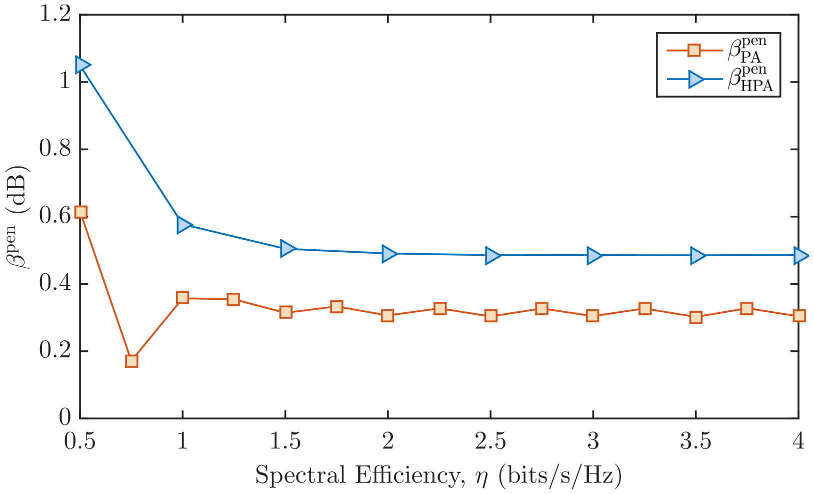

FIGURE 2.38: The penalty in terms of required $E_{b_{(\text{opt})}}/N_0$ for HTP-ACO-OFDM compared to that of FTP-ACO-OFDM.

The optical and electrical SNR per bit for HTP-ACO-OFDM employing $\sqrt{M}$-PAM alphabets can be evaluated as:

$$\frac{E_{\mathrm{b}_{\mathrm{(opt)}}}}{N_0} = \frac{P_{\mathrm{(opt,HPA)}}}{2\eta_{\mathrm{HPA}} B N_0} \tag{2.103}$$

and

$$\frac{E_{\mathrm{b}_{\mathrm{(elec)}}}}{N_0} = \frac{P_{\mathrm{(elec,HPA)}}}{2\eta_{\mathrm{HPA}} B N_0}, \tag{2.104}$$

respectively. Furthermore, the relationship between $E_{\mathrm{b}_{\mathrm{(opt)}}}/N_0$ and $E_{\mathrm{b}_{\mathrm{(elec)}}}/N_0$ is given as:

$$\frac{E_{\mathrm{b}_{\mathrm{(opt)}}}}{N_0} = \frac{1}{\alpha_{\mathrm{HPA}}^{\mathrm{OE}}} \frac{E_{\mathrm{b}_{\mathrm{(elec)}}}}{N_0}. \tag{2.105}$$

2.4.8 Single-Carrier Optical Frequency Division Multiplexing (SCO-FDM)

Single-carrier optical frequency division multiplexing (SCO-OFDM) [125] is another approach which averts the use of HS to attain real-valued TD signal for IM-DD implementation. In SCO-FDM, the M-QAM alphabets are first precoded using DFT and are then allocated to different subchannels. Owing to the arrangemet of the precoded alphabets in different subchannels, the TD samples after IDFT exhibit asymmetric repetition from which real-valued non-negative signal can be obtained. SCO-FDM exhibits the same BER performance as that of ACO-OFDM in an AWGN channel with a lesser PAPR compared to ACO-OFDM, FTP-ACO-OFDM and HTP-ACO-OFDM.

Consider that N subchannels are available at the transmitter of SCO-FDM shown in Fig. 2.39.

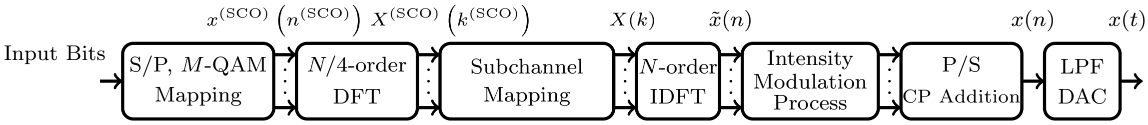

FIGURE 2.39: Block diagram of SCO-FDM transmitter.

The serial input bits are first transformed into parallel data streams and are then mapped onto $N/4$ complex-valued TD M-ary QAM alphabets expressed as $x^{(\mathrm{SCO})}\left(n^{(\mathrm{SCO})}\right)$, where $n^{(\mathrm{SCO})} = 0, 1, \cdots, N/4-1$. Firstly, via $N/4$-order DFT, FT precoding is performed which is given as:

$$X^{(\mathrm{SCO})}\left(k^{(\mathrm{SCO})}\right) = \mathrm{DFT}\left[x^{(\mathrm{SCO})}\left(n^{(\mathrm{SCO})}\right)\right], \tag{2.106}$$

for $k^{(\mathrm{SCO})} = 0, 1, \cdots, N/4-1$. Subsequently, subchannel mapping is performed such that $X^{(\mathrm{SCO})}\left(k^{(\mathrm{SCO})}\right)$ are allocated to an N-subchannel signal, $X(k)$ as:

$$X(k) = \begin{cases} X^{(\mathrm{SCO})}\left(k^{(\mathrm{SCO})}\right), & k = 4k^{(\mathrm{SCO})} \\ 0, & \text{elsewhere} \end{cases}, \tag{2.107}$$

where $k = 0, 1, \cdots, N-1$. It is important to note that three zeros are appended between two precoded FD symbols. $X(k)$ is then transformed into a TD signal, $\tilde{x}(n)$ via N-order IDFT as:

$$\tilde{x}(n) = \mathrm{IDFT}\left[X(k)\right], \tag{2.108}$$

where $n = 0, 1, \cdots, N-1$. Moreover, $\tilde{x}(n)$ are complex-valued symbols. Due to the frame structure of $X(k)$, where three subchannels are left blank between two modulated subchannels, $\tilde{x}(n)$ exhibits the following property:

$$\underbrace{\tilde{x}\left(n^{(\mathrm{SCO})}\right)}_{:=\tilde{x}_1\left(n^{(\mathrm{SCO})}\right)} = \underbrace{\tilde{x}\left(n^{(\mathrm{SCO})} + \frac{N}{4}\right)}_{:=\tilde{x}_2\left(n^{(\mathrm{SCO})}\right)} = \underbrace{\tilde{x}\left(n^{(\mathrm{SCO})} + \frac{N}{2}\right)}_{:=\tilde{x}_3\left(n^{(\mathrm{SCO})}\right)} = \underbrace{\tilde{x}\left(n^{(\mathrm{SCO})} + \frac{3N}{4}\right)}_{:=\tilde{x}_4\left(n^{(\mathrm{SCO})}\right)}, \tag{2.109}$$

for $n^{(\mathrm{SCO})} = 0, 1, \cdots, N/4-1$. Because of asymetrically repetitive structure, intensity modulation process (IMP) is used. In IMP, $\tilde{x}(n)$ is divided into four groups, $\tilde{x}_1\left(n^{(\mathrm{SCO})}\right)$, $\tilde{x}_2\left(n^{(\mathrm{SCO})}\right)$, $\tilde{x}_3\left(n^{(\mathrm{SCO})}\right)$ and $\tilde{x}_4\left(n^{(\mathrm{SCO})}\right)$ as described in (2.109), from which the positive values of real components, $r^+\left(n^{(\mathrm{SCO})}\right)$, negative values of real components, $r^-\left(n^{(\mathrm{SCO})}\right)$, positive values of imaginary components, $i^+\left(n^{(\mathrm{SCO})}\right)$ and negative values of imaginary components, $i^-\left(n^{(\mathrm{SCO})}\right)$, are respectively evaluated. Mathematically, this can be represented by:

$$r^+\left(n^{(\mathrm{SCO})}\right) = \begin{cases} \Re\left[\tilde{x}_1\left(n^{(\mathrm{SCO})}\right)\right], & \tilde{x}_1\left(n^{(\mathrm{SCO})}\right) > 0 \\ 0, & \text{elsewhere} \end{cases}, \tag{2.110}$$

$$r^-\left(n^{(\mathrm{SCO})}\right) = \begin{cases} \Re\left[\tilde{x}_2\left(n^{(\mathrm{SCO})}\right)\right], & \tilde{x}_2\left(n^{(\mathrm{SCO})}\right) < 0 \\ 0, & \text{elsewhere} \end{cases}, \tag{2.111}$$

$$i^+\left(n^{(\mathrm{SCO})}\right) = \begin{cases} \Im\left[\tilde{x}_3\left(n^{(\mathrm{SCO})}\right)\right], & \tilde{x}_3\left(n^{(\mathrm{SCO})}\right) > 0 \\ 0, & \text{elsewhere} \end{cases}, \tag{2.112}$$

and

$$i^-\left(n^{(\mathrm{SCO})}\right) = \begin{cases} \Im\left[\tilde{x}_4\left(n^{(\mathrm{SCO})}\right)\right], & \tilde{x}_4\left(n^{(\mathrm{SCO})}\right) < 0 \\ 0, & \text{elsewhere} \end{cases}. \tag{2.113}$$

Subsequently, $r^+\left(n^{(\mathrm{SCO})}\right)$, $r^-\left(n^{(\mathrm{SCO})}\right)$, $i^+\left(n^{(\mathrm{SCO})}\right)$ and $i^-\left(n^{(\mathrm{SCO})}\right)$ are arranged to form $x(n)$ as

$$x(n) = \begin{cases} r^+\left(n^{(\mathrm{SCO})}\right), & 0 < n < N/4-1 \\ -r^-\left(n^{(\mathrm{SCO})}\right), & N/4 < n < N/2-1 \\ i^+\left(n^{(\mathrm{SCO})}\right), & N/2 < n < 3N/4-1 \\ -i^-\left(n^{(\mathrm{SCO})}\right), & 3N/4 < n < N-1 \end{cases}. \tag{2.114}$$

After digital-to-analog conversion of $x(n)$ and addition of CP for each sub-block, a continuous real-valued non-negative TD signal, $x(t)$ is obtained, which is transmitted through an LED.

SCO-FDM in [125] does not clearly explain how the equalization can be performed. The scheme (only receiver structure) is modified so that equalization process can be incorporated (see SCO-FDM receiver figure). The BER and other performance parameters in the modified version remain the same as in [125]. The receiver structure of SCO-FDM is presented in Fig. 2.40.

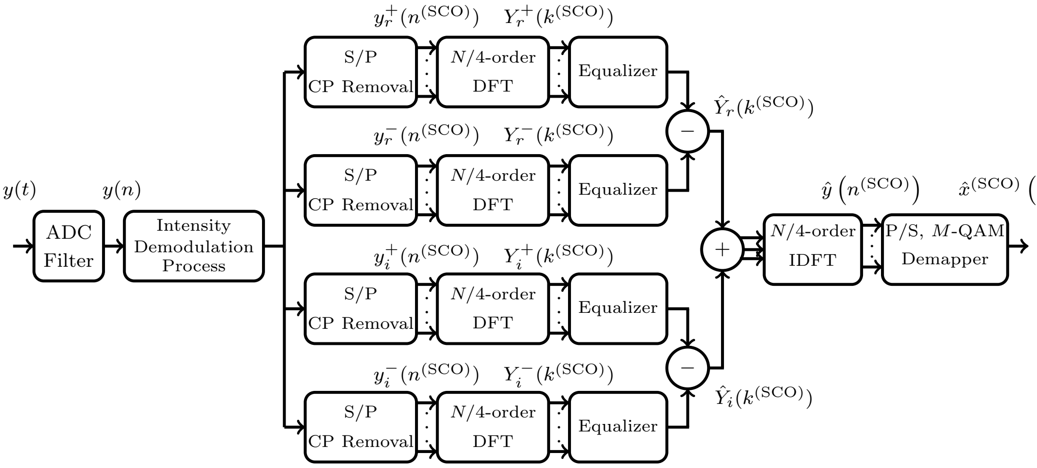

FIGURE 2.40: Block diagram of SCO-FDM receiver.

The received signal, $y(t)$ is first converted into a digital signal, $y(n)$ using an ADC. Using intensity demodulation process (IDP), the received counterparts of $r^+\left(n^{(\mathrm{SCO})}\right)$, $-r^-\left(n^{(\mathrm{SCO})}\right)$, $i^+\left(n^{(\mathrm{SCO})}\right)$ and $-i^-\left(n^{(\mathrm{SCO})}\right)$, i.e., $y_r^+\left(n^{(\mathrm{SCO})}\right)$, $y_r^-\left(n^{(\mathrm{SCO})}\right)$, $y_i^+\left(n^{(\mathrm{SCO})}\right)$, and $y_i^-\left(n^{(\mathrm{SCO})}\right)$ are identified as:

$$y(n) = \begin{cases} y_r^+\left(n^{(\mathrm{SCO})}\right), & 0 < n < N/4-1 \\ y_r^-\left(n^{(\mathrm{SCO})}\right), & N/4 < n < N/2-1 \\ y_i^+\left(n^{(\mathrm{SCO})}\right), & N/2 < n < 3N/4-1 \\ y_i^-\left(n^{(\mathrm{SCO})}\right), & 3N/4 < n < N-1 \end{cases}. \tag{2.115}$$

for $n^{(\mathrm{SCO})} = 0, 1, \cdots, N/4-1$. Subsequently, $y_r^+\left(n^{(\mathrm{SCO})}\right)$, $y_r^i\left(n^{(\mathrm{SCO})}\right)$, $y_i^+\left(n^{(\mathrm{SCO})}\right)$ and $y_i^-\left(n^{(\mathrm{SCO})}\right)$ are transformed into FD by applying $N/4$-order DFT as:

$$\begin{aligned} Y_r^+\left(k^{(\mathrm{SCO})}\right) &= \mathrm{DFT}\left[y_r^+\left(n^{(\mathrm{SCO})}\right)\right], \\ Y_r^-\left(k^{(\mathrm{SCO})}\right) &= \mathrm{DFT}\left[y_r^-\left(n^{(\mathrm{SCO})}\right)\right], \\ Y_i^+\left(k^{(\mathrm{SCO})}\right) &= \mathrm{DFT}\left[y_i^+\left(n^{(\mathrm{SCO})}\right)\right], \\ Y_i^-\left(k^{(\mathrm{SCO})}\right) &= \mathrm{DFT}\left[y_i^-\left(n^{(\mathrm{SCO})}\right)\right]. \end{aligned} \tag{2.116}$$

These FD samples are then independently equalized to yield $\hat{Y}_r^+\left(k^{(\mathrm{SCO})}\right)$, $\hat{Y}_r^-\left(k^{(\mathrm{SCO})}\right)$, $\hat{Y}_i^+\left(k^{(\mathrm{SCO})}\right)$ and $\hat{Y}_i^-\left(k^{(\mathrm{SCO})}\right)$. The real and the imaginary components equalized FD samples are obtained as:

$$\begin{aligned} \hat{Y}_r\left(k^{(\mathrm{SCO})}\right) &= \hat{Y}_r^+\left(k^{(\mathrm{SCO})}\right) - \hat{Y}_r^-\left(k^{(\mathrm{SCO})}\right), \\ \hat{Y}_i\left(k^{(\mathrm{SCO})}\right) &= \hat{Y}_i^+\left(k^{(\mathrm{SCO})}\right) - \hat{Y}_i^-\left(k^{(\mathrm{SCO})}\right), \end{aligned} \tag{2.117}$$

which are then combined as:

$$\hat{Y}\left(k^{(\mathrm{SCO})}\right) = \hat{Y}_r\left(k^{(\mathrm{SCO})}\right) + j \cdot \hat{Y}_i\left(k^{(\mathrm{SCO})}\right). \tag{2.118}$$

These samples are then FT decoded to obtain an estimate of the transmitted data as:

$$\hat{y}\left(n^{(\mathrm{SCO})}\right) = \mathrm{IDFT}\left[\hat{Y}\left(k^{(\mathrm{SCO})}\right)\right]. \tag{2.119}$$

Finally, the decision on the received data can be made as:

$$\hat{x}^{(\mathrm{SCO})}\left(n^{(\mathrm{SCO})}\right) = \arg\min_{X_Q \in \mathcal{Q}} \left\|\hat{y}\left(n^{(\mathrm{SCO})}\right) - X_Q\right\|. \tag{2.120}$$

The SE of SCO-FDM, η_{SCO} is the same as that of ACO-OFDM, i.e., $\eta_{\mathrm{SCO}} = \eta_{\mathrm{ACO}}$.

Moreover, the PAPR of SCO-FDM for different modulation alphabets is presented in Fig. 2.41. It can be discerned that the PAPR of SCO-FDM among all the precoded and non-precoded approaches. However, it is important to highlight that SCO-FDM cannot attain the minimum PAPR which is manifested by I-SCFDMA for RF systems. Furthermore, it can also be concluded that if the precoded modulation approach somehow averts the HS, the PAPR is can be reduced to a greater extent.

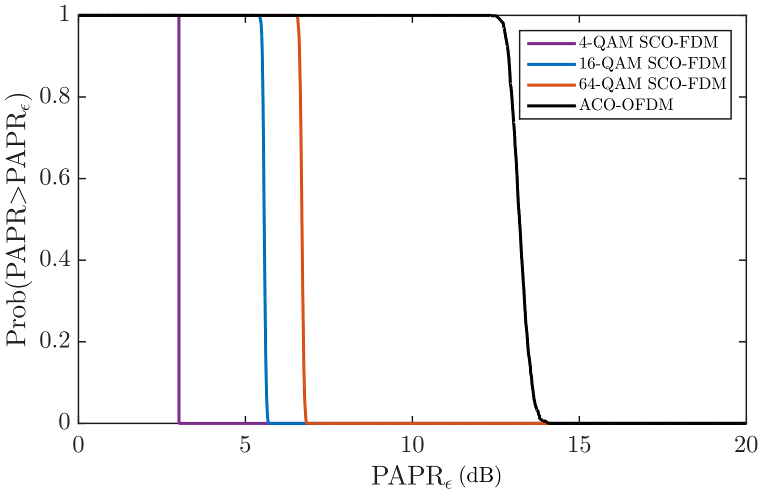

FIGURE 2.41: CCDF curves for PAPR illustration of HTP-ACO-OFDM obtained using $N = 1024$.

Statistical Characterization of SCO-FDM

The statistical characterization of SCO-FDM has not been provided in [125]. However, for the sake of understanding, a succinct characterization of SCO-FDM is presented hereby. The pdf of TD SCO-FDM signals, $x(n)$, using 4-QAM and 16-QAM is presented in Fig. 2.42.

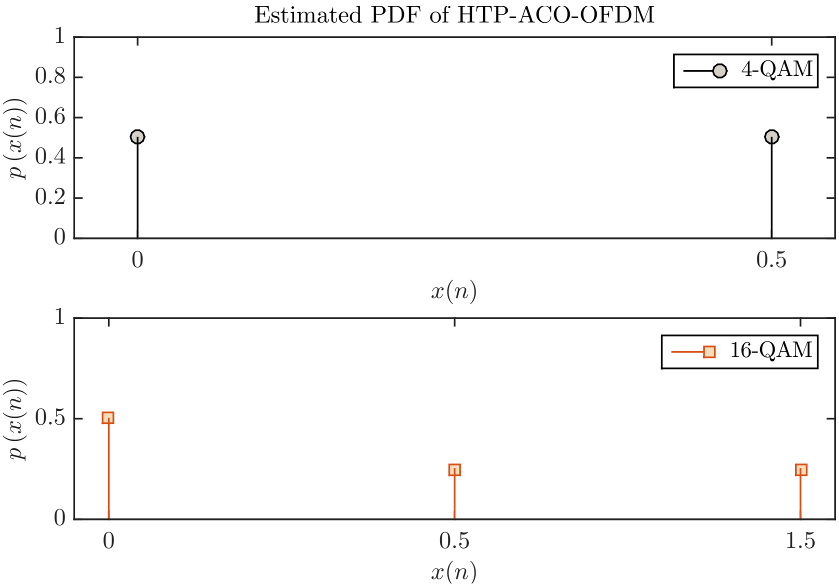

FIGURE 2.42: Estimated pdf for SCO-FDM.

For square M-QAM constellations, the pdf of $x(n)$ can be given as:

$$p\left(x(n)\right) = \frac{1}{2}\delta(0) + \frac{1}{\sqrt{M}} \sum_{i=0}^{\sqrt{M}/2} \delta\left(\frac{\sqrt{M} - [2(i-1)+1]}{2}\right). \tag{2.121}$$

Furthermore, the optical and the electrical power for (square M-QAM based) SCO-FDM can be evaluated as:

$$P_{(\text{opt,SCO})} = E\left(|x(n)|\right) = \sum_{i=0}^{\sqrt{M}/2} \underbrace{\text{prob}\left(x(n) = \frac{\sqrt{M} - [2(i-1)+1]}{2}\right)}_{:=\frac{1}{\sqrt{M}}} \left(\frac{\sqrt{M} - [2(i-1)+1]}{2}\right), \tag{2.122}$$

where prob$(x = a)$ stands for the probability that x would be equal to a. Moreover,

$$P_{(\text{elec,SCO})} = E\left(|x(n)|^2\right) = \frac{M-1}{24}, \tag{2.123}$$

since the average symbol energy for M-QAM is $2/3(M-1)$. Using (2.122) and (2.123), the optical-to-electrical conversion efficiency can be evaluated by scaling $P_{(\text{opt,SCO})} = 1$ as:

$$\alpha_{\text{SCO}}^{\text{OE}} = \frac{P_{(\text{elec,SCO})}}{P_{(\text{opt,SCO})}}. \tag{2.124}$$

A graphical illustration of $\alpha_{\text{SCO}}^{\text{OE}}$ is presented in Fig. 2.43 which reveals that the optical-to-electrical conversion efficiency of SCO-FDM is the least compared to ACO-OFDM, FTP-ACO-OFDM and HTP-ACO-OFDM which essentially implies that SCO-FDM requires more $E_{b_{(\text{opt})}}/N_0$ to attain a given BER.

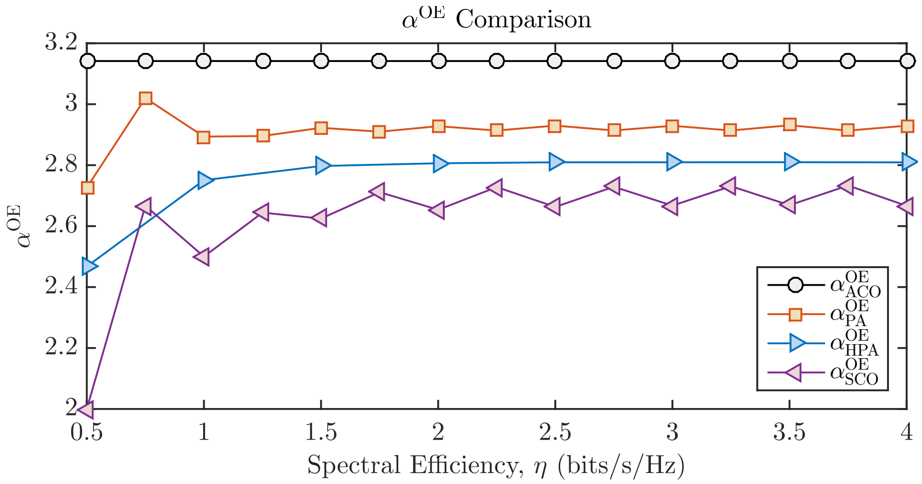

FIGURE 2.43: Comparison of α^{OE} for ACO-OFDM, FTP-ACO-OFDM, HTP-ACO-OFDM and SCO-FDM for different spectral efficiencies.

The penalty for SCO-FDM relative to ACO-OFDM can be calculated as:

$$\beta^{\mathrm{pen}}_{\mathrm{SCO}} = 10\log_{10}\left(\frac{\alpha^{\mathrm{OE}}_{\mathrm{ACO}}}{\alpha^{\mathrm{OE}}_{\mathrm{SCO}}}\right) \quad \text{(dB)}. \tag{2.125}$$

A gaphical illustration of $\beta^{\mathrm{pen}}_{\mathrm{SCO}}$ is presented in Fig. 2.44, which reveals that the penalty for SCO-FDM is highest compared to other alternatives, such as FTP-ACO-OFDM and HTP-ACO-OFDM. Mathematically, this can be given as:

$$\beta^{\mathrm{pen}}_{\mathrm{SCO}} > \beta^{\mathrm{pen}}_{\mathrm{HPA}} > \beta^{\mathrm{pen}}_{\mathrm{PA}}. \tag{2.126}$$

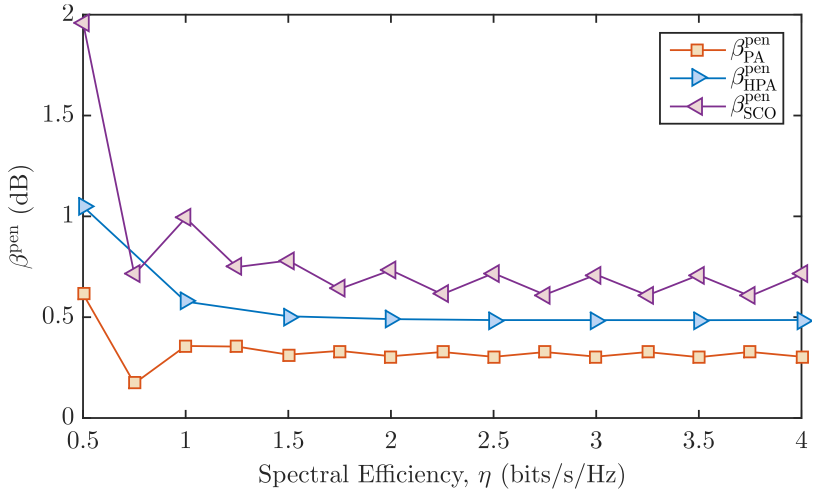

FIGURE 2.44: The penalty in terms of required $E_{\mathrm{b}_{(\mathrm{opt})}}/N_0$ for SCO-FDM compared to that of FTP-ACO-OFDM and HTP-ACO-OFDM.

$E_{\mathrm{b}_{(\mathrm{opt})}}/N_0$ and $E_{\mathrm{b}_{(\mathrm{elec})}}/N_0$ for SCO-FDM can be evaluated by using (2.59) and (2.60) and replacing $P_{(\mathrm{opt,ACO})}$ and $P_{(\mathrm{elec,ACO})}$ with $P_{(\mathrm{opt,SCO})}$ and $P_{(\mathrm{elec,SCO})}$, and also replacing η_{ACO} with η_{SCO}. Similarly, the relationship between $E_{\mathrm{b}_{(\mathrm{opt})}}/N_0$ and $E_{\mathrm{b}_{(\mathrm{elec})}}/N_0$ for FTP-ACO-OFDM is evaluated by replacing $\alpha^{\mathrm{OE}}_{\mathrm{ACO}}$ with $\alpha^{\mathrm{OE}}_{\mathrm{SCO}}$ in (2.61).

2.5 Comparisons

The following comparisions can be drawn for the state-of-the-art modulation approaches:

1. In terms of spectral efficiency, DCO-OFDM and FTP-DCO-OFDM possess the highest spectral efficiency, whereas, the spectral efficiency of the remaining approaches is half of DCO-OFDM/FTP-DCO-OFDM. However, it can be noticed that DCO-OFDM and FTP-DCO-OFDM manifest high and moderate PAPR values, respectively, which can be an issue when these approaches are used. Moreover, the use of bias-index for these approaches would also result in high optical power consumption.
2. In terms for PAPR, SCO-FDM has the lowest PAPR but the spectral efficiency is half of DCO-OFDM. Consequently, if same modulation alphabets are used for both SCO-FDM and DCO-OFDM with same number of subcarrier/subchannels, then, the data-rate of SCO-FDM would be half of DCO-OFDM. Moreover, it is important to highlight that SCO-FDM cannot attain the same PAPR as that of I-SCFDMA of RF systems. Additionally, as seen previously in Fig. 2.44, the optical-to-electrical conversion efficiency of SCO-FDM is least among the modulation approaches which do not require bias-index to overcome non-negativity.
3. In terms of complexity, it can be observed that generally, the precoded approaches have moderate computational complexity. However, HTP-ACO-OFDM is less complex among all the precoded approaches because it used IDHT/DHT rather IDFT/DFT for multiplexing and demultiplexing, respectively.
4. It may also be noticed that if HS is used for precoded approaches, the resulting TD signal would have lower PAPR compared to non-precoded approaches, however, that reduction would not be significant. Therefore, ideally, HS should be avoided for precoded approaches, so that lower values of PAPR can be attained.

The results are summarized in the following table:

TABLE 2.2: Comparison between state-of-the-art modulation approaches

Modulation Approach	**SE w.r.t. DCO-OFDM**	**PAPR**	**Complexity**	**HS**	**Remark**
DCO-OFDM	100%	High	Low	Required	Requires bias-index
ACO-OFDM	50%	High	Low	Required	Power efficient for low SE
FTP-DCO-OFDM	100%	Moderate	Moderate	Required	Requires bias-index
FTP-ACO-OFDM	50%	Moderate	Moderate	Required	Power efficient for low SE
HTP-ACO-OFDM	50%	Low	Low	Not Required	Power efficient for low SE
SCO-FDM	50%	Low	Moderate	Not Required	Power efficient for low SE

From the results and comparison, it is obvious that there would always be a trafe-off between which modulation approach to use, e.g., if high data-rates are required DCO-OFDM or FTP-DCO-OFDM approaches are better but the PAPR manifested by these approaches may not be the least. On the other hand, SCO-FDM is used, lower PAPR can be achieved, but, in this case the achieved data-rates could be lower. It would be safe to conclude that there is no approaches (among the presented) which could have a superior performance for all the analyzed parameters.

2.6 Contributions relative to the state-of-the-art

From the study of these techniques, it can be ascertained that O-OFDM techniques, particularly non-precoded techniques pose some serious practical limitations for OWC systems because of their vulnerability to the nonlinear distortions imposed by the LED, primarily due to a high PAPR [101]. Moreover, high PAPR also results in energy inefficiency as it can be seen for DCO-OFDM; for which a higher bias-index is needed to sufficiently bias the TD signal. To counteract the high PAPR of state-of-the-art O-OFDM techniques, i.e., DCO-OFDM and ACO-OFDM, PAPR reduction techniques have been investigated in the literature. It has been determined that the most convenient approach to scale down the high PAPR and fit the signal in the narrow amplitude modulation dynamic range of the LED is to clip it to a pre-defined amplitude. On the other hand, clipping generates significant distortion which could severely diminish the performance of the system. In this context, two iterative decision-directed methods essentially for clipping mitigation are introduced in this work. The objective is to clip the signal to a given threshold before transmission and try to restore the lost information by using the proposed methods at the receiver. These methods fulfill the conditions of IM-DD and are pertinent to both DCO-OFDM and ACO-OFDM. Statistical analysis of clipping is also presented. One of the proposed methods alleviate the clipping distortion in TD and the other one mitigates it in FD. Based on the domain of operation, the methods are referred as time-domain clipped sample reconstruction (TD-CSR) and frequency-domain clipping distortion removal (FDCDR). The results of these methods are compared with selected-mapping (SLM). This work has led to publications [126, 127, 80].

From the work on PAPR reduction techniques, it is determined that PAPR reduction methods inflict a considerable complexity overhead, which is undesirable. Accordingly, it is established that O-SCFDMA/precoding could be the most suitable choice to reduce PAPR without extending the computational complexity. To be coherent with IM-DD constraints, the O-SCFDMA/precoded approaches, such as FTP-DCO-OFDM and FTP-ACO-OFDM apply HS constraint because of which the PAPR cannot be lowered substantially [121]. So, the approaches which preclude the use of HS, e.g., HTP-ACO-OFDM and SCO-FDM can manifest lower PAPR compared to other O-SCFDMA approaches which use HS. However, for HTP-ACO-OFDM, the PAPR reduction becomes less compelling when the modulation alphabet is increased, and for SCO-FDM, the non-negative signal generation process does not allow to reduce PAPR significantly. Other SC approaches, such as, PAM SC frequency domain equalization (PAM-SCFDE) [87] and Decomposed Quadrature Optical SCFDE (DQO-SCFDE) [119] can also reduce the signal PAPR, however, these approaches are not capable of (FD) MA. Against this background, HS free (HSF) O-SCFDMA (HSFO-SCFDMA) is proposed which is capable of MA and also averts the use of HS.

For the state-of-the art O-OFDM/O-SCFDMA approaches, all the available subcarriers/subchannels cannot be modulated because of HS requirement. Half of the subcarriers/subchannels have to be relinquished to make way for the HS. Moreover, for ACO-OFDM and FTP-ACO-OFDM, to generate a non-negative signal, merely the odd subcarriers can be modulated which further reduces the SE. This entails that ACO-OFDM and FTP-ACO-OFDM approaches are spectrally less efficient than DCO-OFDM and FTP-DCO-OFDM. However, ACO-OFDM and FTP-ACO-OFDM are power efficient compared to DCO-OFDM and FTP-DCO-OFDM for lower order modulation alphabets. To augment the SE and to maintain the power advantage of ACO-OFDM over DCO-OFDM for both low and high order modulation alphabets, layered ACO-OFDM (LACO-OFDM) is proposed. Howbeit, half of the subcarriers are sacrificed to incorporate HS, and LACO-OFDM still manifests high PAPR. PAPR reduction methods for such approaches require large computation resources. Therefore, the performance of Fourier transform and Hartley transform precoding is studied for LACO-OFDM. It is submitted that if one uses Hartley transform (for precoding/decoding and multiplexing/demultiplexing) with PAM alphabets, an approach can be developed, i.e., HTP-LACO-OFDM in which all the subchannels can be modulated and an intensity waveform can be realized without the use of HS. The analyzed techniques FTP-LACO-OFDM and HTP-LACO-OFDM are the layered variants of FTP-ACO-OFDM and HTP-ACO-OFDM, respectively. This work has to be published.

Finally, experimental demonstrations have been presented for TDCSR/FDCDR and HSFO-SCFDMA using fiber based IM-DD system. Fiber based IM-DD system is used because of unavailability of OWC prototype. The experimental results are in accordance with simulation results.

Chapter 3

Decision-Directed Iterative Methods for PAPR Reduction in Optical Wireless OFDM Systems

In this chapter, two iterative decision-directed methods for peak-to-average power ratio (PAPR) reduction in optical-orthogonal frequency division multiplexing (O-OFDM) are presented. These methods are applicable to state-of-the-art intensity modulation-direct detection (IM-DD) O-OFDM techniques for optical wireless communication (OWC) systems, including direct-current (DC) biased O-OFDM (DCO-OFDM) and asymmetrically clipped O-OFDM (ACO-OFDM). One of the straightforward and efficient method to counteract high PAPR is the clipping of the O-OFDM signal to a pre-defined threshold. However, clipping being itself nonlinear function, results in an inevitable nonlinear distortion leading to the loss of useful information, therefore, clipping mitigation is prescribed. The proposed iterative decision-directed methods operate at the receiver and retrieve the lost information by alleviating the clipping distortion. Simulation results acknowledge that the high PAPR of O-OFDM is curtailed by clipping, and the proposed methods can lessen the derogatory effects of clipping with a reasonable complexity compared to standard PAPR reduction methods.

3.1 Review of PAPR reduction techniques

Several PAPR reduction techniques for O-OFDM have been investigated in the literature, the taxonomy of which is given in Fig. 3.1 and are classified as

- *Signal Distortion Techniques*: In these techniques, high PAPR is reduced by distorting the O-OFDM signal prior to its transmission through the LED. Most common signal distortion techniques are (i) clipping and filtering [128, 129], (ii) companding [130] and (iii) peak windowing [131]. The idea behind clipping of the signal is that the high peaks occur only rarely, therefore, small amount of distortions resulting from clipping the peaks can be tolerable. In companding, large amplitudes of the signal are compressed at the transmitter before being expanded at the receiver to recover the original waveform, but leading to significant increase of noise contribution.

- *Multiple signaling and probabilistic techniques*: In these techniques, numerous candidate signals containing the same information are generated and the one with lowest PAPR is selected for transmission. Most common probabilistic techniques are: (i) partial transmit sequences (PTS) [132], (ii) selected-mapping (SLM) [132], (iii) tone-reservation (TR) [133] and (iv) pilot-assisted (PA) [134]. Typically, these methods require side information to be passed on along with the data. Using side information to restore the original data block reduces the useful data rate and increases the computational complexity.
- *Coding techniques*: In these techniques, coding schemes that are generally used for error detection and correction are adapted to perform the additional function of PAPR reduction. You and Kahn [135] proposed a block coding technique for PAPR reduction in O-OFDM, this approach is derived from RF-OFDM and involves block coding between the information bits and the amplitudes that have been modulated onto the subcarriers. In another approach by Kang and Hranilovic [136], in-band trellis coding and out-of-band carrier design is introduced to curtail the negative peaks of the electrical signal. The techniques [135, 136], however, require an expanded transmission bandwidth and exhibits a substantial complexity overhead.
- *O-OFDM structure specific techniques*: In these techniques, the frame structure of O-OFDM is exploited to reduce the PAPR. Semi-definite relaxation based PAPR reduction method for DCO-OFDM has been proposed Whang *et al.* [137]. In ellipse-based DCO-OFDM [138], DCO-OFDM is modified based on the concept of constant envelope OFDM [139] to reduce PAPR.

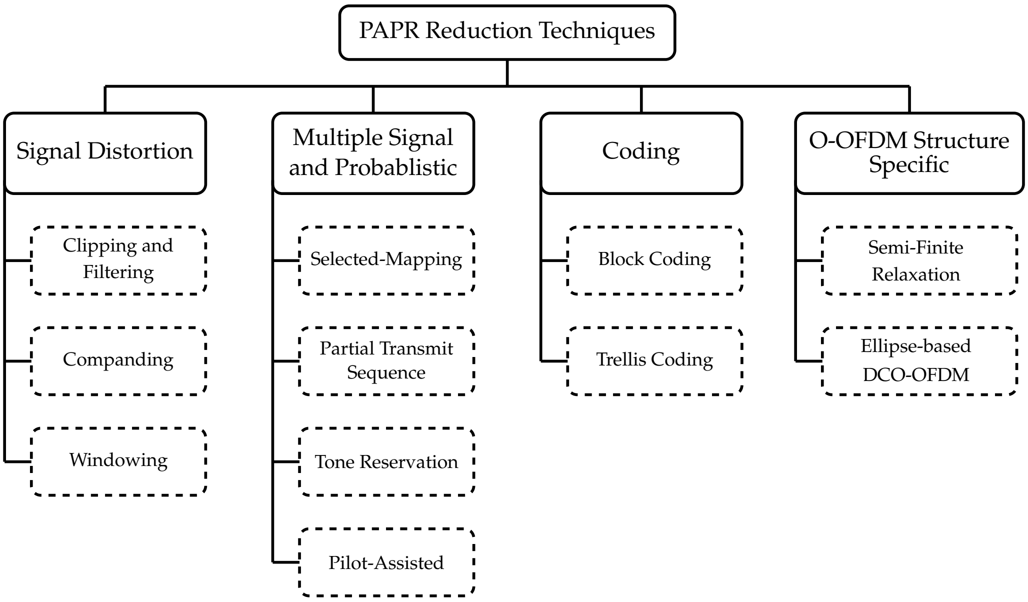

FIGURE 3.1: Taxonomy of PAPR reduction techniques

In the proposed approaches, the high PAPR is counteracted by deliberate clipping of the TD signal, limiting the signal amplitude to a pre-specified threshold. As clipping degrades the system performance, distortion compensation techniques are needed to mitigate clipping distortion [140]. It is essential to recognize that clipping characteristics in O-OFDM differ from that of RF-OFDM counterparts in the following aspects [141]:

- in RF-OFDM, the TD signal is complex-valued, whereas, in O-OFDM, the TD signal is real-valued;

- the primary power limitation in O-OFDM is the average optical power rather than average electrical power as in RF-OFDM.

Therefore, most of the theory formulated regarding clipping characteristics for RF-OFDM cannot be generalized to O-OFDM.

In this work, to compensate the clipping distortion generated by deliberate clipping of TD O-OFDM signal, two receiver-based iterative decision-directed non-linear distortion mitigation methods; time-domain clipped sample reconstruction (TDCSR), and frequency-domain clipping distortion removal (FDCDR), based on Bussgang decomposition in line with [142] and [143], respectively, are proposed for PAPR reduction in O-OFDM systems. The underlying idea of the proposed methods is that, if the nonlinear characteristics of the transmitter are known at the receiver, the nonlinear distortions can be regarded as a deterministic function of the received data, and accordingly, can be mitigated. Furthermore, the techniques in [142] and [143] cannot be applied to IM-DD based O-OFDM systems, since they are restricted to be suitable on complex-valued bipolar RF OFDM signals. Also, the methods [142] and [143], are not equipped to deal with the bias-index of DCO-OFDM, and the anti-symmetric property of ACO-OFDM. Hence, the uniqueness of TDCSR and FDCDR comes from the obligation to handle the real-valued nature of TD signals, the bias-index in DCO-OFDM, anti-symmetric property in ACO-OFDM, and the manner in which the input to the iteration is updated. TDCSR reconstructs the affected (or lost) clipped samples iteratively in the TD, whereas FDCDR estimates the distortion instigated due to clipping and mitigates it iteratively in the FD. TDCSR and FDCDR are applicable to both DCO- and ACO-OFDM, and are accustomed to the constraints enforced by IM-DD. Simulations performed under different clipping conditions reveal that the methods can substantially mitigate the clipping distortions. Moreover, owing to the reduction of bias-index, significant reduction in terms of power consumption can be foreseen for DCO-OFDM. The performance of TDCSR and FDCDR is compared with that of SLM when clipping mitigation methods are used with DCO-OFDM. When ACO-OFDM with clipping mitigation is applied, FTP-ACO-OFDM and SLM are adopted for comparison.

The rest of the chapter is organized as follows. In section 3.2, an overview of SLM is presented. In section 3.3, the impact of clipping on O-OFDM is presented. System model for clipped O-OFDM is provided in 3.4. Section 3.5 provides a statistical analysis of clipped O-OFDM, along with analytical models. Section 3.6 explains TDCSR and FDCDR methods for clipping mitigation in details. Section 3.7 presents several simulation results on the performance of the proposed methods considering both DCO-OFDM and ACO-OFDM. The complexity implications of TDCSR and FDCDR have been discussed in section 3.8. Section 3.9 draws conclusions.

TABLE 3.1: Comparison of trade-offs involved in various PAPR reduction schemes

Scheme	**Increase in BER**	**Data-rate Loss**	**Computational Complexity**
SLM	No	Yes	High
PTS	No	Yes	High
PA	No	Yes	High
TR	No	Yes	High
Clipping	Yes	No	Low
Companding	Yes	No	Low

3.2 Review of Adpated Selected-Mapping (SLM) for IM-DD

The performance of the proposed decision-directed PAPR reduction methods is compared with SLM. Hence, for clarity an overview of SLM is hereby provided.

The block diagram of SLM is presented in Fig. 3.2. The IM-DD adapted variant of SLM is proposed by Nadal *et al.* in [132]. In SLM, a set of U independent candidate signals, representing the same information is generated at the transmitter using M-ary QAM alphabets. The beneficial signal as regards to the minimum PAPR is chosen to be transmitted. U signals are obtained by weighting the samples of O-OFDM FD signal, $X(k)$ by the U statistically independent phase sequences, $P^{(u)}(k)\ \forall\, k = 0, 1, \cdots, N-1$ and $u = 1, 2\cdots, U$. The modified signal is given as:

$$R^{(u)}(k) = P^{(u)}(k)X(k). \tag{3.1}$$

The elements of phase sequence, $P^{(u)}(k)$ are chosen, such that, HS of $X(k)$ is retained. Therefore, $N/2-1$ components of phase sequence are randomly and uniformly chosen from the set $\{-1, +1\}$. Moreover, all elements of $P^{(1)}(k) = 1,\ \forall\, k = 0, 1, \cdots, N-1$ are set to 1 to accommodate the original signal, i.e., $R^{(1)}(k) = X(k)$. Hence, the degree of freedom on the choice for phase sequences, $P^{(u)}$, is $U-1$. Further, via an N-order IDFT of U modified signals, $R^{(u)}(k)$, the TD signals $r^{(u)}(n) = \text{IDFT}\left[R^{(u)}(k)\right]$, $n = 0, 1, \cdots, N-1$ are realized. PAPR, $\lambda^{(u)}$, of each TD modified signal $r^{(u)}(n)$ is calculated. The modified signal which manifests minimum $\lambda^{(u)}$ is chosen to be transmitted. The signal with the lowest $\lambda^{(u)}$ is referred as $x(n)$.

To recover data at the receiver, the knowledge about the chosen phase sequence, $P^{(u)}(k)$ which gives the minimum $\lambda^{(u)}$ requires to be explicitly transmitted along with $x(n)$. Since, U statistically independent candidate signals are dealt with, therefore, SLM requires U times N-order IDFT computations at the transmitter, while the number of bits needed for transmission of side information is $\log_2\lfloor U\rfloor_{\mathbb{Z}}$, where $\log_2\lfloor z\rfloor_{\mathbb{Z}}$ denotes the greatest integer lower than z. PAPR reduction in SLM depends on the number of phase sequences, U. Increasing them culminates in noteworthy reduction in peak power, however, results in an increase in the number of IDFT computations. SLM makes the occurrence of the peaks less frequent rather to eradicate them absolutely. Moreover, SLM can be adopted for any number of N, however, the overhead of side information which is corelated to N also needs to be transmitted to the receiver along with the signal[1].

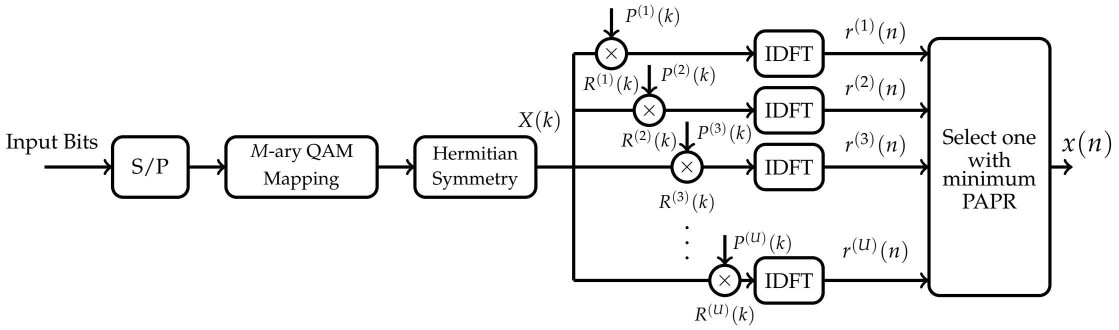

FIGURE 3.2: Block diagram of selected-mapping (SLM) technique.

---

[1] In our implementation of SLM, we consider that the phase vector of the chosen lowest PAPR signal is known at the receiver.

3.3 Impact of Clipping on O-OFDM

In DCO-OFDM, the bias-index needed to avert lower level signal clipping should be equal to the negative peak of the TD signal, consequently, the average optical power which is directly proportional to the bias-index is high [135, 134]. However, if TD DCO-OFDM signal is clipped, besides a reduction in PAPR, the expected bias-index can be lowered, lessening the required average optical power. Clipping can further assist in reducing the bit resolution of the DAC, since, the clipped signal requires less quantization levels, contrary to an un-clipped DCO-OFDM signal [127]. For ACO-OFDM, clipping ensures a reduction of PAPR and reduces the bit resolution requirement of the DAC. A comprehensive investigation on the impact of LED non-linearity (clipping in particular) on O-OFDM is presented by Dimitrov *et al.* [92], along with analytical models for clipped O-OFDM. [92] also examines the impact of clipping on the BER, power efficiency, etc.

3.4 System Model for Clipped O-OFDM

Consider an O-OFDM transmission with N subcarriers, where $x(n)$ for $n = 0, 1, \cdots, N-1$, denotes the discrete TD signal for both DCO-OFDM and ACO-OFDM as realized in Chapter 2.

By using the central limit theorem (CLT) and considering $N \to \infty$, $x(n)$ is modeled as Gaussian distributed, i.e., $\mathcal{N}(0, \sigma_x^2)$. For brevity, we use $p\,(x(n))$ to represent the probability density function (pdf) of $x(n)$, which is expressed as:

$$p(x(n)) \approx \frac{1}{\sigma_x \sqrt{2\pi}} \exp\left(-\frac{x(n)^2}{2\sigma_x^2}\right), \tag{3.2}$$

where σ_x^2 is the mean power of the O-OFDM signal given as $\sigma_x^2 = E(|x(n)|^2)$.

To counteract the high PAPR, the TD symbols, $x(n)$, are subjected to amplitude clipping at given upper (ξ_{upper}) and lower (ξ_{lower}) levels, prior to the DAC stage. For DCO-OFDM, the clipping operation is expressed as:

$$x^{\text{c}}(n) = \text{clip}\,(x(n), \gamma) = \begin{cases} \xi_{\text{upper}}, & x(n) > \xi_{\text{upper}} \\ x(n), & \xi_{\text{lower}} \le x(n) \le \xi_{\text{upper}} \\ \xi_{\text{lower}}, & x(n) < \xi_{\text{lower}} \end{cases}. \tag{3.3}$$

Symmetric clipping, i.e., $\xi_{\text{upper}} = |\xi_{\text{lower}}| = \gamma\sigma_x$ is considered for DCO-OFDM, where γ is the clipping threshold which measures the severity of clipping. For ACO-OFDM, as $x(n)$ is already clipped at zero, accordingly, only upper level clipping is executed, which restrains the positive amplitudes to $\xi_{\text{upper}} = \gamma\sigma_x$. The clipped signal, $x^{\text{c}}(n)$ for ACO-OFDM reads

$$x^{\text{c}}(n) = \text{clip}\,(x(n), \gamma) = \begin{cases} \xi_{\text{upper}}, & x(n) > \xi_{\text{upper}} \\ x(n), & 0 \le x(n) \le \xi_{\text{upper}} \\ 0, & x(n) < 0 \end{cases}. \tag{3.4}$$

By exercising Bussgang decomposition [144, 145] and considering $x(n) \sim \mathcal{N}(0, \sigma_x^2)$, $x^{\text{c}}(n)$ is statistically modeled as a sum of two uncorrelated parts as:

$$x^{\text{c}}(n) = \alpha x(n) + d(n) \tag{3.5}$$

where α is a linear attenuation factor, and $d(n)$ are the clipping distortion realizations statistically uncorrelated to $x(n)$. Moreover, α is a function of the non-linear distortion, which in this case, is clipping.

An analog waveform, $x^{\mathrm{c}}(t)$ is realized by feeding $x^{\mathrm{c}}(n)$ to a DAC. Then, a bias $\beta_{\mathrm{DC}}^{(\mathrm{D})}$ is introduced to attain a non-negative waveform for DCO-OFDM. $\beta_{\mathrm{DC}}^{(\mathrm{D})}$ is adjusted, such that, sufficient biasing is realized, i.e., $\beta_{\mathrm{DC}}^{(\mathrm{D})} = |\min[x^{\mathrm{c}}(t)]| = |\xi_{\mathrm{lower}}| = \xi_{\mathrm{upper}}$ [134]. The intensity waveform, $x(t)$, for DCO-OFDM is characterized as:

$$x(t) = x^{\mathrm{c}}(t) + \beta_{\mathrm{DC}}^{(\mathrm{D})} = \begin{cases} 2\xi_{\mathrm{upper}}, & x(t) > \xi_{\mathrm{upper}} \\ x(t) + \xi_{\mathrm{upper}}, & \xi_{\mathrm{lower}} \leq x(t) \leq \xi_{\mathrm{upper}} \\ 0, & x(t) < 0 \end{cases}. \tag{3.6}$$

In case of ACO-OFDM, the expression of $x(t)$ would be the analog counterpart of (3.4).

In what follows, we assume that $x^{\mathrm{c}}(t)$ corresponds to the dynamic range $\Delta\xi \triangleq \xi_{\mathrm{upper}} - \xi_{\mathrm{lower}}$ of the LED and the input limits of the DAC [134].

At the receiver, $y(n)$ is attained after analog-to-digital conversion of the photo-detected signal $y(t)$. For simplicity, an ideal channel is considered, i.e., $h(t) = \delta(t)$. Therefore, $y(n)$ is given as:

$$y(n) = x^{\mathrm{c}}(n) + w(n), \tag{3.7}$$

where $w(n)$ are additive white Gaussian noise (AWGN) samples with zero mean with a mono-lateral power spectral density (PSD) of N_0. After N-order DFT on (3.7), the received FD symbols are expressed as:

$$\hat{Y}(k) = \mathrm{DFT}\left[y(n)\right] = X^{\mathrm{c}}(k) + W(k), \tag{3.8}$$

where $\hat{Y}(k)$, $X^{\mathrm{c}}(k)$,and $W(k)$ are FD counterparts of $y(n)$, $x^{\mathrm{c}}(n)$ and $w(n)$, respectively. The naive receivers for O-OFDM neglect the distortions instigated by the clipping process, i.e., $X^{\mathrm{c}}(k) \neq X(k)$ to identify the transmitted symbols as:

$$\hat{X}\left(k^{(\mathrm{D})} + 1\right) = \arg\min_{X_Q \in \mathcal{Q}} \left\|\hat{Y}\left(k^{(\mathrm{D})} + 1\right) - X_Q\right\|, \tag{3.9}$$

and

$$\hat{X}\left(2k^{(\mathrm{A})} + 1\right) = \arg\min_{X_Q \in \mathcal{Q}} \left\|2\hat{Y}\left(2k^{(\mathrm{A})} + 1\right) - X_Q\right\|, \tag{3.10}$$

for DCO-OFDM and ACO-OFDM, respectively. X_Q represents all the possible quadrature-amplitude modulation (QAM) alphabets in the constellation set $\mathcal{Q} = \{\mathcal{Q}_0, \mathcal{Q}_1, \cdots, \mathcal{Q}_{M-1}\}$. $k^{(\mathrm{A})} = 0, 1, \cdots, N/4 - 1$ and $k^{(\mathrm{D})} = 0, 1, \cdots, N/2 - 2$ as defined in Chapter 2, which identify the modulated subcarriers for DCO-OFDM and ACO-OFDM, respectively. The decisions on the modulated data presented in (3.9) and (3.10) will lead to an impaired performance as the clipping distortion in entirely neglected.

3.5 Statistical Analysis of Clipping

In this section, statistical analysis of clipping on O-OFDM is investigated. The analysis provided here is a specific case of [92], as symmetric clipping is recognized for DCO-OFDM, and only upper clipping is analyzed for ACO-OFDM.

Contrary to the approximation that $x(n)$ is Gaussian distributed, i.e., $x(n) \sim \mathcal{N}(0, \sigma_x^2)$, the clipped TD O-OFDM signal, $x^{\mathrm{c}}(n)$, follows a truncated Gaussian distribution, referred as $p(x^{\mathrm{c}}(n))$. For DCO-OFDM, the distribution of $x^{\mathrm{c}}(n)$ is Gaussian; with positive and negative tails clipped at ξ_{lower} and ξ_{upper}, respectively. Whereas, for ACO-OFDM, $x^{\mathrm{c}}(n)$ follows a Gaussian distribution with positive tail clipped at ξ_{upper} and clipped negative side, since $\xi_{\text{lower}} = 0$. (3.11) and (3.12) follow from (3.3) and (3.4), respectively, thus, $p(x^{\mathrm{c}}(n))$ for DCO-OFDM and ACO-OFDM is given as:

$$p(x^{\mathrm{c}}(n)) = \begin{cases} \frac{1}{2}\mathrm{erfc}\left(\frac{\xi_{\text{upper}}}{\sigma_x\sqrt{2}}\right)\delta(x^{\mathrm{c}}(n) - \xi_{\text{upper}}), & x^{c}(n) \geq \xi_{\text{upper}} \\ \frac{1}{\sigma_x\sqrt{2\pi}}\exp\left(-\frac{x(n)^2}{2\sigma_x^2}\right), & -\xi_{\text{upper}} < x^{c}(n) < \xi_{\text{upper}} \\ \frac{1}{2}\mathrm{erfc}\left(\frac{\xi_{\text{upper}}}{\sigma_x\sqrt{2}}\right)\delta(x^{\mathrm{c}}(n) + \xi_{\text{upper}}), & x^{c}(n) \leq -\xi_{\text{upper}} \end{cases} \tag{3.11}$$

and

$$p(x^{\mathrm{c}}(n)) = \begin{cases} \frac{1}{2}\mathrm{erfc}\left(\frac{\xi_{\text{upper}}}{\sigma_x\sqrt{2}}\right)\delta(x^{\mathrm{c}}(n) - \xi_{\text{upper}}), & x^{c}(n) \geq \xi_{\text{upper}} \\ \frac{1}{\sigma_x\sqrt{2\pi}}\exp\left(-\frac{x(n)^2}{2\sigma_x^2}\right), & 0 < x^{c}(n) < \xi_{\text{upper}} \\ \frac{1}{2}\delta(x^{\mathrm{c}}(n)), & x^{c}(n) \leq 0 \end{cases}, \tag{3.12}$$

where $\mathrm{erfc}(\psi)$ is the complementary error function given as:

$$\mathrm{erfc}(\psi) = 1 - \mathrm{erf}(\psi), \tag{3.13}$$

with

$$\mathrm{erf}(\psi) = 2/\sqrt{\pi}\int_0^{\psi}\exp(-t^2)\mathrm{d}t, \tag{3.14}$$

and $\delta(\cdot)$ is the Dirac distribution. Refer to Fig. 3.3 for an illustration of $p(x^{\mathrm{c}}(n))$ for clipped DCO- and ACO-OFDM. Dirac distribution, $\delta(\cdot)$, appears at the clipping thresholds and is multiplied by the probability of the samples to be clipped.

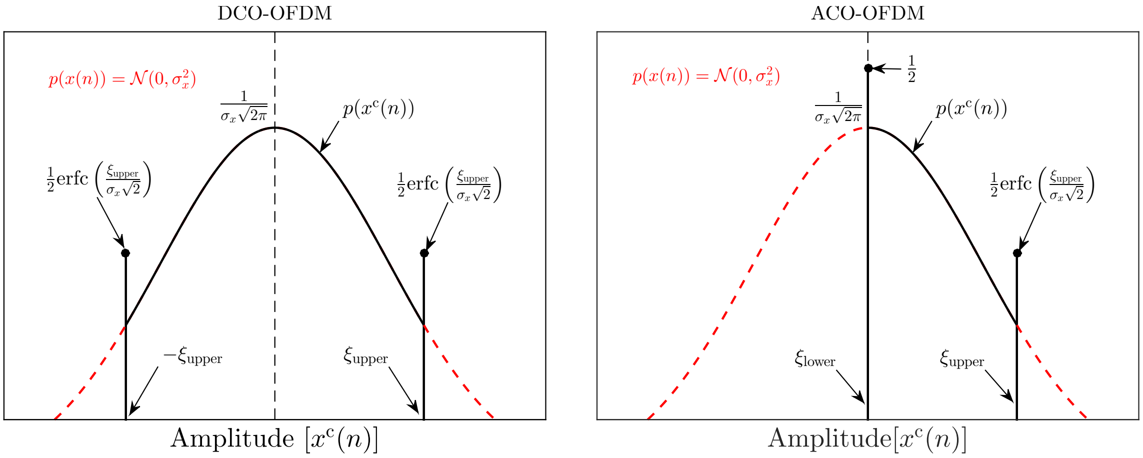

FIGURE 3.3: An illustration of probability density function, $p(x^{\mathrm{c}}(n))$ of clipped DCO- and ACO-OFDM. Solid line represents the distribution of clipped DCO- and ACO-OFDM while the dashed line represents the Gaussian distribution of unclipped DCO- and ACO-OFDM.

The power of clipped O-OFDM, $\sigma_{x^c}^2 = E\left(|x^c(n)|^2\right)$ is attained after integration by parts from the distributions of DCO-OFDM and ACO-OFDM given in (3.11) and (3.12) as:

$$\begin{aligned}\sigma_{x^c}^2 &= 2\int_0^{\xi_{\text{upper}}} \frac{x^2}{\sigma_x\sqrt{2\pi}} \exp\left(-\frac{x^2}{2\sigma_x^2}\right) \mathrm{d}x + \xi_{\text{upper}}^2 \operatorname{erfc}\left(\frac{\xi_{\text{upper}}}{\sigma_x\sqrt{2}}\right) \\ &= \sigma_x^2\left[1 - \sqrt{\frac{2}{\pi}}\gamma \exp\left(-\frac{\gamma^2}{2}\right) - (1-\gamma^2)\operatorname{erfc}\left(\frac{\gamma}{\sqrt{2}}\right)\right],\end{aligned} \tag{3.15}$$

where $\xi_{\text{upper}} = \gamma\sigma_x$ and

$$\begin{aligned}\sigma_{x^c}^2 &= \int_0^{\xi_{\text{upper}}} \frac{x^2}{\sigma_x\sqrt{2\pi}} \exp\left(-\frac{x^2}{2\sigma_x^2}\right) \mathrm{d}x + \frac{\xi_{\text{upper}}^2}{2} \operatorname{erfc}\left(\frac{\xi_{\text{upper}}}{\sigma_x\sqrt{2}}\right) \\ &= \frac{\sigma_x^2}{2}\left[1 - \sqrt{\frac{2}{\pi}}\gamma \exp\left(-\frac{\gamma^2}{2}\right) - (1-\gamma^2)\operatorname{erfc}\left(\frac{\gamma}{\sqrt{2}}\right)\right],\end{aligned} \tag{3.16}$$

respectively.

Moreover, α in (3.5) is evaluated by exploiting the Bussgang Theorem [144] as:

$$\alpha = \frac{\operatorname{cov}\left[x(n), x^c(n)\right]}{\sigma_x^2} = \frac{1}{2}\operatorname{erf}\left(\frac{\xi_{\text{upper}}}{\sigma_x\sqrt{2}}\right) - \frac{1}{2}\operatorname{erf}\left(\frac{\xi_{\text{lower}}}{\sigma_x\sqrt{2}}\right). \tag{3.17}$$

Precisely, α indicates the shrinkage of the signal amplitude due to clipping. From (3.17), the power dissipation owing to the attenuation factor, α^2, for DCO-OFDM and ACO-OFDM is given as:

$$\alpha^2 = \begin{cases} \operatorname{erf}^2\left(\frac{\gamma}{\sqrt{2}}\right), & \text{DCO-OFDM} \\ \frac{1}{4}\operatorname{erf}^2\left(\frac{\gamma}{\sqrt{2}}\right), & \text{ACO-OFDM.} \end{cases} \tag{3.18}$$

Owing to (3.5), the modified power of the TD signal O-OFDM signal is

$$\sigma_{x^c}^2 = \alpha^2\sigma_x^2 + \sigma_{\text{d}}^2, \tag{3.19}$$

where σ_{d}^2 is the power of instigated distortions, i.e., $\sigma_{\text{d}}^2 = E\left(|d(n)|^2\right)$. For DCO-OFDM, the distortions incur due to clipping of the TD signal, accordingly, the power of clipping distortion is $\sigma_{\text{d}}^2 = \sigma_{\text{c}}^2$. Whereas, for ACO-OFDM, the distortions are brought about due to clipping and DC component induced by the clipping process. The DC component is inconsequential to the clipping noise variance on the data-carrying subcarriers. So, for ACO-OFDM, we have $\sigma_{\text{d}}^2 = \sigma_{\text{c}}^2 + \sigma_{\text{DC}}^2$, where σ_{DC}^2 is the power of the DC component. Thus, the power of clipping distortion for DCO- and ACO-OFDM is given as:

$$\begin{aligned}\sigma_{\text{c}}^2 &= \sigma_{x^c}^2 - \alpha^2\sigma_x^2 \\ &= \sigma_x^2\left[1 - \operatorname{erf}^2\left(\frac{\gamma}{\sqrt{2}}\right) - \sqrt{\frac{2}{\pi}}\gamma \exp\left(-\frac{\gamma^2}{2}\right) - (1-\gamma^2)\operatorname{erfc}\left(\frac{\gamma}{\sqrt{2}}\right)\right],\end{aligned} \tag{3.20}$$

and

$$
\begin{aligned}
\sigma_{\mathrm{c}}^2 &= \sigma_{x^{\mathrm{c}}}^2 - \alpha^2\sigma_x^2 - \sigma_{\mathrm{DC}}^2 \\
&= \frac{\sigma_x^2}{2}\left[1 - \frac{1}{2}\mathrm{erf}^2\left(\frac{\gamma}{\sqrt{2}}\right) - \sqrt{\frac{2}{\pi}}\gamma\exp\left(-\frac{\gamma^2}{2}\right) - (1-\gamma^2)\mathrm{erfc}\left(\frac{\gamma}{\sqrt{2}}\right)\right] - \underbrace{\left\{\int_0^{\zeta_{\mathrm{upper}}} x^{\mathrm{c}}(n)p(x^{\mathrm{c}})\mathrm{d}x^{\mathrm{c}}\right\}^2}_{:=\text{DC Component}} \\
&= \frac{\sigma_x^2}{2}\left[1 - \frac{1}{2}\mathrm{erf}^2\left(\frac{\gamma}{\sqrt{2}}\right) - \frac{1}{\pi}\left\{1 - \exp\left(-\frac{\gamma^2}{2}\right)\right\}^2 - \sqrt{\frac{2}{\pi}}\gamma\exp\left(-\frac{\gamma^2}{2}\right) - (1-\gamma^2)\mathrm{erfc}\left(\frac{\gamma}{\sqrt{2}}\right)\right],
\end{aligned}
\tag{3.21}
$$

respectively. α and σ_{c}^2 are independent of the QAM alphabet size, M, and the IDFT/DFT order, (assumed equal to N), however, both are a function of γ.

Using (3.20), (3.21), considering the impact of an AWGN and perfect equalization, an analytical expression for electrical SNR per bit Γ_{elec} can be derived as:

$$
\Gamma_{\mathrm{elec}} = \frac{\alpha^2\sigma_x^2/\zeta_{\mathrm{B}}}{\sigma_{\mathrm{c}}^2 + N_0\zeta_{\mathrm{B}}/\zeta_{\mathrm{DC}}},
\tag{3.22}
$$

when the power of the enabled subcarriers is scaled to $\sigma_x^2/\zeta_{\mathrm{B}}$, where ζ_{B} is the utilization factor of double sided bandwidth B is defined as:

$$
\zeta_{\mathrm{B}} = \begin{cases} \frac{N-2}{N}, & \text{for DCO-OFDM} \\ \frac{1}{2}, & \text{for ACO-OFDM} \end{cases}.
\tag{3.23}
$$

ζ_{DC} is the attenuation of the useful electrical signal power due to the bias-index and is given as:

$$
\zeta_{\mathrm{DC}} = \begin{cases} \frac{1}{1+\gamma^2}, & \text{for DCO-OFDM} \\ 1, & \text{for ACO-OFDM} \end{cases}.
\tag{3.24}
$$

$\zeta_{\mathrm{DC}} = 1$ for ACO-OFDM, reflects the fact that no bias is contemplated. (3.22) describes the ratio between the attenuated signal power and total noise power per symbol. Once Γ_{elec} is appraised using (3.22), approximate closed-form expression for the BER performance of M-ary QAM in AWGN is exploited to evaluate the BER behaviour of O-OFDM under different clipping conditions. The analytical expression for the BER is given as [146]:

$$
\mathrm{BER} \cong \frac{\sqrt{M}-1}{\sqrt{M}\log_2\left(\sqrt{M}\right)}\mathrm{erfc}\left(\sqrt{\Gamma_{\mathrm{elec}}}\right) + \frac{\sqrt{M}-2}{\sqrt{M}\log_2\left(\sqrt{M}\right)}\mathrm{erfc}\left(3\sqrt{\Gamma_{\mathrm{elec}}}\right).
\tag{3.25}
$$

Hereafter, we refer to the model described in this section as *analytical model*.

3.6 Proposed Clipping Mitigation Techniques

Two iterative decision-directed methods for PAPR reduction, more precisely for clipping distortion mitigation of O-OFDM are presented in this section. A block diagram describing how the proposed methods can be employed in an O-OFDM system is given in Fig. 3.4.

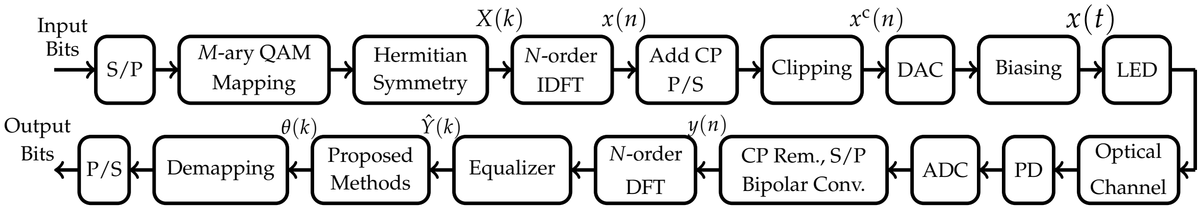

FIGURE 3.4: Block diagram of an O-OFDM system explaining how the proposed iterative decision-directed methods can be employed.

3.6.1 Concept of the Proposed Methods

The concept of the proposed methods is that if the non-linear peculiarities of the transmitter are known at the receiver, the non-linear distortions can be perceived as a deterministic function of the received data, and accordingly, can be reduced. TDCSR restores the altered samples iteratively in the TD, whereas FDCDR determines the distortion instigated due to clipping and mitigates it iteratively in the FD. Both of these methods are based on peak regrowth phenomenon. It is a process of making *hard decisions* on the received data followed by an IDFT; in the resulting TD signal, the clipped samples exhibit peak regrowth, which is exploited to mitigate the clipping distortion in TD or FD with TDCSR and FDCDR, respectively. A graphical illustration of the peak regrowth process is portrayed in Fig. 3.5.

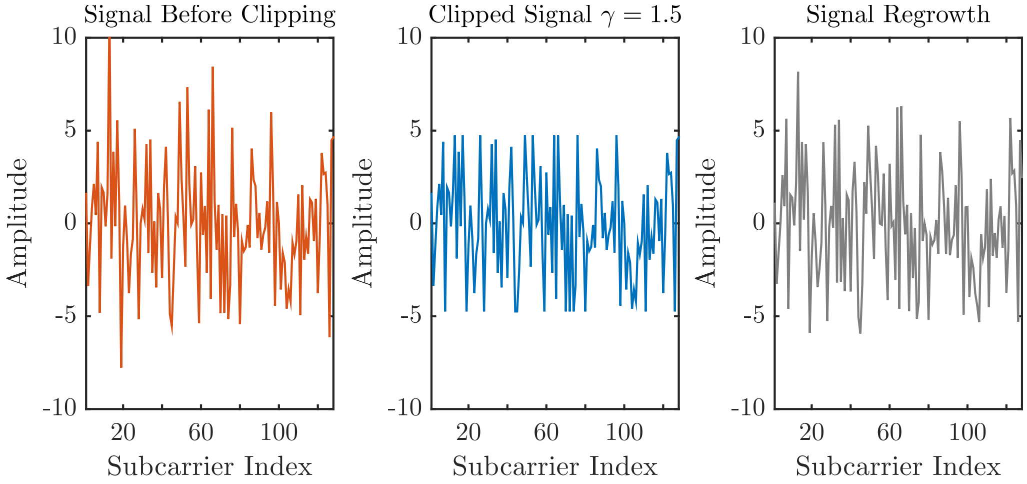

FIGURE 3.5: Illustration of peak regrowth (noiseless scenario) of clipped samples. DCO-OFDM with 16-QAM constellation and $N = 128$ is used.

3.6.2 Conditions for Clipping Mitigation

Prior to clipping mitigation, following conditions have to be satisfied:

- For DCO-OFDM, the DC component has to be eliminated. This is done by removing the bias from the received unipolar signal or by setting $\hat{X}(0) = 0$.
- For ACO-OFDM, the anti-symmetric property is exploited on to retrieve the negative samples that have been clipped during the zero-level clipping process at the transmitter. Another forthright

approach is to multiply the received signal by 2 prior to feeding the received data to the clipping mitigation methods.

- In case of dispersive channel, the equalized signal at the receiver should be the input for clipping mitigation.
- For DCO-OFDM, the minimum clipping threshold for 4-, 16-, 64- and 256-QAM at which TDCSR and FDCDR can work is recommended to be 1, 1.4, 1.9 and 2.5, respectively. For ACO-OFDM, minimum clipping threshold of 0.7, 1.1, 1.6 and 2.3 can be employed for 4-, 16-, 64- and 256-QAM alphabets, respectively. The minimum clipping threshold for TDCSR and FDCDR is determined by performing simulations with a broad variety of systems setup, and considering a target BER of 10^{-3} (at which the Forward Error Correcting (FEC) codes can be implemented) and 3 iterations of the iterative structure. Once the recommended range is determined, a clipping threshold within the recommended range can be considered for the simulations. Note that these values of clipping threshold may differ for different BER and number of iterations.

3.6.3 Time-Domain Clipped Sample Reconstruction (TDCSR)

In TDCSR, clipping is mitigated by reconstructing the affected samples in the TD. The iterative structure of TDCSR is presented in Fig. 3.6, and the iterative process is presented as follows:

1. The reference TD signal, $\hat{r}(n)$, is obtained from the set of received FD equalized symbols, $\hat{Y}(k)$, as $\hat{r}(n) = \text{IDFT}\{\hat{Y}(k)\}$, and is subsequently buffered. This step is executed once, accordingly, it is not a part of the iterative structure of TDCSR illustrated in Fig. 3.6.
2. Decisions for the ith iteration are made on $\theta^{(i)}(k)$ to achieve a set of retrieved symbols, $\hat{\theta}^{(i)}(k) = \text{Slicer}\{\theta^{(i)}(k)\}$, where $\text{Slicer}\{\cdot\}$ describes a hard symbol estimator. For the first iteration, $i = 1$, $\theta^{(1)}(k) = \hat{Y}(k)$, i.e., the set of received FD symbols, $\hat{Y}(k)$, are used to seed the TDCSR iterative process.
3. $\hat{\theta}^{(i)}(k)$ are transformed to TD to obtain an expected O-OFDM signal, $\hat{s}^{(i)}(n)$, which is appraised as $\hat{s}^{(i)}(n) = \text{IDFT}\{\hat{\theta}^{(i)}(k)\}$. This transformation of $\hat{\theta}^{(i)}(k)$ to $\hat{s}^{(i)}(n)$ alleviates the clipping noise because of the peak regrowth of clipped samples in $\hat{s}^{(i)}(n)$. This peak regrowth in $\hat{s}^{(i)}(n)$ is exploited to reconstruct the affected clipped samples in $\hat{r}(n)$.
4. The clipped samples in $\hat{r}(n)$ are identified by recreating an identical clipping process as at the transmitter, acknowledging that clipping threshold, γ, is known at the receiver.
5. The clipped samples in $\hat{r}(n)$, are swapped with corresponding samples from $\hat{s}^{(i)}(n)$, resulting in a reconstructed TD O-OFDM signal, $\tilde{r}^{(i)}(n)$, given by:

$$\tilde{r}^{(i)}(n) = \begin{cases} \hat{s}^{(i)}(n) & \hat{s}^{(i)}(n) > \xi_{\text{upper}} \\ \hat{r}(n) & \xi_{\text{lower}} \leq \hat{s}^{(i)}(n) \leq \xi_{\text{upper}} \\ \hat{s}^{(i)}(n) & \hat{s}^{(i)}(n) < \xi_{\text{lower}} \end{cases} . \tag{3.26}$$

6. The reconstructed TD O-OFDM signal, $\tilde{r}^{(i)}(n)$, is transformed to FD as $\theta_r^{(i)}(k) = \text{DFT}\{\tilde{r}^{(i)}(n)\}$, following in a different set of reconstructed symbols, $\theta_r^{(i)}(k)$.

7. Iteration counter is increased, $i = i+1$, and $\theta^{(i)}(k)$ is updated as $\theta^{(i)}(k) = \theta_r^{(i-1)}(k)$; which are operated as an input for the succeeding iteration to further improve the TD reconstruction process.

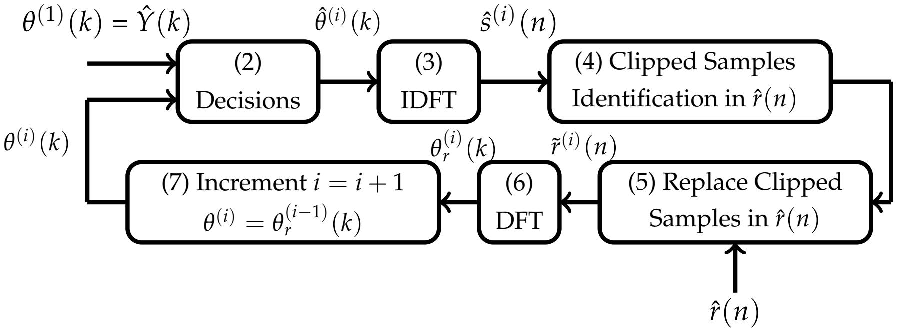

FIGURE 3.6: Iterative structure for time-domain clipped sample reconstruction (TDCSR).

3.6.4 Frequency-Domain Clipping Distortion Removal (FDCDR)

In FDCDR, clipping mitigation is achieved by clipping distortion cancellation in the FD. The iterative structure for FDCDR is presented in Fig. 3.7, and the technique is described as follows:

1. Decisions for the ith iteration are made on $\theta^{(i)}(k)$, to achieve a set of retrieved symbols, $\hat{\theta}^{(i)}(k) = \text{Slicer}\{\theta^{(i)}(k)\}$. For the first iteration, $i = 1$, which seeds the algorithm, clipping distortion contribution in the FD is disregarded, i.e., $D^{(1)}(k) = 0$, and the received FD symbols, $\hat{Y}(k)$, are used as an input to the FDCDR iterative process, i.e., $\theta^{(1)}(k) = \hat{Y}(k)$.
2. An estimated TD O-OFDM signal, $\hat{s}^{(i)}(n)$, is evaluated via $\hat{s}^{(i)}(n) = \text{IDFT}\{\hat{\theta}^{(i)}(k)\}$.
3. Considering that the clipping threshold is known at the receiver, $\hat{s}^{(i)}(n)$ are administered to an identical clipping process as at the transmitter to generate a clipped TD O-OFDM signal, $\hat{c}^{(i)}(n)$.
4. The clipped version of $\hat{\theta}^{(i)}(k)$, $\hat{\theta}_c^{(i)}(k)$, is achieved as $\hat{\theta}_c^{(i)}(k) = \text{DFT}\{\hat{c}^{(i)}(n)\}$. By mimicking a similar clipping process as at the transmitter (Fig. 3.5), a distortion, contribution in the FD, $D^{(i)}(k)$, comparable to the one introduced at the transmitter is now instigated in $\hat{\theta}_c^{(i)}(k)$, where $\hat{\theta}_c^{(i)}(k) = \hat{\theta}^{(i)}(k) + D^{(i)}(k)$.
5. An estimate of the clipping distortion, $D^{(i)}(k)$, is made by subtracting $\hat{\theta}^{(i)}(k)$ from $\hat{\theta}_c^{(i)}(k)$, as $D^{(i)}(k) = \hat{\theta}_c^{(i)}(k) - \hat{\theta}^{(i)}(k)$.
6. Iteration counter is raised $i = i+1$.
7. The input for the subsequent iteration is updated as $\theta^{(i)}(k) = \theta^{(i-1)}(k) - D^{(i-1)}(k)$, i.e., by getting rid of the expected clipping distortion from the set of retrieved symbols.
8. Updated $\theta^{(i)}(k)$ is employed in subsequent iteration to attain an improved estimate of the clipping distortion.

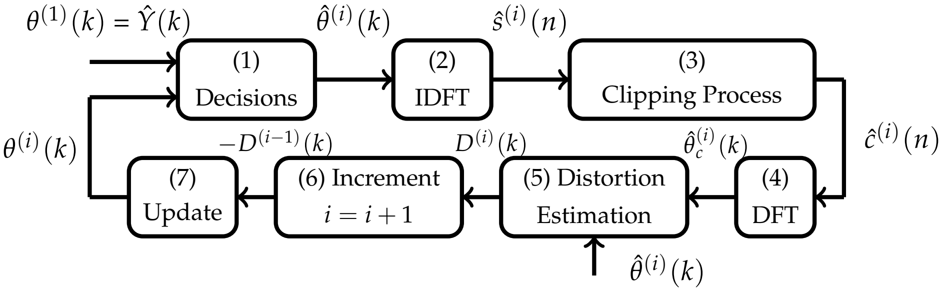

FIGURE 3.7: Iterative structure for frequency-domain clipping distortion removal (FDCDR).

3.7 Performance evaluation of TDCSR and FDCDR

In this section, simulation results are presented to validate and compare the performance of the proposed TDCSR and FDCDR techniques with other PAPR reduction methods available in the literature, such as SLM [132] and techniques which embody inherently low PAPR, e.g., FTP-ACO-OFDM [119, 94, 120]. Unless otherwise specified, 16−QAM alphabet is used (64− and 256−QAM are acknowledged for power efficiency analysis). 1024 subcarriers and 2000 independent realizations are considered for simulation results. Performance of the proposed methods is assessed considering 3 iterations. Simulations are carried out to evaluate BER in AWGN channel, considering uniform quantization and also by varying the number of iterations. Complementary cumulative distribution function (CCDF) curves are presented to illustrate the PAPR of the clipped O-OFDM signals. Further, power efficiency is evaluated if TDCSR and FDCDR are employed for DCO-OFDM and ACO-OFDM and is compared with power efficiencies of conventional DCO-OFDM, ACO-OFDM (without clipping), SLM and FTP-ACO-OFDM.

3.7.1 Bit error rate performance

Firstly, BER performance for DCO-OFDM employing TDCSR and FDCDR and clipping thresholds of 1.5 and 1.8 is evaluated and is portrayed in Fig. 3.8 and Fig. 3.9, respectively. The results are compared with SLM using $U = 128$. The number of phase sequences for SLM is significant, therefore, the performance illustrated here can be regarded as an upper-bound on the schemes performance. DCO-OFDM (without clipping) with $\beta_{\mathrm{DC}}^{(\mathrm{D})} = 7$ dB is adopted as benchmark. Analytical BER is presented to corroborate the simulation model for clipped DCO-OFDM. It may be noticed that once clipping has been alleviated using TDCSR and FDCDR, there is a substantial improvement in BER for both methods over conventional DCO-OFDM. The gain in BER is because after clipping the bias, $\beta_{\mathrm{DC}}^{(\mathrm{D})}$ is lowered from 7 dB to 5.1 dB for $\gamma = 1.5$, and from 7 dB to 6.3 dB for $\gamma = 1.8$. The performance of FDCDR is better than for TDCSR. Whereas, a marginal gain is observed for TDCSR over SLM for BER $\leq 10^{-3}$ and $\gamma = 1.5$. This gain is more significant for FDCDR over SLM for $\gamma = 1.5$. The enhancement in SLM performance is due to the fact that when $\beta_{\mathrm{DC}}^{(\mathrm{D})} = 7$ dB is used, then, after PAPR reduction, the number of clipped samples after the addition of the bias-index are less compared to conventional DCO-OFDM.

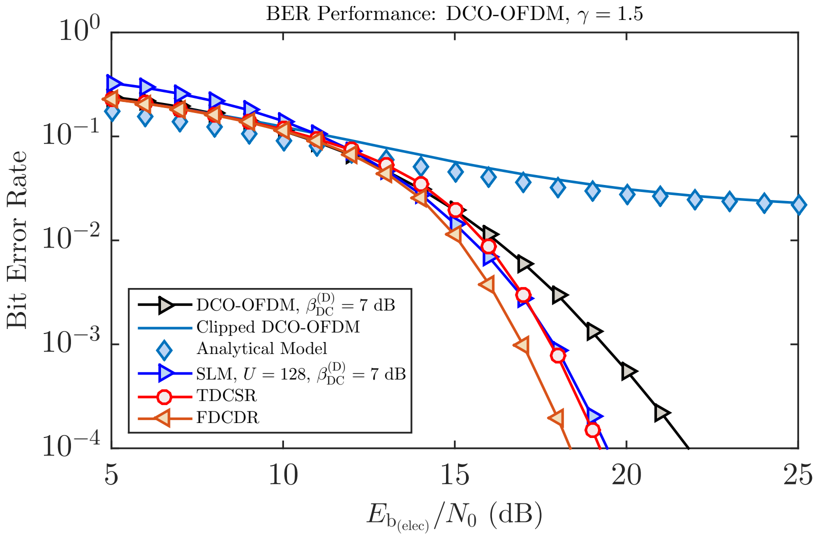

FIGURE 3.8: BER comparison of clipped DCO-OFDM, clipped DCO-OFDM with clipping mitigation using TDCSR and FDCDR, and SLM with $U = 128$ for 16-QAM constellation, $N = 1024$ and $\gamma = 1.5$.

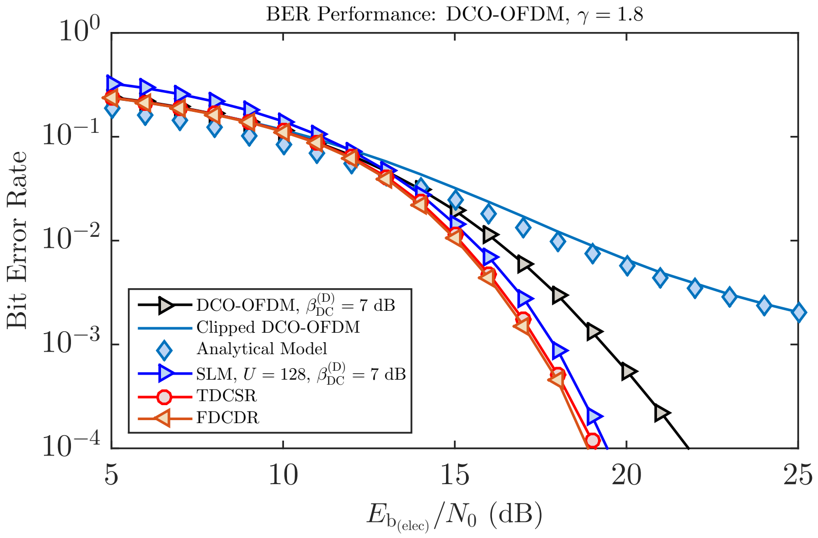

FIGURE 3.9: BER comparison of clipped DCO-OFDM, clipped DCO-OFDM with clipping mitigation using TDCSR and FDCDR, and SLM with $U = 128$ for 16-QAM constellation, $N = 1024$ and $\gamma = 1.8$.

The BER performance of ACO-OFDM using TDCSR and FDCDR is depicted in Fig. 3.10 and Fig. 3.11 for clipping thresholds of1.2 and 1.3, respectively. BER performance of conventional ACO-OFDM is presented as reference. For comparison, FTP-ACO-OFDM and SLM with $U = 128$ are analyzed. The estimated BER from the analytical model is provided to substantiate the clipping model used for simulations. Compared to the BER performance of FTP-ACO-OFDM and SLM, TDCSR demonstrates a comparable performance, howbeit, a marginal performance loss is observed for FDCDR. It should be recognized that in practical scenarios, clipping is appropriated for both ACO-OFDM and FTP-ACO-OFDM to fit the TD signal in the limited dynamic range of the LED. So, the performance improvement by adopting the proposed methods for ACO-OFDM could be noteworthy, because, the TD signal is already clipped and could fit the dynamic range of the LED without need of any additional clipping.

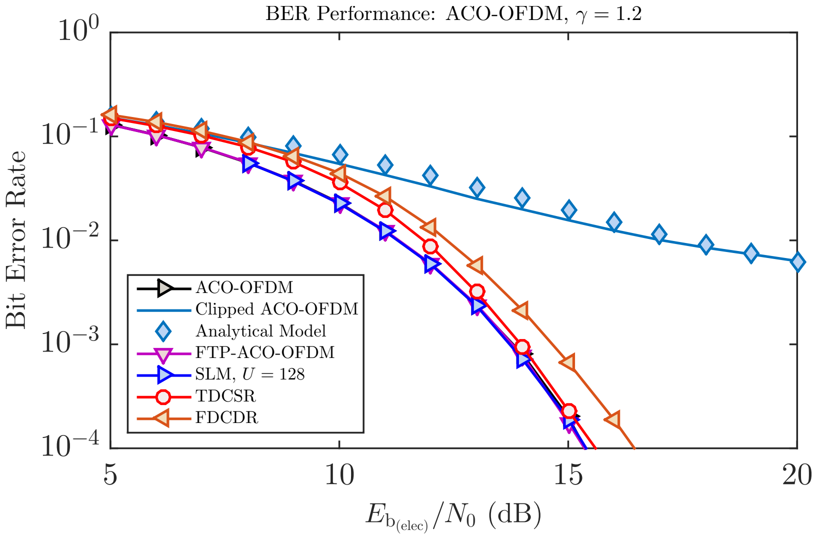

FIGURE 3.10: BER comparison of clipped ACO-OFDM, clipped ACO-OFDM with clipping mitigation using TDCSR and FDCDR, FTP-ACO-OFDM and SLM with $U = 128$ for 16-QAM constellation, $N = 1024$ and $\gamma = 1.2$.

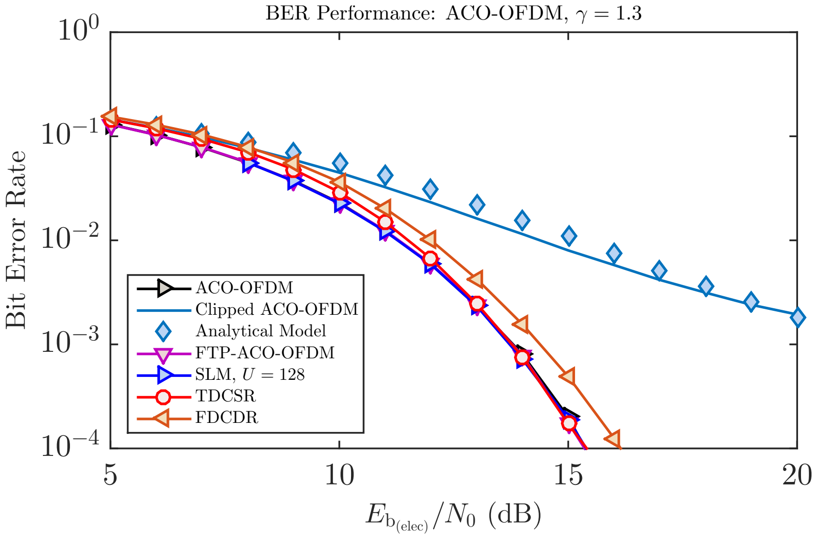

FIGURE 3.11: BER comparison of clipped ACO-OFDM, clipped ACO-OFDM with clipping mitigation using TDCSR and FDCDR, FTP-ACO-OFDM and SLM with $U = 128$ for 16-QAM constellation, $N = 1024$ and $\gamma = 1.3$.

3.7.2 PAPR Analysis

PAPR evaluated using clipping and SLM for DCO-OFDM is presented in Fig. 3.12. It can be observed that the reduction incurred in PAPR by clipping DCO-OFDM is almost equal to 5.4 dB and 4.3 dB for γ equal to 1.5 and 1.8 at CCDF= 0.1, respectively, compared to the case when no clipping is used. Whereas, with SLM, PAPR is lowered by approximately 2.2 dB when $U = 128$ is employed. PAPR reduction for SLM using $U = 6$ (not presented here) is merely 1.3 dB, which is negligible.

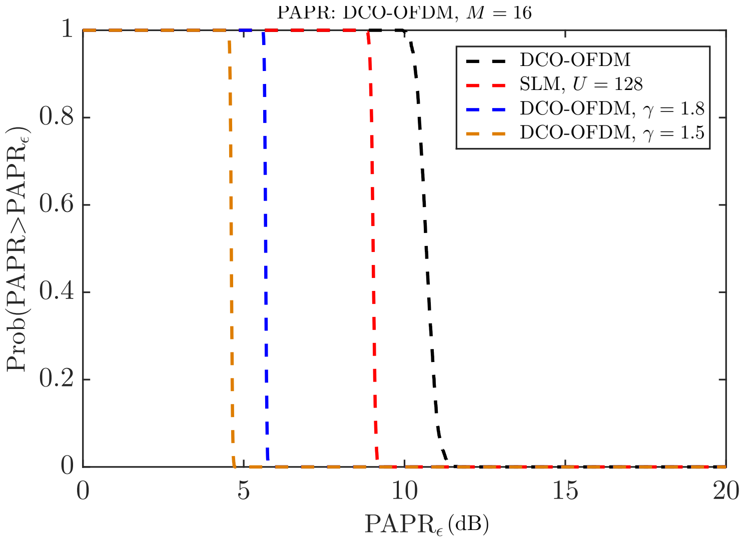

FIGURE 3.12: PAPR comparison of clipped DCO-OFDM, DCO-OFDM and SLM with $U = 128$. γ equal to 1.5 and 1.8 is used for DCO-OFDM.

The PAPR evaluated using clipping and SLM for ACO-OFDM and FTP-ACO-OFDM is shown in Fig. 3.13. The reduction in PAPR is a function of γ, which means that smaller values of γ within the prescribed range could culminate in a substantially lesser PAPR compared to the PAPR reduction obtained using FTP-ACO-OFDM and SLM, as shown in Fig. 3.13. The reduction in PAPR by using clipping compared to when no clipping is used is equal to almost 5.6 dB and 5.3 dB for γ of 1.2 and 1.3, respectively at CCDF$=$ 0.1. Furthermore, the reduction in PAPR for FTP-ACO-OFDM and SLM with $U = 128$ is almost 1.8 dB and 2.3 dB, respectively, compared to state-of-the-art ACO-OFDM. From these results, it can be ascertained that the PAPR reduction using clipping is noteworthy compared to when FTP-ACO-OFDM is used [111, 122]. PAPR reduction is imperative for practical scenarios, where the performance of the system is further restricted by the limited bit resolution of DAC/ADC.

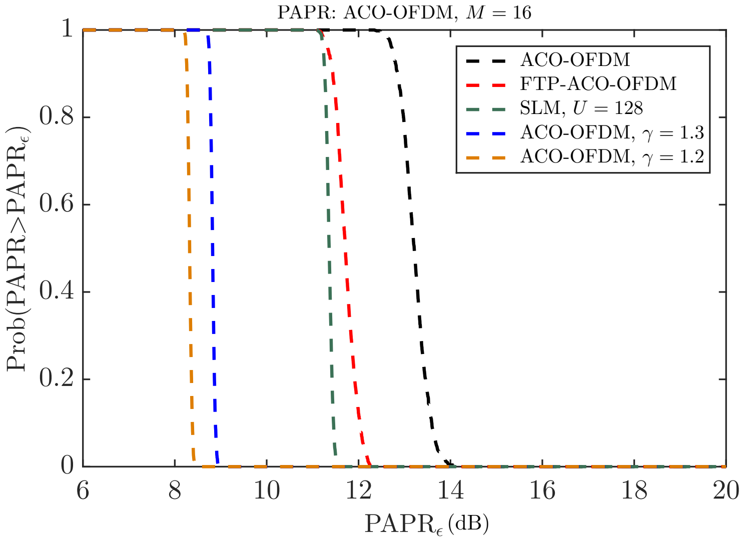

FIGURE 3.13: PAPR comparison of clipped ACO-OFDM, ACO-OFDM, FTP-ACO-OFDM and SLM with $U = 128$. γ equal to 1.2 and 1.3 is used for clipped ACO-OFDM.

3.7.3 Bit error rate analysis considering impairment from DAC quantization noise

Digital to analog conversion might induce significant quantization distortion depending on signal PAPR. To evaluate the performance considering quantization noise, DAC with uniform quantization and Q_b effective number of bits (ENOB) defining $\mathcal{L} = 2^{Q_b}$ quantization levels is considered. The resolution or step-size, μ, of the quantizer, which is the difference between two adjacent quantization levels is given as $\mu = \triangle\xi/2^{Q_b}$, where $\triangle\xi = \xi_{\text{upper}} - \xi_{\text{lower}}$ is the signal amplitude dynamic. The quantization noise for clipped O-OFDM is modeled as an additive, uniformly distributed white noise, with variance of [147]:

$$\sigma^2_{\text{DAC}} = \frac{\alpha\mu^2}{12} \tag{3.27}$$

where α integrates the attenuation due to signal clipping (3.17). (3.27) implies that signal clipping can lessen the quantization noise because $\triangle\xi$ is decreased. Based on the signal clipping defined in (3.15) and (3.16), the variance of quantization noise for DCO-OFDM and ACO-OFDM is respectively given as:

$$\sigma^2_{\text{DAC}} = \begin{cases} \frac{\alpha\xi^2_{\text{upper}}}{3(2^{2Q_b})}, & \text{for DCO-OFDM} \\ \frac{\alpha\xi^2_{\text{upper}}}{12(2^{2Q_b})}, & \text{for ACO-OFDM} \end{cases} \tag{3.28}$$

where $\xi_{\text{upper}} = \gamma\sigma_x$. (3.28) entails that the signal excursion of DCO-OFDM is twice the signal excursion of ACO-OFDM, accordingly, the quantization noise variance for DCO-OFDM is four times greater than ACO-OFDM [147].

The BER performance of TDCSR and FDCDR for DCO-OFDM considering the joint impact of clipping and quantization is presented in Fig. 3.14. γ is equal to 1.5 and Q_b is equal to 5. The number of iterations i for TDCSR and FDCDR are fixed at 3. The performance is compared with SLM ($U = 128$) and conventional DCO-OFDM. For DCO-OFDM and SLM, only quantization noise is recognized and the impact of clipping distortion is disregarded. It is noted that even in the presence of both clipping and quantization noise, the BER performance attained using TDCSR and FDCDR is superior compared to SLM and conventional DCO-OFDM at BER of 10^{-3}. More importantly, the result likewise confirms that if either TDCSR or FDCDR (with signal clipping) is employed for DCO-OFDM, the bit resolution of the DAC can be lowered, unlike conventional DCO-OFDM and SLM, where a high bit resolution DAC might be required. This result is directly linked to the drastic PAPR reduction by clipping combined with signal distortion compensation at the receiver.

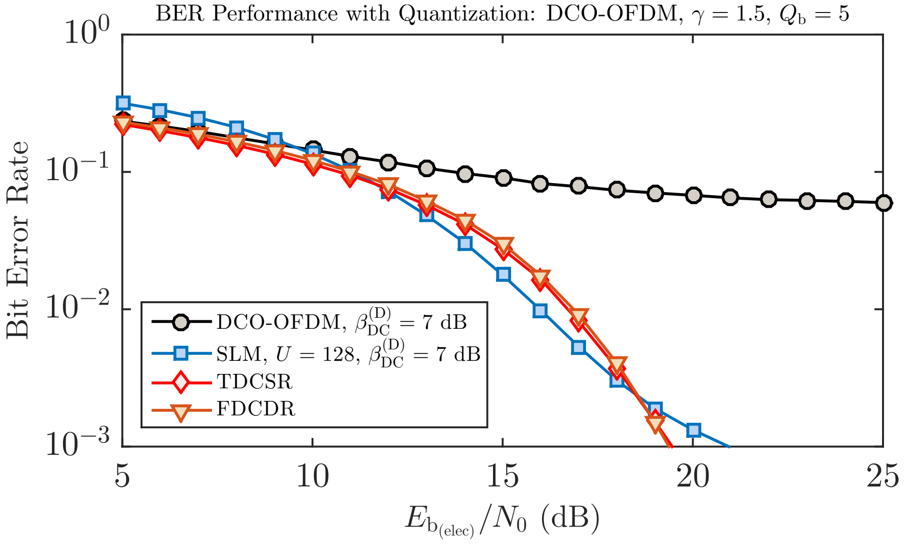

FIGURE 3.14: BER performance of TDCSR and FDCDR considering quantization noise for DCO-OFDM. γ is set equal to 1.5 and Q_b is equal to 5.

The BER performance attained using TDCSR and FDCDR for ACO-OFDM with quantization and clipping is displayed in Fig. 3.15 and is compared with conventional ACO-OFDM and FTP-ACO-OFDM (without clipping). Q_b, γ and i are set equal to 3, 1.2 and 3, respectively. It is observed that the performance of ACO-OFDM and FTP-ACO-OFDM drastically deteriorates in the presence of strong quantization noise, whereas, both TDCSR and FDCDR perform adequately in a similar scenario. It is recalled that the impact of quantization on the clipped signal is less stringent compared to an unclipped signal. However, due to clipping, distortions are instigated. Both TDCDR and FDCDR can effectively reduce the clipping distortion, proceeding in a superior performance. It can be established that for ACO-OFDM if either TDCSR or FDCDR is considered, the bit resolution requirement is less compared to conventional ACO-OFDM or FTP-ACO-OFDM.

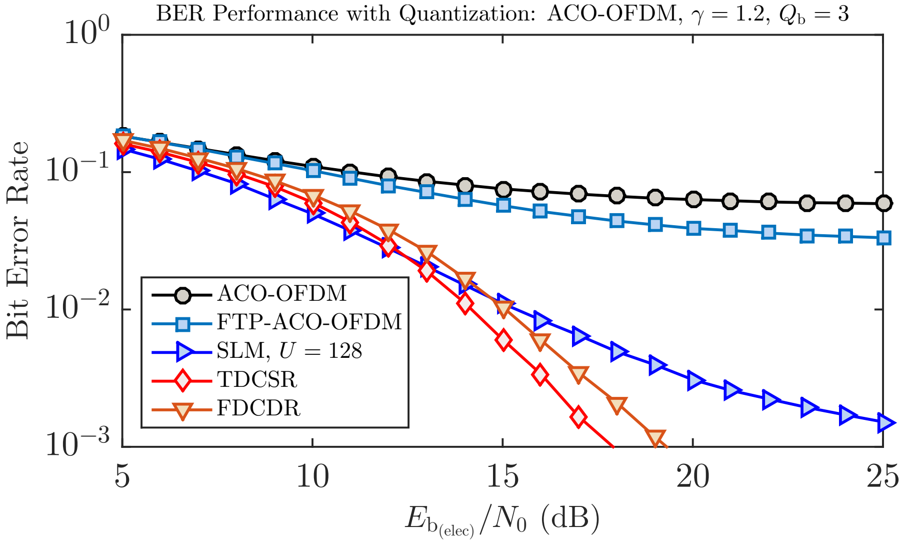

FIGURE 3.15: BER performance of TDCSR and FDCDR considering quantization noise for ACO-OFDM. The clipping ratio, γ is set equal to 1.2, the effective number of bits for quantization, Q_b are set equal to 3.

3.7.4 Bit error rate performance dependance with the number of iterations

Since both TDCSR and FDCDR are iterative, the performance evaluation considering different number of iterations is logical. It is valuable in interpreting the trade-off between the gain in performance and the complexity that can be endured with each increment in iteration. The performance of the TDCSR and FDCDR for DCO-OFDM with $\gamma = 1.5$ for iterations $i = 1 \rightarrow 4$ is illustrated in Fig. 3.16 and Fig. 3.17, respectively.

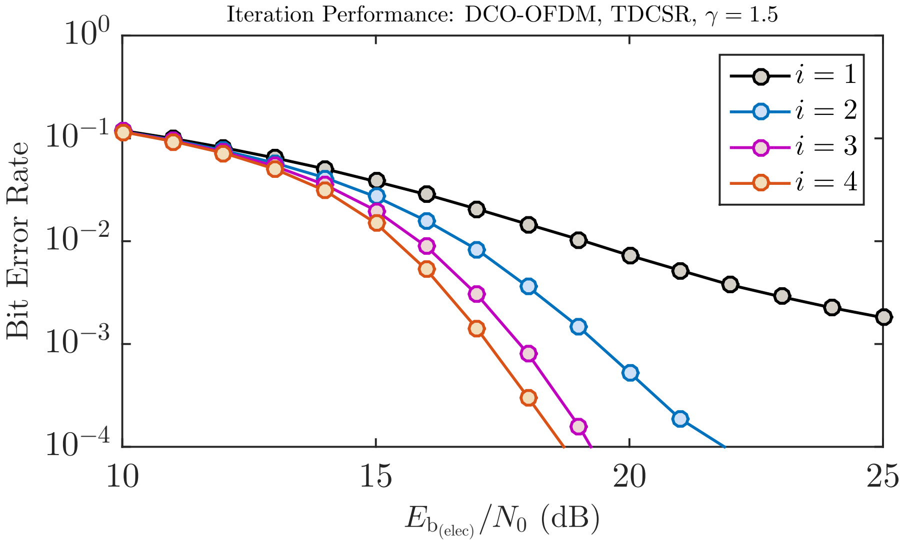

FIGURE 3.16: Performance of TDCSR for DCO-OFDM considering different number of iterations. The clipping ratio, γ, of 1.5 has been used for simulations.

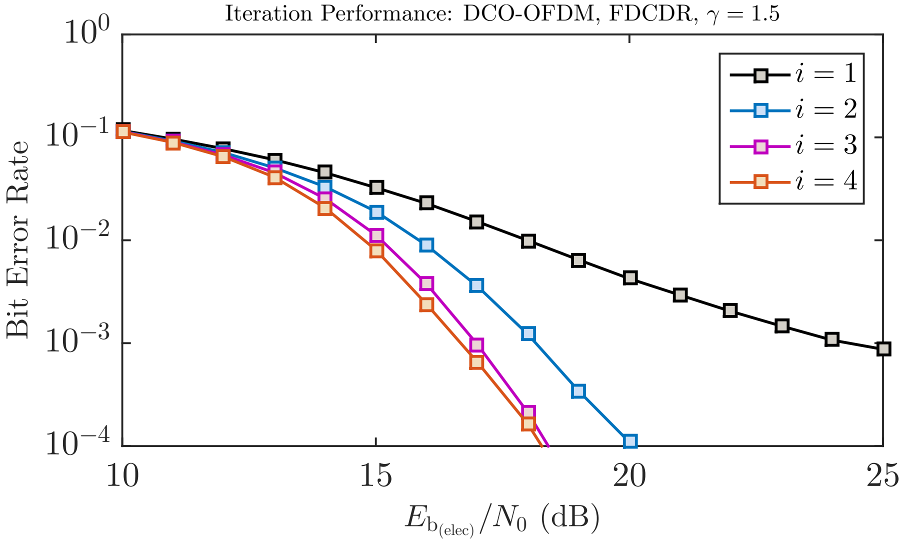

FIGURE 3.17: Performance of FDCDR for DCO-OFDM considering different number of iterations. The clipping ratio, γ, of 1.5 has been used for simulations.

The iteration performance of the proposed methods for ACO-OFDM considering $i = 1 \rightarrow 4$ is depicted in Fig. 3.18 and Fig. 3.19. It is recognized that with each increment in iteration from $i = 1$ to $i = 3$, the performance of proposed methods is increased considerably. However, the gain in performance by increasing the number of iterations to $i = 4$ is marginal but will induce a significant increase in complexity. Accordingly, in simulations, three iterations are used for TDCSR and FDCDR.

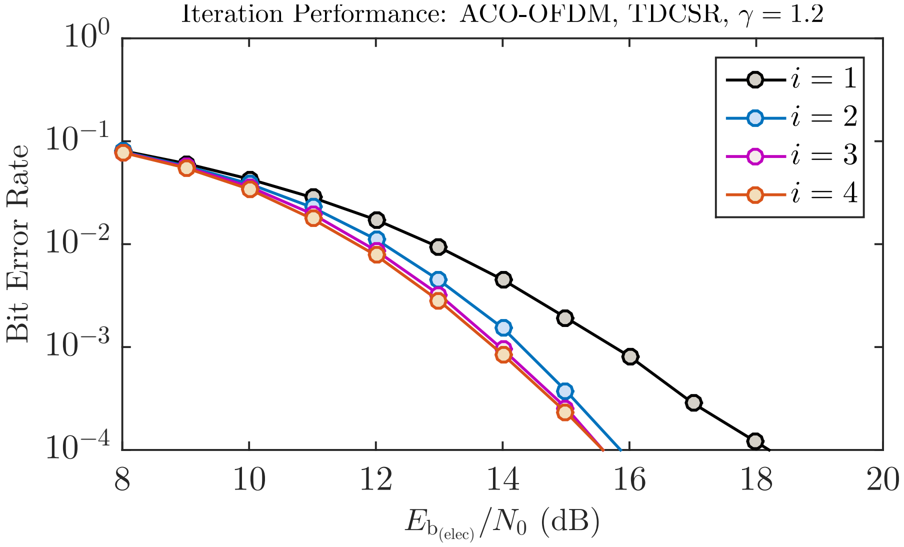

FIGURE 3.18: Performance of TDCSR for ACO-OFDM considering different number of iterations. The clipping ratio, γ, of 1.2 has been used for simulations.

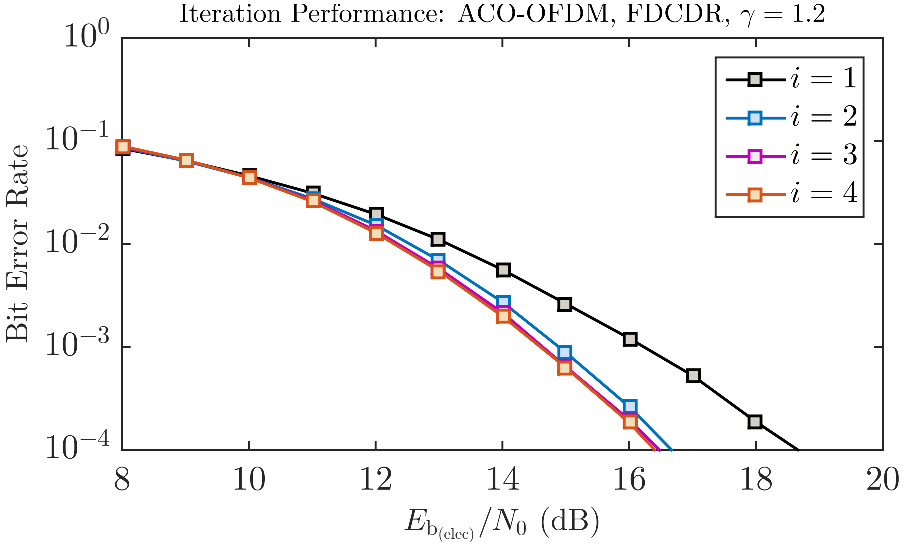

FIGURE 3.19: Performance of FDCDR for ACO-OFDM considering different number of iterations. The clipping ratio, γ, of 1.2 has been used for simulations.

3.7.5 Investigation of power efficiency as a function of spectral efficiency

Fig. 3.20 and Fig. 3.21 depict how $\langle E_{b_{(elec)}}/N_0 \rangle$ (the expected $E_{b_{(elec)}}/N_0$ for a BER of 10^{-3}) alters with SE, η. Note, here, no quantization noise is considered. γ for 16−, 64− and 256−QAM is set equal to 1.5, 2 and 2.7, respectively for DCO-OFDM. Whereas, for ACO-OFDM, γ is equal to 1.2, 1.6 and 2.3 for 16−, 64− and 256−QAM, respectively. Certainly, both TDCSR and FDCDR bring about substantial improvements for DCO-OFDM, whereas, a marginal loss is noticed in case of ACO-OFDM, when compared to conventional ACO-OFDM, FTP-ACO-OFDM and SLM when no clipping is considered. In practical scenarios, the signal for ACO-OFDM and FTP-ACO-OFDM would be clipped (double-sided) to fit the signal in the limited dynamic range of the LED. Thus, in these scenarios, the gain of the proposed approaches would be considerable because BER degradation is foreseen for ACO-OFDM and FTP-ACO-OFDM (Fig. 3.10 and Fig. 3.11). Note that the performance of TDCSR with clipped ACO-OFDM is identical to the performance of conventional ACO-OFDM and FTP-ACO-OFDM, but with a lower PAPR (see Fig. 3.13), which can be beneficial in enhancing the modulation efficiency of the LED. It is worth pointing out that TDCSR suffers from a 4.5 dB $E_{b_{(elec)}}/N_0$ penalty for ACO-OFDM (Fig. 3.21) with 256−QAM. It may come from the fact that for higher order modulations, the symbol error rate is very large to operate on a right decision on the FD symbols, thus, the reconstruction of the FD symbols might no longer be adequate.

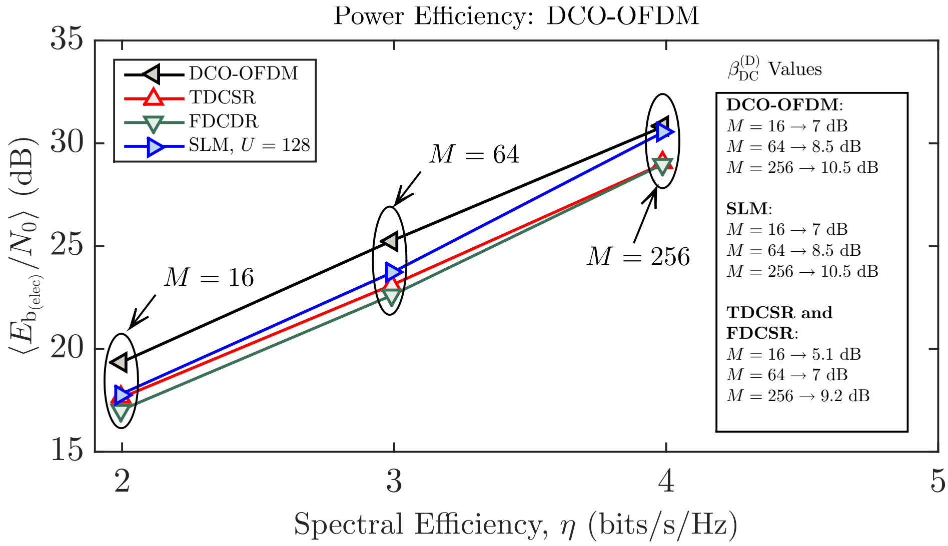

FIGURE 3.20: $\langle E_{b_{(elec)}}/N_0 \rangle$ against η for DCO-OFDM, SLM, and DCO-OFDM with clipping mitigation using 16−, 64− and 256−QAM constellations and $N = 1024$. The bias-index used for each scheme is presented in the inset.

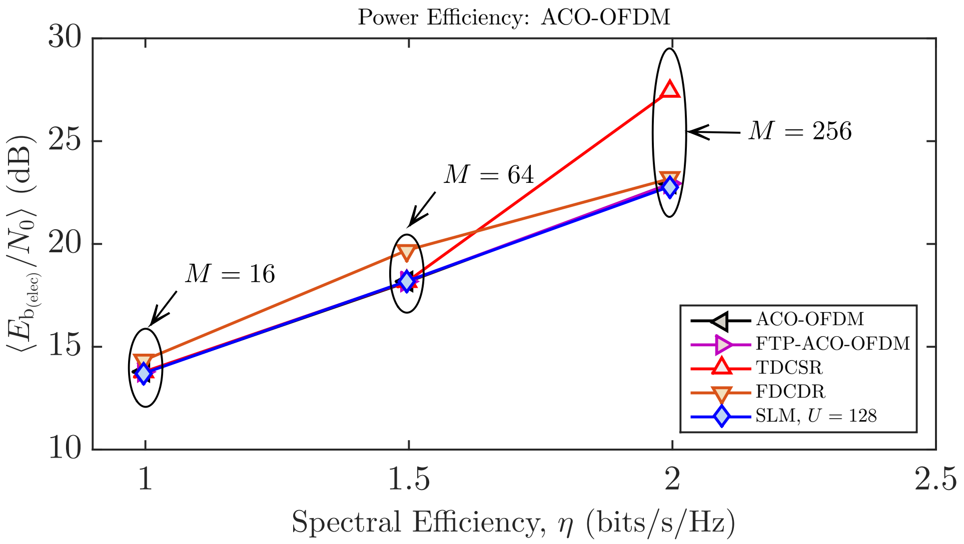

FIGURE 3.21: $\langle E_{b_{(elec)}}/N_0 \rangle$ against η for ACO-OFDM, FTP-ACO-OFDM, SLM and ACO-OFDM with clipping mitigation using 16−, 64− and 256−QAM constellations and $N = 1024$.

3.8 Complexity Analysis

The complexity analysis of the TDCSR and FDCDR in terms of probability of convergence, theoretical run-time boundaries is cumbersome, since the complexity of the problem is directly correlated with the size of DFT/IDFT, N. Hereby, the complexity is calculated be determining the total number of the arithmetic operations needed by each scheme. It is considered that DFT and IDFT are efficiently implemented using fast Fourier transform (FFT) algorithm and inverse FFT (IFFT), respectively. N-order FFT/IFFT requires approximately $4N\log_2(N)$ real arithmetic operations, consisting of multiplications and additions [148]. It is considered that a block of N data-symbols is taken as an input by the transceivers (which is equal to DFT/IDFT order). For O-OFDM, the complexity is due to the FFT/IFFT and equalization. The equalization process can be realized in $\mathcal{O}(N)$ operations, accordingly, in the sequel, we simply consider the complexity incurred due to multiplexing and demultiplexing process by IFFT/FFT. Complexities for the different schemes are evaluated as:

- For DCO-OFDM and ACO-OFDM, N-order IFFT and N-order FFT are required at the transmitter and at the receiver, respectively. This ends up in a total complexity of $8N\log_2(N)$.
- To incorporate SLM with either DCO- or ACO-OFDM, the number of N-order IFFT expected at the transmitter are equal to the number of phase sequences, U. Accordingly, at the transmitter, $4UN\log_2(N)$ arithmetic operations are needed. However, at the receiver one N-order FFT is required. Then, the overall complexity of SLM (with either DCO- or ACO-OFDM) is almost $4(U+1)N\log_2(N)$.
- For FTP-ACO-OFDM, $N/4$-order FFT and N-order IFFT are needed at the transmitter, whereas, at the receiver, FFT/IFFT are reversed, i.e., N-order FFT and $N/4$-order IFFT are needed. Consequently, the total number of the arithmetic operations involved are $10N\log_2(N)$.
- When TDCSR is used for clipping mitigation, no additional operations are required at the transmitter, thus, only one N-order IFFT is need at the transmitter. At the receiver, apart from one N-order FFT needed for TD to FD conversion, N-order FFT and N-order IFFT per iteration are also required. N-order IFFT (step (01) of TDCSR) is also needed. So, the total number of arithmetic operations prescribed for TDCSR are $8(i+1.5)N\log_2(N)$.
- For FDCDR, the transmitter complexity of the system using FDCDR is equal to the conventional O-OFDM. However, at the receiver, N-order FFT and N-order IFFT per iteration are required besides standard N-order FFT. Accordingly, the complexity in terms of number of arithmetic operations is equal to $8(i+1)N\log_2(N)$.

The system complexities are compiled in Table 3.2 and are plotted as a function of N in Fig. 3.22. TDCSR is marginally more complex than FDCDR because of one additional N-order IFFT which is used only once. It is recalled that a considerable number of phase sequences, U, are needed for SLM to significantly counterbalance the high PAPR, consequently, there is a radical increase in the complexity. It has been established in Section 3.7.4 that three iterations of the iterative algorithms are adequate to mitigate the clipping noise, hence, the complexity of TDCSR and FDCDR has been evaluated for $i=3$ and compared with SLM with $U=128$ for which significant PAPR reduction is observed (Fig. 3.12 and Fig. 3.13). From Fig. 3.22 it is confirmed that the complexity of SLM is exponentially greater than both TDCSR and FDCDR. Furthermore, it is ascertained that FTP-ACO-OFDM is somewhat more complex than ACO-OFDM. However, FTP-ACO-OFDM is less complex compared to the case when TDCSR and FDCDR are integrated with either DCO- or ACO-OFDM.

TABLE 3.2: Complexity Comparison of O-OFDM, FTP-ACO-OFDM, SLM, TDCSR and FDCDR

Approach	**Complexity**
O-OFDM	$8N\log_2(N)$
FTP-ACO-OFDM	$10N\log_2(N)-4N$
SLM	$4(U+1)N\log_2(N)$
TDCSR	$8(i+1.5)N\log_2(N)$
FDCDR	$8(i+1)N\log_2(N)$

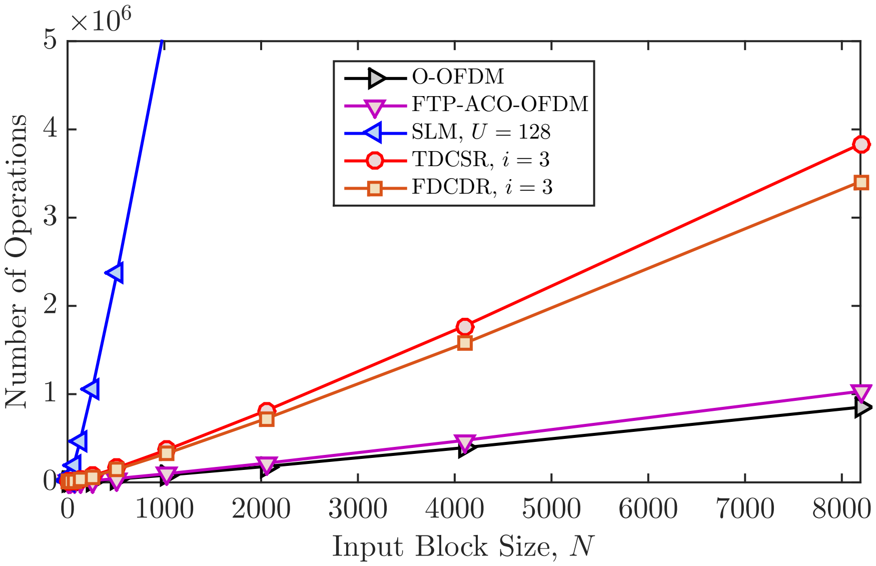

FIGURE 3.22: Complexity comparison of proposed PAPR reduction methods.

3.9 Conclusion

In this work, deliberate clipping is adopted to limit the high peaks of O-OFDM signal to pre-defined threshold in order to reduce O-OFDM PAPR. Two decision-directed iterative methods are proposed to alleviate the distortions instigated because of signal clipping. From this study, it is concluded that:

1. The proposed TDCSR and FDCDR methods can successfully mitigate clipping distortion for both DCO-OFDM and ACO-OFDM.
2. When either TDCSR or FDCDR is operated along with DCO-OFDM, substantial performance gains in terms of optical performance over conventional DCO-OFDM are attained. Howbeit, there exists a marginal performance loss for ACO-OFDM over conventional ACO-OFDM and FTP-ACO-OFDM. It is essential to understand that if clipping is introduced by the LED, a drastic deterioration in performance for conventional ACO-OFDM and FTP-ACO-OFDM is expected. So, in such scenarios, it is foreseen that the performance of proposed methods would be better.

3. The PAPR reduction due to clipping of DCO-OFDM is greater compared to SLM because the PAPR reducing potential of SLM is intrinsically less efficient. Besides, the BER achieved by using either TDCSR or FDCDR for DCO-OFDM is better compared to SLM.
4. For O-OFDM, peak power reduction due to clipping is high, whereas, the reduction in peak power using FTP-ACO-OFDM and SLM is slighter.
5. The dynamic range of clipped O-OFDM is less compared to O-OFDM and precoded techniques, proceeding in a noticeable reduction in quantization noise. This facilitates the practical implementation of O-OFDM with limited bit resolution DACs.
6. FDCDR performs better than TDCSR for DCO-OFDM, whereas, TDCSR has better performance for ACO-OFDM for low order constellations, i.e., 16- and 64-QAM for a target BER of 10^{-3}.
7. The total number of arithmetic operations required for FDCDR is less than TDCSR.
8. The overall complexity of TDCSR and FDCDR is less compared to SLM since many phase sequences are needed to reduce the high PAPR. Since, fewer iterations for TDCSR and FDCDR are called for. However, the number of operations for TDCSR and FDCDR are increased compared to FTP-ACO-OFDM. A complete system complexity also includes the complexity of the DAC. For FTP-ACO-OFDM, the DAC has a large bit resolution obligation, however, when either TDCSR or FDCDR (with clipping), the bit resolution can be relieved.

It is concluded that with a moderate increase in complexity, the proposed methods can be of interest for PAPR reduction in IM-DD O-OFDM systems.

Chapter 4

Hermitian Symmetry Free Optical-Single-Carrier Frequency Division Multiple Access for Visible Light Communication

Optical-orthogonal frequency-division multiplexing (O-OFDM) is an effective scheme for visible light communication (VLC) which allows a candid extension to multiple access (MA) scenarios by using optical-orthogonal frequency division multiple access (O-OFDMA). However, O-OFDMA exhibits high peak-to-average power ratio (PAPR), which exacerbates the nonlinear distortions from the light-emitting diode (LED). To reduce high PAPR while sustaining MA, optical-single-carrier frequency-division multiple access (O-SCFDMA) is utilized. For both O-OFDMA and O-SCFDMA, Hermitian symmetry (HS) constraint is imposed in the frequency-domain (FD) to achieve a real-valued time-domain (TD) signal for intensity-modulation with direct-detection (IM-DD) implementation of VLC. Howbeit, HS results in an increase of PAPR for O-SCFDMA. Accordingly, HS free (HSF) O-SCFDMA (HSFO-SCFDMA) is proposed. The performance of HSFO-SCFDMA is compared with several approaches in key parameters, such as, bit error rate (BER), optical power penalty, PAPR, quantization, electrical power efficiency and system complexity. BER performance and optical power penalty is evaluated considering multipath VLC channel and taking into account the bandwidth limitation of LED in combination with its optimized driver. It is illustrated that HSFO-SCFDMA outperforms other alternatives in terms of BER and PAPR with lower computational complexity compared to most of the state-of-the-art techniques.

4.1 Introduction

To realize a complete networking VLC system, MA is essential to address different users in the most effective manner [149, 150]. O-OFDM provides a straightforward extension to MA through O-OFDMA, where the subcarriers are allocated to different users based on a pre-defined resource allocation matrix. However, O-OFDMA approaches also manifests high PAPR, therefore, the nonlinear distortions from the LED are inevitable. To surmount the distortions and to accommodate MA, O-SCFDMA is used[1]. O-SCFDMA is the precoded variant of O-OFDMA and its foremost advantage is the lower PAPR [94]. In the literature, O-OFDMA inspired O-SCFDMA schemes, e.g., Fourier transform precoded (FTP) asymmetrically clipped O-OFDM (FTP-ACO-OFDM) and FTP-direct-current biased-OFDM (FTP-DCO-OFDM) [94] have been introduced. Both approaches manifest lower PAPR relative to O-OFDMA counterparts, but, are constrained to satisfy the HS. Recently, Wu *et al.* [121] identified that in precoded approaches, only half of the TD symbols exploit single-carrier (SC) like benefits because of HS, hence, precoding results in a less compelling PAPR reduction compared to their radio counterparts. Consequently, the precoded schemes which preclude HS, surpass others (which use HS) in their efficacy for PAPR reduction. Recently, SC optical frequency division multiplexing (SCO-FDM) has been investigated in [125]. SCO-FDM exhibits lower PAPR compared to ACO-OFDMA/SCFDMA and demonstrates the same BER in an additive white Gaussian noise (AWGN) channel. However, the PAPR is not reduced to the same level as in interleaved (I)-SCFDMA used in radio-frequency (RF) systems because of insertion of zeros in the TD signal [121]. Low complexity pulse-amplitude modulation (PAM) based Hartley transform precoded (HTP) ACO-OFDM, i.e., HTP-ACO-OFDM is proposed by Zhou and Qiao [111] and [122] which also averts HS. HTP-ACO-OFDM features lower PAPR compared to FTP-ACO-OFDM, however, with an increase in size of modulation alphabet, PAPR reduction becomes less efficient.

Against what has been reported in the literature, we propose an O-SCFDMA approach capable of attaining superior performance compared to other alternatives. The main contributions of this work are:

1. An O-SCFDMA approach, HSFO-SCFDMA is introduced which yields several concrete advantages over other alternatives, such as, lower PAPR, power and cost efficiency.
2. For comparison, together with HSFO-SCFDMA, FTP-ACO-OFDM, HTP-ACO-OFDM, SCO-FDM, and FTP-DCO-OFDM are adopted. Key performance parameters, such as, PAPR, bit error rate (BER), optical power penalty, system complexity, digital-to-analog conversion quantization effect, electrical power and spectral efficiency (SE) are evaluated. For BER evaluation, a time dispersive VLC channel is considered where the dispersions are characterized by the multipath VLC channel impulse response (CIR) and the bandwidth limitation of LED/LED driver combination.
3. Optical power penalty of the aforementioned approaches is analyzed in time dispersive channel. It shall be demonstrated that HSFO-SCFDMA suffers the least optical power penalty.
4. Closed-form PAPR expressions as a function of modulation alphabets for the approaches which exhibit constant PAPR are evaluated.

The remainder of the chapter is organized as follows. In Section 4.2, the proposed modulation approach, HSFO-SCFDMA is presented in detail. Moving on, Section 4.3 provides a succinct analysis of the statistical characterization of HSFO-SCFDMA; where the average electrical and the average optical powers have been evaluated. Further on, Section 4.4 provides simulation results. MA scenario for HSFO-SCFDMA has been explained in Section 4.5. Lastly, based on the results obtained, Section 5.4 draws conclusions.

---

[1] In the sequel, we use the subcarrier and subchannel for O-OFDMA and O-SCFDMA, respectively, to distinguish between the two systems.

4.2 HSFO-SCFDMA

4.2.1 Modulation Concept

The foremost advantage of precluding HS is the low PAPR which is accomplished because all the TD symbols enjoy SC benefits. Contrary to that, if HS is implemented for O-SCFDMA, only half of the TD symbols manifest SC like behaviour, resulting in a less significant PAPR reduction, e.g., as in FTP-ACO-OFDM and FTP-DCO-OFDM (presented in Chapter 2). Nevertheless, it has been established that for both RF [151] and VLC [121] systems, I-SCFDMA culminates the lowest PAPR. Hence, in HSFO-SCFDMA, we couple the technique suggested by F. Barrami *et al.* [152] with I -SCFDMA in HSFO-SCFDMA to realize an approach capable of exhibiting low PAPR, whilst complying with IM-DD constraints. Furthermore, in HSFO-SCFDMA, obtaining a real-valued TD signal is straightforward because by imitating I-SCFDMA, only the even subchannels are modulated, which naturally results in a half-wave symmetric TD signal [151], from which the real and imaginary components of the TD signal are separated in a forthright manner. The condition of a non-negative TD signal for IM-DD is fulfilled by the addition of bias-index to the bipolar signal.

In the sequel, HSFO-SCFDMA is presented considering a simplified scenario (with only one user). Firstly, the transmitter of HSFO-SCFDMA is presented. Subsequently, the details of the dispersive channel are presented and finally, the receiver of HSFO-SCFDMA is described.

4.2.2 Transmitter

The block diagram of HSFO-SCFDMA transmitter is illustrated in Fig. 4.1. The incoming bit stream is parsed into $N/2$ parallel channels using a serial-to-parallel (S/P) converter which is modulated to Gray-mapped complex M-ary quadrature-amplitude modulation (QAM) symbols which are expressed as $x^{(\mathrm{H})}\left(n^{(\mathrm{H})}\right), n^{(\mathrm{H})} = 0, 1, \cdots, N/2-1$. The TD symbols are transformed to FD symbols, $\mathrm{X}^{(\mathrm{H})}\left(k^{(\mathrm{H})}\right)$, for $k^{(\mathrm{H})} = 0, 1, \cdots, N/2-1$ via $N/2$-order DFT as:

$$\mathrm{X}^{(\mathrm{H})}\left(k^{(\mathrm{H})}\right) = \mathrm{DFT}\left[x^{(\mathrm{H})}\left(n^{(\mathrm{H})}\right)\right]. \tag{4.1}$$

(4.1) essentially represents DFT-precoding. Afterwards, subchannel mapping is performed by assigning $N/2$ DFT-precoded symbols $\mathrm{X}^{(\mathrm{H})}\left(k^{(\mathrm{H})}\right)$ to the even subchannels of N-dimensional FD signal $X(k)$, where $k = 0, 1, \cdots, N-1$ as:

$$X(k) = \begin{cases} \mathrm{X}^{(\mathrm{H})}\left(k^{(\mathrm{H})}\right), & k = 2k^{(\mathrm{H})} \\ 0, & k = 2k^{(\mathrm{H})}+1 \end{cases}. \tag{4.2}$$

It may be noticed that the subchannels are mapped in an interleaved manner, because it has already been established that an interleaved subchannel mapping leads to better PAPR performance than localized mapping [121].

After subchannel mapping, $X(k)$ is transformed using IDFT to attain TD symbols:

$$x(n) = \mathrm{IDFT}\left[X(k)\right], \tag{4.3}$$

where $n = 0, 1, \cdots, N-1$ and $x(n) \in \mathbb{C}$. Owing to the frame structure of $X(k)$, $x(n)$ features the following properties:

1. $x(n)$ is a scaled and repeated version of $x^{(\mathrm{H})}\left(n^{(\mathrm{H})}\right)$ [125, 151].
2. $x(n)$ features half-wave symmetry, i.e., $x\left(n^{(\mathrm{H})}\right) = x\left(n^{(\mathrm{H})} + N/2\right)$ $\forall\, n^{(\mathrm{H})} = 0, 1, \cdots, N/2-1$ [153, 151], which is the inherent outcome if only the even subchannels are modulated.

It may be noticed that property 1 suggests that the $N/2$-order DFT and N-order IDFT at the transmitter might be redundant. However, it is accentuated that both processes are imperative for (frequency division) MA (see Section 4.5). Furthermore, by exploiting property 2, the real and the imaginary samples from the half-wave symmetric signal, $x(n)$, are obtained as:

$$\begin{aligned} x_{\Re}\left(n^{(\mathrm{H})}\right) &= \Re\left[x\left(n^{(\mathrm{H})}\right)\right] \\ x_{\Im}\left(n^{(\mathrm{H})}\right) &= \Im\left[x\left(n^{(\mathrm{H})} + \frac{N}{2}\right)\right] \end{aligned} \tag{4.4}$$

for $n^{(\mathrm{H})} = 0, 1, \cdots, N/2-1$ without loss of useful information. Here, $\{x_{\Re}\left(n^{(\mathrm{H})}\right), x_{\Im}\left(n^{(\mathrm{H})}\right)\} \in \mathbb{R}$. From (4.4), it may be inferred that M-QAM (square) constellation is split into two $\sqrt{M}$-PAM constellations.

The block of real and imaginary samples are concatenated as $\tilde{x}(\tilde{n}) = \left[x_{\Re}\left(n^{(\mathrm{H})}\right); x_{\Im}\left(n^{(\mathrm{H})}\right)\right]^{\mathrm{T}}$, after affixing the cyclic prefix (CP) of length equal to channel delay spread, i.e., (N_{CP}) to the block of real and imaginary samples, where $\tilde{n} = 0, 1, \cdots, N + 2N_{\mathrm{CP}} - 1$ and $\tilde{x}(n) \in \mathbb{R}$. Here, for conciseness in notation, even after the addition of CP, the blocks of real and imaginary samples are still expressed as $x_{\Re}(\cdot)$ and $x_{\Im}(\cdot)$. $\tilde{x}(\tilde{n})$ is subsequently impinged on a digital-to-analog converter (DAC) to obtain an analog electrical waveform, $\tilde{x}(t)$, which, however, is bipolar. Therefore, a bias-index, $\beta_{\mathrm{DC}}^{(\mathrm{H})} > 0$, is introduced, such that

$$x(t) = \tilde{x}(t) + \beta_{\mathrm{DC}}^{(\mathrm{H})}, \tag{4.5}$$

where $\beta_{\mathrm{DC}}^{(\mathrm{H})}$ is prescribed as:

$$\beta_{\mathrm{DC}}^{(\mathrm{H})} = \varsigma_{(\mathrm{H})}\sqrt{E\left(|\tilde{x}(t)|\right)^2}, \;\; \varsigma_{(\mathrm{H})} > 0. \tag{4.6}$$

The bias-index on the decibel (dB) scale is defined as $10\log_{10}(\varsigma_{(\mathrm{H})}^2 + 1)$ dB. *Sufficient* biasing [99] is appropriated for HSFO-SCFDMA, where $\varsigma_{(\mathrm{H})}$ is adjusted, such that $\beta_{\mathrm{DC}}^{(H)}$ is equal to the absolute value of the largest negative peak of $\tilde{x}(t)$. $x(t)$ is transmitted through an optical channel by the LED. In what follows, perfect synchronization [80, 134, 81] is considered. A linear response of the LED is considered in system evaluation [80, 134, 81], since, the nonlinearity of the LED can be mitigated using digital pre-distortion [154].

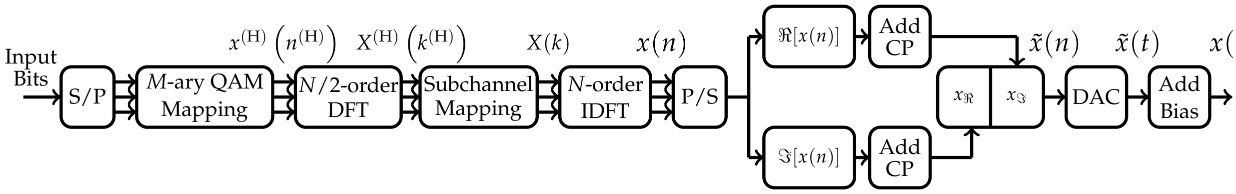

FIGURE 4.1: Block diagram of HSFO-SCFDMA transmitter.

4.2.3 Receiver

The receiver of HSFO-SCFDMA is illustrated in Fig. 4.2. At the receiver, the light intensity is photo-detected using a photo-diode (PD), and the bias is eliminated using a DC blocking capacitor. The received intensity waveform, $y(t)$ is electronically amplified using trans-impedance amplifier (TIA), and then fed to an analog-to-digital converter (ADC) to yield $y(n) = \left[y_{\Re}\left(n^{(\mathrm{H})}\right); y_{\Im}\left(n^{(\mathrm{H})}\right)\right]^{\mathrm{T}}$, from which the real and the imaginary TD symbol vectors are separated after CP removal and are given by:

$$\begin{aligned} \boldsymbol{y}_{\Re} &= \mathbf{H}\boldsymbol{x}_{\Re} + \boldsymbol{w}_{\Re}, \\ \boldsymbol{y}_{\Im} &= \mathbf{H}\boldsymbol{x}_{\Im} + \boldsymbol{w}_{\Im}, \end{aligned} \tag{4.7}$$

respectively, where $\boldsymbol{y}_{\Re} = [y_{\Re}(0), y_{\Re}(1), \cdots, y_{\Re}(N/2-1)]$ and $\boldsymbol{y}_{\Im} = [y_{\Im}(0), y_{\Im}(1), \cdots, y_{\Im}(N/2-1)]$. Moreover, $\mathbf{w}_{\Re}$ and $\mathbf{w}_{\Im}$ are modeled as AWGN. $\mathbf{H}$ is $N/2 \times N/2$ circulant convolution matrix with the first column equal to $\mathbf{h} = [h_0, h_1, \cdots, h_{L-1}, 0, \cdots, 0]$ for L channel coefficients and $h_n = h(nT_{\mathrm{s}})$ with $n \in [0, L-1]$. A stationary channel, i.e., $\mathbf{H} = \mathbf{H}_{\Re} = \mathbf{H}_{\Im}$ is considered. Moreover, the circulant nature of $\mathbf{H}$, allows to diagonalize it using the DFT matrix and write [87]:

$$\mathbf{H} = \mathbf{F}^{\mathrm{H}}\boldsymbol{\Lambda}\mathbf{F}, \tag{4.8}$$

where $\boldsymbol{\Lambda}$ is a diagonal matrix with the channel frequency response on its diagonal and having eigen values $[\Lambda_0, \Lambda_1, \cdots, \Lambda_{N/2}]^{\mathrm{T}}$. Here, $\mathbf{F}^{\mathrm{H}}$ and $\mathbf{F}$ are used to represent $N/2 \times N/2$ IDFT and DFT matrix. The samples of real and imaginary blocks, $y_{\Re}\left(n^{(\mathrm{H})}\right)$ and $y_{\Im}\left(n^{(\mathrm{H})}\right)$, are transformed to FD by $N/2$-order DFT to yield:

$$\begin{aligned} Y_{\Re}\left(k^{(\mathrm{H})}\right) &= \mathrm{DFT}\left[y_{\Re}\left(n^{(\mathrm{H})}\right)\right], \\ Y_{\Im}\left(k^{(\mathrm{H})}\right) &= \mathrm{DFT}\left[y_{\Im}\left(n^{(\mathrm{H})}\right)\right]. \end{aligned} \tag{4.9}$$

for $k^{(\mathrm{H})} = 0, 1, \cdots, N/2-1$. In vectorial form, $\left\{Y_{\Re}\left(k^{(\mathrm{H})}\right), Y_{\Im}\left(k^{(\mathrm{H})}\right)\right\} \; \forall\, k^{(\mathrm{H})} = 0, 1, \cdots, N/2-1$ can be expressed as $\boldsymbol{Y}_{\Re}$ and $\boldsymbol{Y}_{\Im}$, respectively. A FD minimum mean squared error (MMSE) equalizer with the knowledge of channel impulse response is applied to $\boldsymbol{Y}_{\Re}$ and $\boldsymbol{Y}_{\Im}$ to yield equalized FD sub-blocks as:

$$\begin{aligned} \hat{\mathbf{Y}}_{\Re} &= \left(\boldsymbol{\Lambda}^{\mathrm{H}}\boldsymbol{\Lambda} + (E_{\mathrm{b}_{(\mathrm{elec})}}/N_0)^{-1}\boldsymbol{I}\right)\boldsymbol{\Lambda}^{\mathrm{H}}\mathbf{Y}_{\Re}, \\ \hat{\mathbf{Y}}_{\Im} &= \left(\boldsymbol{\Lambda}^{\mathrm{H}}\boldsymbol{\Lambda} + (E_{\mathrm{b}_{(\mathrm{elec})}}/N_0)^{-1}\boldsymbol{I}\right)\boldsymbol{\Lambda}^{\mathrm{H}}\mathbf{Y}_{\Im}, \end{aligned} \tag{4.10}$$

where $\boldsymbol{\Lambda}^{\mathrm{H}}$ indicates the Hermitian of matrix $\boldsymbol{\Lambda}$. $E_{\mathrm{b}_{(\mathrm{elec})}}/N_0$ is the electrical signal-to-noise ratio (SNR) per bit, and $\boldsymbol{I}$ is the identity matrix. $\hat{\mathbf{Y}}_{\Re}$ and $\hat{\mathbf{Y}}_{\Im}$ are explicitly given as $\hat{\mathbf{Y}}_{\Re} = [\hat{Y}_{\Re}(0), \hat{Y}_{\Re}(1), \cdots, \hat{Y}_{\Re}(N/2-1)]$ and $\hat{\mathbf{Y}}_{\Im} = [\hat{Y}_{\Im}(0), \hat{Y}_{\Im}(1), \cdots, \hat{Y}_{\Im}(N/2-1)]$, respectively. Afterwards, $\hat{Y}_{\Re}\left(k^{(\mathrm{H})}\right)$ and $\hat{Y}_{\Im}\left(k^{(\mathrm{H})}\right)$ for $k^{(\mathrm{H})} = 0, 1, \cdots, N/2-1$ are transformed to TD counterparts by using $N/2$-order IDFT as:

$$\begin{aligned} \hat{y}_{\Re}\left(n^{(\mathrm{H})}\right) &= \mathrm{IDFT}\left[\hat{Y}_{\Re}\left(k^{(\mathrm{H})}\right)\right], \\ \hat{y}_{\Im}\left(n^{(\mathrm{H})}\right) &= \mathrm{IDFT}\left[\hat{Y}_{\Im}\left(k^{(\mathrm{H})}\right)\right]. \end{aligned} \tag{4.11}$$

Lastly, $\hat{y}_{\Re}\left(n^{(\mathrm{H})}\right)$ and $\hat{y}_{\Im}\left(n^{(\mathrm{H})}\right)$, are combined as:

$$y\left(n^{(\mathrm{H})}\right) = \sqrt{\kappa}\left(\hat{y}_{\Re}\left(n^{(\mathrm{H})}\right) + j \cdot \hat{y}_{\Re}\left(n^{(\mathrm{H})}\right)\right), \tag{4.12}$$

where $\kappa = 2$, if only one user is considered. M-ary QAM demapping is performed on the serial symbols to obtain the output bits.

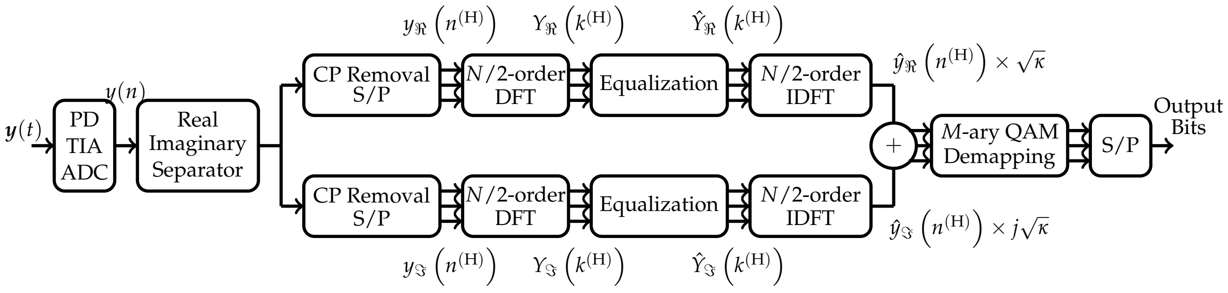

FIGURE 4.2: Block diagram of HSFO-SCFDMA receiver.

4.3 Statistical characterization

By adopting sufficient biasing, the average electrical and the average optical powers for HSFO-SCFDMA are given by:

$$P_{(\mathrm{elec,HSFO})} = E\left(|x^{(\mathrm{H})}(t)|^2\right) = E\left(\tilde{x}^2(t)\right) + \left(\beta_{\mathrm{DC}}^{(\mathrm{H})}\right)^2, \tag{4.13}$$

and

$$P_{(\mathrm{opt,HSFO})} = E\left(|x^{(\mathrm{H})}(t)|\right) = \beta_{\mathrm{DC}}^{(\mathrm{H})}, \tag{4.14}$$

respectively. The ratio of $P_{(\mathrm{elec,HSFO})}$ and $P_{(\mathrm{opt,HSFO})}$ can be expressed as:

$$\alpha_{\mathrm{HSFO}}^{\mathrm{OE}} = \frac{P_{(\mathrm{elec,HSFO})}}{P_{(\mathrm{opt,HSFO})}} = \frac{1 + \varsigma_{(\mathrm{H})}^2}{\varsigma_{(\mathrm{H})}^2}, \tag{4.15}$$

where $\alpha_{\mathrm{HSFO}}^{\mathrm{OE}}$ is the optical-to-electrical power conversion efficiency. $\alpha_{\mathrm{HSFO}}^{\mathrm{OE}}$ varies exactly like $\alpha_{\mathrm{DCO}}^{\mathrm{OE}}$ for DCO-OFDM as depicted in Fig. 2.14. However, it should be realized that for HSFO-SCFDMA, the bias-index is considerably less (shall be demonstrated later). Hence, $\alpha_{\mathrm{HSFO}}^{\mathrm{OE}}$ is always less than $\alpha_{\mathrm{DCO}}^{\mathrm{OE}}$.

Moreover, for any value of $E_{\mathrm{b}_{(\mathrm{elec})}}/N_0$, the corresponding $E_{\mathrm{b}_{(\mathrm{opt})}}/N_0$ is obtained using (4.15) and normalizing the optical power to unity (i.e., $P_{(\mathrm{opt,HSFO})} = 1$) as:

$$\frac{E_{\mathrm{b}_{(\mathrm{opt})}}}{N_0} = \left(\frac{1}{\alpha_{\mathrm{HSFO}}^{\mathrm{OE}}}\right) \frac{E_{\mathrm{b}_{(\mathrm{elec})}}}{N_0}. \tag{4.16}$$

It is highlighted that $E_{\mathrm{b}_{(\mathrm{opt})}}/N_0$ required for HSFO-SCFDMA will always be less than what is required for DCO-OFDM.

4.4 Performance evaluation

In this section, simulation and analytical results are provided to demonstrate and compare the performance of HSFO-SCFDMA with other state-of-the-art alternatives, which are; FTP-ACO-OFDM, HTP-ACO-OFDM, SCO-FDM, and FTP-DCO-OFDM. Unless otherwise mentioned, spectral efficiencies of $\eta = \{1, 2\}$ bits/s/Hz are considered[2]. Firstly, the SE implications for different modulation techniques are discussed. Secondly, the PAPR characteristics manifested by different approaches have been presented. Additionally, closed-form analytical expressions of PAPR for the modulation schemes having deterministic peak values of the TD signal are evaluated. Moving on, the bias-index required by HSFO-SCFDMA for sufficient biasing is analyzed, and closed-form expressions of bias-index as a function of modulation index, M are determined. Monte Carlo results for BER in LOS and multipath VLC channels are provided. Subsequently, optical power penalty relative to on-off Keying (OOK) is evaluated and analyzed for different modulation approaches. Further on, complexity implications of different modulation schemes are discussed. Lastly, quantization characteristics, electrical and optical power efficiency for different modulation approaches are investigated.

4.4.1 Spectral efficiency

SE is the data-rate that can be transmitted over a given bandwidth. Here, the spectral efficiencies of different modulation schemes are evaluated relative to those of classical state-of-the-art schemes, like ACO-OFDM and DCO-OFDM. It is recalled that ACO-OFDM has half the SE of DCO-OFDM.

- Both FTP-ACO-OFDM and FTP-DCO-OFDM have the same SE as that of their O-OFDM counterparts, i.e., ACO-OFDM and DCO-OFDM, respectively.
- HTP-ACO-OFDM and SCO-FDM manifest the same SE as ACO-OFDM.
- HSFO-SCFDMA exhibits the same SE as DCO-OFDM, therefore, it is spectrally efficient compared to FTP-ACO-OFDM, HTP-ACO-OFDM, and SCO-FDM.

It should be recognized that M^2-QAM FTP-ACO-OFDM and SCO-FDM would result in a same SE as M-QAM FTP-DCO-OFDM and HSFO-SCFDMA. Moreover, M'-PAM based HTP-ACO-OFDM and M-QAM based FTP-DCO-OFDM and HSFO-SCFDMA exhibit the same SE, with $M' = M$. The spectral efficiencies of different modulation approaches have been summarized in Table 4.1, considering only one user and ignoring the impact of the CP.

---

[2] $\eta = 1$ bits/s/Hz is obtained by using $4-$QAM HSFO-SCFDMA and FTP-DCO-OFDM, and using $16-$QAM for FTP-ACO-OFDM and SCO-FDM. For HTP-ACO-OFDM, $\eta = 1$ bits/s/Hz is obtained using $4-$PAM constellation.

TABLE 4.1: Spectral efficiencies of different mdoulation schemes. N represents the number of available subchannels. M and M' are the modulation index for QAM and PAM constellations, respectively.

Modulation Scheme	**Spectral Efficiency (η)**
HSFO-SCFDMA	$0.5\log_2(M)$
FTP-ACO-OFDM	$0.25\log_2(M)$
HTP-ACO-OFDM	$0.5\log_2(M')$
SCO-FDM	$0.25\log_2(M)$
FTP-DCO-OFDM	$\approx 0.5\log_2(M)$

4.4.2 PAPR analysis

PAPR (λ) of a signal is graphically illustrated using complementary cumulative distribution function (CCDF) which is the probability that PAPR of signal will exceed a given threshold, PAPR_ϵ, i.e., CCDF $=$ $\text{Prob}(\text{PAPR} > \text{PAPR}_\epsilon)$. CCDF curves are illustrated in Fig. 4.3 and Fig. 4.4 for spectral efficiencies of $\eta = 1$ bits/s/Hz and $\eta = 2$ bits/s/Hz, respectively, which reveal that HSFO-SCFDMA distinctly has the lowest PAPR. For $\eta = 1$ bits/s/Hz, HSFO-SCFDMA manifests approximately 5.4 dB, 8.2 dB, 8.7 dB and 12 dB lesser PAPR compared to SCO-FDM, FTP-DCO-OFDM, FTP-ACO-OFDM and HTP-ACO-OFDM, respectively. Likewise, for $\eta = 2$ bits/s/Hz, the PAPR of HSFO-SCFDMA is approximately 4.8 dB, 6.4 dB, 7.5 dB and 9.4 dB less than SCO-FDM, FTP-DCO-OFDM, FTP-ACO-OFDM and HTP-ACO-OFDM, respectively.

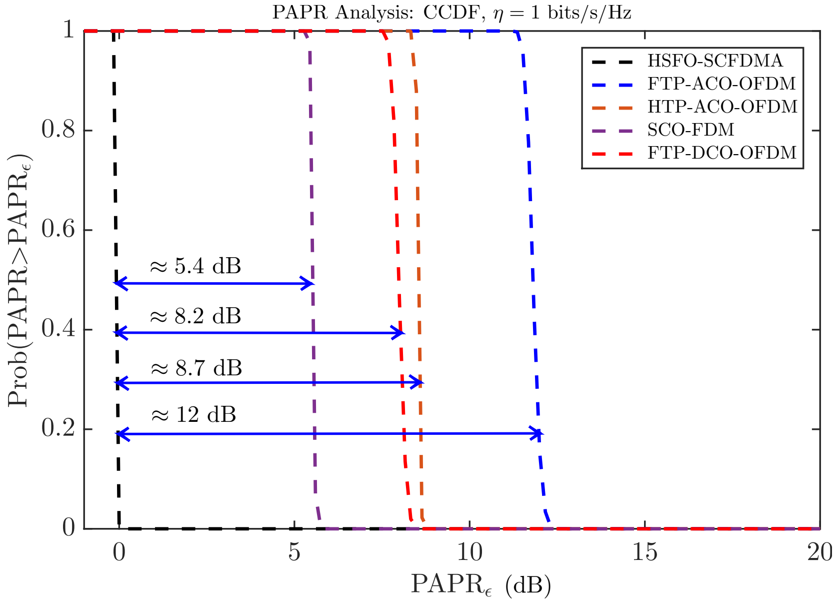

FIGURE 4.3: PAPR comparison of different modulation schemes for $\eta = 1$ bits/s/Hz.

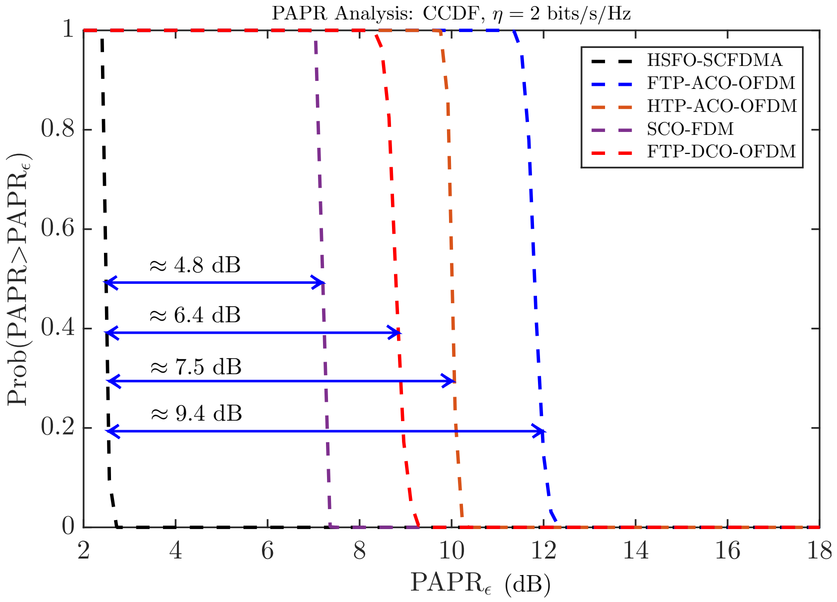

FIGURE 4.4: PAPR comparison of different modulation schemes for $\eta = 2$ bits/s/Hz.

The closed-form PAPR expressions as a function of modulation index can be readily evaluated for HSFO-SCFDMA, SCO-FDM and HTP-ACO-OFDM, because the peak values of the TD signals are deterministic. Besides, the variance of the TD signal can be easily obtained. The analytical PAPR expressions are evaluated considering $M = \{4, 8, 16, 32, 64, 128, 256, 512, 1024, 2048\}$ for HSFO-SCFDMA and SCO-FDM, whereas, a generalized expression considering M'-PAM is obtained for HTP-ACO-OFDM.

For HSFO-SCFDMA, the peak value, $\xi_{\text{peak,HSFO}}$, and the variance, σ^2_{HSFO}, of the TD signal is given by:

$$\xi_{\text{peak,HSFO}} = \begin{cases} \frac{\sqrt{M}-1}{\sqrt{2}}, & \text{for } M = 4, 16, 64, 256, 1024 \\ \frac{\log_2(M)}{\sqrt{2}}, & \text{for } M = 8, 32 \\ \frac{2\log_2(M)-3}{\sqrt{2}}, & \text{for } M = 128 \\ \frac{2\log_2(M)+5}{\sqrt{2}}, & \text{for } M = 512 \\ \frac{4\log_2(M)+3}{\sqrt{2}}, & \text{for } M = 2048 \end{cases}, \tag{4.17}$$

and

$$\sigma^2_{\text{HSFO}} = \begin{cases} \frac{M-1}{6}, & \text{for } M = 4, 16, 64, 256, 1024 \\ \frac{2.5M-2}{12}, & \text{for } M = 8 \\ \frac{31M-32}{192}, & \text{for } M = 32, 128, 512, 2048 \end{cases}, \tag{4.18}$$

respectively. Using (4.17) and (4.18), closed-form expressions for the PAPR of HSFO-SCFDMA are evaluated as:

$$\lambda_{\text{HSFO}} = \xi^2_{\text{peak,HSFO}} / \sigma^2_{\text{HSFO}} \tag{4.19}$$

and are summarized in Table 4.2. For SCO-FDM, $\xi_{\text{peak,SCO}} = (1/\sqrt{2})\xi_{\text{peak,HSFO}}$ and $\sigma^2_{\text{SCO}} = (1/4)\sigma^2_{\text{HSFO}}$. Hence, we have

$$\lambda_{\text{SCO}} = 2\lambda_{\text{HSFO}}. \tag{4.20}$$

where, λ_{SCO} is the PAPR exhibited by SCO-FDM. Moreover, for HTP-ACO-OFDM, $\xi_{\text{peak,HTP-ACO}} \approx$

$M'-1$, and $\sigma^2_{\text{HTP}-\text{ACO}} = (M'^2-1)/12$, with M' being the PAM alphabet size. So, using $\xi_{\text{peak,HTP}-\text{ACO}}$ and $\sigma^2_{\text{peak,HTP}-\text{ACO}}$, the PAPR manifested by HTP-ACO-OFDM, $\xi_{\text{HTP}-\text{ACO}}$, is given as:

$$\lambda_{\text{HTP}-\text{ACO}} = \frac{\xi^2_{\text{peak,HTP}-\text{ACO}}}{\sigma^2_{\text{HTP}-\text{ACO}}} = \frac{12(M'-1)}{M'+1}. \tag{4.21}$$

TABLE 4.2: Closed-form analytical expressions for the PAPR exhibited be HSFO-SCFDMA, λ_{HSFO}, as a function of modulation order, M, for QAM constellations. Here $\nu := 96/(31M-32)$.

Modulation Order (M)	**PAPR (λ_{HSFO})**
4, 16, 64, 256, 1024	$\frac{3(\sqrt{M}-1)}{\sqrt{M}+1}$
8	$\frac{6[\log_2(M)]^2}{2.5M-2}$
32	$[\log_2(M)]^2\nu$
128	$[2\log_2(M)-3]^2\nu$
512	$[2\log_2(M)+5]^2\nu$
2048	$[4\log_2(M)+3]^2\nu$

Observe that to obtain the PAPR illustrated in Fig. 4.3 and Fig. 4.4, the SE, η, for different modulation schemes has to be taken into account, i.e., the PAPR of M-QAM HSFO-SCFDMA should be compared to that of M^2-QAM SCO-FDM and so on so forth.

The evaluation of PAPR expressions for the remaining approaches are skipped for brevity. Refer to [155] for a comprehensive analysis of PAPR of ACO-OFDM and DCO-OFDM, which may be extended to precoded counterparts.

4.4.3 Bias-index evaluation

For sufficiently biased HSFO-SCFDMA, the bias-index (on the linear scale) is a function of the peak value, $\xi_{\text{peak,HSFO}}$, of the TD signal, which, in turn, depends on the modulation index, M (see Sec. 4.4.2). Thus, considering a given $\xi_{\text{peak,HSFO}}$, $\varsigma_{(\text{H})}$ is evaluated as:

$$\varsigma_{(\text{H})} = \frac{\xi_{\text{peak,HSFO}}}{\sigma_{\text{HSFO}}} = \sqrt{\lambda \text{HSFO}}. \tag{4.22}$$

From (4.22), it can be observed that $\varsigma_{(\text{H})}$ can be directly obtained by evaluating the square root of the PAPR for HSFO-SCFDMA, i.e., λ_{HSFO}. So, once $\varsigma_{(\text{H})}$ is known, the bias-index on dB scale can be obtained as $10\log_{10}(\varsigma^2_{(\text{H})}+1)$.

The TD signals for HSFO-SCFDMA, FTP-DCO-OFDM, and DCO-OFDM obtained using 4−QAM constellation are presented in Fig. 4.5. These TD signals can be viewed as a raw illustration to surmise the required bias-index for achieving non-negativity and also the PAPR. It can be observed from Fig. 4.5, that the peak value, ξ_{peak}, of HSFO-SCFDMA is by far less compared to FTP-DCO-OFDM and DCO-OFDM. Consequently, the required bias-index for sufficient biasing would also be less and so does the PAPR. The bias-index to sufficiently bias HSFO-SCFDMA, FTP-DCO-OFDM, and DCO-OFDM for different spectral efficiencies is presented in Fig. 4.6. It is illustrated that HSFO-SCFDMA needs significantly lower bias-index compared to what is required for FTP-DCO-OFDM and DCO-OFDM. It is recalled that bias-index has a direct impact on optical power efficiency of a modulation scheme. If a higher bias-index is used, the optical-to-electrical power conversion efficiency for the modulation scheme is less efficient. From Fig. 4.6, it is evident that the required bias-index for HSFO-SCFDMA to realize sufficient biasing is the least, therefore, it would suffer the least penalty on $E_{\text{b}_{(\text{opt})}}/N_0$ compared to FTP-DCO-OFDM and DCO-OFDM.

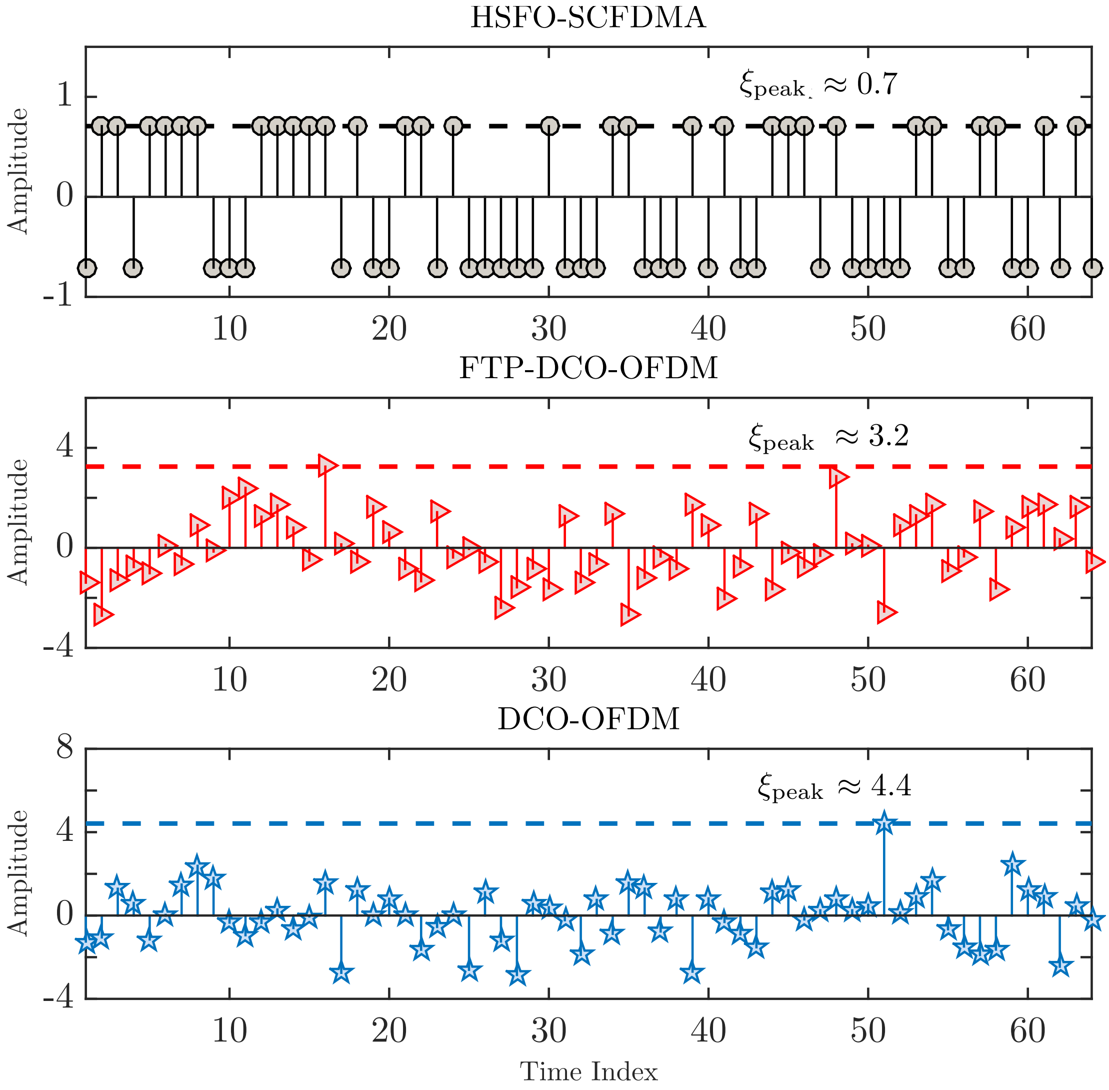

FIGURE 4.5: TD signals for HSFO-SCFDMA, FTP-DCO-OFDM, and DCO-OFDM using 4−QAM constellation.

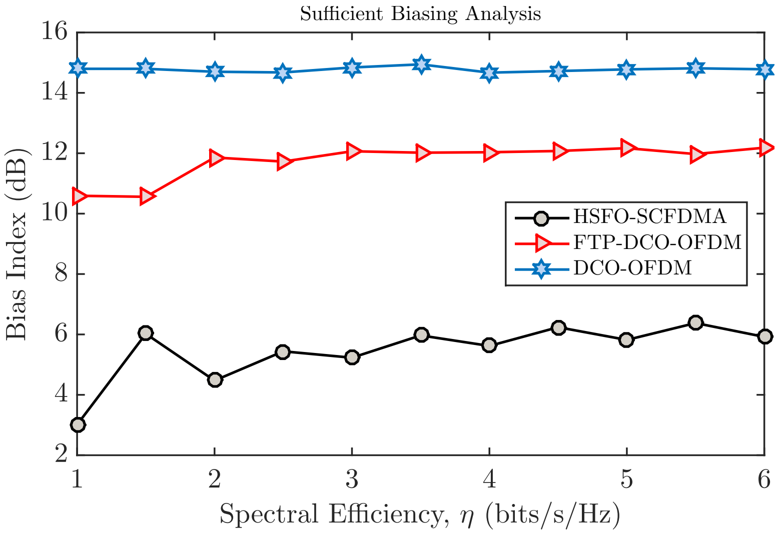

FIGURE 4.6: Analysis of sufficient biasing for HSFO-SCFDMA, FTP-DCO-OFDM, and DCO-OFDM for different spectral efficiencies, η. The results are obtained using $N = 1024$ and are averaged for 200000 symbols.

4.4.4 Bit error rate performance

Here, the BER performance of HSFO-SCFDMA is investigated and is compared with that of FTP-ACO-OFDM, HTP-ACO-OFDM, SCO-FDM, and FTP-DCO-OFDM considering $\eta = \{1, 2\}$ bits/s/Hz. The multipath VLC channel presented in Chapter 2 is considered with the LED 3 dB bandwidth $f_{3\text{dB}}$ set at 150 MHz and the noise modeled as AWGN. For FTP-DCO-OFDM, bias-index, $\beta_{\text{DC}}^{(\text{PD})}$, of 6 dB and 10 dB is used for $\eta = 1$ bits/s/Hz and $\eta = 2$ bits/s/Hz, respectively, whereas, HSFO-SCFDMA is sufficiently biased. Data-rate, R_{b} equal to 200 Mbps is considered. Thus, for $\eta = 1$ bits/s/Hz, the bandwidth (BW) of the transmitted signal is 200 MHz culminating in a prominent impact of the bandwidth limitation of the LED/LED driver combination. Whereas, for $\eta = 2$ bits/s/Hz, BW of the transmitted signal is 100 MHz, hence, evading the bandwidth limitation of the LED/LED driver combination. As a reference, BER of HSFO-SCFDMA, FTP-DCO-OFDM (with bias-index of 6 dB) and FTP-ACO-OFDM in AWGN without considering bandwidth limitation of LED/LED driver combination for $\eta = 1$ bits/s/Hz and $\eta = 2$ bits/s/Hz is presented. Unless otherwise specified, all results are averaged over 2000 Monte Carlo runs with the number of subchannels, $N = 512$. The results for BER versus $E_{\text{b}_{(\text{elec})}}/N_0$ for $\eta = 1$ bits/s/Hz and $\eta = 2$ bits/s/Hz are presented in Fig. 4.7 and Fig. 4.8, respectively, from which it can be discerned that:

- The $E_{\text{b}_{(\text{elec})}}/N_0$ required to achieve BER of 10^{-4} for FTP-ACO-OFDM, HTP-ACO-OFDM, SCO-FDM, and FTP-DCO-OFDM is almost the same for $\eta = 1$ bits/s/Hz. However, for $\eta = 2$ bits/s/Hz, FTP-ACO-OFDM, HTP-ACO-OFDM, and SCO-FDM become less efficient compared to FTP-DCO-OFDM, as higher order modulation alphabets are required.
- For both $\eta = \{1, 2\}$ bits/s/Hz, HSFO-SCFDMA signifies a superior performance compared to other alternatives. It may be noticed that for $\eta = 1$ bits/s/Hz at BER of 10^{-4}, $E_{\text{b}_{(\text{elec})}}/N_0$ gain of approximately 2 dB over FTP-ACO-OFDM and HTP-ACO-OFDM, and around 3 dB over FTP-DCO-OFDM and SCO-FDM is observed for HSFO-SCFDMA. In case of $\eta = 2$ bits/s/Hz, for BER

of 10^{-4}, a gain of almost 6 dB over FTP-DCO-OFDM, and nearly 7 dB over FTP-ACO-OFDM, HTP-ACO-OFDM, and SCO-FDM is achieved for HSFO-SCFDMA.

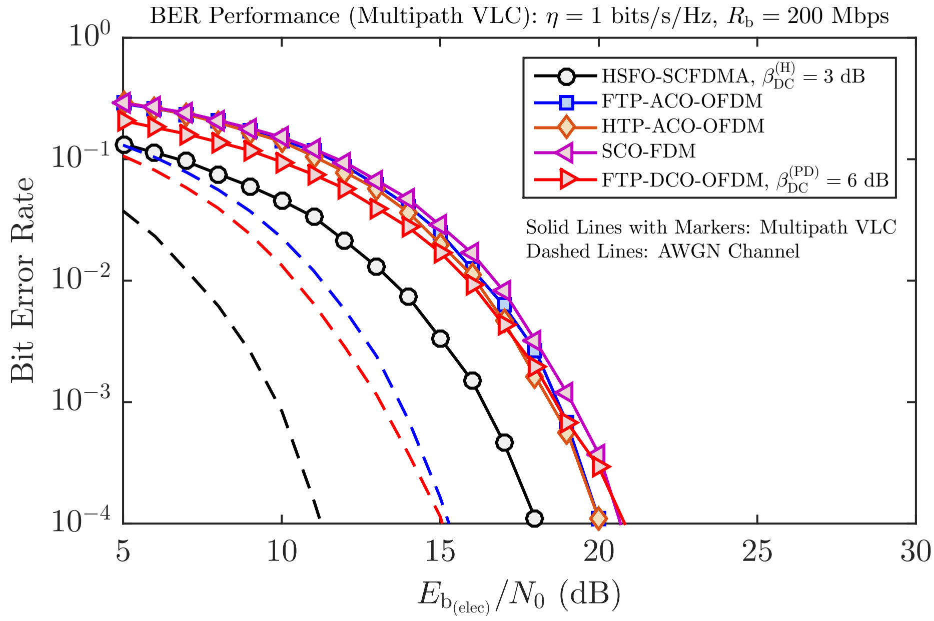

FIGURE 4.7: BER performance as a function of $E_{b_{(elec)}}/N_0$ in a multipath VLC channel considering a SE of $\eta = 1$ bits/s/Hz. $R_b = 200$ Mbps and $f_{3dB} = 150$ MHz are considered. The bias-index for DCO-SCFDMA is 6 dB, while HSFO-SCFDMA is sufficiently biased. The dashed curves represent the performance of different modulation schemes in an AWGN channel.

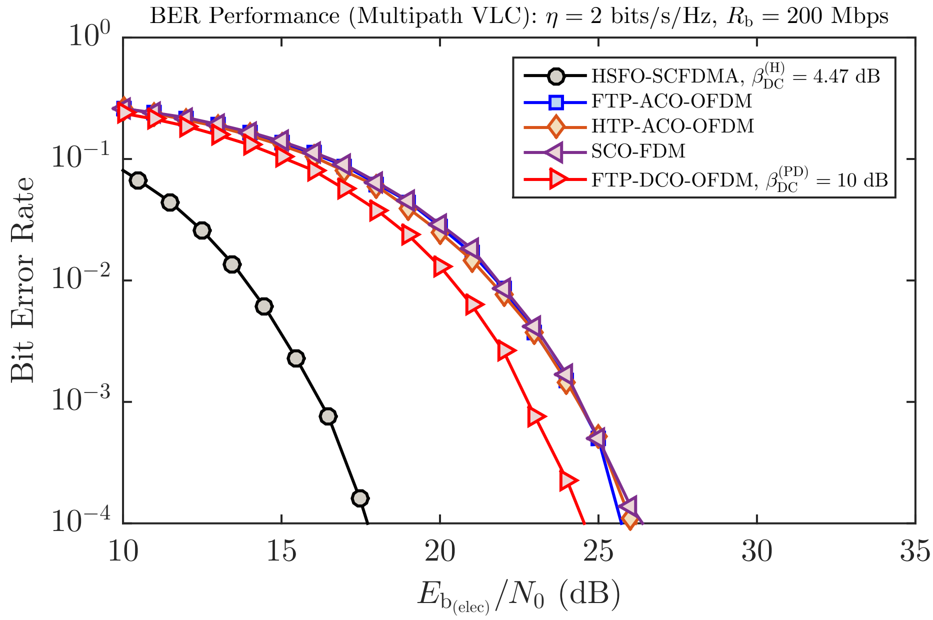

FIGURE 4.8: BER performance as a function of $E_{b_{(elec)}}/N_0$ in a multipath VLC channel considering a SE of $\eta = 2$ bits/s/Hz. $R_b = 200$ Mbps and $f_{3dB} = 150$ MHz are considered. The bias-index of DCO-SCFDMA is 10 dB, while HSFO-SCFDMA is sufficiently biased.

Comparing HSFO-SCFDMA with FTP-DCO-OFDM, the $E_{b_{(elec)}}/N_0$ gain is correlated to the difference in bias-index required to achieve non-negativity for both approaches. Compared to FTP-DCO-OFDM, a lower bias-index is required for HSFO-SCFDMA because of lower PAPR. Whereas, for the remaining approaches, the $E_{\mathrm{b}_{(\mathrm{elec})}}/N_0$ gain for HSFO-SCFDMA is realized because lower order constellations are needed to achieve a given SE. If $R_{\mathrm{b}} = 200$ Mbps is considered for $\eta = 2$ bits/s/Hz, the BER performance of all the schemes approaches to their performance in AWGN because the dispersive impact of the VLC multipath channel and the bandwidth limitation of the LED/LED driver combination is averted due to the low bandwidth of the transmitted signal.

4.4.5 Optical power penalty

In this section, the optical power penalty for different modulation approaches incurred due to the dispersive channel is analyzed. For a given BER, P_{b}, the optical power penalty is obtained by normalizing the required optical power by the average optical SNR per bit required for OOK in an AWGN channel with no bandwidth limitation expressed as $E^{\mathrm{OOK}}_{\mathrm{b}_{(\mathrm{opt})}}/N_0$ and is given as:

$$E^{\mathrm{OOK}}_{\mathrm{b}_{(\mathrm{opt})}}/N_0 = \mathrm{erfc}^{-2}\left(2P_{\mathrm{b}}\right), \tag{4.23}$$

where $\mathrm{erfc}(\phi)$ is the complementary error function expressed as $\mathrm{erfc}(\phi) = 1 - 2/\sqrt{\pi}\int_0^{\phi}\exp(-t^2)\mathrm{d}t$. The results are obtained by setting $P_{\mathrm{b}} = 10^{-3}$, $\eta = 2$ bits/s/Hz and varying the ratio of the data-rate to the 3 dB optical cut-off frequency, i.e., $R_{\mathrm{b}}/f_{3\mathrm{dB}}$. Fig. 4.9 and Fig. 4.10 illustrate the optical power penalties for different modulation schemes in multipath VLC channel for $\eta = 1$ bits/s/Hz and $\eta = 2$ bits/s/Hz, respectively, from which the following observations can be drawn:

- FTP-DCO-OFDM experiences the highest optical power penalty because of the bias-index required to achieve non-negativity.
- The optical power penalty for SCO-FDM is marginally higher compared to FTP-ACO-OFDM and HTP-ACO-OFDM.
- HTP-ACO-OFDM undergoes approximately the same optical power penalty as that of ACO-SCFDMA.
- HSFO-SCFDMA experiences minimum optical power penalty for all the values of $R_{\mathrm{b}}/f_{3\mathrm{dB}}$. For $\eta = 1$ bits/s/Hz and $R_{\mathrm{b}}/f_{3\mathrm{dB}} < 1.11$, HSFO-SCFDMA incurs approximately 2 dB, 2.5 dB and 5 dB less optical power penalty compared to FTP-ACO-OFDM, SCO-FDM and FTP-DCO-OFDM, respectively. The performance of HSFO-SCFDMA is expected to be better than OOK when the multipath VLC channel along with bandwidth limitation of the LED is considered for OOK (here, for reference purpose, AWGN is considered for OOK). Whereas, for $\eta = 2$ and $R_{\mathrm{b}}/f_{3\mathrm{dB}} \leq 1.90$, FTP-DCO-OFDM and SCO-FDM, respectively, perform approximately 6 dB and 3.5 dB worse compared to HSFO-SCFDMA, whereas, FTP-ACO-OFDM and HTP-ACO-OFDM are penalized 3 dB more than HSFO-SCFDMA.

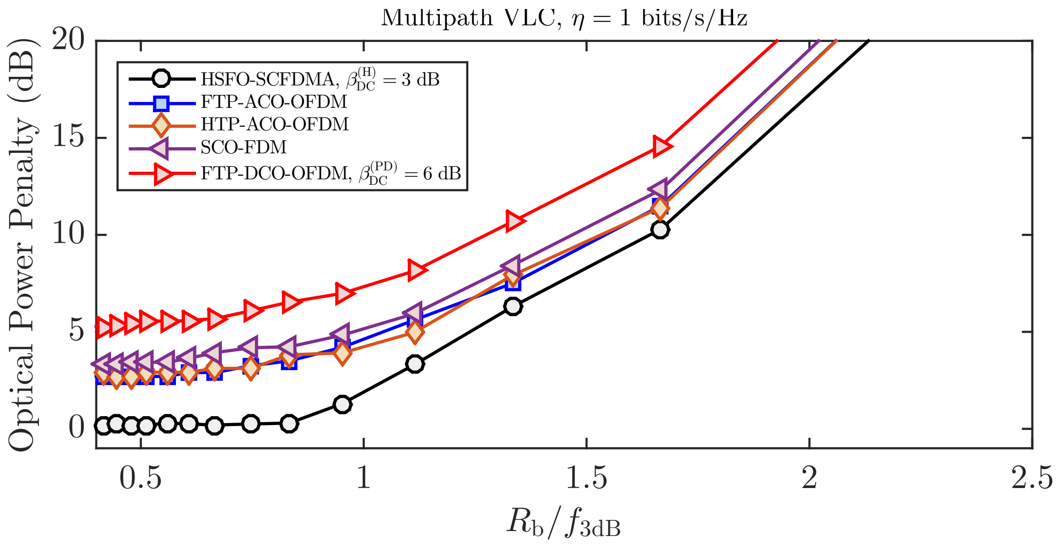

FIGURE 4.9: Optical power penalty as a function of R_b/f_{3dB} for HSFO-SCFDMA, FTP-ACO-OFDM, HTP-ACO-OFDM, SCO-FDM, and FTP-DCO-OFDM in multipath VLC channel. SE of $\eta = 1$ and $f_{3dB} = 150$ MHz is considered. The bias-index for FTP-DCO-OFDM is 6 dB, while HSFO-SCFDMA is sufficiently biased.

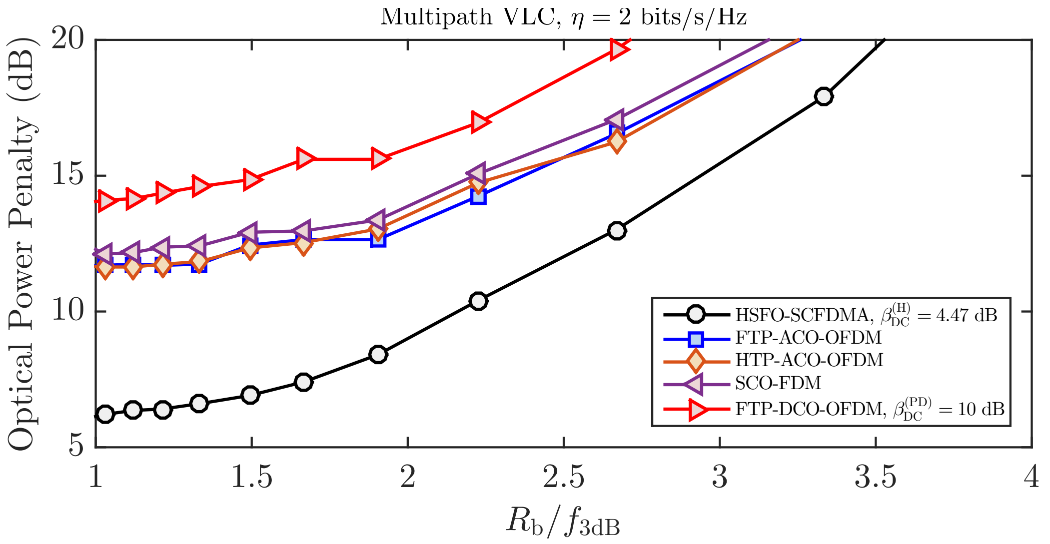

FIGURE 4.10: Optical power penalty as a function of R_b/f_{3dB} for HSFO-SCFDMA, FTP-ACO-OFDM, HTP-ACO-OFDM, SCO-FDM, and FTP-DCO-OFDM in multipath VLC channel. SE of $\eta = 2$ and $f_{3dB} = 150$ MHz is considered. The bias-index for FTP-DCO-OFDM is 10 dB, while HSFO-SCFDMA is sufficiently biased.

4.4.6 Complexity Analysis

In this section, the system complexities of various modulation schemes are analyzed. The complexity analysis in terms of probability of convergence, theoretical run-time boundaries etc. is cumbersome. Hence, system complexity is calculated in terms of a total number of required arithmetic operations at the transceiver. A block of N data symbols is taken as an input for the transceivers and is equal to the DFT/IDFT order. For an efficient implementation, DFT and IDFT are implemented utilizing fast Fourier transform (FFT) and inverse FFT (IFFT) algorithms, respectively. N-order FFT/IFFT approximately requires $4N\log_2(N)$ arithmetic operations [148]. For both O-OFDMA and O-SCFDMA systems, the complexity is either due to FFT/IFFT or equalization. Due to the diagonal nature of $\boldsymbol{\Lambda}$, equalization is realized in $\mathcal{O}(N)$ operations [156], thus, in the sequel, the complexity incurred due to FFT/IFFT is considered. The complexities of different modulation approaches are:

- For HSFO-SCFDMA, $N/2$-order FFT and N-order IFFT are performed at the transmitter, whereas, at the receiver, two $N/2$-order FFT and two $N/2$-order IFFT are required.
- For FTP-ACO-OFDM, $N/4$-order FFT and N-order IFFT are required at the transmitter, whereas, at the receiver, FFT/IFFT are inverted, i.e., N-order FFT and $N/4$-order IFFT are needed.
- In HTP-ACO-OFDM, real constellations along with DHT are used. N-order DHT approximately requires $2N\log_2(N)$ arithmetic operations [157]. At the transmitter, $N/2$-order DHT and N-order IDHT are performed. Additionally, at the receiver, N-order DHT and $N/2$-order IDHT are taken.
- For SCO-FDM, at the transmitter, $N/4$-order FFT and N-order IFFT operations are required, whereas, at the receiver, four $N/4$-order FFT and one $N/4$-order IFFT are needed.
- For FTP-DCO-OFDM, $N/2-1$-order FFT and N-order IFFT are required at the transmitter, while N-order FFT and $N/2-1$-order IFFT are taken at the receiver.

The system complexities are compiled in Table 4.3 and plotted as a function of input block size, N scaled by η, in Fig. 4.11. Scaling is performed to ensure a fair comparison, e.g., for a given R_b, if HSFO-SCFDMA requires an input block size of N, FTP-ACO-OFDM (or a scheme with similar SE) would require a block size of $2N$. Fig. 4.11 reveals that FTP-DCO-OFDM and HTP-ACO-OFDM manifest the least system complexity, whereas, HSFO-SCFDMA is less complex than FTP-ACO-OFDM and SCO-FDM. It is highlighted that even though the system complexity of HSFO-SCFDMA is marginally higher than FTP-DCO-OFDM and HTP-ACO-OFDM, yet, HSFO-SCFDMA demonstrates superior performance compared to these approaches in other performance parameters.

TABLE 4.3: Computational complexity of different modulation techniques.

Modulation Scheme	**Complexity**
HSFO-SCFDMA	$4N\log_2(N) + 10N\log_2(N/2)$
FTP-ACO-OFDM	$8N\log_2(N) + 2N\log_2(N/4)$
HTP-ACO-OFDM	$4N\log_2(N) + 2N\log_2(N/2)$
SCO-FDM	$4N\log_2(N) + 6N\log_2(N/4)$
FTP-DCO-OFDM	$8N\log_2(N) + (4N-8)\log_2(N/2-1)$

4.4.7 Quantization Characteristics

In this subsection, the impact of quantization by evaluating the effective number of bits (ENOB) required to achieve a target BER is investigated. Following [147], the required electrical SNR in AWGN, $\Gamma_{(\text{elec})}$, for the target BER, P_b, is evaluated from which the ENOB are calculated. Target BER of 10^{-3} and uniform quantization are considered. The quantization noise is modeled as an additive, uniformly distributed white noise [147].

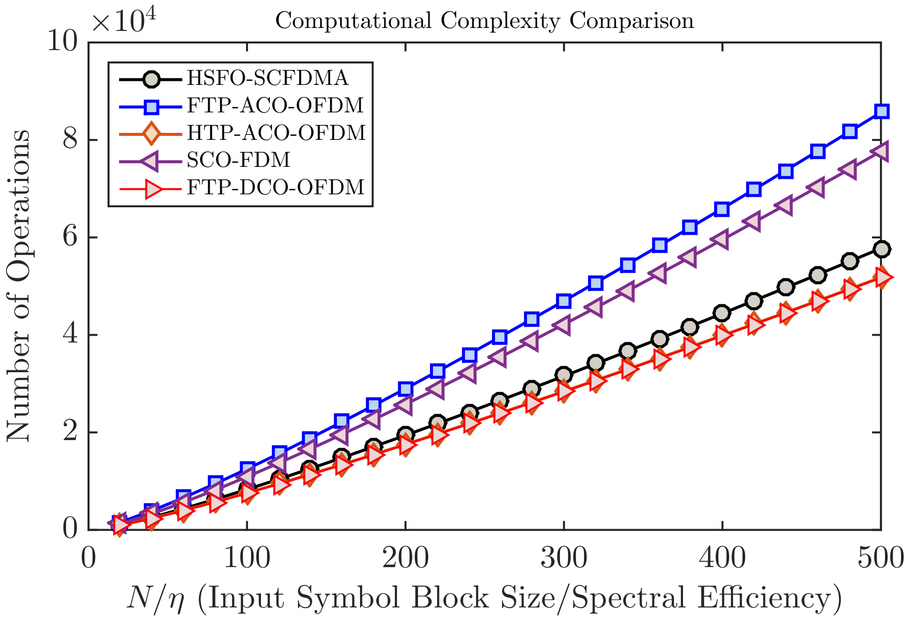

FIGURE 4.11: Complexity comparison of different modulation schemes. The block size N is normalized with the SE, η to ensure the same data-rate.

As ξ_{peak}, for HSFO-SCFDMA, HTP-ACO-OFDM, and SCO-FDM, are deterministic (see section 4.4.2), calculating the effective number of bits is rather straightforward. At the transmitter, for HSFO-SCFDMA and SCO-FDM, the TD signal manifests distinct number of levels as a function of the modulation index, M which are represented as $\gamma_{(\text{H})}$ and $\gamma_{(\text{S})}$. This simplifies the evaluation of the required effective number of bits for the transmitter of HSFO-SCFDMA and SCO-FDM which are evaluated using $\gamma_{(\text{H})}$ and $\gamma_{(\text{S})}$, therefore, does not depend on $\Gamma_{(\text{elec})}$. Whereas, for remaining approaches, Monte Carlo averaging is needed to obtain an estimate of ξ_{peak}. For simplicity, the same ENOB are considered at the transmitter and at the receiver [147]. However, for HSFO-SCFDMA and SCO-FDM, the effective number of bits required at the transmitter and at the receiver differ because the received signal would be analog and suffer from the noise, therefore, at the receiver, the bits are evaluated using $\Gamma_{(\text{elec})}$.

Table 4.4 presents the analytical formulae to compute the effective number of bits at the transmitter and receiver to achieve a BER of 10^{-3}. Graphical illustrations are provided in Fig. 4.12 and Fig. 4.13 and show that for, a given η, the ENOB required by the transmitter or the receiver of HSFO-SCFDMA are less compared to other counterparts. From the results, we can perceive that the bit resolution requirement of both the ADC and DAC can be relaxed if HSFO-SCFDMA is adopted which is due to drastic reduction of signal PAPR, consequently, the overall cost of the system can be reduced.

TABLE 4.4: Effective number of bits required at the transmitter and the receiver for different modulation schemes. $\lceil\cdot\rceil$ represents ceiling operation to nearest integer. $\gamma_{(\mathrm{H})}$ and $\gamma_{(\mathrm{S})}$, respectively, are the number of distinct levels of TD signal for HSFO-SCFDMA and SCO-FDM, respectively. $\varsigma_{(\mathrm{PD})}$ is the bias coefficient for FTP-DCO-OFDM. σ^2 represents the transmitted signal power for the respective modulation scheme. ξ_{peak} for FTP-ACO-OFDM has been evaluated after clipping.

TRANSMITTER	
Modulation Scheme	**Effective Number of Bits**
HSFO-SCFDMA	$\lceil \log_2[\gamma_{(\mathrm{H})}] \rceil$
FTP-ACO-OFDM	$\left\lceil 0.5\log_2\left[\frac{\xi^2_{\mathrm{peak}}}{6\sigma^2}\Gamma_{(\mathrm{elec})}\right]\right\rceil$
HTP-ACO-OFDM	$\left\lceil 0.5\log_2\left[\frac{2(M'-1)}{(M'+1)}\Gamma_{(\mathrm{elec})}\right]\right\rceil$
SCO-FDM	$\lceil \log_2[\gamma_{(\mathrm{S})}] \rceil$
FTP-DCO-OFDM	$\left\lceil 0.5\log_2\left[\frac{4\xi^2_{\mathrm{peak}}+\left(\lambda_{\mathrm{peak}}+\varsigma_{(\mathrm{PD})}\sigma\right)^2}{12\sigma^2}\Gamma_{(\mathrm{elec})}\right]\right\rceil$
RECEIVER	
Modulation Scheme	**Effective Number of Bits**
HSFO-SCFDMA	$\left\lceil 0.5\log_2\left[\frac{\xi^2_{\mathrm{peak}}}{3\sigma^2}\Gamma_{(\mathrm{elec})}\right]\right\rceil$
SCO-FDM	$\left\lceil 0.5\log_2\left[\frac{\xi^2_{\mathrm{peak}}}{12\sigma^2}\Gamma_{(\mathrm{elec})}\right]\right\rceil$

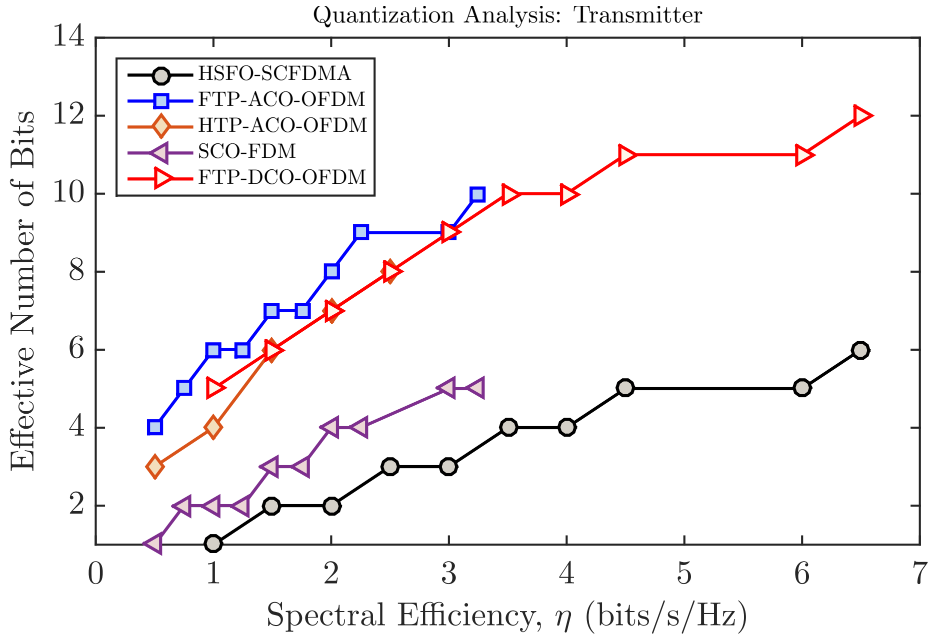

FIGURE 4.12: Effective number of bits required for quantization by the transmitter for different modulation schemes.

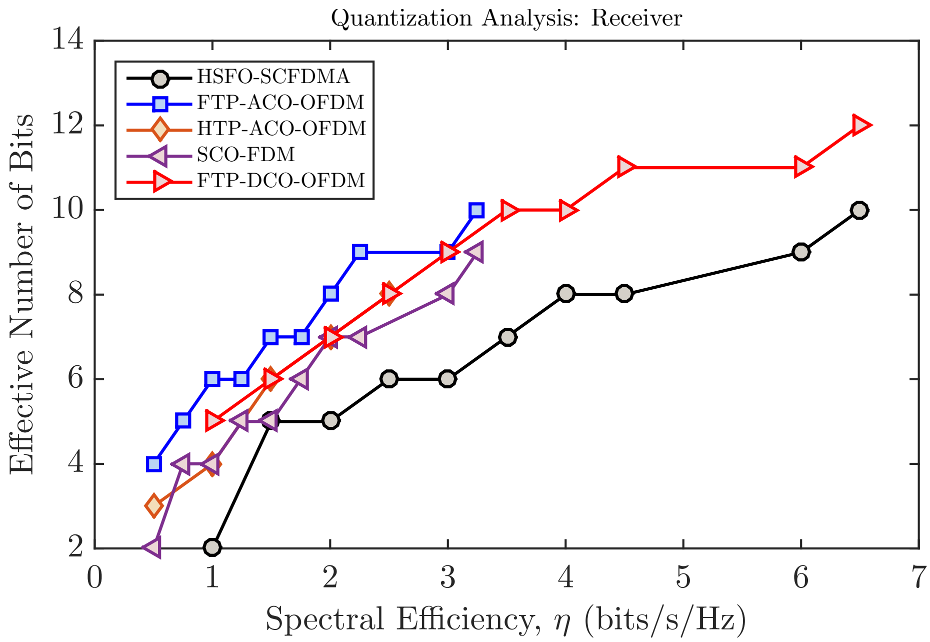

FIGURE 4.13: Effective number of bits required for quantization by the receiver for different modulation schemes.

4.4.8 Power efficiency

Fig. 4.14 and Fig. 4.15, respectively, depicts how $\langle E_{b_{(elec)}}/N_0\rangle$ and $\langle E_{b_{(opt)}}/N_0\rangle$ (the required $E_{b_{(elec)}}/N_0$ and $E_{b_{(opt)}}/N_0$ to achieve a target BER of 10^{-3}) varies with the SE, η, in an AWGN channel. A similar progession is foreseen for line-of-sight (LOS) or multipath VLC channel with limited bandwidth of LED/LED driver combination. For HSFO-SCFDMA and FTP-DCO-OFDM, η between $[1, 6.5]$ bits/s/Hz is considered, whereas, for FTP-ACO-OFDM, SCO-FDM, η between $[0.5, 3.25]$ bits/s/Hz is taken into account. Note that, $\eta = 3.25$ bits/s/Hz (for FTP-ACO-OFDM and SCO-FDM) corresponds to 8192-QAM, hence, evaluating the power efficiencies for $\eta > 3.25$ bits/s/Hz might not be meaningful. For HTP-ACO-OFDM, η between $[0.5, 2.5]$ bits/s/Hz is investigated. Besides, for FTP-DCO-OFDM, the results are obtained by recognizing 6 dB bias-index for $\eta = 1$ bits/s/Hz, 7.5 dB for $\eta = 1.5$ bits/s/Hz and a bias-index of 10 dB for $\eta \geq 2$ bits/s/Hz.

Fig. 4.14 compares the electrical power efficiencies of different modulation schemes. It is demonstrated that HSFO-SCFDMA attains superior performance compared to other alternatives, e.g., for $\eta = 2$ bits/s/Hz, a power gain of almost 5.2 dB over FTP-DCO-OFDM, and approximately 8 dB over FTP-ACO-OFDM, HTP-ACO-OFDM and SCO-FDM is observed. Moreover, for smaller values of η, FTP-DCO-OFDM signifies the same power requirement as that of FTP-ACO-OFDM, HTP-ACO-OFDM, and SCO-FDM. However, for larger values of η, FTP-DCO-OFDM becomes more power efficient compared to other approaches apart from HSFO-SCFDMA.

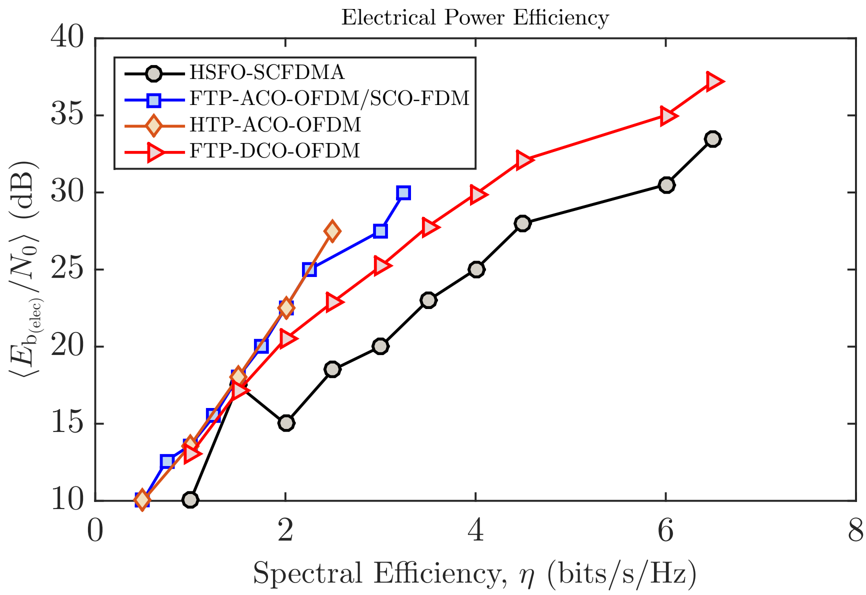

FIGURE 4.14: Analysis of electrical power efficiency of different modulation techniques. The average $E_{b_{(elec)}}/N_0$ for a BER of 10^{-3} represented as $\langle E_{b_{(elec)}}/N_0 \rangle$ has been evaluated for different spectral efficiencies, η.

Furthermore, HSFO-SCFDMA also exhibits better performance in terms of optical power efficiency compared to other counterparts as demonstrated in Fig. 4.15. It can be observed from Fig. 4.15 that FTP-DCO-OFDM requires higher $E_{b_{(opt)}}/N_0$ compared to FTP-ACO-OFDM, HTP-ACO-OFDM and SCO-FDM to achieve same BER because of the addition of the bias. Moreover, for $\eta = 3$ bits/s/Hz, HSFO-SCFDMA requires approximately 5 dB less optical power compared to FTP-ACO-OFDM, HTP-ACO-OFDM and SCO-FDM, whereas, it achieves an optical power gain of about 8 dB over FTP-DCO-OFDM for the same SE.

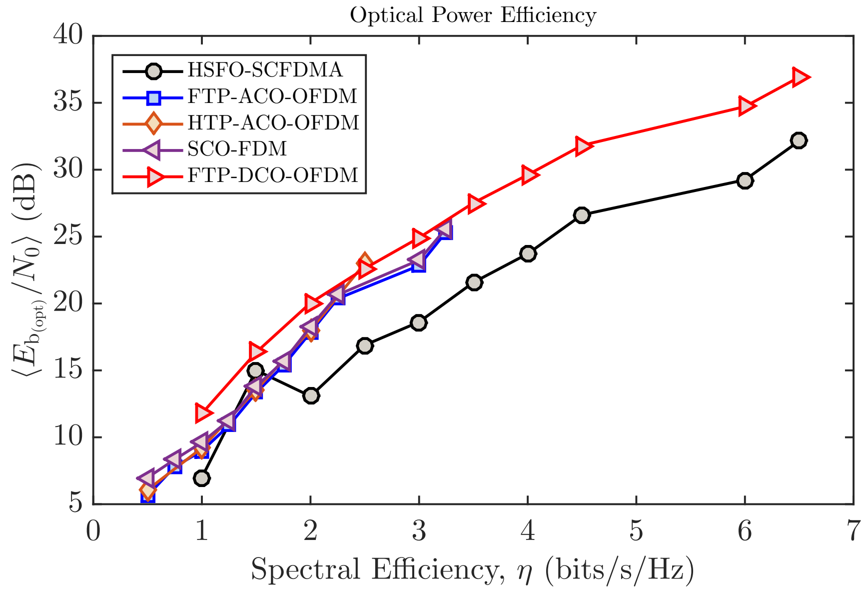

FIGURE 4.15: Analysis of optical power efficiency of different modulation techniques. The average $E_{b_{(opt)}}/N_0$ for a BER of 10^{-3} represented as $\langle E_{b_{(opt)}}/N_0 \rangle$ has been evaluated for different spectral efficiencies, η.

4.5 Multiple Access

In this section, the MA capability of HSFO-SCFDMA is presented. LED lighting source comprising a LED array, K users (constrained to be even) and N subchannels is considered. All the users use the same M-ary QAM constellations and have the feasibility to modulate $N/2^K$ subchannels. For the lth user, the TD symbol are $x_l^{(\mathrm{H})}\left(n^{(l)}\right)$ for $n^{(l)} = 0, 1, \cdots, N/2^K - 1$, whilst their corresponding DFT-precoded FD counterparts are obtained by using $N/2^K$-order DFT as:

$$X_l^{(\mathrm{H})}\left(k^{(l)}\right) = \mathrm{DFT}\left[x_l^{(\mathrm{H})}\left(n^{(l)}\right)\right], \tag{4.24}$$

for $k^{(l)} = n^{(l)}$. From (4.24), it is inferred that for K users, $N/2^K$-order DFT-precoding is required. Subchannel mapping is performed such that each user is allocated unique subchannels. For lth user, the FD precoded symbols $X_l^{(\mathrm{H})}\left(k^{(l)}\right)$ are mapped to $X_l\left(k\right)$ $\forall\, k = 0, 1, \cdots, N-1$ on indexes $2(l-1) : 2^K : N$, with $2^K - 1$ zeros padded between the two adjacent modulated subchannels. The TD counterparts of $X_l\left(k\right)$ for $l = 1, \cdots, K$ are transmitted using different LEDs in the array as depicted in Fig. 4.16 for a system with $K = 2$. N-order IDFT is applied to $X_l\left(k\right)$ to obtain:

$$x_l(n) = \mathrm{IDFT}\left[X_l\left(k\right)\right] \tag{4.25}$$

for $n = 0, 1, \cdots, N-1$. $x_l(n)$ exhibits a half-wave symmetry, from which, the real and imaginary sub-blocks for lth user are obtained as:

$$\begin{aligned} x_{\Re,l}\left(n^{(\mathrm{H})}\right) &= \Re\left[x_l\left(n^{(\mathrm{H})}\right)\right] \\ x_{\Im,l}\left(n^{(\mathrm{H})}\right) &= \Im\left[x_l\left(n^{(\mathrm{H})} + \frac{N}{2}\right)\right] \end{aligned} \tag{4.26}$$

$\forall\, n^{(\mathrm{H})} = 0, 1, \cdots, N/2 - 1$, respectively, where $\left\{x_{\Re,l}\left(n^{(\mathrm{H})}\right), x_{\Im,l}\left(n^{(\mathrm{H})}\right)\right\} \in \mathbb{R}\ \forall\, l = 1, \cdots, K$. The IM-DD consistent signal $\left[x_{\Re,l}\left(n^{(\mathrm{H})}\right); x_{\Im,l}\left(n^{(\mathrm{H})}\right)\right]^{\mathrm{T}}$ is transmitted through LEDs.

The receiver is the same as presented in Fig. 4.2. At the receiver, a signal containing the sum of all the users is obtained. After processing, the received symbols for different users are distinguished by choosing the appropriate subchannels. Note that the received symbol vector would always be $N/2$-order, from which the allocated subchannels for the lth user are obtained as $(l-1) : K : N/2$. Moreover, κ also depends on the number of users in the system, thus, if K users are considered, the value of κ would be equal to 2^K. From the presented analysis, it can be ascertained that HSFO-SCFDMA can be used in a VLC down-link scenario, for which each LED in the array transmits the data/information for a different user.

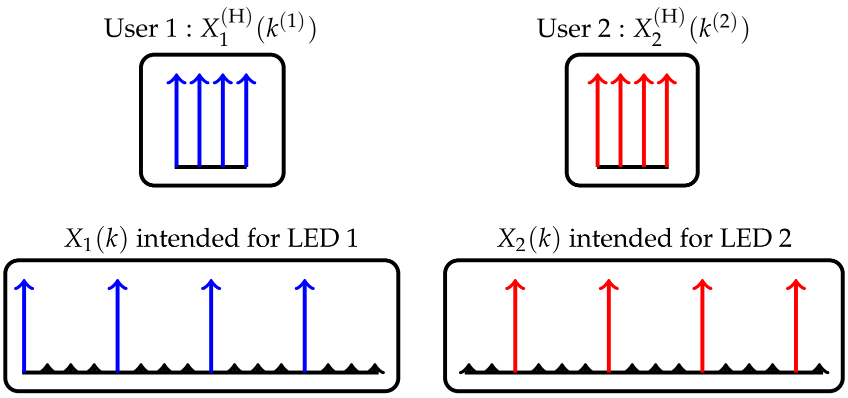

FIGURE 4.16: Illustration of subchannel mapping for two different users.

4.6 Conclusions

In this chatper, O-SCFDMA is studied as an alternate to O-OFDMA. From the study of the proposed HSFO-SCFDMA, following conclusions are drawn:

1. HSFO-SCFDMA possesses the same SE as FTP-DCO-OFDM, whereas, the spectral efficiencies of FTP-ACO-OFDM, HTP-ACO-FDM and SCO-FDM are half of HSFO-SCFDMA. The same SE as that of HSFO-SCFDMA is obtained by employing higher modulation alphabets for FTP-ACO-OFDM, HTP-ACO-FDM and SCO-FDM.
2. HSFO-SCFMA manifests significantly lower PAPR which results in power efficiency and less sensitivity to any nonlinear impairments from the LED. Moreover, the power efficiency is vital to enhance the battery life if considered for user terminal.
3. As expected from 1) and 2), it is demonstrated that the bit resolution requirement of both DAC and ADC can be relaxed for HSFO-SCFDMA, consequently, the overall cost of the system can be reduced.
4. HSFO-SCFDMA exhibits superior BER performance compared to other state-of-the-art alternatives considering a dispersive channel.
5. HSFO-SCFDMA undergoes the least optical power penalty compared to other alternatives. Besides, HSFO-SCFDMA achieves the lowest optical power penalty floor compared to other counterparts.
6. HSFO-SCFDMA is less complex than FTP-ACO-OFDM and SCO-FDM. However, it is more complex compared to FTP-DCO-OFDM and HTP-ACO-OFDM, but surpasses them in other performance parameters.
7. HSFO-SCFDMA is the most power efficient approach in terms of electrical and optical power dissipation to achieve BER of 10^{-3}.

Chapter 5

Performance Analysis of Precoded Layered ACO-OFDM for Visible Light Communication Systems

Optical-orthogonal frequency division multiplexing (O-OFDM) is as an effective scheme for intensity modulation and direct detection (IM-DD) based visible light communication (VLC) systems. State-of-the-art O-OFDM approaches complying with IM-DD constraints are; direct-current (DC) biased O-OFDM (DCO-OFDM) and asymmetrically clipped (AC) O-OFDM (ACO-OFDM). ACO-OFDM is spectrally less efficient than DCO-OFDM, howbeit, the spectral efficiency (SE) of ACO-OFDM can be augmented towards that of DCO-OFDM using layered ACO-OFDM (LACO-OFDM). Nevertheless, LACO-OFDM also suffers from high peak-to-average power ratio (PAPR), which exacerbates the non-linear distortions from the light emitting diode (LED). Forthright extention of PAPR reduction techniques devised for ACO-OFDM to LACO-OFDM is cumbersome. Therefore, precoding can be exploited as an alternative to counteract the high PAPR. As contribution, the performance of discrete Fourier transform (DFT) and discrete Hartley transform (DHT) precoding on LACO-OFDM is analyzed. The bit error rate (BER) performance is evaluated considering additive white Gaussian noise (AWGN) and time dispersive channel. The impact of superimposition of layers, PAPR, and optical-to-electrical conversion efficiency is also investigated. Moreover, the system complexities of LACO-OFDM systems with and without precoding are evaluated.

5.1 Introduction

Numerous procedures exist to generate a non-negative signal. As aforementioned, a forthright approach is to include a bias to eliminate the negative excursions, yet, the addition of bias translates to an optical energy inefficacy as in DCO-OFDM [99]. Other approaches capitalize on the frame structure of O-OFDM to attain a non-negative signal. These approaches include ACO-OFDM [100], pulse-amplitude-modulation-discrete multi-tone (PAM-DMT), Flip-OFDM [104], unipolar (U)-OFDM [105]. In ACO-OFDM and PAM-DMT, an anti-symmetric TD signal is generated, for which, the negative signal amplitudes are clipped to zero without loss of information. Besides, Flip-OFDM and U-OFDM are conceptually identical, where, the postive and the reversed-negative samples of the bipolar signals are sequentially transmitted.

To generate a non-negative TD signal for ACO-OFDM, PAM-DMT, Flip-OFDM, and U-OFDM half of the SE is sacrifized compared to DCO-OFDM. To augment the SE towards that of DCO-OFDM, so-called *hybrid* approaches are proposed. These schemes maintain the power advantage over DCO-OFDM without relinquishing half of the SE. The hybrid counterpart of ACO-OFDM is LACO-OFDM [107, 108], which stacks numerous layers of ACO-OFDM with each successive layer modulating the empty subcarriers left by the preceding layers. Similarly, augmented SE-DMT (ASE-DMT) [109] and enhanced U-OFDM (eU-OFM) [110] are hybrid systems for PAM-DMT and U-OFDM/Flip-OFDM, respectively. In eU-OFDM, TD signals are superimposed at different depths. Lowery [158] has identified that eU-OFDM experiences a cascade of bit errors and calls for either complex TD equalization or additional cyclic prefixes between the positive and the negated-negative frames.

O-OFDM approaches (conventional or hybrid) suffer from high PAPR which aggravates the impact of the nonlinear distortions from the LED. Moreover, high PAPR also leads to significant quantization noise which may limit the optical modulation efficiency [80, 40]. Albeit, numerous approaches exist to oust high PAPR of O-OFDM, e.g., [80, 134, 132], but, their candid implementation to hybrid approaches is cumbersome. Recently, Zhang *et al.* [108] introduced a tone injection based PAPR reduction approach for LACO-OFDM, however, it is associated with a substantial complexity overhead. Besides, PAPR reduction techniques such as selected-mapping (SLM), pilot assisted (PA), etc., precoding can be utilized to scale down the high PAPR because it results in a quasi single-carrier (SC) like behavior without imposing a significant complexity overhead as demonstrated in Chapter 4. In the literature, Fourier tranform precoded (FTP) ACO-OFDM (FTP-ACO-OFDM) [119, 94, 120] and Hartley transform precoded (HTP) ACO-OFDM (HTP-ACO-OFDM) [111] are investigated. FTP-ACO-OFDM is essentially identical to ACO-OFDM, however, the modulated symbols are FT precoded prior to being mapped onto different subchannels. Moreover, HTP-ACO-OFDM is also similar to ACO-OFDM, however, HS is averted because of real-valued DHT and the use of (HT precoded) PAM alphabets. Ranjha *et al.* examined the performance of precoding for ACO-OFDM and PAM-DMT [120]. However, it shall be demonstrated that the layered structure results in a different performance for precoded and non-precoded LACO-OFDM, accordingly, the conclusions rendered in [120] cannot be drawn-out for the layered counterparts.

Against this background, the performance of FTP-LACO-OFDM and HTP-LACO-OFDM is presented and is compared with that of LACO-OFDM. A comprehensive performance analysis of precoded and non-precoded LACO-OFDM has never been investigated until now. The contributions of this work are:

1. FTP-LACO-OFDM and HTP-LACO-OFDM are introduced. HTP-LACO-OFDM is distinctive from LACO-OFDM and FTP-LACO-OFDM because it precludes HS, employs PAM alphabets, and uses DHT and inverse DHT (IDHT) for multiplexing and demultiplexing rather than using DFT or inverse DFT (IDFT). The BER performance is evaluated considering AWGN and time dispersive channels. The dispersive channel incorporates the multipath VLC channel and bandwidth limitation of LED in combination with its optimized driver.

2. The impact of superimposed layered structure on the required electrical signal-to-noise ratio (SNR) per bit, $E_{\mathrm{b}_{(\mathrm{elec})}}/N_0$, PAPR and optical-to-electrical conversion efficiency are analyzed.

The chapter is organized as follows. In Section 5.2, LACO-OFDM, FTP-LACO-OFDM and HTP-LACO-OFDM are presented. Section 5.3 compares the performance of aforementioned schemes. Conclusions are drawn in Section 5.4.

Moreover, LACO, FTP and HTP in the subscript of a parameter, e.g., $(\cdot)_{\mathrm{LACO}}$, $(\cdot)_{\mathrm{FTP}}$ and $(\cdot)_{\mathrm{HTP}}$ is used to distinguish between LACO-OFDM, FTP-LACO-OFDM and HTP-LACO-OFDM. Alternatively, for brevity, $(\cdot)$ in the subscript of a parameter is used to specify all the approaches, e.g., $\alpha_{(\cdot)}$ means α_{LACO}, α_{FTP} and α_{HTP}.

5.2 Layered ACO-OFDM and Precoding

In this section, LACO-OFDM, FTP-LACO-OFDM and HTP-LACO-OFDM are presented. N subcarriers/subchannels and L layers for each approach are considered. A generalized transmitter structure of precoded and non-precoded LACO-OFDM is presented in Fig. 5.1. Moreover, the receiver structures of LACO-OFDM and precoded LACO-OFDM are illustrated in Fig. 5.3 and Fig. 5.4, respectively. The modulators for ACO-OFDM, FTP-LACO-OFDM and HTP-ACO-OFDM are illustrated in Fig. 5.2.

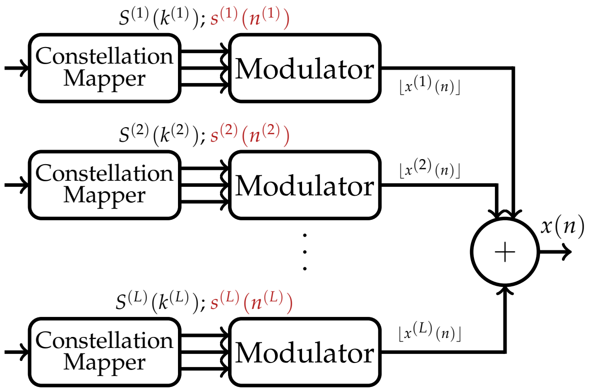

FIGURE 5.1: Transmitter structure for the layered approaches. For LACO-OFDM, the input to the modulator is expressed in black. For FTP-LACO-OFDM and HTP-LACO-OFDM, the input to the modulator is expressed in red.

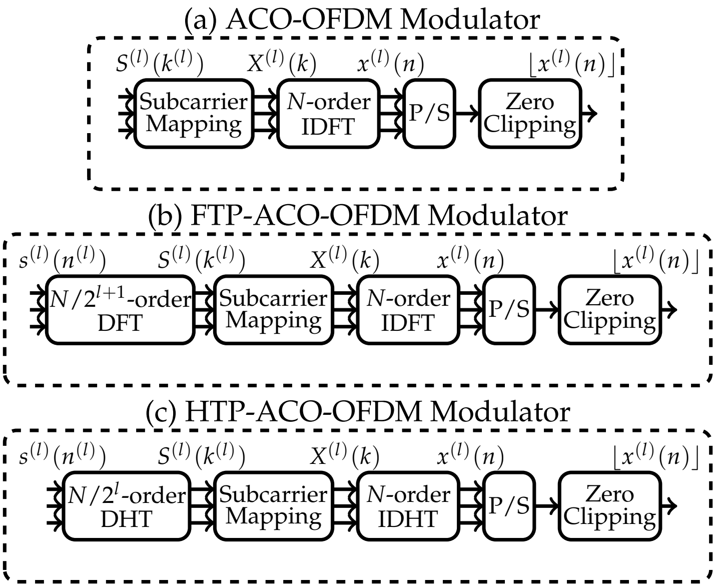

FIGURE 5.2: Modulators for LACO-OFDM, FTP- LACO-OFDM and HTP-LACO-OFDM.

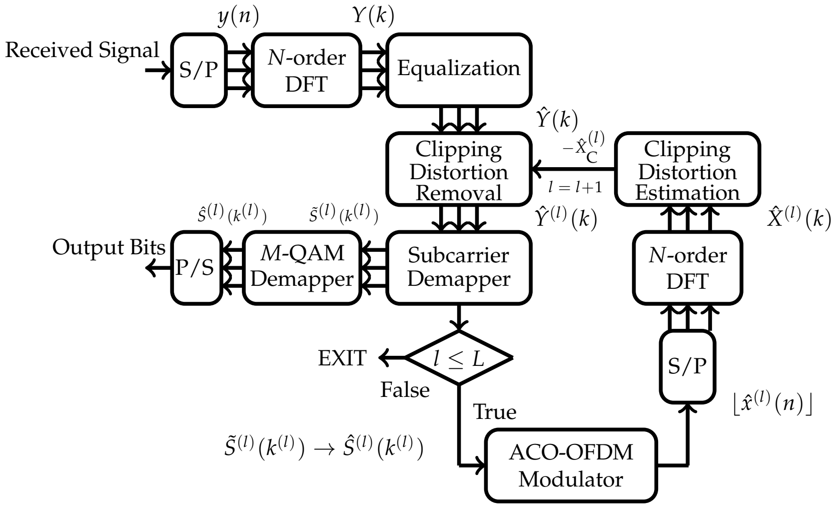

FIGURE 5.3: Receiver structure for the LACO-OFDM.

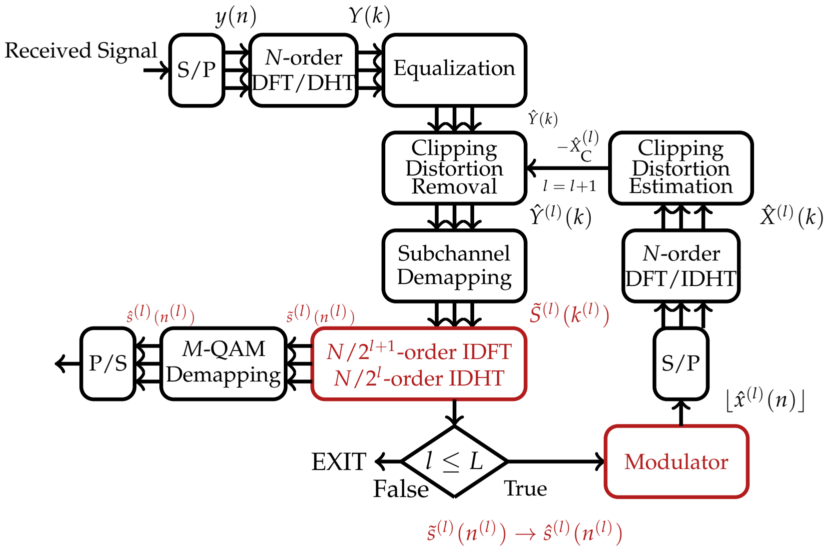

FIGURE 5.4: Receiver structure for the precoded LACO-OFDM approaches.

5.2.1 LACO-OFDM

For lth layer, the incoming bit stream is mapped onto M-ary quadrature-amplitude modulation (QAM) FD symbols, $S^{(l)}\left(k^{(l)}\right), k^{(l)} = 0, 1, \cdots, N/2^{l+1} - 1$, taken from constellation set $\mathcal{Q} = \{\mathcal{Q}_0, \mathcal{Q}_1, \cdots, \mathcal{Q}_{M-1}\}$. $S^{(l)}\left(k^{(l)}\right)$ are assigned to N-length signal, $X^{(l)}(k), k = 0, 1, \cdots, N-1$ by adhering to HS as:

$$X^{(l)}(k) = \begin{cases} S^{(l)}(k^{(l)}), & k = 2^{l-1}\left(2k^{(l)}+1\right) \\ S^{*(l)}(k^{(l)}), & k = N - 2^{l-1}\left(2k^{(l)}+1\right) \\ 0, & \text{elsewhere} \end{cases} . \tag{5.1}$$

As an example, the FD signals for LACO-OFDM considering $L = 3$ and $N = 16$ are presented in Fig. 5.5.

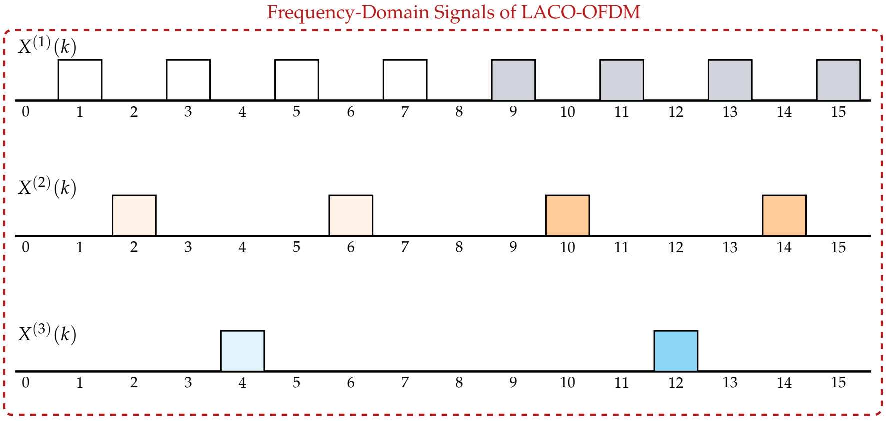

FIGURE 5.5: FD signals for LACO-OFDM considering $L = 3$ and $N = 16$. The lighter shades represent the data symbols and the darker shades are used for Hermitian symmetric symbols.

A TD signal, $x^{(l)}$ is obtained via an N-order IDFT as:

$$x^{(l)}(n) = \text{IDFT}\left[X^{(l)}(k)\right], \tag{5.2}$$

for $n = 0, 1, \cdots, N-1$. $x^{(l)}$ is anti-symmetric, i.e.,

$$x^{(l)}\left(\tilde{n}^{(l)}\right) = -x^{(l)}\left(\tilde{n}^{(l)} + \frac{N}{2^l}\right)$$

with $\tilde{n}^{(l)} = 0, 1, \cdots, N/2^l - 1$. Moreover, for $l > 1$, $x^{(l)}(n) = x^{(l)}\text{mod}\left(n, N/2^{l-1}\right)$, where $\text{mod}(\cdot, N)$ is the modulo N operator. An illustration of TD signals of LACO-OFDM at different layers is given in Fig. 5.6.

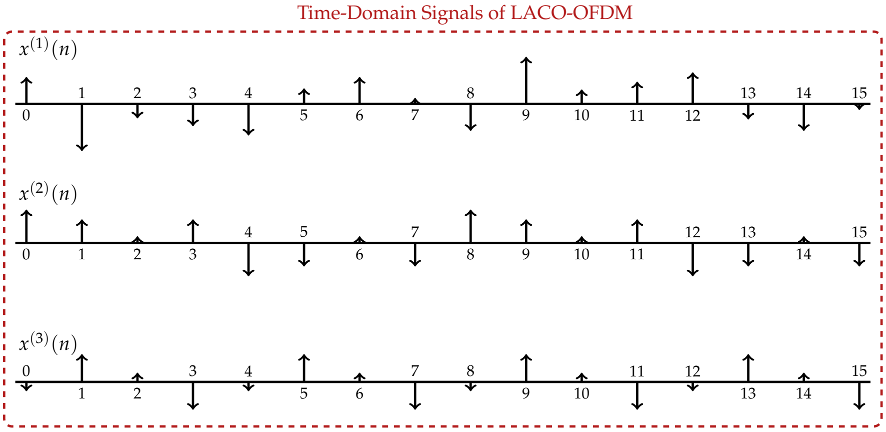

FIGURE 5.6: TD signals for LACO-OFDM considering $L = 3$ and $N = 16$.

Since, $x^{(l)}(n)$ for different layers is anti-symmetric, hence, it can be clipped to zero without loss of information to yield:

$$\lfloor x^{(l)}(n) \rfloor = \begin{cases} x^{(l)}(n), & x^{(l)}(n) \geq 0 \\ 0, & x^{(l)}(n) < 0 \end{cases} = x_{\text{D}}^{(l)}(n) + x_{\text{C}}^{(l)}(n), \tag{5.3}$$

where $x_{\mathrm{D}}^{(l)}(n)$ and $x_{\mathrm{C}}^{(l)}(n)$ is the data-carrying signal and the clipping distortion for lth layer, respectively. $x_{\mathrm{D}}^{(l)}(n)$ and $x_{\mathrm{C}}^{(l)}(n)$ are given as [159]:

$$x_{\mathrm{D}}^{(l)}(n) = \frac{1}{2}x^{(l)}(n), \tag{5.4}$$

and

$$x_{\mathrm{c}}^{(l)}(n) = |x^{(l)}(n)|, \tag{5.5}$$

respectively. The subcarriers at indexes $k_{\mathrm{D}}^{(l)} = 2^{l-1}\left(2k^{(l)}+1\right)$ are data-carrying, whereas, the clipping distortion falls on subcarriers with indexes $k_{\mathrm{C}}^{(l)} = 2^{l}k^{(l)}$. $\lfloor\cdot\rfloor$ respresents zero level clipping operation. The TD and FD view of the clipped LACO-OFDM signals at different layers are presented in Fig. 5.7 and Fig. 5.8, respectively.

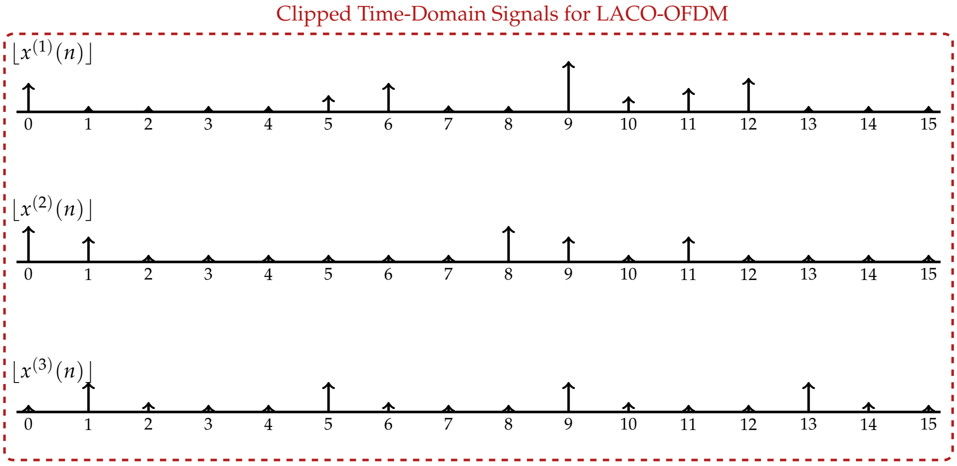

FIGURE 5.7: Clipped TD signals for LACO-OFDM considering $L = 3$ and $N = 16$.

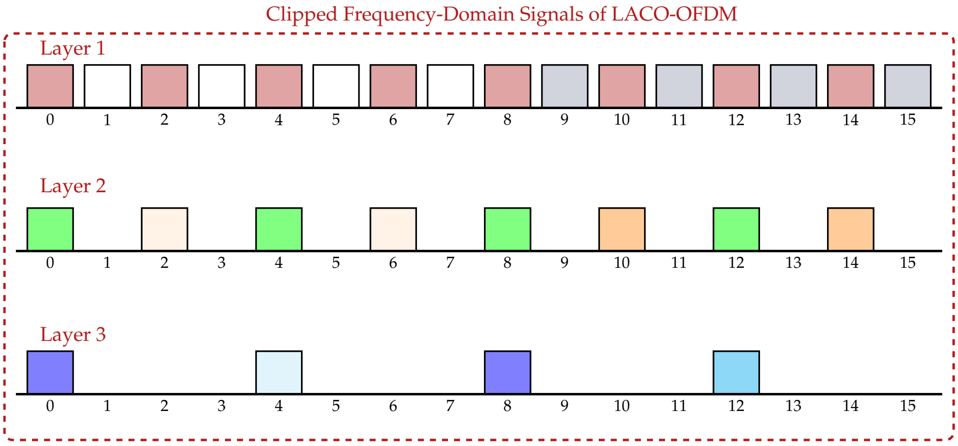

FIGURE 5.8: TD signals for LACO-OFDM considering $L = 3$ and $N = 16$. For $L = 1$, $L = 2$ and $L = 3$, the pink, green and purple shades represents the FD clipping distortion.

The clipped signals for all the layers, i.e., $\lfloor x^{(l)}(n) \rfloor$ for $l = 1, 2, \cdots, L$ are combined as:

$$x(n) = \sum_{l=1}^{L} \lfloor x^{(l)}(n) \rfloor, \tag{5.6}$$

to attain a TD signal compatible with IM-DD constraints; an illustration of which is presented in Fig. 5.9. After digital-to-analog conversion of $x(n)$ via digital-to-analog converter (DAC), $x(t)$ is obtained which is transmitted to an optical wireless channel using LED.

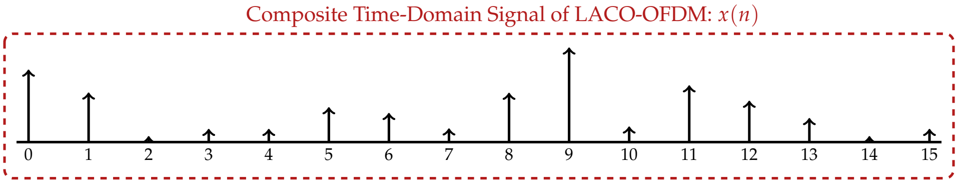

FIGURE 5.9: The composite TD LACO-OFDM signal obtained after the addition of clipped TD signals at different layers. Here, $N = 16$ and $L = 3$ are considered.

Moreover, an illustration of the FD view of the composite LACO-OFDM is given in Fig. 5.10. It can be observed that the data of $L = 1$ can be easily obtained, however, for subsequent layers, the data is embedded with the distortion from the previous layer. Hence, for correct detection of the data at a given layer, the distortion imposed by the previous layers has to be alleviated. It can be observed that the receiver structure of LACO-OFDM illustrated in Fig. 5.3, has an iterative structure which mitigates the clipping distortion from the previous layer prior to obtaining the data for the given layer.

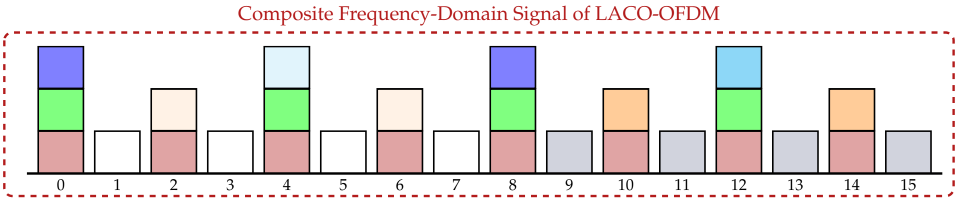

FIGURE 5.10: The composite FD LACO-OFDM signal obtained after the addition of clipped FD signals at different layers. Here, $N = 16$ and $L = 3$ are considered.

At the receiver, the received signal is impinged on an analog-to-digital converter (ADC) to obtain $y(n)$, which is then fed to N-order DFT to yield:

$$Y(k) = \text{DFT}\left[y(n)\right] = H(k)X(k) + W(k), \tag{5.7}$$

with $H(k)$ being the channel frequency response for the kth subcarrier. A single-tap equalization (either minimum mean square equalization (MMSE) or zero-forcing (ZF)) is applied on $Y(k)$, which yields:

$$\hat{Y}(k) = \hat{X}(k) + Z(k). \tag{5.8}$$

where $Z(k)$ is the FD colored noise after equalization. The equalized signal, $\hat{Y}(k)$ can be rewritten for LACO-OFDM as:

$$\hat{Y}(k) = \sum_{l=1}^{L} \hat{X}_{\text{D}}^{(l)}(k) + \sum_{l=1}^{L} \hat{X}_{\text{C}}^{(l)}(k) + Z(k), \tag{5.9}$$

where $\hat{X}_{\mathrm{D}}^{(l)}(k)$ and $\hat{X}_{\mathrm{C}}^{(l)}(k)$ are FD counterparts of $x_{\mathrm{D}}^{(l)}(n)$ and $x_{\mathrm{C}}^{(l)}(n)$ after equalization. Transmitted data on different layers is detected on a layer-to-layer basis. For layer 1, no clipping distortion falls on data-carrying subcarriers, hence, $\hat{X}_{\mathrm{C}}^{(1)}(k) = 0$ and $\hat{Y}^{(1)}(k) = \hat{Y}(k)$, from which, the transmitted data is retrieved by selecting the appropriate subcarriers identified by $k_{\mathrm{D}}^{(1)}$ as $\tilde{S}^{(1)}\left(k^{(1)}\right) = \hat{Y}^{(1)}\left(k_{\mathrm{D}}^{(1)}\right)$. Decisions on which are made as:

$$\hat{S}^{(1)}\left(k^{(1)}\right) = \arg \min_{X_Q \in \mathcal{Q}} \left\| 2\tilde{S}^{(1)}\left(k^{(1)}\right) - X_Q \right\|, \tag{5.10}$$

for $k^{(1)} = 0, 1, \cdots, N/4 - 1$. For successive layers, $l > 1$, clipping distortion influencing the data-carrying subcarriers comes from $(l-1)$th layer, therefore, $\hat{Y}^{(l)}(k) = \hat{Y}^{(l-1)}(k) - \hat{X}_{\mathrm{C}}^{(l)}(k)$. $\hat{X}_{\mathrm{C}}^{(l)}(k)$ is estimated using $\hat{S}^{(l-1)}\left(k^{(l-1)}\right)$ and subtracted from $\hat{Y}^{(l)}(k)$. The transmitted data is obtained as $\tilde{S}^{(l)}\left(k^{(l)}\right) = \hat{Y}^{(l)}\left(k_{\mathrm{D}}^{(l)}\right)$ and identified as:

$$\hat{S}^{(l)}\left(k^{(l)}\right) = \arg \min_{X_Q \in \mathcal{Q}} \left\| 2\tilde{S}^{(l)}\left(k^{(l)}\right) - X_Q \right\|, \tag{5.11}$$

for $k^{(l)} = 0, 1, \cdots, N/2^{l+1} - 1$.

5.2.2 FTP-LACO-OFDM

For FTP-LACO-OFDM, besides the operations required by LACO-OFDM, FT precoding and FT decoding are required at the transmitter and the receiver, respectively. The serially incoming bits at lth layer are mapped onto M-ary QAM TD symbols, $s^{(l)}\left(n^{(l)}\right), n^{(l)} = 0, 1, \cdots, N/2^{l+1} - 1$ drawn from $\mathcal{Q}$ (rather than onto FD symbols as in LACO-OFDM). Afterwards, $s^{(l)}\left(n^{(l)}\right)$ are DFT precoded via $N/2^{l+1}$-order DFT to yield $S^{(l)}\left(k^{(l)}\right)$ as:

$$S^{(l)}\left(k^{(l)}\right) = \mathrm{DFT}\left[s^{(l)}\left(n^{(l)}\right)\right], \tag{5.12}$$

for $k^{(l)} = n^{(l)}$. The subsequent operations required at the transmitter of FTP-LACO-OFDM are the same as demonstrated in (5.1)-(5.6) for LACO-OFDM. However, the receiver, DFT decoding is needed prior to the detection of transmitted data. For each layer, after obtaining $\tilde{S}^{(l)}\left(k^{(l)}\right)$ as in LACO-OFDM, FT decoding is implemented via $N/2^{l+1}$-order IDFT to achieve $\tilde{s}^{(l)}\left(n^{(l)}\right)$ as:

$$\tilde{s}^{(l)}\left(n^{(l)}\right) = \mathrm{IDFT}\left[\tilde{S}^{(l)}\left(k^{(l)}\right)\right], \tag{5.13}$$

Following which, the transmitted data on layer l is detected as:

$$\hat{s}^{(l)}\left(n^{(l)}\right) = \arg \min_{X_Q \in \mathcal{Q}} \left\| 2\tilde{s}^{(l)}\left(n^{(l)}\right) - X_Q \right\|. \tag{5.14}$$

Contrary to LACO-OFDM, where the estimate of clipping distortion for lth layer, $\hat{X}_{\mathrm{C}}^{(l)}(k)$ is obtained using $\hat{S}^{(l-1)}\left(k^{(l-1)}\right)$, in FTP-LACO-OFDM, $\hat{X}_{\mathrm{C}}^{(l)}(k)$ is estimated via $\hat{s}^{(l-1)}\left(n^{(l-1)}\right)$.

5.2.3 HTP-LACO-OFDM

It is recalled that HTP-LACO-OFDM differs from both LACO-OFDM and FTP-LACO-OFDM. Some of the main contrasts are:

1. the transmitted symbols are drawn from $\sqrt{M}$-ary PAM constellations rather than M-ary QAM alphabets;
2. HS is not enforced as in both LACO-OFDM and FTP-LACO-OFDM;
3. real-valued IDHT/DHT is used for multiplexing/demultiplexing rather than IDFT/DFT.

For layer l, the bits are mapped to $\sqrt{M}$-ary PAM TD symbols, $s^{(l)}\left(n^{(l)}\right)$, $n^{(l)} = 0, 1, \cdots, N/2^l - 1$, drawn from constellation $\boldsymbol{\mathcal{P}} = \left\{\mathcal{P}_0, \mathcal{P}_1, \cdots, \mathcal{P}_{\sqrt{M}-1}\right\}$. $s^{(l)}\left(n^{(l)}\right)$ are precoded using $N/2^l$-order DHT as:

$$S^{(l)}\left(k^{(l)}\right) = \text{DHT}\left[s^{(l)}\left(n^{(l)}\right)\right], \tag{5.15}$$

for $k^{(l)} = n^{(l)}$. Subchannel mapping is performed by allocating $S^{(l)}\left(k^{(l)}\right)$ to the N-length signal, $X^{(l)}(k), k = 0, 1, \cdots, N-1$ as:

$$X^{(l)}(k) = \begin{cases} S^{(l)}(k^{(l)}), & k = 2^{l-1}\left(2k^{(l)}+1\right) \\ 0, & \text{elsewhere} \end{cases}. \tag{5.16}$$

(5.16) differs from (5.1) because HS is precluded. Afterwards, the subchannels are multiplexed using N-order IDHT as:

$$x^{(l)}(n) = \text{IDHT}\left[X^{(l)}(k)\right], \tag{5.17}$$

for $n = 0, 1, \cdots, N-1$. $x^{(l)}(n)$ also follow anti-symmetric characteristics, i.e.,

$$x^{(l)}\left(n^{(l)}\right) = -x^{(l)}\left(n^{(l)} + \frac{N}{2^l}\right). \tag{5.18}$$

$x^{(l)}(n)$ is then clipped as indicated in (5.3) to yield $\lfloor x^{(l)}(n) \rfloor$. Afterwards, $x(n)$ is attained as demonstrated in (5.6) by adding $\lfloor x^{(l)}(n) \rfloor$ for all the layers and then transmitted through the LED after digital-to-analog conversion. Similarly to LACO-OFDM and FTP-LACO-OFDM, in HTP-LACO-OFDM, the data-carrying subchannels on lth layer are identified by indexes $k_{\text{D}}^{(l)} = 2^{l-1}\left(2k^{(l)}+1\right)$, whereas, the lth layer clipping distortion falls on subchannels with index $k_{\text{C}}^{(l)} = 2^l k^{(l)}$.

The equalized signal for HTP-LACO-OFDM is written as (5.9), however, the equalization process for DHT/IDHT based techniques is different, therefore, it can be carried out as explained for HTP-ACO-OFDM in Chapter 2. To identify the transmitted data, the clipping distortion for the corresponding layer has to be removed, hence, $\hat{Y}^{(l)}(k) = \hat{Y}^{(l-1)}(k) - \hat{X}_{\text{C}}^{(l)}(k)$. For $l = 1$, no clipping distortion falls on the data-carrying subcarriers, i.e., $\hat{X}_{\text{C}}^{(1)}(k) = 0$, therefore, $\hat{Y}^{(1)}(k) = \hat{Y}(k)$. Whereas, for the following layers, $l > 1$, $\hat{X}_{\text{C}}^{(l)}(k)$ is obtained via $\hat{s}^{(l-1)}\left(n^{(l-1)}\right)$ and is subtracted from $\hat{Y}^{(l)}(k)$. For each layer, the appropriate subcarriers are identified as $\tilde{S}^{(l)}\left(k^{(l)}\right) = \hat{Y}^{(l)}\left(k_{\text{D}}^{(l)}\right)$. Afterwards, HT decoding is performed using $N/2^l$-order IDHT, which yields:

$$\tilde{s}^{(l)}\left(n^{(l)}\right) = \text{IDHT}\left[\tilde{S}^{(l)}\left(k^{(l)}\right)\right], \tag{5.19}$$

Lastly, the transmitted data is identified as:

$$\hat{s}^{(l)}\left(n^{(l)}\right) = \arg \min_{X_P \in \mathcal{P}} \left\| 2\tilde{s}^{(l)}\left(n^{(l)}\right) - X_P \right\|. \tag{5.20}$$

5.3 Performance evaluation and discussion

5.3.1 Layering attenuation

Recognizing the same modulation alphabets for all layers, fair power allocation is adopted, wherein, the average electrical power apportioned to a layer corresponds to the number of data-carrying subcarriers/subchannels. Thus, the average electrical power of the lth layer, $P^{(l)}_{(\text{elec},\cdot)}$ is half of $(l-1)$th layer, $P^{(l-1)}_{(\text{elec},\cdot)}$ yielding

$$P^{(l)}_{(\text{elec},\cdot)} = \frac{1}{2} P^{(l-1)}_{(\text{elec},\cdot)}, \tag{5.21}$$

for $l = 2, 3, \cdots, L$. For M-ary QAM based LACO-OFDM and FTP-LACO-OFDM, $P^{(1)}_{(\text{elec,LACO})} = P^{(1)}_{(\text{elec,FTP})} = \sigma_x^2/2 = (M-1)/6$, whereas, for HTP-LACO-OFDM using $\sqrt{M}$-ary PAM, $P^{(1)}_{(\text{elec,HTP})} = \sigma_x^2/2 = (M-1)/12$. σ_x^2 is defined as $E\left(|x^{(1)}(n)|^2\right)$ for all approaches.

It is highlighted that the evaluation of closed-form expressions for $P_{(\text{elec,LACO})}$ is easy as the TD signal at each layer, i.e., $x^{(l)}(n)$ manifests a Gaussian distribution. Therefore, the distribution of the composite signal which is sum of all the TD signals (unclipped) is also Gaussain, which leads to a simple analysis. A graphical illustration of unclipped TD LACO-OFDM signals is presented in Fig. 5.11. This implies that the distribution of $x(n)$ would be truncated Gaussian with the negative half entirely clipped.

The evaluation of closed-form expressions for the distribution of unclipped TD signals for FTP-LACO-OFDM and HTP-LACO-OFDM is cumbersome. The graphical illustration of pdf for unclipped TD signals is demonstrated in Fig. 5.12 and Fig. 5.13 which reveals that a significant mathematical modeling is required to determine the closed-form expressions for the distributions. Even then, the distribution would change with change in the size of modulation alphabet, M or $\sqrt{M}$. Hence, for every modulation alphabet, a unique expression for the distribution has to be evaluated.

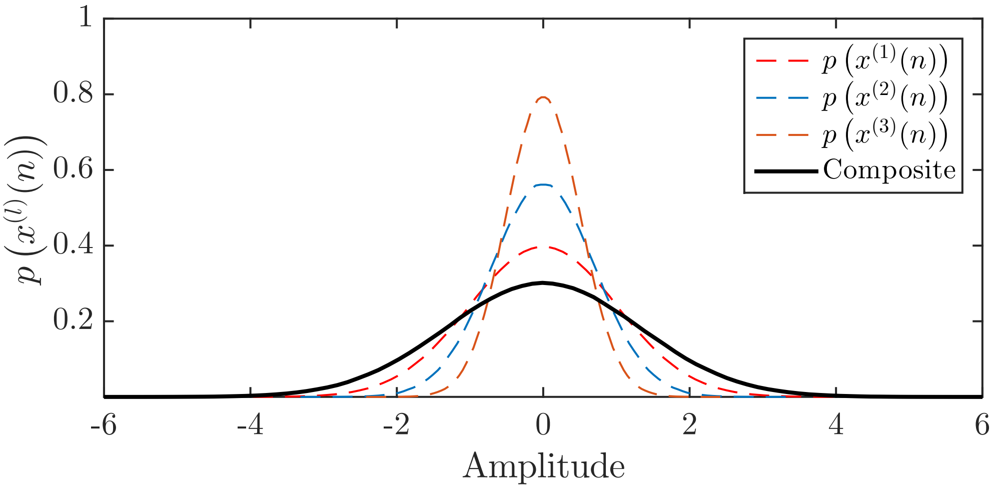

FIGURE 5.11: Probability density function for unclipped TD LACO-OFDM signals.

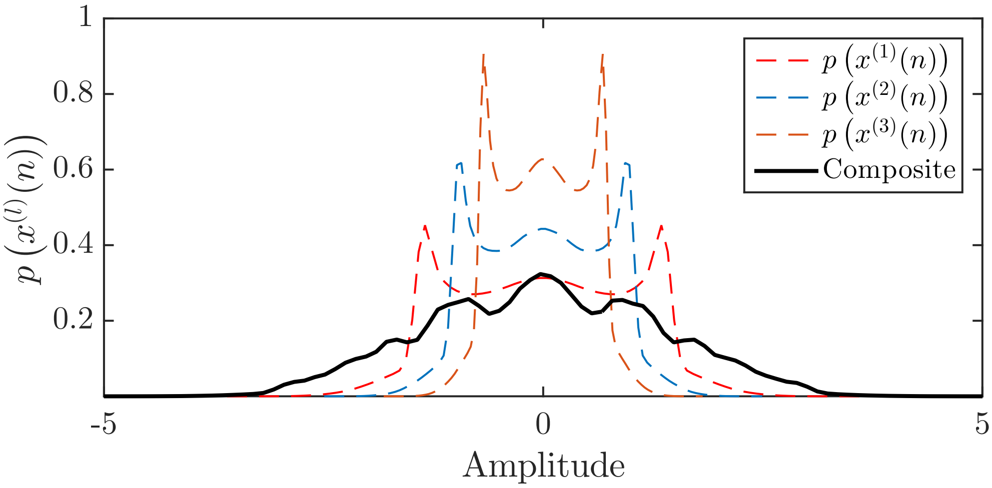

FIGURE 5.12: Probability density function for unclipped TD FTP-LACO-OFDM signals.

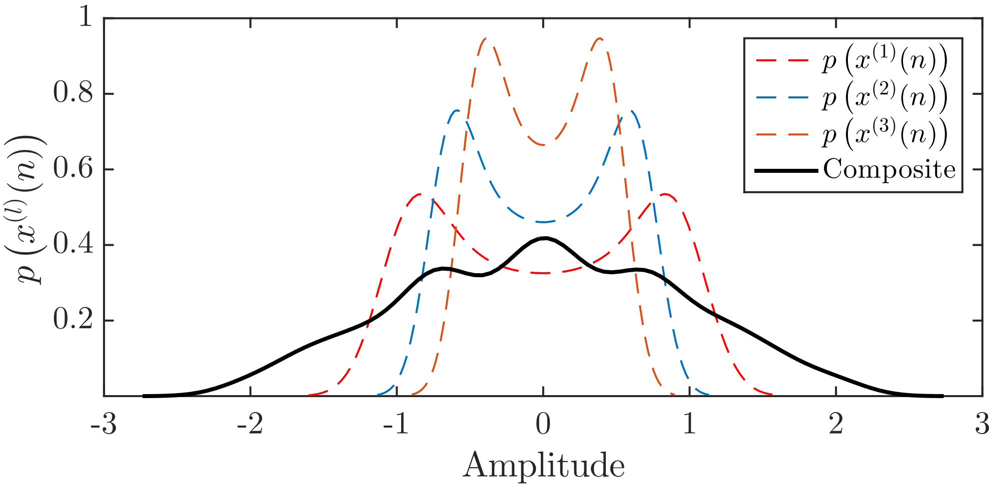

FIGURE 5.13: Probability density function for unclipped TD HTP-LACO-OFDM signals.

The average number of bits encoded in layered variants with L layers are:

$$\Theta = 2 - \frac{1}{2^{L-1}} 1 \tag{5.22}$$

times more than the number of bits encoded in traditional counterparts [110]. The layered variants; LACO-OFDM, FTP-LACO-OFDM and HTP-LACO-OFDM emanate an increase in required $E_{\mathrm{b}_{(\mathrm{elec})}}/N_0$ (as for that matter in $E_{\mathrm{b}_{(\mathrm{opt})}}/N_0$) compared to their conventional counterparts. This increase is quantified using (5.21) as [110, 109]:

$$\alpha_{(\cdot)}(L,\cdot) = \frac{1}{\Theta}\left(\frac{P_{(\mathrm{elec},\cdot)}}{P^{(1)}_{(\mathrm{elec},\cdot)}}\right). \tag{5.23}$$

For LACO-OFDM, $\alpha_{(\cdot)}(L,\cdot)$ depends only on the number of layers, L, whereas, for FTP-LACO-OFDM and HTP-LACO-OFDM, $\alpha_{(\cdot)}(L,\cdot)$ depends on both the number of layers, L, and modulation alphabet size, M or $\sqrt{M}$. Hence, this can be explicity written as $\alpha_{\mathrm{LACO}}(L)$, $\alpha_{\mathrm{FTP}}(L,M)$ and $\alpha_{\mathrm{HTP}}(L,\sqrt{M})$.

Simulation results obtained using (5.23) are presented in Fig. 5.14 which reveals that

$$\alpha_{\text{LACO}}(L) < \alpha_{\text{FTP}}(L, M) < \alpha_{\text{HTP}}(L, \sqrt{M}), \tag{5.24}$$

hence, it can be concluded that LACO-OFDM incurs a lower deterioration in $E_{\text{b}_{\text{(elec)}}}/N_0$ than FTP-LACO-OFDM and HTP-LACO-OFDM for both $M = \{4, 16\}$. Another distinctive pattern which can be observed from Fig. 5.14 is that the attenuation that is caused by stacking of layers for FTP-LACO-OFDM and HTP-LACO-OFDM decreases with the increase in modulation alphabet size, M or $\sqrt{M}$.

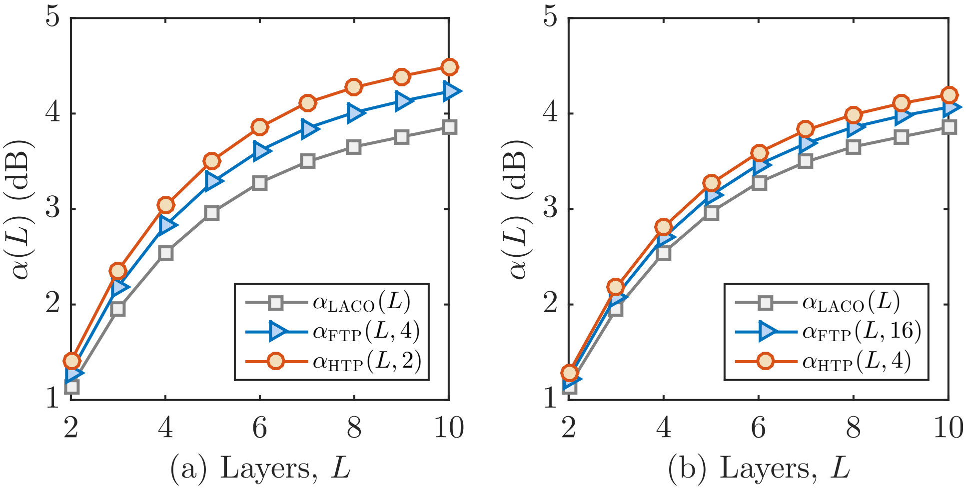

FIGURE 5.14: Increase in $E_{\text{b}_{\text{(elec)}}}/N_0$ as a function of number of layers, L: (a) $M = 4$; (b) $M = 16$.

5.3.2 Optical-to-electrical conversion efficiency

The optical-to-electrical conversion efficiency is obtained as:

$$\alpha_{(\cdot)}^{\text{OE}} = \frac{P_{(\text{elec},\cdot)}}{P_{(\text{opt},\cdot)}}, \tag{5.25}$$

where, $P_{(\text{opt},\cdot)}$ is the average optical power which is scaled to unity for each approach to obtain $\alpha_{(\cdot)}^{\text{OE}}$. Owing to (5.25), the relationship between the electrical SNR per bit, $E_{\text{b}_{\text{(elec)}}}/N_0$ and optical SNR per bit, $E_{\text{b}_{\text{(opt)}}}/N_0$, is given as:

$$\alpha_{(\cdot)}^{\text{OE}} \frac{E_{\text{b}_{\text{(opt)}}}}{N_0} = \frac{E_{\text{b}_{\text{(elec)}}}}{N_0}. \tag{5.26}$$

Therefore, for any $E_{\text{b}_{\text{(elec)}}}/N_0$, the corresponding $E_{\text{b}_{\text{(opt)}}}/N_0$ can be obtained by scaling $E_{\text{b}_{\text{(elec)}}}/N_0$ by $\alpha_{(\cdot)}^{\text{OE}}$. Higher value of $\alpha_{(\cdot)}^{\text{OE}}$ implies better optical-to-electrical conversion efficiency. For LACO-OFDM, $\alpha_{(\cdot)}^{\text{OE}}$ depends on the number of layers, L, whereas, for FTP-LACO-OFDM and HTP-LACO-OFDM, $\alpha_{(\cdot)}^{\text{OE}}$ is constrained by L and the modulation alphabet size, M or $\sqrt{M}$. So, explicitly, we can write as $\alpha_{\text{LACO}}^{\text{OE}}(L)$, $\alpha_{\text{FTP}}^{\text{OE}}(L, M)$ and $\alpha_{\text{HTP}}^{\text{OE}}(L, \sqrt{M})$. The simulated $\alpha_{(\cdot)}^{\text{OE}}$ is depicted in Fig. 5.15, which reveals that LACO-OFDM has the best optical-to-electrical conversion efficiency. Moreover, FTP-LACO-OFDM is more efficient than HTP-LACO-OFDM, i.e.,

$$\alpha^{\mathrm{OE}}_{\mathrm{LACO}}(L) > \alpha^{\mathrm{OE}}_{\mathrm{FTP}}(L, M) > \alpha^{\mathrm{OE}}_{\mathrm{HTP}}(L, \sqrt{M}). \tag{5.27}$$

Furthermore, $\alpha^{\mathrm{OE}}_{\mathrm{FTP}}(L, M)$ and $\alpha^{\mathrm{OE}}_{\mathrm{HTP}}(L, \sqrt{M})$ increases with an increase in modulation alphabet, M or $\sqrt{M}$, respectively.

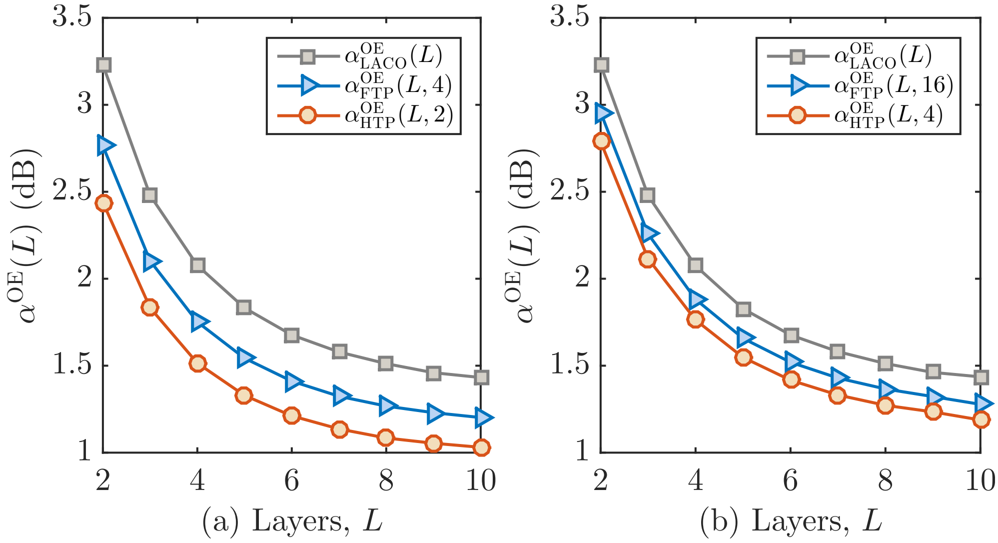

FIGURE 5.15: Optical-to-electrical conversion gain for LACO-OFDM: (a) $M = 4$; (b) $M = 16$.

5.3.3 Impact of multipath channel

In multipath VLC channel (presented in Chapter 2), the noise variance for LACO-OFDM post equalization is $N_0/|H(k)|^2$ (for ZF equalization), whilst, for the FTP-LACO-OFDM and HTP-LACO-OFDM, because of decoding at the receiver, there is an averaging effect on the noise variance, which is expressed as $1/N \sum_{k=0}^{N-1} N_0/|H(k)|^2$ [120]. Consequently, in precoded approaches, all the subchannels experience the same SNR. Howbeit, in LACO-OFDM, SNR varies per subcarrier, thus, introducing a BER degradation [120]. The BER gain in $E_{\mathrm{b}_{(\mathrm{elec})}}/N_0$ for FTP-LACO-OFDM and HTP-LACO-OFDM over LACO-OFDM is

$$\beta_{\mathrm{FTP}} = 3 - \left(\frac{\alpha_{\mathrm{FTP}}(L, M)}{\alpha_{\mathrm{LACO}}(L)}\right) \quad (\mathrm{dB}), \tag{5.28}$$

and

$$\beta_{\mathrm{HTP}} = 3 - \left(\frac{\alpha_{\mathrm{HTP}}(L, \sqrt{M})}{\alpha_{\mathrm{LACO}}(L)}\right) \quad (\mathrm{dB}), \tag{5.29}$$

respectively. BER results obtained for multipath VLC channel presented in subsequent section confirms this analysis.

5.3.4 Spectral efficiency

The SE of LACO-OFDM employing M-QAM [107] and HTP-LACO-OFDM utilizing $\sqrt{M}$-PAM is given by:

$$\eta_{\text{LACO}}(L) = \frac{\log_2(M)\sum_{l=1}^{L}(N/2^{l+1})}{(N+N_{\text{CP}})} \quad \text{(bits/s/Hz)}, \tag{5.30}$$

and

$$\eta_{\text{HTP}}(L) = \frac{\log_2(\sqrt{M})\sum_{l=1}^{L}(N/2^{l})}{(N+N_{\text{CP}})} \quad \text{(bits/s/Hz)}, \tag{5.31}$$

respectively. The SE of FTP-LACO-OFDM is same as that of LACO-OFDM, i.e., $\eta_{\text{FTP}}(L) = \eta_{\text{LACO}}(L)$.

The objective of the layered approaches is to augment the SE towards that of DCO-OFDM, η_{DCO}, i.e., $\lim_{L\to\infty}\eta_{(\cdot)}(L) = \eta_{\text{DCO}}$ as shown in Fig. 5.16. It can be observed that the SE of layered approaches increases with an increase in L [107, 110], and can theoretically achieve η_{DCO} for $L \to \infty$. For example, by increasing $L = 2$ to $L = 5$, $\eta_{(\cdot)}$ increases from 75% to approximately 96.9% of η_{DCO}.

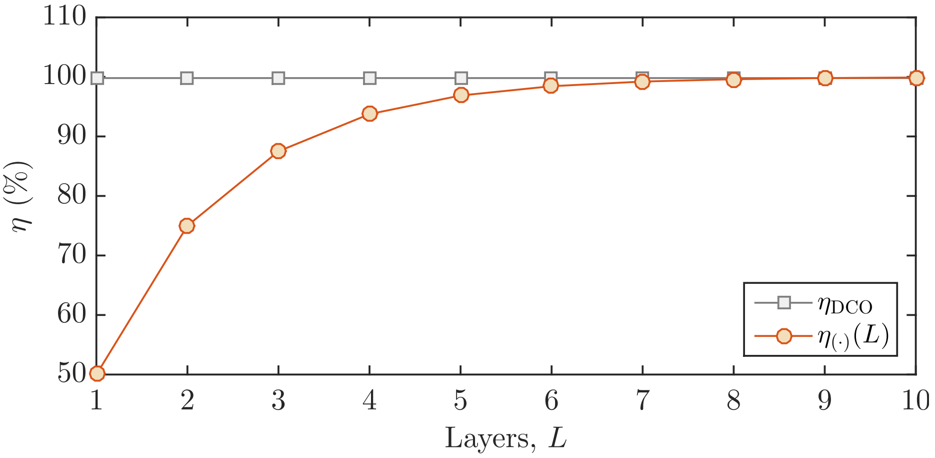

FIGURE 5.16: An illustration of spectral efficiency enhancement of layered approaches with increment of layers.

5.3.5 PAPR analysis

PAPR is evaluated using complementary cumulative distribution function (CCDF) which is the probability that the signal amplitude will transcend a given threshold, PAPR_ϵ, i.e., $\text{CCDF} = \text{Prob}(\text{PAPR} > \text{PAPR}_\epsilon)$. For comparison purpose, a parameter $\lambda_{(\cdot)}^{\max}$ is introduced which quantifies the maximum value of PAPR at CCDF $= 0.1$. The PAPR of LACO-OFDM depends on number of layers, L, and is independent of the modulation order. However, for FTP-LACO-OFDM and HTP-LACO-OFDM, the PAPR also depends on the modulation alphabet. Therefore, we have $\lambda_{\text{LACO}}^{\max}(L)$, $\lambda_{\text{FTP}}^{\max}(L, M)$ and $\lambda_{\text{HTP}}^{\max}(L, \sqrt{M})$. PAPR behavior of LACO-OFDM, FTP- LACO-OFDM and HTP-LACO-OFDM as a function of number of layers, L, is plotted in Fig. 5.17(a) and Fig. 5.17(b) using $N = 2048$. The variation in PAPR considering different modulation alphabets for FTP-LACO-OFDM and HTP-LACO-OFDM is likewise evaluated. It is observed that for $M = 4$ and $L = 5$, FTP-LACO-OFDM and HTP-LACO-OFDM manifest approximately 3.4 dB and 1.4 dB lesser PAPR than LACO-OFDM. For $M = 16$, the gain is reduced to roughly 2 dB and 1 dB. Indeed, HTP-LACO-OFDM shows the least PAPR among all the approaches.

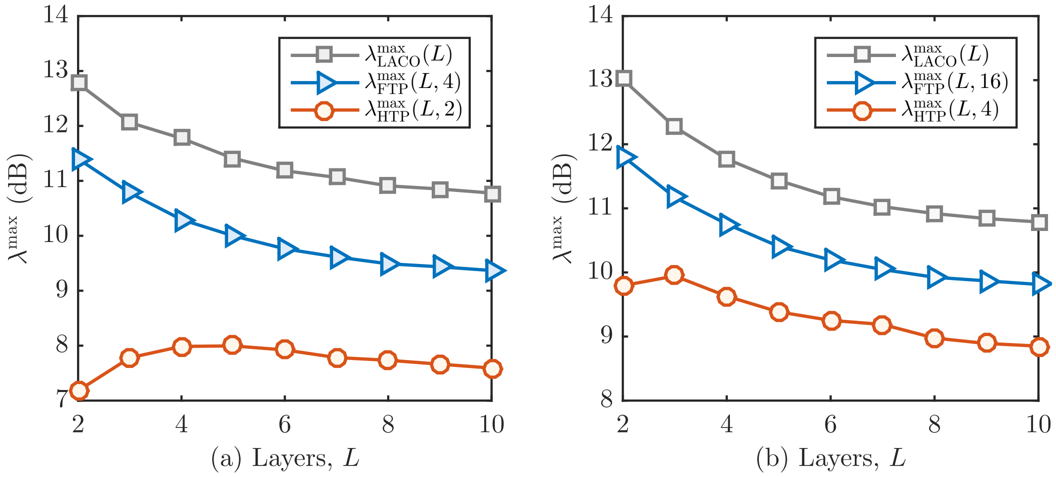

FIGURE 5.17: PAPR at CCDF = 0.1 as a function of L for LACO-OFDM, FTP-LACO-OFDM and HTP-LACO-OFDM: (a) $M = 4$; (b) $M = 16$.

5.3.6 BER performance

Additive white Gaussian noise (AWGN) channel

Fig. 5.18 depicts the BER performance versus $E_{\mathrm{b}_{(\mathrm{elec})}}/N_0$ for LACO-OFDM, FTP-LACO-OFDM and HTP-LACO-OFDM in an AWGN channel ($h(t) = 1$), for $\eta_{(\cdot)} \approx \{2, 3, 4, 5\}$ bits/s/Hz and $L = 5$ averaged over 2000 independent realizations with $N = 1024$. The SE is 96.9% of DCO-OFDM. It is ascertained that BER performance of LACO-OFDM is better than FTP-LACO-OFDM and HTP-LACO-OFDM because it experiences a lesser increase in $E_{\mathrm{b}_{(\mathrm{elec})}}/N_0$ compared to FTP-LACO-OFDM and HTP-LACO-OFDM, respectively, due to the superimposed structure. The increase in $E_{\mathrm{b}_{(\mathrm{elec})}}/N_0$ is as quantified by $\alpha(L, \cdot)$ and is shown in Fig. 5.14. It can also be determined that HTP-LACO-OFDM manifests the highest increase in $E_{\mathrm{b}_{(\mathrm{elec})}}/N_0$ via ($\alpha(L, \cdot)$ which can be seen from the BER curve in Fig. 5.18.

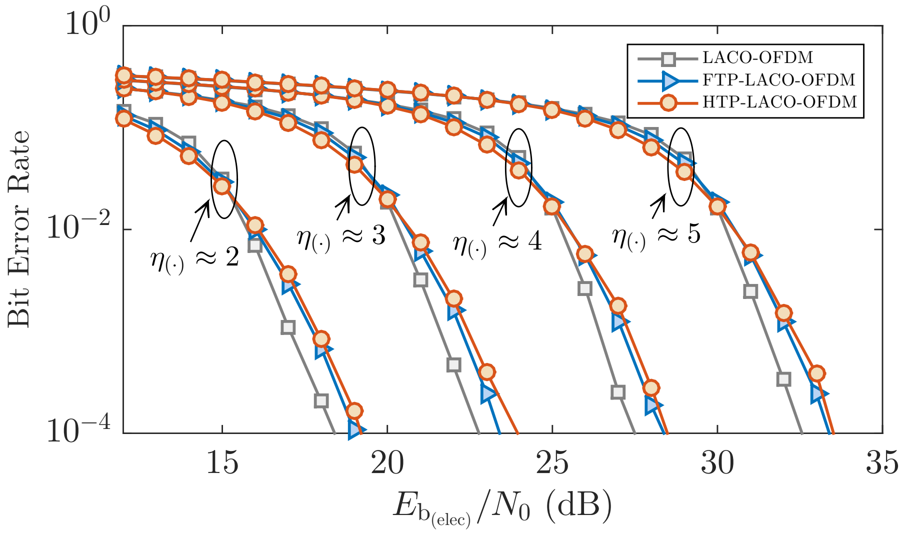

FIGURE 5.18: BER comparison of LACO-OFDM, FTP-LACO-OFDM and HTP-LACO-OFDM considering AWGN and $\eta_{(\cdot)} \approx \{2, 3, 4, 5\}$ bits/s/Hz and $L = 5$.

Considering upper level (UL) clipping

In practical scenarios, the transmitted signal may experience UL clipping, either due to the saturation of the light source or because of maximum current and optical emission constraints [110]. This UL clipping may drastically impact the BER performance. However, it is foreseen that if signal manifests lower PAPR, clipping distortion impact would be less. To assimilate UL clipping, clipping ratio is defined as:

$$\tau = 10\log_{10}(\gamma^2/P_{(\text{elec},\cdot)}) \quad (\text{dB}), \tag{5.32}$$

where γ is the clipping threshold. Fig. 5.19(a)-(d) portray the BER performance of LACO-OFDM, FTP-LACO-OFDM and HTP-LACO-OFDM for $\eta_{(\cdot)} \approx 2$ and $N = 1024$ considering $\tau = \{5, 7, 9, 11\}$ dB. It is discerned that FTP-LACO-OFDM and HTP-LACO-OFDM perform better than LACO-OFDM for smaller values of τ because of low PAPR (Fig. 5.19(a)-(b)). However, as τ increases, the performance of all schemes converge to that in AWGN channel because of reduction in clipping distortion (Fig. 5.19(d)). It can also be observed from the BER performance for $\tau = 9$ dB (depicted in Fig. 5.19(d)) that FTP-LACO-OFDM is more susceptible to the clipping distortion.

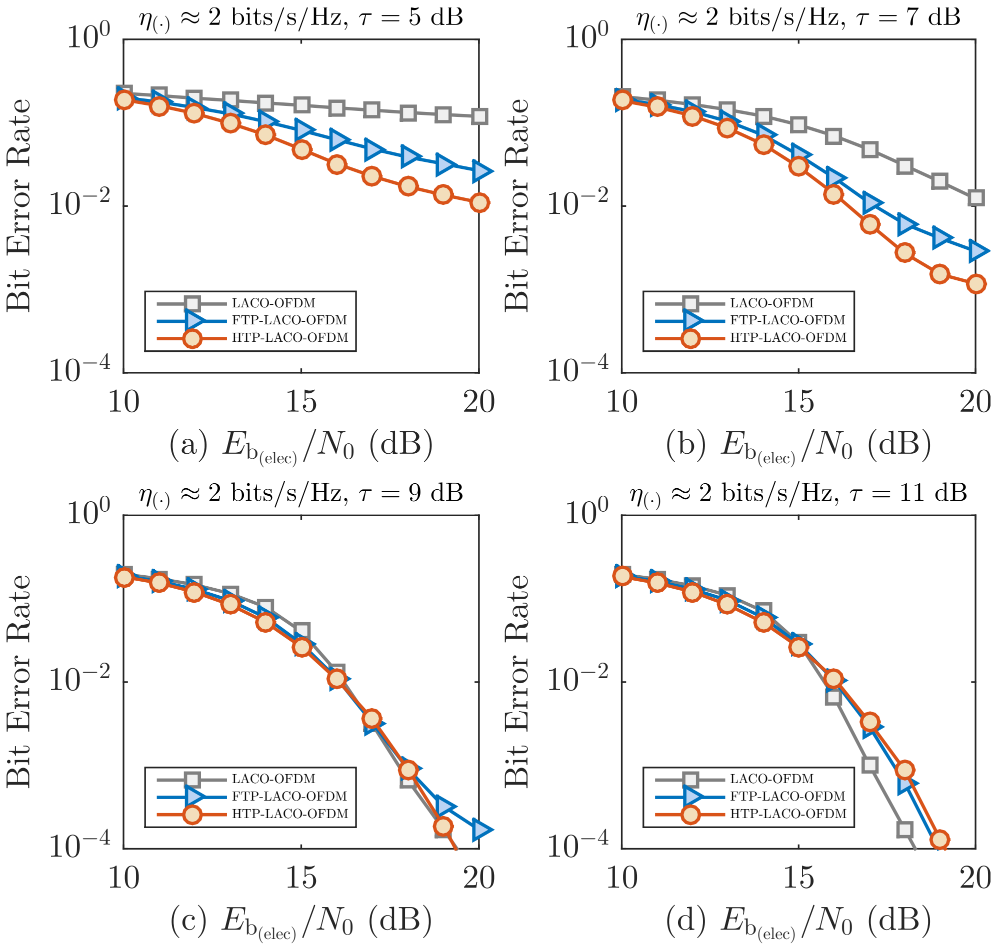

(a) $E_{\text{b}_{(\text{elec})}}/N_0$ (dB)

(b) $E_{\text{b}_{(\text{elec})}}/N_0$ (dB)

(c) $E_{\text{b}_{(\text{elec})}}/N_0$ (dB)

(d) $E_{\text{b}_{(\text{elec})}}/N_0$ (dB)

FIGURE 5.19: BER comparison of LACO-OFDM, FTP-LACO-OFDM and HTP-LACO-OFDM considering AWGN and UL clipping and $\eta_{(\cdot)} \approx 2$ bits/s/Hz with $L = 5$.

Dispersive Chanel

Multipath VLC channel presented in Chapter 2 is employed and the 3 dB optical cut-off frequency of the LED, $f_{3\text{dB}}$, is considered to be 150 MHz. The bandwidth (BW) of transmitted signal for $\eta_{(\cdot)} \approx \{1, 2\}$ bits/s/Hz is set at 200 MHz, thus, culminating a noticeable impact of bandwidth limitation of the LED/LED driver combination. Fig. 5.20 illustrates the performance of LACO-OFDM, FTP-LACO-OFDM and HTP-LACO-OFDM, which indicates that FTP-LACO-OFDM and HTP-LACO-OFDM exhibit superior performance compared to LACO-OFDM. This substantiates the findings where it is identified that FTP-LACO-OFDM and HTP-LACO-OFDM exhibit a gain of β_{FTP} dB and β_{HTP} dB, respectively, over LACO-OFDM.

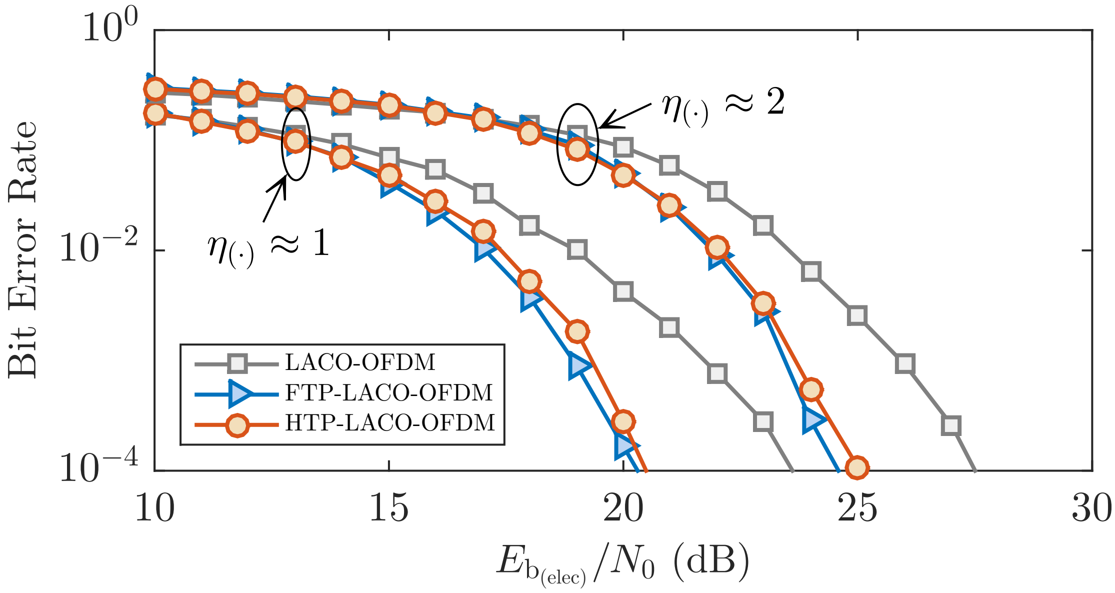

FIGURE 5.20: BER comparison of LACO-OFDM, FTP-LACO-OFDM and HTP-LACO-OFDM considering a multipath VLC channel for $\eta_{(\cdot)} \approx \{1, 2\}$ bits/s/Hz and $L = 5$ and $f_{3\text{dB}} = 150$ MHz.

5.3.7 Optical power penalty

For a given BER, P_{b}, optical power penalty is obtained by normalizing the required optical power by the average optical power needed for OOK in an AWGN channel with no bandwidth limitation, $E^{\text{OOK}}_{\text{b}_{(\text{opt})}}/N_0$. $E^{\text{OOK}}_{\text{b}_{(\text{opt})}}/N_0$ to reach P_{b} is attained as $\text{erfc}^{-2}(2P_{\text{b}})$, where $\text{erfc}(\cdot)$ is the complementary error function. Considering a dispersive channel, $P_{\text{b}} = 10^{-3}$, and $\eta \approx \{1, 2\}$ bits/s/Hz, the optical power penalty is analyzed by varying the ratio of data-rate to the 3 dB cut-off frequency, i.e., $R_{\text{b}}/f_{3\text{dB}}$, as rendered in Fig. 5.21 and Fig. 5.22. It is observed that FTP-LACO-OFDM suffers the lowest optical power penalty whilst, HTP-LACO-OFDM manifests marginally more optical power penalty compared to FTP-LACO-OFDM. A low optical power penalty for the precoded approaches is observed for the high data-rates due to precoding, whereas, for low data-rates, optical power penalties of LACO-OFDM, FTP-LACO-OFDM and HTP-LACO-OFDM are almost the same.

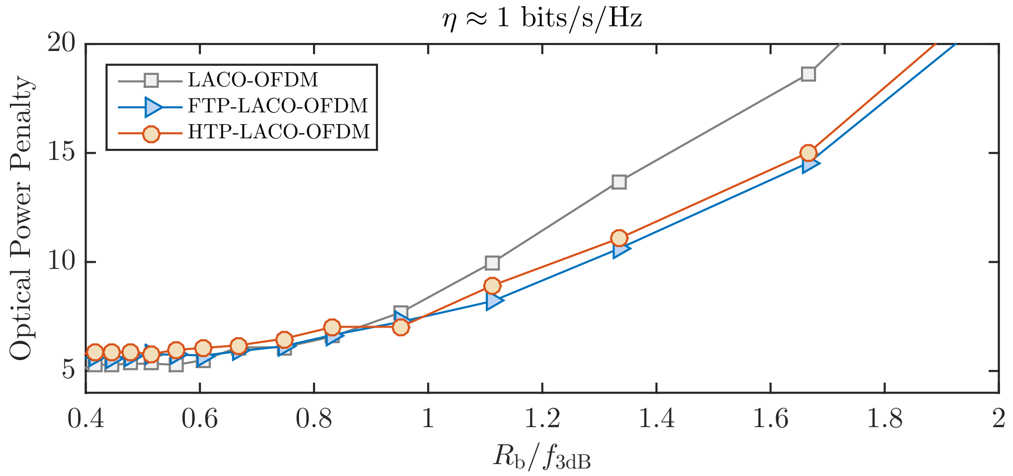

FIGURE 5.21: Optical power penalties of LACO-OFDM, FTP-LACO-OFDM and HTP-LACO-OFDM for $\eta \approx 1$ bits/s/Hz.

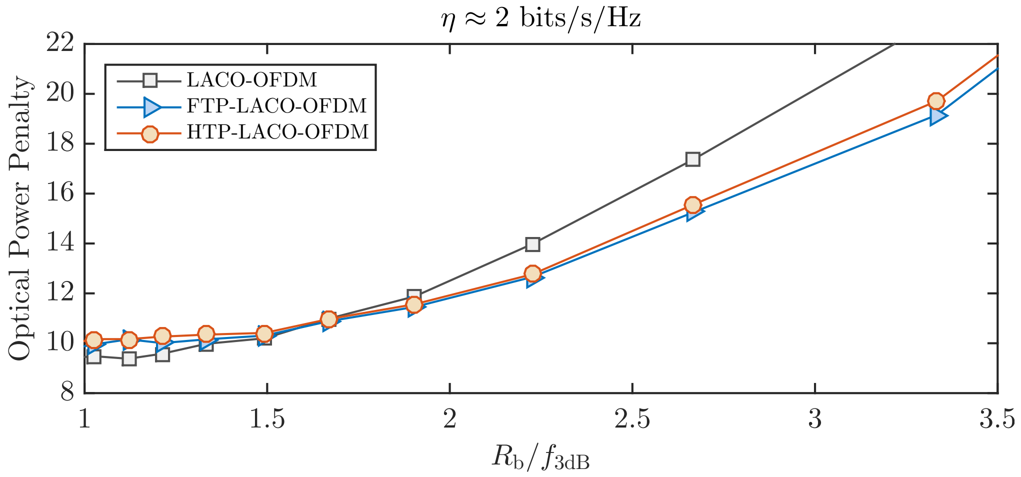

FIGURE 5.22: Optical power penalties of LACO-OFDM, FTP-LACO-OFDM and HTP-LACO-OFDM for $\eta \approx 2$ bits/s/Hz

5.3.8 Complexity analysis

The complexities of LACO-OFDM, FTP-LACO-OFDM and HTP-LACO-OFDM are assessed by computing the total number of required arithmetic operations at the transceiver. DFT and IDFT are realized using fast Fourier transform (FFT) and inverse FFT (IFFT) algorithms, respectively. An N-order FFT/IFFT approximately require $4N\log_2(N)$ arithmetic operations [148], whereas N-order DHT/IDHT nearly requires $2N\log_2(N)$ arithmetic operations [157]. Considering the complexity incurred owing to IFFT/FFT, LACO-OFDM and FTP-LACO-OFDM require

$$\mathcal{C}_{\text{LACO}} = 4N\log_2(N)[3L-1], \tag{5.33}$$

and

$$\mathcal{C}_{\text{FTP}} = 4N\log_2(N)[3L-1] + \left(\frac{N}{2^{L-2}}\right)[\log_2(N) - L - 1] + 12\sum_{l=1}^{L-1}\left(\frac{N}{2^{l+1}}\right)\log_2\left(\frac{N}{2^{l+1}}\right), \tag{5.34}$$

arithmetic operations, respectively. By taking into account the complexity imposed by DHT/IDHT, HTP-LACO-OFDM requires

$$\mathcal{C}_{\text{LDHTS}} = 2N\log_2(N)[3L-1] + \left(\frac{N}{2^{L-2}}\right)[\log_2(N) - L] + 6\sum_{l=1}^{L-1}\left(\frac{N}{2^l}\right)\log_2\left(\frac{N}{2^l}\right), \tag{5.35}$$

operations. From (5.33) and (5.34), it is obvious that the complexity of LACO-OFDM is less than FTP-LACO-OFDM. Whereas, comparing (5.34) and (5.35), it is realized that HTP-LACO-OFDM exhibits the least complexity. To illustrate the reduction in complexity, we introduce a relative gain parameter,

$$\mathcal{G}(N,L) = \left[1 - \frac{\mathcal{C}_{\text{HTP}}}{\mathcal{C}_{\text{LACO}}}\right] \times 100\%, \tag{5.36}$$

which is illustrated in Fig. 5.23 and indicates that HTP-LACO-OFDM is appreciably less complex than LACO-OFDM. Besides, the gain increases with an increase in number of superimposed layers, approaching $\approx 43\%$ for $\{L, \log_2(N)\} = 5$. The complexity of LACO-OFDM is evaluated considering the most recent article [108]. However, an implementation with lower order IDFT/DFT is presented in [107]. It should be recognized that an implementation of FTP-LACO-OFDM and HTP-LACO-OFDM with lower order IDFT/DFT and IDHT/DHT, respectively, is likewise feasible. Moreover, for HTP-LACO-OFDM, the encoding structure presented in [111] may be exploited to further reduce the complexity.

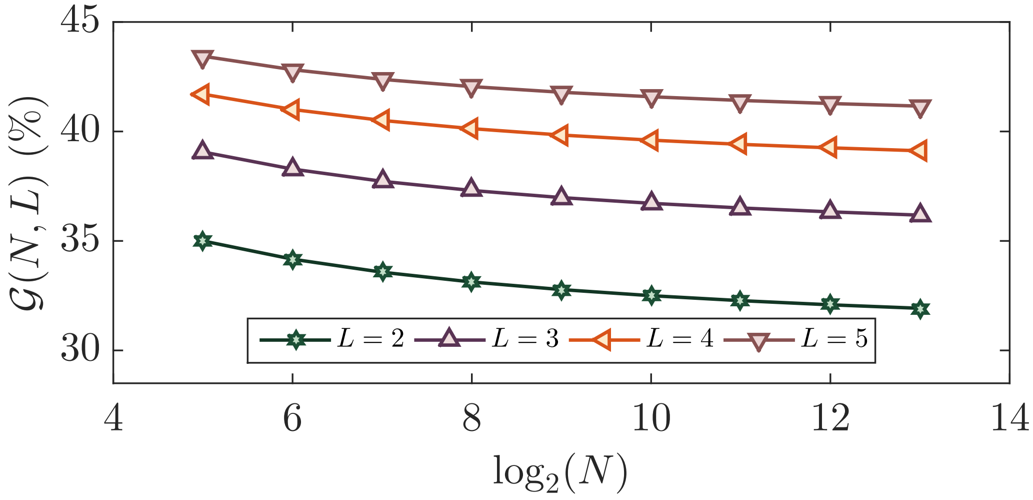

FIGURE 5.23: Relative complexity gain of HTP-LACO-OFDM over LACO-OFDM.

5.3.9 Comparisons

Based on the performance for all the approaches, following comparisons can be rendered:

1. With and increase in number of layers, L, the increase in $E_{\text{b}_{(\text{elec})}}/N_0$ is lesser for LACO-OFDM compared to FTP-LACO-OFDM and HTP-LACO-OFDM. This implies that for a given increase in $E_{\text{b}_{(\text{elec})}}/N_0$, it might be possible to superimpose more layers (refer to Fig. 5.14) for LACO-OFDM. Moreover, for the same L, BER degradation for LACO-OFDM is less for FTP-LACO-OFDM and HTP-LACO-OFDM in an AWGN channel if no additional clipping from the LED is considered.

2. The optical-to-electrical conversion efficiency for LACO-OFDM is better than FTP-LACO-OFDM and HTP-LACO-OFDM. Therefore, the optical power consumption for LACO-OFDM would be reduced compared to precoded variants in an AWGN channel.
3. In a dispersive channel which emulates a practical scenario, the BER of FTP-LACO-OFDM and HTP-LACO-OFDM is considerably better than LACO-OFDM because of averaging effect of the decoder at the receiver. Moreover, among the precoded approaches, FTP-LACO-OFDM performs marginally better than HTP-LACO-OFDM.
4. It has been establised that HS incurs a SE loss of factor two and four for DCO-OFDM and ACO-OFDM, respectively, compared with base-band unipolar modulation schemes, e.g. PAM [40]. For LACO-OFDM and FTP-LACO-OFDM, SE loss by a factor of two yet exists because of HS requirement. However, for HTP-ACO-OFDM, as HS is no longer required, all the subcarriers can transmit data if sufficient layers are superimposed (theoretically $L = \infty$), thus, excluding the SE loss.
5. Both precoded approaches manifest lower PAPR compared to LACO-OFDM, with HTP-LACO-OFDM featuring the least. The low PAPR of HTP-LACO-OFDM is expected because HS is no longer prescribed. Several studies, e.g., [121] indicate that HS contributes toward an increase of PAPR. So, by eliminating HS, PAPR is reduced. The low PAPR results in power gain as higher modulation power is realized after DAC. Besides, cost of the converters can be decreased.
6. The system complexity of HTP-LACO-OFDM is less than both LACO-OFDM and FTP-LACO-OFDM. FTP-LACO-OFDM manifest the highest complexity.

5.4 Conclusion

In this work, the performance of LACO-OFDM and precoded LACO-OFDM approaches is evaluated. The dispersive environments considered hereby assimilate multipath VLC channel and integrates the bandwidth limitation of LED along with its optimized driver. It is ascertained from the simulation results that in an AWGN channel, BER performance LACO-OFDM is better than that of precoded LACO-OFDM approaches. This improvement in BER is due to a lesser increase in required SNR per bit because of the layered implementation. BER performance of FTP-LACO-OFDM is marginally better than HTP-LACO-OFDM because the latter approach culminates the highest increase in SNR because of superimposed structure. However, in a multipath VLC channel channel, the precoded approaches, that are, FTP-LACO-OFDM and HTP-LACO-OFDM, result in a superior BER performance because of averaging impact of decoder at the receiver. Furthermore, precoded LACO-OFDM approaches exhibit lower PAPR compared to LACO-OFDM. Among the precoded approaches, HTP-LACO-OFDM demonstrates the lowest PAPR because of precoding and by averting HS. The complexity of FTP-LACO-OFDM is higher than LACO-OFDM, the ramifications of which dominate other improvements. Howbeit, the complexity of HTP-LACO-OFDM is lesser compared to LACO-OFDM, while it likewise sustains a BER improvement in a dispersive channel and manifests lower PAPR. Hence, HTP-LACO-OFDM can be a formidable substitute to LACO-OFDM for VLC systems.

Chapter 6

Experimental Validations

In the preceding chapters, the performance of the iterative decision-directed peak-to-average-power ratio (PAPR) techniques and Hermitian symmetry free optical-single-carrier frequency division multiple access (HSFO-SCFDMA) has been evaluated using numerical simulations. Hereby, in this chapter, the proof-of-concept of PAPR reduction methods, i.e., time-domain clipped sample reconstruction (TD-CSR), frequency-domain clipping distortion removal (FDCDR) and HSFO-SCFDMA is validated via experimental results. Signal processing techniques, particularly for channel estimation, have been provided. SNR estimation is realized through error vector magnitude (EVM) measurements, with respect to the bias current of the light source.

6.1 Experimental setup

Due to unavailability of optical wireless communication (OWC) prototype, all the experimental validations have been carried out using Laser diode (LD) and fiber based system realizing intensity-modulation and direct detection (IM-DD) optical system.

A basic block diagram of the experimental setup is given in Fig. 6.1. The first block of the experimental setup is the offline processing of the signal using MATLAB. Random bits are generated which are modulated using M-ary quadrature-amplitude modulation (QAM). For optical-orthogonal frequency division multiplexing (O-OFDM)/O-SCFDMA, inverse discrete Fourier transform (IDFT) is performed in MATLAB to generate a time-domain (TD) signal. Generally, over-sampling is also performed to adjust the bandwidth of the transmit signal with respect to the sampling frequency of the waveform generator. The discrete samples of TD signal of O-OFDM/O-SCFDMA schemes are passed to an arbitrary waveform generator (AWG), Tektronix 7122B which performs digital-to-analog conversion using 8 bits digital-to-analog converter (DAC) and outputs an analog waveform. The maximum dynamic range of the AWG DAC is 1 Volt peak-to-peak. The sampling frequency is prescribed to be 5 GSamples/s. A direct-current (DC) signal is added to the unbiased analog signal using a bias tee and feeded to modulate the bias of a single mode distributed feedback (DFB) LD and operate intensity modulation (IM). The optical wavelength of the DFB LD is around 1550 nm and the threshold current is 11 mA.

The IM signal is fed into a standard single mode fiber of length 2 m. Though the optical fiber channel cannot emulate an optical wireless channel, howbeit, the main aim was to validate the proof-of-concept for the proposed approaches for an IM-DD optical system, which can be adequately done using an LD as transmitter front-end and optical fiber as a channel. It is highlighted that the 3 dB bandwidth of the LD is around 4 GHz which is greater than that of a light emitting diode (LED).

At the receiver, the light intensity is directly detected using a photodiode (PD) which is integrated with a transimpedance amplifier (TIA) of gain 500 V/A (Picometrix PT-10B optical receiver). The bandwidth of the optical receiver is around 9 GHz. After photodetection the signal is low pass filtered to attenuate out-of-band noise and captured using a digital storage oscilloscope (DSO), Tektronix TDS6604B integrating an analog-to-digital converter (ADC) with a sampling frequency of 5 GSamples/s. The digitized signal is retrieved from the DSO and is subsequently processed offline in MATLAB which includes steps like synchronization, DFT, channel estimation, equalization and demodulation. The aim of the experiment is to quantify the impact of the LD DC bias relatively to the received SNR through the measurement of the EVM.The bias current applied to the LD is tuned and the corresponding EVM is measured.

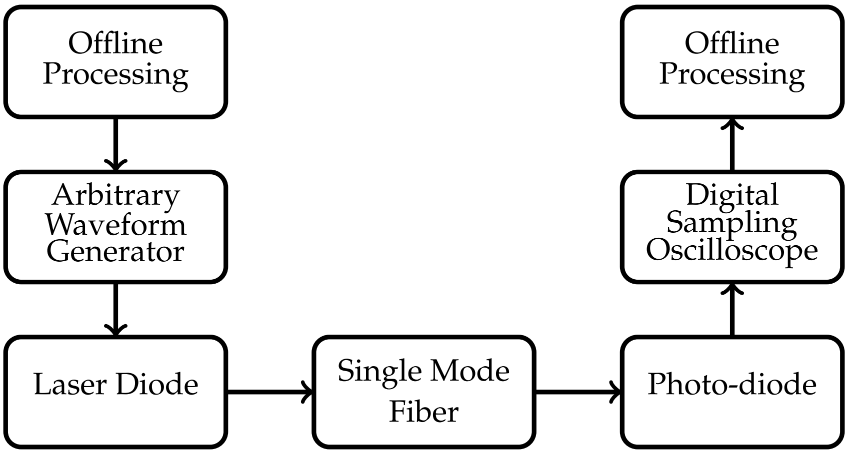

FIGURE 6.1: A block diagram of the experimental setup.

6.2 Basic definitions

EVM is a figure of merit to evaluate the transmission accuracy. Various distortions cause the actual constellation points of a given modulation to deviate from the ideal locations at the receiver. This deviation can be evaluated using EVM which is essentially a measure of how far the points are from the ideal locations. Considering some arbitrary parameters, I_k and Q_k which represent the ideal constellation points for the kth symbol, and $\tilde{I}_k$ and $\tilde{Q}_k$ which represents the constellation points of the received kth symbol, then the EVM can be mathematically evaluated as:

$$\text{EVM} = \sqrt{\frac{\frac{1}{N}\sum_0^{N-1} e_k}{\frac{1}{N}\sum_0^{N-1}\left(I_k^2 + Q_k^2\right)}}, \tag{6.1}$$

where N is the total number of samples and e_k is the error vector evaluated as $e_k = (I_k - \tilde{I}_k)^2 + (Q_k - \tilde{Q}_k)^2$. EVM can be linked with SNR as:

$$\text{SNR} = \frac{1}{\text{EVM}^2}. \tag{6.2}$$

6.3 Signal processing techniques

The received TD signal at the PD after analog-to-digital conversion can be given as

$$y(n) = h(n) \otimes x(n) + w(n), \tag{6.3}$$

where $x(t)$ is the transmitted signal, $h(n)$ is the impulse response of the communication channel which includes the LD, the optical fiber and the optical receiver, $w(n)$ is the noise in the channel and $\otimes$ denotes the convolution operator. Thus, in order to mitigate the impact of the communication channel, a suitable equalization approach has to be adopted at the receiver. Accordingly, for equalization of the received signal, the impulse response of the communication channel has to be known at the receiver. The received signal, after the DFT is given as:

$$Y(k) = H(k)X(k) + W(k), \tag{6.4}$$

where $Y(k)$, $H(k)$, $X(k)$ and $W(k)$ are the FD counterparts of $y(n)$, $h(n)$, $x(n)$ and $w(n)$, respectively. It is considered that $H(k)$ consists of all the frequency dependent attenuation and phase rotation induced by the channel.

In the experiments, the channel frequency coefficients, $H(k)$ are estimated by transmitting known O-OFDM/O-SCFDMA FD symbol. Only one O-OFDM/O-SCFDMA symbol is transmitted to evaluate the channel frequency response, however, better estimation can be obtained by using multiple O-OFDM/O-SCFDMA symbols. Thus, the channel frequency coefficients, $H(k)$ can be estimated with a conventional mean estimator as:

$$\hat{H}(k) = \frac{Y(k)}{X(k)}. \tag{6.5}$$

Subsequently, this estimator is employed for zero-forcing (ZF) equalization, which can be achieved as:

$$\hat{Y}(k) = \frac{H(k)X(k)}{\hat{H}(k)} + \frac{W(k)}{\hat{H}(k)}. \tag{6.6}$$

It should be noted that the equalization process is dependent on a number of factors: (i) if less number of subcarriers/subchannels are used for O-OFDM/O-SCFDMA, a good equalization performance cannot be achieved because the channel response can not be considered as flat over each carrier bandwidth; (ii) if only less number of symbols are used for equalization, in this case as well, the equalization performance is not ideal.

Another important parameter which is essential to the performance is the synchronization at receiver. Hereby, the synchronization at the receiver is achieved by using zeros which correspond to one symbol duration. In the given experimental setup, the AWG and DSO have a limited memory, therefore, just a few symbols can be transmitted.

6.4 Experimental results

The experimental results cannot be mapped exactly on the simulation results due to certain limitations; one of them being the requirement of bias current to overcome the threshold current of the LD. The other one being a large dependency of the LD intensity noise relatively to the bias current (variaion of the relative intensity noise (RIN)), which is not to be considered in optical wireless IMDD. Nevertheless, the performance trends obtained from numerical simulations can be verified from the experimental results presented in this section.

6.4.1 PAPR reduction methods

The relevant parameters for experimental verification of PAPR reduction methods, that are, TDCSR and FDCDR are:

1. the experimental results are verified by only considering DCO-OFDM;
2. the DFT size and number of subcarriers are equal to $N = 256$; of which only 32 subcarriers are modulated while the remaing subcarriers are used for Hermitian symmetry (HS) and to accommodate an oversampling ratio of 4. As a consequence, the subcarrier spacing is around 5 MHz which is supposed to be large enough comparatively to the coherence bandwidth of the channel (estimated to be larger than a few tens of MHz). The occupied signal bandwidth is around 400 MHz. The data-rates are 1.25 Gbps and 2.5 Gbps for 4-QAM and 16-QAM DCO-OFDM.
3. a total of 10 O-OFDM symbols were transmitted from which one was used for synchronization and another one was reserved for channel estimation;
4. the experimental results which shall be depicted for DCO-OFDM are obtained without any clipping;
5. the experimental for TDCSR and FDCDR are obtained by clipping the same TD DCO-OFDM signal by using clipping threshold of γ equal to 1 and 1.2.
6. only two iterations for TDCSR and FDCDR are used.

The results are depicted in Fig. 6.2 and Fig. 6.3 for 4-QAM and 16-QAM. It is highlighted that both TDCSR and FDCDR are essentially used for clipping distortion mitigation. A back to back EVM of approximately 5 % is obtained resulting, mainly, from the noise of the optical receiver. The results demonstrate that both TDCSR and FDCDR are capable of mitigating the clipping distortion and achieve better EVM performance compared to un-clipped DCO-OFDM. From the results it can be discerned that

- as depicted in the simulation results, the performance of TDCSR is better than FDCDR for DCO-OFDM;
- a better EVM is obtained if lower values of clipping thresold are used; similar conclusions were drawn from the simulation results;
- both the methods are capable of obtaining at least a similar EVM as obtained for un-clipped DCO-OFDM.

Moreover, for 16-QAM, it can be observed that the EVM performance of FDCDR is similar to that of un-clipped DCO-OFDM, whereas, the performance of TDCSR is relatively better. The reason might be due to imperfect FD equalization leading to wrong estimation of distortion in FD. For TDCSR, since the signal is reconstructed in TD from the equalized FD symbols, if the symbols are correctly retrieved, imperfect equalization does not impact TD signal reconstruction.

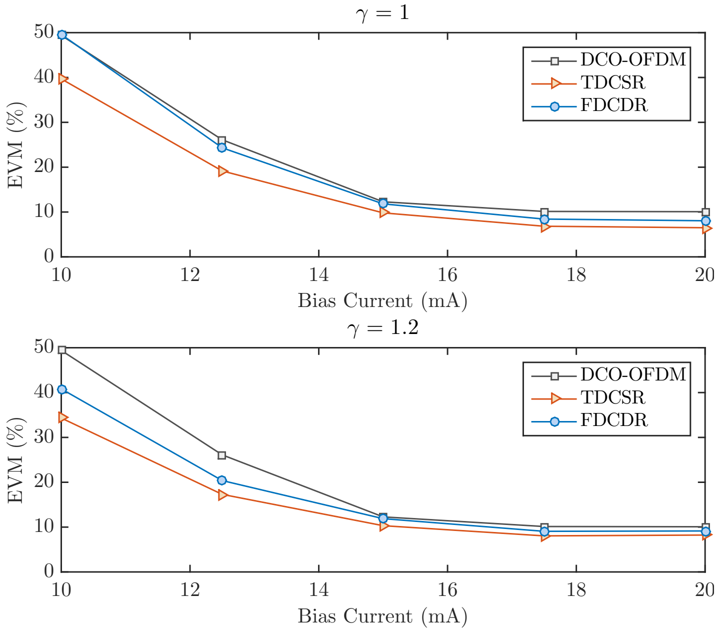

FIGURE 6.2: EVM performance comparision of TDCSR and FDCDR for DCO-OFDM determined experimentally for 4-QAM.

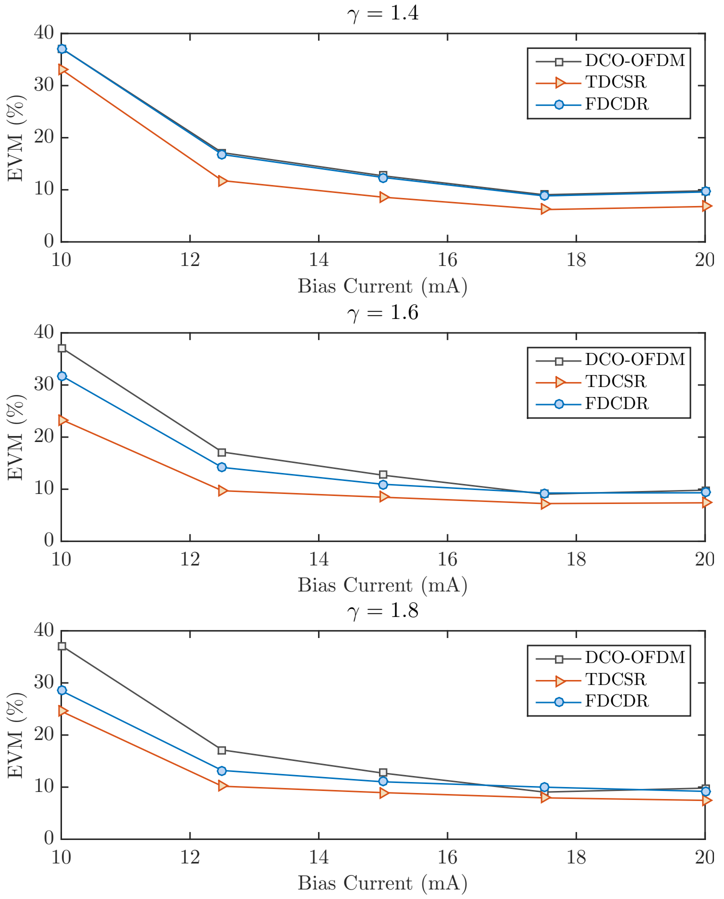

FIGURE 6.3: EVM performance comparision of TDCSR and FDCDR for DCO-OFDM determined experimentally for 16-QAM.

6.4.2 HSFO-SCFDMA

The performance of HSFO-SCFDMA is compared with that of DCO-OFDM using 4-QAM modulation alphabet. The parameters for experimental verification are:

1. the EVM performance of DCO-OFDM and HSFO-SCFDMA is analyzed and compared;
2. the order of DFT and number of subcarriers/subchannels is set equal to $N = 64$;
3. an oversampling ratio of 4 is used, therefore, only 16 subcarriers/subchannels are modulated with unique information;
4. 10 O-OFDM/O-SCFDMA symbols are sequentially transmitted among which one is used for synchronization and one for equalization;
5. no clipping has been used for DCO-OFDM.

The EVM performance is depicted in Fig. 6.4. It is highlighted that the performance of DCO-OFDM is different from the one depicted in Fig. 6.2 because at the time of experiment, a suitable low pass filter was missing to reject the out-of-band noise. The performance of equalization performance is not optimal. The back to back EVM in this case is approximately 13 %.

For the results presented in Fig. 6.4, following conclusions can be drawn:

- for any bias current value, the value of EVM for HSFO-SCFDMA is better than DCO-OFDM. The performance of DCO-OFDM is worst than HSFO-SCFDMA because at low bias current value, the lower level clipping due to the LD threshold current significantly degrades the performance as the signal has inherently high PAPR.
- it is distinctly obvious that the required bias current to target a given EVM (i.e a target SNR) for HSFO-SCFMA is considerably smaller than what is required for DCO-OFDM as a result the optical power consumption is reduced.
- the performance of HSFO-SCFDMA is better because the DAC conversion efficiency is optimal because of lower PAPR.

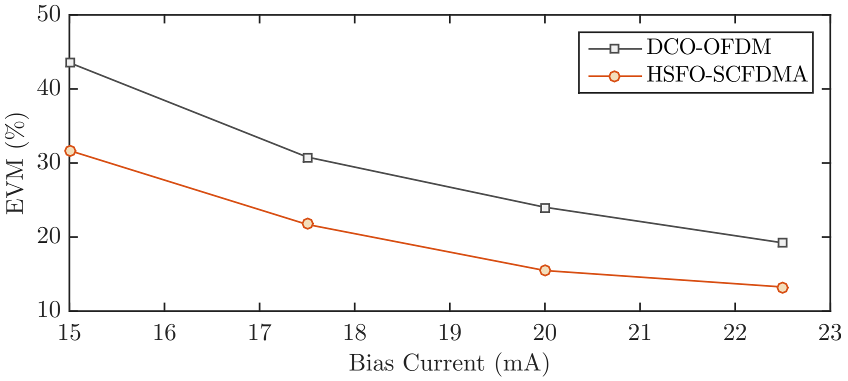

FIGURE 6.4: EVM performance comparision of DCO-OFDM and HSFO-SCFDMA determined experimentally for 4-QAM.

These experimental results prove that HSFO-SCFDMA is better than DCO-OFDM and can be a good alternative to DCO-OFDM.

6.5 Summary

In this chapter, the experimental performance of PAPR reduction methods and HSFO-SCFDMA is presented. It is experimentally demonstrated that both TDCSR and FDCDR are capable of achieving a good clipping mitigation performance and better performance than that of un-clipped DCO-OFDM. Moreover, the experimental results of HSFO-SCFDMA are better than DCO-OFDM. For every value of bias current, the EVM performance of HSFO-SCFDMA is better than DCO-OFDM because of low PAPR. The experimental results demonstrate the feasibility of both the PAPR reduction methods and HSFO-SCFDMA.

Conclusion

Over the past couple of decades, there has been an exponential growth in deployment of radio-frequency (RF) wireless systems, which has led to RF spectral congestion. The RF spectrum has been subjected to an excessive spatial reuse, hence, the co-channels interferences have given rise to serious quality-of-service concerns. Besides, the amount of data traffic is also continuously increasing. Therefore, alternate approaches to overcome the spectral bottleneck are urgently required. Recently, optical wireless communication (OWC) has been recognized as a complementary technology to looming RF spectral crisis. Additionally, with onset of incoherent high power light emitting diodes (LEDs) and highly sensitive photo-detectors (PDs), OWC has gained a significant interest. Along with some intriguing advantages, such as license free virtually unlimited optical bandwidth, high-security and no electromagnetic interference, OWC is particularly enticing as it can offer both lighting and communication concurrently. In this thesis, novel modulation approahes for OWC which manifest inherently low peak-to-average power ratio (PAPR) and distortion methods for OWC have been deveoped.

The classical optical-orthogonal frequency division multiplexing (O-OFDM) approaches for IM-DD based OWC systems are direct-current biased (DC)O-OFDM, asymmetrically clipped (AC)O-OFDM. As aforementioned, both these approaches manifest high PAPR which results in performance degradation due to limited dynamic range of the LEDs because the intensity-modulated (IM) signal that lies beyond the dynamic range of the LED is clipped. Several methods to reduce high PAPR of O-OFDM have been proposed. Howbeit, these methods are not optimal primarily because of high computational complexity. Some of these complex classical approaches are selected-mapping (SLM), pilot-assisted (PA), tone reservation (TR) etc. In this work, the high PAPR of the IM O-OFDM signal is reduced by hard clipping the signal to a pre-defined threshold. The clipping of the signal results in clipping distortion. Two iterative decision-directed clipping mitigation approaches have been proposed to mitigate the clipping distortion at the receiver. The basic idea behind the proposed methods is that, if the nonlinear characteristics of the transmitter (which is LED in this case), e.g., the clipping threshold etc. are known at the receiver, the distortions can be recognized as a deterministic function of the received data and hence can be mitigated. One of the proposed approaches, mitigates the clipping distortion be reconstructing the clipped samples in time-domain (TD) and is therefore, referred to as time-domain clipped sample reconstruction (TDCSR). While, the other proposed approach, alleviates the clipping distortion is the frequency-domain (FD) and is referred to as frequency-domain clipping distortion removal (FDCDR). The bit-error-rate (BER) performance of TDCSR and FDCDR is computed in an additive white Gaussian noise (AWGN) channel. The performance of the methods have been also analyzed considering the impact of quantization from the digital-to-analog converter (DAC) and analog-to-digital converter (ADC) and different number of iterations for the iterative structure. It has been concluded that the performance of TDCSR and FDCDR is much better than other classical PAPR reduction methods with lower computational complexity. Statistical model for clipping of DCO-OFDM and ACO-OFDM is also presented.

Even though TDCSR and FDCDR perform much better than other PAPR reduction methods in AWGN channel, however, the computational complexity overhead is still high, which might overshadow the performance improvement achieved with these methods. Therefore, other viable solutions with reduced complexity are needed. One way to reduce the PAPR without imposing considerable complexity is to use optical-single-carrier frequency division multiple access (O-SCFDMA) approaches. In this context, DCO-OFDM and ACO-OFDM inspired O-SCFDMA approaches, which in this work are referred to as Fourier transform precoded (FTP)-DCO-OFDM and FTP-ACO-OFDM, respectively are studied. These approaches manifest lower PAPR than their O-OFDM counterparts, however, it is determined that the Hermitian symmetry (HS) requirement to achieve a real-valued TD signal bounds the level of PAPR that can be reduced. This entails that same level of PAPR cannot be achieved by precoding in IM-DD based OWC systems as can be achieved in RF systems.

A novel O-SCFDMA approach which averts the use of HS termed as Hermitian symmetry free O-SCFDMA (HSFO-SCFDMA) has been proposed. This modulation approach overcomes the constraint imposed by the HS and can achieve the same PAPR performance as precoding can achieve for RF systems. In HSFO-SCFDMA, only the even subchannels (in the thesis, the term subchannel is used for O-SCFDMA approaches) are modulated which results in a half-wave symmetric TD complex signal, from which a real-valued TD signal can be attained forthrightly (refer to Chapter 4 for details). The non-negativity is achieved by using bias as in DCO-OFDM. It is accentuated that the impact of bias on HSFO-SCFDMA is substantially less than DCO-OFDM because the TD HSFO-SCFDMA signal manifests lower PAPR, hence the bias required to achieve non-negativity is also less resulting in a lesser penalty on optical power consumption than DCO-OFDM or FTP-DCO-OFDM. Moreover, HSFO-SCFDMA has the same spectral efficiency (SE) as that of DCO-OFDM. The performance of HSFO-SCFDMA is evaluated in multipath visible light communication (VLC) channel and also considering the bandwidth limitation of the LED. Additionally, closed-form expressions for PAPR and effective number of bits (ENOB) required for quantization are also determined. The PAPR of HSFO-SCFDMA is always less than other O-OFDM and O-SCFDMA, therefore, this approach is less susceptible to nonlinear distortions from the LED. HSFO-SCFDMA also has the capability to incorporate FD multiple access (MA) which most of the other single-carrier (SC) approaches are unable to incorporate simply.

Though HSFO-SCFDMA approach manifests low PAPR, however, like other O-OFDM/O-SCFDMA approaches, all the subchannels cannot be modulated, i.e., the odd subchannels have to be left blank to attain half-symmetric TD signal. This results in inefficient utilization of the bandwidth. In state-of-the-art O-OFDM approaches, at least half of the subcarriers are sacrificed for HS to attain real-valued TD signal, while for approaches, such as ACO-OFDM further subcarriers have to be relinquished to achieve a non-negative TD signal. This signifies that ACO-OFDM has half the SE of DCO-OFDM. The SE of ACO-OFDM can be enhanced by using LACO-OFDM, however, LACO-OFDM has following practical limitations: (i) HS is required, so, half of the subcarriers go un-used; (ii) LACO-OFDM also manifest high PAPR; and (iii) the computational complexity is significantly higher. To overcome the dilemma of PAPR, performance of DFT and DHT precoding is analyzed for LACO-OFDM because PAPR reduction methods (only a few are available) require high computational resources. The corresponding approaches are termed as FTP-LACO-OFDM and HTP-LACO-OFDM. In FTP-LACO-OFDM, quadrature-amplitude modulation (QAM) modulation alphabets and DFT/IDFT (for both precoding/decoding and multiplexing/demultiplexing) are used, while in HTP-LACO-OFDM, pulse-amplitude modulation (PAM) alphabets with real-valued DHT/IDHT are used. In HTP-LACO-OFDM, the HS requirement is averted and virtually all the subchannels can be modulated, thus, providing an efficient utilization of bandwidth. Nevertheless, the SE cannot be increased from that of DCO-OFDM because of use of PAM alphabets. In terms of PAPR, HTP-LACO-OFDM manifests the lowest PAPR among the three approaches. Though the PAPR of FTP-LACO-OFDM is less than LACO-OFDM, however, it is more than HTP-LACO-OFDM because of HS requirement. In terms of the computational complexity, HTP-LACO-OFDM has the lowest computational complexity. Thus, all the limitations of LACO-OFDM can be eliminated using HTP-LACO-OFDM. On the other hand, due to the superimposed structure, the penalty in terms of power requirement is higher for HTP-LACO-OFDM compared to LACO-OFDM.

Finally, experimental demonstrations have been presented for TDCSR/FDCDR and HSFO-SCFDMA using fiber based IM-DD system. Fiber based IM-DD system is used because of unavailability of OWC prototype. The experimental results are in accordance with simulation results. From the experimental measurements for TDCSR/FDCDR, it is discerned that the both approaches are capable for recovering the information lost because of clipping. The experimental results of HSFO-SCFDMA reveals that the approach performs significantly better than DCO-OFDM.

Prospects of Future Work

Multiplexing of different modulation techniques

In general, in this work, the approaches with high spectral efficiency, such as, O-OFDM and O-SCFDMA have been presented. In the future, a hybrid implementation by multiplexing several modulation approaches can be a logical extention of this work. For example, it is easy to implement a hybrid version by multiplexing HSFO-SCFDMA and On-off keying (OOK) together. The demodulatio of OOK signal at the receiver is easy because the HSFO-SCFDMA signal possess ditinct amplitudes in the TD.

Faster than Nyquist Implementation of HSFO-SCFDMA

Another possible extention of this work could be the Faster than Nyquist (FTN) implementation of HSFO-SCFDMA approach. FTN is a time domain technique which aims to reduce the transmission time for each symbol, resulting in an improvement in overall spectral efficiency. In other words, the spacing between the subcarriers becomes a fraction of the modulating symbol rate for each subcarrier. This is done by compressing the bandwidth by (α which results in $(1-\alpha)\times 100$ % reduction in bandwidth when sending the same amount of data. In the recent past, several FTN approaches have been proposed for VLC, e.g., [160] and [161]. Our objective is to develop a FTN approach for HSFO-SCFDMA because, in general the performance of HSFO-SCFDMA is superior than other approaches.

Highly Energy Efficient Modulation Techniques for Internet of Things VLC

In the recent past, the number of communication devices have increased substantially and as predicted will keep on increasing. With emerging Internet-of-Things (IoT), long range and low data-rate communications are gaining substantial interest. A couple of characteristics for a communication system to fulfill the requirements of such applications are: (i) an energy efficient modulation approach for long range; and (ii) diminished impact on the environment.

So, for an energy efficient modulation approach, lower levels of photo-diode (PD) receiver sensitivity are prescribed to guarantee a quality of service. The PD sensitivity is expressed as:

$$\rho^{\text{dBm}} = \left(\frac{E_{\text{b}_{(\text{elec})}}}{N_0}\right)^{\text{dB}}_{\text{min}} + 10\log_{10}(\eta) + 10\log_{10}(N_0 B), \tag{6.7}$$

where $E_{\text{b}_{(\text{elec})}}/N_0$ is the electrical signal-to-noise ratio (SNR) per bit, η is the SE in bits/s/Hz, B is the mono-lateral bandwidth of the signal in Hertz (Hz) and N_0 is the mono-lateral noise spectral density. Eq. (6.7) entails that if the SE is relinquished, lower levels of receiver sensitivity can be realised. It is bounded by Shannon's limit of the information theory which defines the maximum transmission rate with arbitrarily low bit error probability for a given SNR and specified bandwidth in an AWGN channel. The limit can be reformulated in terms of η and $E_{\text{b}_{(\text{elec})}}/N_0$ as:

$$\frac{E_{\text{b}_{(\text{elec})}}}{N_0} \geq \frac{2^{\eta}-1}{\eta}. \tag{6.8}$$

The asymptote $E_{\text{b}_{(\text{elec})}}/N_0$ that can be achieved is approximately -1.6 dB when η tends to 0. This can be achieved by the use of M-ary orthogonal modulations, hence, these techniques are more energy efficient than linear modulations, such as M-ary pulse-amplitude modulation (M-ary PAM) or On-off keying (OOK), where the energy efficiency can be enhanced by surrendering the SE (increase in size of alphabet, M). This comportment is in complete contradiction with linear modulations where the energy efficiency diminishes with an increase in alphabet size.

In this work, for the first time, another class of M-ary orthogonal modulations for IM-DD based OWC system, i.e., M-ary frequency-shift keying (FSK) is explored. In M-ary FSK, in a symbol period, T, M distinct frequencies are available, out of which, just one frequency is chosen for the transmit waveform. Numerous approaches to attain an IM-DD compatible signal shall be developed.

List of Publications

Journal Publications

- **Ali W. Azim**, Yannis Le Guennec, Ghislaine Maury, "Decision-Directed Iterative Methods for PAPR Reduction in Optical Wireless OFDM Systems", Vol. 389, pg 318-330, *Elsevier Optics Communication*, 2017.
- **Ali W. Azim**, Yannis Le Guennec, Ghislaine Maury, "Hermitian Symmetry Free Optical-Single-Carrier Frequency Division Multiple Access for Visible Light Communication", Vol. 415, pg 177-185, *Elsevier Optics Communication*, 2018.
- **Ali W. Azim**, Yannis Le Guennec, Ghislaine Maury, "Spectrally Augmented Hartley Tranfom Precoded ACO-OFDM for VLC", accepted for publication in *IEEE Photonics Technology Letters*, 2018.
- **Ali W. Azim**, Yannis Le Guennec, Ghislaine Maury, "Performance Analysis of Precoded Layered ACO-OFDM for Visible Light Communication Systems ", to be submitted 2018.

Conference Publications

- **Ali W. Azim**, Yannis Le Guennec, Ghislaine Maury, "Enhanced DC-biased optical OFDM for Intensity-Modulated optical OFDM Access Systems", 18th *International Conference on Transparent Optical Networks* (ICTON), Trento, Italy, July, 2016.
- **Ali W. Azim**, Yannis Le Guennec, Ghislaine Maury, "OFDM for Optical Wireless Systems under Severe Clipping Conditions", *IEEE* 2nd *Conference on Advances in Wireless and Optical Communications*, Riga, Latvia, November, 2016.

Communications

- **Ali W. Azim**, Yannis Le Guennec, Ghislaine Maury, "Optical Wireless Communications: Theory and Applications", *GDROndes*, Grenoble, France, 2017.
- **Ali W. Azim**, "Receiver based Iterative PAPR Reduction Methods for Optical OFDM", *Journee des Doctorants*, Grenoble, France, 2016.

Bibliography

[1] Cisco. *Visual Network Index Global Fixed and Mobile Internet Traffic Forecasts*. Tech. rep. Cisco, 2017.

[2] L. Hanzo et al. “Wireless myths, realities, and futures: from 3G/4G to optical and quantum wireless”. In: *Proceedings of the IEEE* 100.Special Centennial Issue (2012), pp. 1853–1888.

[3] J. M. Kahn and J. R. Barry. “Wireless infrared communications”. In: *Proc. IEEE* 85.2 (1997), pp. 265–298.

[4] M. A. Khalighi and M. Uysal. “Survey on free space optical communication: A communication theory perspective”. In: *IEEE Communications Surveys Tutorials* 16.4 (), pp. 2231–2258.

[5] D. Karunatilaka et al. “LED Based Indoor Visible Light Communications: State of the Art”. In: *IEEE communications surveys and tutorials* 17.3 (2015), pp. 1649–1678.

[6] J. K. Kim and E. F. Schubert. “Transcending the replacement paradigm of solid-state lighting”. In: *Optics Express* 16.26 (2008), pp. 21835–21842.

[7] S. Zhao, J. Xu, and O. Trescases. “A dimmable LED driver for visible light communication (VLC) based on LLC resonant DC-DC converter operating in burst mode”. In: *Applied Power Electronics Conference and Exposition (APEC)* (2013), pp. 2144–2150.

[8] H. Ma, L. Lampe, and S. Hranilovic. “Integration of indoor visible light and power line communication systems”. In: *IEEE International Symposium on Power Line Communications and Its Applications (ISPLC)* (2013), pp. 291–296.

[9] M. Biagi, T. Borogovac, and T. D.C. Little. “Adaptive receiver for indoor visible light communications”. In: *Journal of Lightwave Technology* 31.23 (2013), pp. 3676–3686.

[10] C. W. Chow et al. “Adaptive scheme for maintaining the performance of the in-home white-LED visible light wireless communications using OFDM”. In: *Optics Communications* 292 (2013), pp. 49–52.

[11] Y. Wang et al. “Demonstration of 575-Mb/s downlink and 225-Mb/s uplink bi-directional SCM-WDM visible light communication using RGB LED and phosphor-based LED”. In: *Optics express* 21.1 (2013), pp. 1203–1208.

[12] B. A. Ranjha. *OFDM based RF and optical wireless systems*. The Pennsylvania State University, 2014.

[13] A. Jovicic, J. Li, and T. Richardson. “Visible light communication: opportunities, challenges and the path to market”. In: *IEEE Communications Magazine* 51.12 (2013), pp. 26–32.

[14] D. C. O’Brien et al. “Visible light communications: Challenges and possibilities”. In: (2008), pp. 1–5.

[15] M. Z. Chowdhury et al. “A comparative study of optical wireless technologies: Architectures and Applications”. In: *IEEE Access* (2018), pp. 1–21.

[16] M. Uysal and H. Nouri. “Optical wireless communications—An emerging technology”. In: *ICTON* (2014), pp. 1–7.

[17] C. Kachris, K. Bergman, and I. Tomkos. *Optical interconnects for future data center networks*. Springer Science and Business Media, 2012.

[18] P. Toumieux et al. “Optical wireless connected objects for healthcare”. In: *Healthcare technology letters* 2.5 (2015), pp. 118–122.

[19] L. Chevalier, S. Sahuguede, and A. Julien-Vergonjanne. “Optical wireless links as an alternative to radio-frequency for medical body area networks”. In: *IEEE Journal on Selected Areas in Communications* 33.9 (2015), pp. 2002–2010.

[20] H. Haan, M. Gerken, and M Tausendfreund. “Long-range laser communication terminals: Technically interesting, commercially incalculable”. In: *International Symposium on Communication Systems, Networks and Digital Signal Processing (CSNDSP)*. IEEE. 2012, pp. 1–4.

[21] T. Tolker-Nielsen and G. Oppenhauser. “In-orbit test result of an operational optical intersatellite link between ARTEMIS and SPOT4, SILEX”. In: *Free-Space Laser Communication Technologies XIV*. Vol. 4635. International Society for Optics and Photonics. 2002, pp. 1–16.

[22] B. Smutny et al. “5.6 Gbps optical intersatellite communication link”. In: *Free-Space Laser Communication Technologies XXI*. Vol. 7199. International Society for Optics and Photonics. 2009, p. 719906.

[23] R. Boubezari et al. “Smartphone camera based visible light communication”. In: *Journal of Lightwave Technology* 34.17 (2016), pp. 4121–4127.

[24] D. Tsonev, S. Videv, and H. Haas. “Towards a 100 Gb/s visible light wireless access network”. In: *Optics express* 23.2 (2015), pp. 1627–1637.

[25] S. Dimitrov and H. Haas. *Principles of LED light communications: towards networked Li-Fi*. Cambridge University Press, 2015.

[26] H.-H. Lu et al. “A 56 Gb/s PAM4 VCSEL-based LiFi transmission with two-stage injection-locked technique”. In: *IEEE Photonics Journal* 9.1 (2017), pp. 1–8.

[27] H. Haas. “LiFi: Conceptions, misconceptions and opportunities”. In: *IEEE Photonics Conference (IPC)*. IEEE. 2016, pp. 680–681.

[28] M. Ayyash et al. “Coexistence of WiFi and LiFi toward 5G: concepts, opportunities, and challenges”. In: *IEEE Communications Magazine* 54.2 (2016), pp. 64–71.

[29] S. Li, A. Pandharipande, and F. M. J. Willems. “Unidirectional visible light communication and illumination with LEDs”. In: *IEEE Sensors Journal* 16.23 (2016), pp. 8617–8626.

[30] W. Yuanquan and C. Nan. “A high-speed bi-directional visible light communication system based on RGB-LED”. In: *China Communications* 11.3 (2014), pp. 40–44.

[31] W.-S. Tsai et al. “A 20-m/40-Gb/s 1550-nm DFB LD-based FSO link”. In: *IEEE Photonics Journal* 7.6 (2015), pp. 1–7.

[32] A. H. A. El-Malek et al. “Effect of RF Interference on the Security-Reliability Tradeoff Analysis of Multiuser Mixed RF/FSO Relay Networks With Power Allocation”. In: *Journal of Lightwave Technology* 35.9 (2017), pp. 1490–1505.

[33] H. Kaushal and G. Kaddoum. “Optical communication in space: Challenges and mitigation techniques”. In: *IEEE communications surveys and tutorials* 19.1 (2017), pp. 57–96.

[34] I. Takai et al. “LED and CMOS image sensor based optical wireless communication system for automotive applications”. In: *IEEE Photonics Journal* 5.5 (2013), pp. 6801418–6801418.

[35] T. Nguyen et al. “Current status and performance analysis of optical camera communication technologies for 5G networks”. In: *IEEE Access* 5 (2017), pp. 4574–4594.

[36] T. Nguyen, A. Islam, and Y. M. Jang. “Region-of-interest signaling vehicular system using optical camera communications”. In: *IEEE Photonics Journal* 9.1 (2017), pp. 1–20.

[37] D. Yamanaka, S. Haruyama, and M. Nakagawa. “The design of high-speed image sensor chip for receiving the data of visible-light ID system”. In: *IEICE tech. rep* 107.300 (2007), pp. 97–102.

[38] T. Yamazato et al. “Vehicle motion and pixel illumination modeling for image sensor based visible light communication”. In: *IEEE Journal on Selected Areas in Communications* 33.9 (2015), pp. 1793–1805.

[39] M. S. Islim and H. Haas. “Modulation techniques for Lifi”. In: *ZTE communications* 14.2 (2016), pp. 29–40.

[40] M.-A. Khalighi et al. “PAM and CAP based Transmission Schemes for Visible-Light Communications”. In: *IEEE Access* 5 (2017), pp. 27002–27013.

[41] A. G. Bell. “Selenium and the photophone”. In: *Nature* 22.569 (1880), pp. 500–503.

[42] M. I. Nathan et al. “Stimulated emission of radiation from GaAs p-n junctions”. In: *Applied Physics Letters* 1.3 (1962), pp. 62–64.

[43] R. N. Hall et al. “Coherent light emission from GaAs junctions”. In: *Physical Review Letters* 9.9 (1962), p. 366.

[44] F. E. Goodwin. “A review of operational laser communication systems”. In: *SPIE milestone series* 30 (1991), pp. 3–9.

[45] F. R. Gfeller and U. Bapst. “Wireless in-house data communication via diffuse infrared radiation”. In: *Proceedings of the IEEE* 67.11 (1979), pp. 1474–1486.

[46] P. Barker and A. C. Boucouvalas. “Performance modeling of the IrDA protocol for infrared wireless communications”. In: *IEEE Communications magazine* 36.12 (1998), pp. 113–117.

[47] D. C. O’Brien et al. “Gigabit optical wireless for a Home Access Network”. In: (2009), pp. 1–5.

[48] M. Faulwaßer, F. Deicke, and T. Schneider. “10 Gbit/s bidirectional optical wireless communication module for docking devices”. In: (2014), pp. 512–517.

[49] G. W. Marsh and J. M. Kahn. “Performance evaluation of experimental 50-Mb/s diffuse infrared wireless link using on-off keying with decision-feedback equalization”. In: *IEEE Transactions on Communications* 44.11 (1996), pp. 1496–1504.

[50] J. B. Carruthers and J. M. Kahn. “Angle diversity for nondirected wireless infrared communication”. In: 3 (1998), pp. 1665–1670.

[51] S. Jivkova and M. Kavehrad. “Holographic optical receiver front end for wireless infrared indoor communications”. In: *Applied optics* 40.17 (2001), pp. 2828–2835.

[52] H. Haas, C. Chen, and D. O’Brien. “A guide to wireless networking by light”. In: *Progress in Quantum Electronics* 55 (2017), pp. 88–111.

[53] S. D. Dimitrov. “Analysis of OFDM-based intensity modulation techniques for optical wireless communications”. In: (2013).

[54] H. Elgala, R. Mesleh, and H. Haas. “Indoor broadcasting via white LEDs and OFDM”. In: *IEEE Transactions on consumer electronics* 55.3 (2009).

[55] T Komine and M. Nakagawa. “Performance evaluation of visible-light wireless communication system using white LED lightings”. In: 1 (2004), pp. 258–263.

[56] T. Komine and M. Nakagawa. “Fundamental analysis for visible-light communication system using LED lights”. In: *IEEE Transactions on Consumer Electronics* 50.1 (2004), pp. 100–107.

[57] J. Grubor et al. “Broadband information broadcasting using LED-based interior lighting”. In: *Journal of Lightwave technology* 26.24 (2008), pp. 3883–3892.

[58] G. Pang et al. “Led traffic light as a communications device”. In: (1999), pp. 788–793.

[59] M. Afgani et al. “Radio frequency signature correlation based speed estimation for indoor positioning”. In: *Journal of Communications* 4.2 (2009), pp. 96–107.

[60] “Visible Light Communication Consortium (VLCC)”. In: *[Online]* (2007).

[61] A.M. Khalid et al. “1-Gb/s transmission over a phosphorescent white LED by using rate-adaptive discrete multitone modulation”. In: *IEEE Photonics Journal* 4.5 (2012), pp. 1465–1473.

[62] G. Cossu et al. “3.4 Gbit/s visible optical wireless transmission based on RGB LED”. In: *Optics express* 20.26 (2012), B501–B506.

[63] IEEE Standard Association et al. “IEEE Std. for Local and metropolitan area networks-Part 15.7: Short-Rang Wireless Optical Communication Using Visible Light”. In: *IEEE computer Society* (2011).

[64] “Home Gigabit Access Network”. In: *[Online]* (2012).

[65] A. Neumann et al. “Four-color laser white illuminant demonstrating high color-rendering quality”. In: *Optics express* 19.104 (2011), A982–A990.

[66] C. Basu, M. Meinhardt-Wollweber, and B. Roth. “Lighting with laser diodes”. In: *Advanced Optical Technologies* 2.4 (2013), pp. 313–321.

[67] P. H. Pathak et al. “Visible light communication, networking, and sensing: A survey, potential and challenges”. In: *IEEE communications surveys and tutorials* 17.4 (2015), pp. 2047–2077.

[68] H Le Minh et al. “100-Mb/s NRZ visible light communications using a postequalized white LED”. In: *IEEE Photonics Technology Letters* 21.15 (2009), pp. 1063–1065.

[69] J.M.M. Santos et al. “Visible light communication using InGaN optical sources with AlInGaP nanomembrane down-converters”. In: *Optics express* 24.9 (2016), pp. 10020–10029.

[70] I. Dursun et al. “Perovskite nanocrystals as a color converter for visible light communication”. In: *Acs Photonics* 3.7 (2016), pp. 1150–1156.

[71] R. G. Baets et al. “Resonant-cavity light-emitting diodes: a review”. In: *Light-Emitting Diodes: Research, Manufacturing, and Applications VII*. Vol. 4996. International Society for Optics and Photonics. 2003, pp. 74–87.

[72] L. Geng et al. “3 Gbit/s LED-based step index plastic optical fiber link using multilevel pulse amplitude modulation”. In: *Optical Fiber Communication Conference*. Optical Society of America. 2013, OTh4A–1.

[73] J. Armstrong, R. J. Green, and M. D. Higgins. “Comparison of three receiver designs for optical wireless communications using white LEDs”. In: *IEEE Communications Letters* 16.5 (2012), pp. 748–751.

[74] J. M. Kahn and J. R. Barry. “Wireless infrared communications”. In: *Proceedings of the IEEE* 85.2 (1997), pp. 265–298.

[75] J. Liu et al. “Foundational analysis of spatial optical wireless communication utilizing image sensor”. In: *IEEE International Conference on Imaging Systems and Techniques*. IEEE. 2011, pp. 205–209.

[76] C. Chen, W.-D. Zhong, and D. Wu. “Non-Hermitian symmetry orthogonal frequency division multiplexing for multiple-input multiple-output visible light communications”. In: *Journal of Optical Communications and Networking* 9.1 (2017), pp. 36–44.

[77] Z. Wang et al. “Towards self-powered solar panel receiver for optical wireless communication”. In: *IEEE International Conference on Communications*. IEEE. 2014, pp. 3348–3353.

[78] S. Schmid et al. “An LED-to-LED Visible Light Communication system with software-based synchronization”. In: *IEEE Globecom Workshops*. IEEE. 2012, pp. 1264–1268.

[79] D. Giustiniano, N. O. Tippenhauer, and S. Mangold. “Low-complexity visible light networking with LED-to-LED communication”. In: *IFIP Wireless Days*. IEEE. 2012, pp. 1–8.

[80] A. W. Azim, Y. Le Guennec, and G. Maury. “Decision-directed iterative methods for PAPR reduction in optical wireless OFDM systems”. In: *Opt. Commun.* 389 (2017), pp. 318–330.

[81] A. Weiss, A. Yeredor, and M. Shtaif. “Iterative Symbol Recovery for Power-Efficient DC-Biased Optical OFDM Systems”. In: *J. Lightw. Techn.* 34.9 (2016), pp. 2331–2338.

[82] D. Tsonev et al. “A 3-Gb/s single-LED OFDM-based wireless VLC link using a gallium nitride μLED”. In: *IEEE Photon. Technol. Lett.* 26.7 (2014), pp. 637–640.

[83] L. Grobe and K.-D. Langer. “Block-based PAM with frequency domain equalization in visible light communications”. In: *IEEE Globecom Workshops*. IEEE. 2013, pp. 1070–1075.

[84] M. Wolf et al. “Transmission schemes for visible light communications in multipath environments”. In: *Intl. Conf. on Transparent Opt. Networks* (2015), pp. 1–7.

[85] J. R. Barry et al. “Simulation of multipath impulse response for indoor wireless optical channels”. In: *IEEE journal on selected areas in communications* 11.3 (1993), pp. 367–379.

[86] K. Lee, H. Park, and J. R. Barry. “Indoor channel characteristics for visible light communications”. In: *IEEE Commun. Lett.* 15.2 (2011), pp. 217–219.

[87] A. Nuwanpriya et al. “PAM-SCFDE for optical wireless communications”. In: *Journal of Lightwave Technology* 33.14 (2015), pp. 2938–2949.

[88] F. Tavernier and M. S. J. Steyaert. “High-speed optical receivers with integrated photodiode in 130 nm CMOS”. In: *IEEE Journal of Solid-State Circuits* 44.10 (2009), pp. 2856–2867.

[89] D. A. Tsonev. “High speed energy efficient incoherent optical wireless communications”. In: (2015).

[90] Kerstin Schneider and Horst Zimmermann. *Highly sensitive optical receivers*. Springer, 2006.

[91] Z. Ghassemlooy, W. Popoola, and S. Rajbhandari. *Optical wireless communications: system and channel modelling with MATLAB®*. CRC press, 2012.

[92] S. Dimitrov, S. Sinanovic, and H. Hass. “Clipping noise in OFDM-based optical wireless communication systems”. In: *IEEE Trans. Commun.* 60.4 (2012), pp. 1072–1081.

[93] H. Elgala, R. Mesleh, and H. Haas. “Non-linearity effects and predistortion in optical OFDM wireless transmission using LEDs”. In: *Intl. J. of Ultra Wideband Commun. Syst.* 1.2 (2009), pp. 143–150.

[94] R. Mesleh, H. Elgala, and H. Haas. “LED nonlinearity mitigation techniques in optical wireless OFDM communication systems”. In: *J. Opt. Commun. and Network.* 4.11 (2012), pp. 865–875.

[95] H.-J. Jang et al. “PWM-based PPM format for dimming control in visible light communication system”. In: *nternational Symposium on Communication Systems, Networks Digital Signal Processing (CSNDSP)*. IEEE. 2012, pp. 1–5.

[96] S. He et al. “M-ary variable period modulation for indoor visible light communication system”. In: *IEEE communications letters* 17.7 (2013), pp. 1325–1328.

[97] S. Arnon. “The effect of clock jitter in visible light communication applications”. In: *journal of lightwave technology* 30.21 (2012), pp. 3434–3439.

[98] H. Marshoud et al. “Non-orthogonal multiple access for visible light communications”. In: *IEEE Photon. Technol. Lett* 28.1 (2016), pp. 51–54.

[99] Carruthers J. B. and J. M. Kahn. “Multiple-subcarrier modulation for nondirected wireless infrared communication”. In: *IEEE J. Sel. Areas Commun.* 14.3 (1996), pp. 538–546.

[100] J. Armstrong and A. J. Lower. “Power efficient optical OFDM”. In: *Electron. Lett* 42.6 (2006), pp. 370–372.

[101] J. Armstrong. “OFDM for optical communications”. In: *J. Lightw. Tech.* 27.3 (2009), pp. 189–204.

[102] H. Elgala, R. Mesleh, and H. Haas. “Indoor optical wireless communication: potential and state-of-the-art”. In: *IEEE Commun. Mag.* 49.9 (2011).

[103] S. C. J. Lee et al. “PAM-DMT for intensity-modulated and direct-detection optical communication systems”. In: *IEEE Photonics Technology Letters* 21.23 (2009), pp. 1749–1751.

[104] N. Fernando, Y. Hong, and E. Viterbo. “Flip-OFDM for unipolar communication systems”. In: *IEEE Trans. Commun.* 60.12 (2012), pp. 3726–3733.

[105] D. Tsonev, S. Sinanovic, and H. Haas. “Novel unipolar orthogonal frequency division multiplexing (U-OFDM) for optical wireless”. In: *IEEE Veh. Tech. Conf.* (2012), pp. 1–5.

[106] J. Armstrong and B. J. C. Schmidt. “Comparison of asymmetrically clipped optical OFDM and DC-biased optical OFDM in AWGN”. In: *IEEE Commun. Lett.* 12.5 (2008), pp. 343–345.

[107] Q. Wang et al. “Layered ACO-OFDM for intensity-modulated direct-detection optical wireless transmission”. In: *Opt. Express* 23.9 (2015), pp. 12382–12393.

[108] X. Zhang et al. “Performance Analysis of Layered ACO-OFDM”. In: *IEEE Access* 5 (2017), pp. 18366–18381.

[109] M. S. Islim and H. Haas. “Augmenting the spectral efficiency of enhanced PAM-DMT-based optical wireless communications”. In: *Opt. Express* 24.11 (2016), pp. 11932–11949.

[110] D. Tsonev, S. Videv, and H. Haas. “Unlocking spectral efficiency in intensity modulation and direct detection systems”. In: *IEEE J. Selec. Areas Commun.* 33.9 (2015), pp. 1758–1770.

[111] J. Zhou and Y. Qiao. “Low-PAPR Asymmetrically Clipped Optical OFDM for Intensity-Modulation Direct-Detection Systems”. In: *IEEE Photon. J.* 7.3 (2015), pp. 1–8.

[112] L. Chen, B. Krongold, and J. Evans. “Diversity combining for asymmetrically clipped optical OFDM in IM/DD channels”. In: *IEEE Globecom*. 2009, pp. 1–6.

[113] D. J. F. Barros, S. K. Wilson, and J. M. Kahn. “Comparison of orthogonal frequency-division multiplexing and pulse-amplitude modulation in indoor optical wireless links”. In: *IEEE Trans. Commun.* 60.1 (2012), pp. 153–163.

[114] S. D. Dissanayake and Jean. Armstrong. “Comparison of ACO-OFDM, DCO-OFDM and ADO-OFDM in IM/DD Systems”. In: *J. Lightwav. Tech.* 31.7 (2013), pp. 1063–1072.

[115] J. Zhou et al. “Asymmetrically Clipped Optical Fast OFDM Based on Discrete Cosine Transform for IM/DD Systems”. In: *J. Lightwav. Tech.* 33.9 (2015), pp. 1920–1927.

[116] J. Armstrong and B. J. C. Schmidt. “Comparison of asymmetrically clipped optical OFDM and DC-biased optical OFDM in AWGN”. In: *IEEE Commun Letters* 12.5 (2008), pp. 343–345.

[117] X. Li, R. Mardling, and J. Armstrong. “Channel capacity of IM/DD optical communication systems and of ACO-OFDM”. In: *IEEE ICC*. 2007, pp. 2128–2133.

[118] S. D. Dissanayake and J. Armstrong. “Novel techniques for combating DC offset in diversity combined ACO-OFDM”. In: *IEEE Commun. Letters* 15.11 (2011), pp. 1237–1239.

[119] K. Acolatse, Y. Bar-Ness, and S. K. Wilson. “Novel techniques of single-carrier frequency-domain equalization for optical wireless communications”. In: *EURASIP J. Adv. Sig. Process.* 2011 (2011), p. 4.

[120] B. Ranjha, Z. Zhou, and M. Kavehrad. “Performance analysis of precoding-based asymmetrically clipped optical orthogonal frequency division multiplexing wireless system in additive white Gaussian noise and indoor multipath channel”. In: *Opt. Eng.* 53.8 (2014), pp. 086102–086102.

[121] C. Wu, H. Zhang, and W. Xu. “On visible light communication using LED array with DFT-spread OFDM”. In: *IEEE ICC* (2014), pp. 3325–3330.

[122] J. Zhou and Y. Qiao. “Low-peak-to-average power ratio and low-complexity asymmetrically clipped optical orthogonal frequency-division multiplexing uplink transmission scheme for long-reach passive optical network”. In: *Optics letters* 40.17 (2015), pp. 4034–4037.

[123] R. N. Bracewell. "Discrete Hartley transform". In: *JOSA* 73.12 (1983), pp. 1832–1835.

[124] J. Zhou et al. "Low-PAPR Layered/Enhanced ACO-SCFDM for Optical-Wireless Communications". In: *IEEE Photonics Technology Letters* 30.2 (2017), pp. 165–168.

[125] O. Saied et al. "Single carrier optical FDM in visible light communication". In: *IEEE CSNDSP* (2016), pp. 1–5.

[126] Ali W. Azim, Y. Le Guennec, and G. Maury. "Enhanced DC-Biased Optical OFDM for Intensity-Modulated Optical OFDM Access Systems". In: *Intl. Conf. on Transparent Opt. Networks* (2016), pp. 1–4.

[127] Ali W. Azim, Y. Le Guennec, and G. Maury. "OFDM for optical wireless systems under severe clipping conditions". In: *IEEE Intl. Conf. Advances in Wireless and Optical Commun.* (2016), pp. 1–4.

[128] Z. P. Wang et al. "Combining discrete cosine transform with clipping for PAPR reduction in intensity-modulated OFDM systems". In: *Optoelectronics Letters* 10.5 (2014), pp. 356–359.

[129] W. Xu et al. "ACO-OFDM-specified recoverable upper clipping with efficient detection for optical wireless communications". In: *IEEE Photon. J.* 6.5 (2014), pp. 1–17.

[130] H. Zhang, L.-L. Yang, and L. Hanzo. "Piecewise companding transform assisted optical-OFDM systems for indoor visible light communications". In: *IEEE Access* 5 (2017), pp. 295–311.

[131] D. Abed and A. Medjouri. "Discrete sliding norm transform-based 50% PAPR reduction in asymmetrically clipped optical OFDM systems for optical wireless communications". In: *Electronics Letters* 51.25 (2015), pp. 2128–2130.

[132] L. Nadal et al. "Comparison of peak power reduction techniques in optical OFDM systems based on FFT and FHT". In: *Intl. Conf. on Transparent Opt. Networks* (2011), pp. 1–4.

[133] J. Bai et al. "PAPR reduction based on tone reservation scheme for DCO-OFDM indoor visible light communications". In: *Optics Express* 25.20 (2017), pp. 24630–24638.

[134] W. O. Popoola, Z. Ghassemlooy, and B. G. Stewart. "Pilot-assisted PAPR reduction technique for optical OFDM communication systems". In: *J. of Lightw. Tech.* 32.7 (2014), pp. 1374–1382.

[135] R. You and J. M. Kahn. "Average power reduction techniques for multiple-subcarrier intensity-modulated optical signals". In: *IEEE Trans. Commun.* 49.12 (2001), pp. 2164–2171.

[136] W. Kang and S. Hranilovic. "Power reduction techniques for multiple-subcarrier modulated diffuse wireless optical channels". In: *IEEE Trans. Commun.* 56.2 (2008), pp. 279–288.

[137] H. Zhang, Y. Yuan, and W. Xu. "PAPR reduction for DCO-OFDM visible light communications via semidefinite relaxation". In: *IEEE Photon. Technol. Lett.* 26.17 (2014), pp. 1718–1721.

[138] T. Mao et al. "Ellipse-based DCO-OFDM for visible light communications". In: *Optics Communications* 360 (2016), pp. 1–6.

[139] S. C. Thompson et al. "Constant envelope OFDM". In: *IEEE transactions on communications* 56.8 (2008).

[140] A. Ali et al. "Receiver-based recovery of clipped OFDM sig. for PAPR reduction: A Bayesian approach". In: *IEEE Access* 2 (2014), pp. 1213–1224.

[141] Z. Yu, R. J. Baxley, and G. T. Zhou. "EVM and achievable data rate analysis of clipped OFDM signals in visible light communication". In: *EURASIP J. Wireless Commun. Network.* 2012.1 (2012), pp. 1–16.

[142] D. Kim and G. L. Stüber. "Clipping noise mitigation for OFDM by decision-aided reconstruction". In: *IEEE Commun. Lett.* 3.1 (1999), pp. 4–6.

[143] J. Tellado, L. M. C. Hoo, and J. M. Cioffi. "Maximum-likelihood detection of nonlinearly distorted multicarrier symbols by iterative decoding". In: *IEEE Trans. Commun.* 51.2 (2003), pp. 218–228.

[144] J. J. Bussgang. “Crosscorrelation functions of amplitude-distorted Gaussian signals”. In: *Res. Lab. Electron, Masssachusetts Inst. Tech., Cambridge, MA, USA, Tech. Rep* (1952).

[145] H. Ochiai and H. Imai. “Performance analysis of deliberately clipped OFDM signals”. In: *IEEE Trans. Commun.* 50.1 (2002), pp. 89–101.

[146] K. Cho and D. Yoon. “On the general BER expression of one-and two-dimensional amplitude modulations”. In: *IEEE Trans. Commun.* 50.7 (2002), pp. 1074–1080.

[147] J. K. Perin, M. Sharif, and J. M. Kahn. “Modulation schemes for single-laser 100 Gb/s links: Multicarrier”. In: *J. Lightw. Techn.* 33.24 (2015), pp. 5122–5132.

[148] S. G. Johnson and M. Frigo. “A modified split-radix FFT with fewer arithmetic operations”. In: *IEEE Trans. Sig. Process.* 55.1 (2007), pp. 111–119.

[149] H. Marshoud et al. “Optical Non-Orthogonal Multiple Access for Visible Light Communication”. In: *arXiv preprint arXiv:1704.07621* (2017).

[150] D. Tsonev, S. Videv, and H. Haas. “Light fidelity (Li-Fi): towards all-optical networking”. In: *SPIE OPTO* (2013), pp. 900702–900702.

[151] Y. S. Cho et al. *MIMO-OFDM wireless communications with MATLAB*. John Wiley & Sons, 2010.

[152] F. Barrami et al. “A novel FFT/IFFT size efficient technique to generate real time optical OFDM signals compatible with IM/DD systems”. In: *Euro. Microw. Conf.* (2013), pp. 1247–1250.

[153] N. Wu and Y.l Bar-Ness. “A novel power-efficient scheme asymmetrically and symmetrically clipping optical (ASCO)-OFDM for IM/DD optical systems”. In: *EURASIP J. Adv. Sig. Process.* 2015.1 (2015), p. 3.

[154] H. Elgala, R. Mesleh, and H. Haas. “Practical considerations for indoor wireless optical system implementation using OFDM”. In: *IEEE ConTEL* (2009), pp. 25–29.

[155] J. Wang et al. “PAPR analysis for OFDM visible light communication”. In: *Opt. Express* 24.24 (2016), pp. 27457–27474.

[156] P. Schniter. “Low-complexity equalization of OFDM in doubly selective channels”. In: *IEEE Trans. Sig. Process.* 52.4 (2004), pp. 1002–1011.

[157] J. Zhou et al. “An improved scheme for Flip-OFDM based on Hartley transform in short-range IM/DD systems”. In: *Opt. Express* 22.17 (2014), pp. 20748–20756.

[158] A. J. Lowery. “Comparisons of spectrally-enhanced asymmetrically-clipped optical OFDM systems”. In: *Optics express* 24.4 (2016), pp. 3950–3966.

[159] M. M. A. Mohammed, C. He, and J. Armstrong. “Diversity Combining in Layered Asymmetrically Clipped Optical OFDM”. In: *Journal of Lightwave Technology* 35.11 (2017), pp. 2078–2085.

[160] J. Zhou et al. “Faster-than-Nyquist non-orthogonal frequency-division multiplexing based on fractional Hartley transform”. In: *Optics letters* 41.19 (2016), pp. 4488–4491.

[161] J. Zhou et al. “Faster-than-Nyquist Non-Orthogonal Frequency-Division Multiplexing for Visible Light Communications”. In: *IEEE Access* 6 (2018), pp. 17933–17941.